Università degli Studi di Bologna
Facoltà di Scienze Matematiche Fisiche
e Naturali

Dottorato di Ricerca in Fisica
XII Ciclo

The Study of Open Beauty in Photoproduction at Hera

Candidato:
Dr. Nicola Coppola

Tutore:
Ch.mo Prof. Maurizio Basile

Coordinatore:
Ch.mo Prof. Giulio Pozzi

Contents

Introduction **1**

1 The HERA collider and the ZEUS detector **3**
1.1 The accelerator 3
1.2 Performance of HERA 6
1.3 The ZEUS Detector 9
1.4 The coordinate system of ZEUS 10
1.5 The magnetic system 11
1.6 Inner tracking devices 12
1.6.1 Vertex Detector (VXD) 12
1.6.2 Central Tracking Detector (CTD) 13
1.6.3 Rear and Forward Tracking Detector (RTD, FTD) 15
1.6.4 Transition Radiation Detector (TRD) 15
1.6.5 dE/dx determination 15
1.7 The Calorimetry system 15
1.7.1 The Uranium-scintillator Calorimeter (UCAL) 16
1.7.2 The Backing Calorimeter (BAC) 18
1.8 The detection system of muons 20
1.8.1 The Forward Muon detector (FMUON) 20
1.8.1.1 Limited Streamer Tube planes (LST) 21
1.8.1.2 The Drift Chambers (DC) 21
1.8.1.3 The Large Angle coverage planes (LW) 22
1.8.1.4 The trigger system of FMUON 22
1.8.2 The Barrel and Rear Muon chambers (BRMUON) 22
1.9 The LUMI detector 25
1.10 The forward scattered proton detectors 26
1.10.1 VETOWall, C5, SRTD 28
1.11 The ZEUS trigger system 28
1.11.1 The First Level Trigger (FLT) 28
1.11.2 The Second Level Trigger (SLT) 30
1.11.3 The Third Level Trigger (TLT) 34

2 Physics at HERA **35**
2.1 ep Processes . . . 35
2.2 Structure Functions . . . 37
2.3 QCD Improved Parton Model . . . 39
2.4 The Evolution of Partonic Densities . . . 40
2.5 The Deep Inelastic Scattering (DIS) Regime . . . 41
2.6 The Photoproduction Regime . . . 44
2.7 Direct Photoproduction . . . 46
2.8 Resolved Photoproduction . . . 46
2.9 Generalised Photoproduction Model . . . 47
2.10 The Structure of the Photon . . . 48
2.10.1 Dijet Photoproduction Results at HERA . . . 49
2.11 The Physics of Heavy quarks . . . 53
2.12 Heavy Quark at Fixed Target Experiments . . . 53
2.13 Heavy Quark Production at HERA . . . 54
2.13.1 Perturbative Formalism of Heavy Quark Photoproduction . . . 56
2.13.2 Massive Scheme . . . 57
2.13.3 Massless Scheme . . . 58
2.13.4 Heavy Quark Results from HERA . . . 59
2.14 Beauty Production at Hadron Colliders . . . 62
2.15 Identification of Open Beauty at HERA . . . 63
2.16 Fragmentation of Heavy Quarks . . . 64
2.17 Semi-leptonic Decays of Heavy Quarks . . . 66
2.18 Heavy Quark Jets . . . 67
2.19 Summary . . . 67

3 Event Reconstruction **69**
3.1 Reconstruction of y and Q^2 . . . 69
3.1.1 Electron Method . . . 69
3.1.2 Jacquet-Blondel Method . . . 70
3.2 Jet Reconstruction . . . 70
3.2.1 Cone Algorithms . . . 71
3.2.2 Clustering Algorithm . . . 71
3.3 μ Reconstruction . . . 73
3.3.1 The Bremat matching package . . . 73
3.4 The Mpmatch matching package . . . 74
3.4.1 Definition of a FMUON track . . . 75
3.5 Reconstruction of $x_\gamma^{\rm obs}$ and $p_T^{\rm rel}$ . . . 75

4 The Monte Carlo simulation **77**
4.1 Generators . . . 79
4.1.1 HERWIG Generator . . . 79
4.1.2 PYTHIA Generator . . . 80
4.2 Monte Carlo Samples Generated . . . 80
4.3 Jet Energy Corrections . . . 84
4.3.1 Jet Resolutions . . . 84
4.3.2 Correction of Jet Energy . . . 85
4.4 Correction of y_{JB} . . . 89
4.5 Corrections for the Presence of a Muon in the Event . . . 90

5 Analysis and data Selection **93**
5.1 The data sample . . . 93
5.2 The Trigger chainfor dijet event selection . . . 93
5.2.1 Jet First Level Trigger (FLT) . . . 93
5.2.2 Jet Second Level Trigger (SLT) . . . 94
5.2.3 Jet Third Level Trigger (TLT) . . . 95
5.3 Efficiency of Trigger Chain for jet selection . . . 96
5.3.1 Jet FLT . . . 96
5.3.2 Jet SLT . . . 96
5.3.3 Jet TLT . . . 96
5.4 The Trigger chain for Muon selection . . . 96
5.4.1 First Level Trigger for Muons in the BR Regions . . . 97
5.4.2 Second Level Trigger for Muons in the BR Regions . . . 100
5.4.3 Third Level Trigger for Muons: GLOEXO . . . 100
5.5 Efficiency of Trigger Chain for BRMUON selection . . . 100
5.5.1 Muon FLT . . . 101
5.5.2 Muon SLT . . . 101
5.5.3 Muon TLT . . . 101
5.6 Efficiency of the Online Chain for FMUON selection . . . 102
5.7 Offline Selection . . . 103
5.7.1 Jet and Photoproduction Selection . . . 103
5.7.2 Muon selection . . . 104
5.7.2.1 Muon selection in the FMUON region . . . 105
5.7.2.2 Muon selection in the BRMUON region . . . 108
5.7.3 Association μ-jet . . . 112
5.8 Background analysis . . . 113
5.8.1 Determination and subtraction of the background from light quark events . . . 114
5.8.2 Determination of the background coming from charm events 115
5.9 Comparison of Data and Monte Carlo . . . 115

6 Results **125**
6.1 The final sample 125
6.2 $p_T^{\rm rel}$ Fit and Determination of the Beauty Fraction 125
6.2.1 Systematic errors to the $p_T^{\rm rel}$ fit 127
6.3 $x_\gamma^{\rm obs}$ distribution 130
6.4 Cross sections 131
6.5 Study of Systematic Uncertainties 134
6.5.1 Uncertainties Arising From the Kinematic Cuts 134
6.5.2 Uncertainties Arising From the Muon Selection 138
6.5.3 Uncertainties Arising From the Limited Knowledge of Detector Efficiency 139
6.5.4 Uncertainties Arising From the Energy Scale 139
6.5.5 Uncertainties Arising From the Model Dependency and Fitting Procedure 139
6.6 Comparison with other measurement 140
6.6.1 Semi-leptonic Decay of b to Electrons 140

Conclusions **143**

A The third level trigger for μ: GLOEXO **145**
A.1 The reconstruction of muons within the B(R)MUI chambers 145
A.2 The Selection of reconstructed tracks inside the CTD 146
A.3 Identification of the global trajectory 147

B The Bremat matching package **151**

Bibliography **155**

List of figures **173**

List of tables **176**

Acknowledgements **177**

Introduction

The study of beauty quark production is very important in high energy physics. Infact the presence of a quite high mass ensures that perturbative QCD can be used reliably to calculate cross section and this allows more stringent tests of the theory when comparing to the data.

With fixed target experiments it was not possible to search for b-production in ep or γp interactions because of the low center-of-mass energy available. These is now possible with the advent of HERA (*Hadron Elektron Ring Anlage*), the electron (positron) proton collider built at the DESY laboratory in Hamburg, where a center-of-mass energy of 300 GeV is reached, two order of magnitude higher than in previous experiments.

The available processes in electron-proton interactions can be divided into two large classes: deep inelastic scattering processes, where the electroweak propagator reaches maximum virtuality equal to 10^5 GeV^2, and photoproduction processes where an almost real photon, emitted by the incoming electron (positron), interacts with the proton.

Both the H1 and ZEUS experiment have published results on photoproduction of hidden beauty in bound states. Also the photoproduction of open $b/\bar{b}$ produced pairs has been investigated by identifying events with two jets and the presence of a lepton coming from semi-leptonic decay products. The H1 experiment has published an analysis on open beauty production looking for dijet events with a central muon. The ZEUS experiment has, instead, shown preliminary results obtained with a sample where the beauty production is tagged via the reconstruction of two or more jets and the identification of a central electron.

In this thesis an analysis of dijet events in photoproduction with an accompanying muon is reported. The study is the first one performed on data collected by the ZEUS experiment and extends the pseudorapidity range where the μ particle is identified by a factor of two compared with the H1 result.

Chapter 1

The HERA collider and the ZEUS detector

1.1 The accelerator

HERA, the *Hadron Elektron Ring Anlage*, is the first and the only lepton-proton collider existing in the world. It has been built at the *Deutsches Elektronen Synchrotron* laboratory (DESY), in Hamburg, Germany. The ring has a circumference of 6.3 km and runs underground the town, at about 30 meter below the ground level. The HERA collider and its pre-accelerator complex are shown in Figure 1.1.

Electrons or positrons[1] are pre-accelerated in a linear accelerator, LINAC I (e^-) or LINAC II (e^+). After accumulation in a small storage ring, they are injected into DESY II to be accelerated up to 7 GeV and transferred to PETRA II. This operation is repeated until PETRA is filled with 70 bunches, each with $4. \cdot 10^{10}$ electrons (positrons). The leptons are accelerated to 12 GeV in PETRA and then injected into the electron ring of HERA. The procedure is repeated twice to fill HERA completely with 210 bunches.

The procedure to obtain the proton beam starts with H^- accelerated to 50 MeV H^- with the aid of a LINAC. The negatively charged ions are stripped upon their injection into DESY III, to be accelerated to 7.5 GeV and transferred to PETRA II. The protons are, then, accelerated further to 40 GeV before injection into the superconducting HERA proton ring.

In HERA, electrons or positrons are accelerated from the injection energy of 12 GeV to 27.5 GeV. In a second ring positioned above the electron ring, protons are accelerated from 40 GeV to 820 GeV (since the beginning of the year 1998

[1]Both these leptons can be accelerated by the machine. In the remaining part of this work we will use the word electron indifferently to indicate both the particle and its anti-particle, unless it is needed to specify the charge of the lepton involved in the description of the actual subject.

Main General Design Parameters of HERA		
Construction time	May 1984 – November 1990	
Circumference of the HERA tunnel	6335.83 m	
Depth underground	15 m – 30 m	
Number of pre–accelerators for HERA	6 (LINAC I, LINAC II, DESY II, PETRA II, H-LINAC, DESY III)	
The HERA Beams	**Electron**	**Proton**
Centre of mass energy (actual)	314 (300) GeV	
Nominal energy (actual)	30 (27.5) GeV	820 GeV
Relative energy spread $\Delta E/E$	10^{-3}	10^{-4}
Injection energy	12 GeV	40 GeV
Luminosity per interaction point	1.6 x 10^{31} $cm^{-2}s^{-1}$	
Design average current	58 mA	163 mA
Particles per bunch	3.65 x 10^{10}	10^{11}
Number of buckets	220	220
Maximum number of bunches	210	210
Beam crossing angle	head–on collision, 0 mrad	
Bunch distance	28.8 m (96ns)	
Bunch length at maximum energy (σ_z)	0.85 cm	19 cm
Beam width at the interaction points (σ_x)	0.286 mm	0.28 mm
Beam height at the interaction points (σ_y)	0.06 mm	0.058 mm
Synchrotron radiation loss per turn	125 MeV	6 x 10^{-6} MeV
Polarization time at 30 GeV	35 min	—
Filling time	15 min	20 min
The HERA Storage Rings	**Electron**	**Proton**
Total number of magnets	2009	1833
Main dipoles	465	422 (s.c.)
Main quadrupoles	605	224 (s.c.)
Number of conventional rf cavities	82	2 (4)
Number of superconducting rf cavities	16	—
Frequency of the rf cavities	500 MHz	52 (208) MHz
Voltage of the rf cavities	200 MV	2.4 MV
Bending radius in the arcs	608.1 m	584 m
Field strength (I_{nom}) of the main dipoles at nominal energy	0.165 T (@ 6767 A)	4.68 T (@ 5024 A)

Table 1.1: Main design parameters of HERA [1]

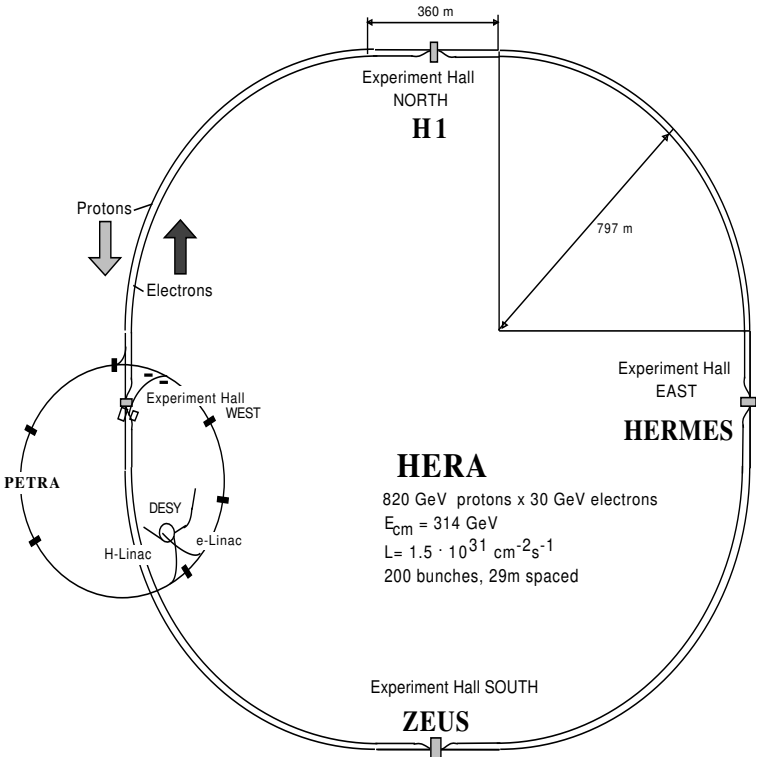

Figure 1.1: Scheme of the *ep* collider HERA, main design values are shown. The South zone accommodates the ZEUS detector.

to 920 GeV). In the proton ring, superconducting bending magnets are used.

HERA's nominal beam energies of 27.5 GeV for electrons and 820 GeV (920 GeV) for protons result in a center-of-mass (c.m.) energy, $2\sqrt{E_1 E_2}$, of 300 GeV (318 GeV), more than an order of magnitude larger than the c.m. energy reached by fixed target deep inelastic scattering experiments (with electron beams at SLAC [2, 3] and muon and neutrino beams at CERN [4, 5] and Fermilab [6, 7]).

Four experimental halls have been built underground to accommodate an equal number of experiments.

The two rings cross each other at two points, where *ep* collisions occur. These are studied with the H1 [8] and ZEUS [9] detectors in the North and South experimental halls respectively. (ZEUS will be described in detail afterward in this chapter.)

The HERMES experiment, in the East hall, studies the scattering of polarized electrons (available at HERA, polarization 60%) on an internal gas-jet target [10]. A fourth experiment, HERA-B [11], is being built to study B-physics by using wire targets in the proton beam halo in the West hall.

HERA operates with a total number of 220 "buckets", equally spaced 96 ns apart, that can be filled with "bunches" of particles. Some buckets are left

empty: when paired with a full bucket, these, so-called "unpaired bunches", allow to estimate the background of interactions originating from the electron or proton beam with the residual gas in the beampipe, beamwall or collimators. When paired with another empty bunch, the non-beam related background can be estimated.

At the moment the running conditions are such that there are on the average 174 colliding bunches, 16 lepton and 6 proton unpaired bunches, while we trigger on 200 bunches; the average currents at the beginning of a fill are of $35 \div 45$ mA for the lepton beam and $80 \div 95$ mA for the proton one.

The 96 ns interval between two bunch crossings puts strong requirements on the data acquisition and trigger system, that have to be able to handle a rate of 10.4 MHz. We will come back to this in the discussion of the trigger at the end of this chapter.

1.2 Performance of HERA

The initial energy of the electron beam has been of 26.7 GeV. In 1994, spin rotators (rotating the spin vector from transverse to longitudinal direction)[2,3] were installed in the HERMES region, requiring a change of beam energy to 27.52 GeV.

During 1994, it was realized that the electron beam current was limited by positively ionized dust particles getting in the beampipe through the pumps, blowing up the electron beam and reducing its lifetime. For this reason HERA switched to positrons in July 1994, allowing for a really significant increase in the

[2]During the revolving motion inside the vacuum beampipe, electrons are polarized transversally to the direction of the motion, with the spins aligned preferentially in the opposite direction to the magnetic field of the curvature dipoles of the ring, for the Sokholov-Ternov's effect [12]. The characteristic polarization time $P(t)$ is determined by the synchrotron radiation and is given by:

$$P(t) = P_0 \left(1 - e^{-\frac{t}{t_P}}\right) \quad ; \quad t_P = \frac{98 r^2 R}{E^5} \tag{1.1}$$

with $P_0 = 92\%$, t_P measured in seconds, r curvature radius in meters, R average radius in meters and E energy of the electron beam in GeV. This is true for a perfect machine; but still small imperfections of the magnets produce depolarizing effects that reduce the maximum achievable polarization. From studies effectuated parasitically the 1994's data-taking it was already shown that, at least, a polarization of 60% is achievable.

[3]The insertion of these systems in the optics of the magnets of the ring has been necessary for the HERMES experiment which uses longitudinally polarized electrons while the magnetic optics of HERA, and of any accumulation ring, is as such to create transversally polarized beams, provided the imperfections of the focalizing and curvature system are not so large.

What happens is this: first a transversally polarized beam is built. When the transverse polarization is large enough the spin rotators, that are uphill and downhill of HERMES and that allow the transformation of the polarization from transversal to longitudinal, are turned on. The beam crosses the gas target and then goes through the rotators again, that this time change the polarization of the electrons from longitudinal to transversal.

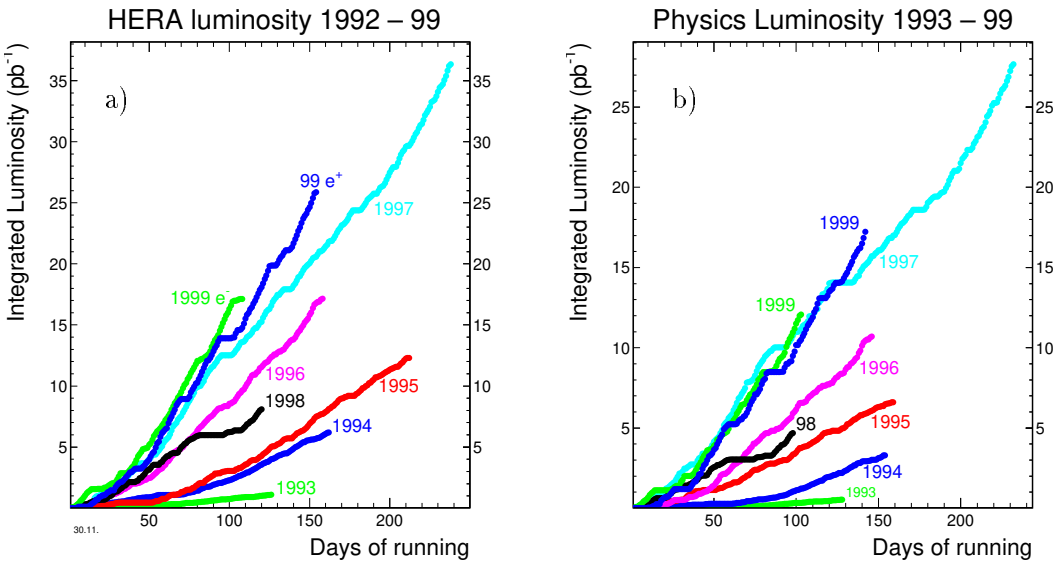

Figure 1.2: Integrated luminosity delivered by HERA (a) and usable for ZEUS physics analysis (b), as of November 1999.

lifetime of the e-beam, resulting in a factor of three increase in the luminosity yield, and without significant loss in physics cross sections (except in the charged current sector, where cross sections are reduced by about a factor of 2).

During the shutdown of 1997-1998 the beam line has been exchanged and the vacuum pumps have been replaced with passive pumps; this has permitted to resume electron running.

The performance of HERA over the last years is shown in Table 1.2 and Figure 1.2.

The energy asymmetry of the beams inside HERA is due to the fact that the energy of the electron beam is limited by the energy loss from synchrotron radiation that, at the nominal current of 58 mA, is equal to a power loss of 6.5 MW, that have to be compensated by the radio-frequency cavities.

The magnetic system of the electron ring is made up by conventional magnets with maximum field of 0.165 T, while for the proton ring superconducting magnets are used with a maximum field of 4.65 T, and conventional magnets in the vicinity of the interaction regions.

The collision takes place at zero angle and the necessary deflection to deviate the electron beams, that for the remaining time travel parallel but under the proton, causes a strong synchrotron radiation in the vicinity of the interaction region. Both the H1 and ZEUS experiments have been equipped with systems of absorbers and collimators of the beams.

The luminosity of HERA has reached instantaneous values of $L \simeq 1.4 \cdot 10^{31}$ cm^{-2}s^{-1}, which is close to the design value. The progress over the years has been steady, as can be seen in Figure 1.2. This luminosity has allowed the

year	colliding particles	E_e(GeV)	E_p(GeV)	$\mathcal{L}$ (in pb^{-1})
1992	e^-p	26.7	820	0.0263
1993	e^-p	26.7	820	0.538
1994	e^-p	27.5	820	0.279
1994	e^+p	27.5	820	3.022
1995	e^+p	27.5	820	6.437
1996	e^+p	27.5	820	10.710
1997	e^+p	27.5	820	27.690
1998	e^-p	27.5	920	4.710
1999	e^-p	27.5	920	12.110
1999	e^+p	27.5	920	18.167

Table 1.2: Summary table of the integrated luminosity collected with the ZEUS detector since the year 1992.

HERA experiments to perform many important measurements, including the observation of the rise of the structure function F_2 with decreasing x,[4] the observation and study of events with a large rapidity gap in the hadronic final state, the observation of resolved photon interactions, and many others. However, the desire was expressed by the experimental groups for an increase in luminosity. The physics motivation for this was studied in a year long workshop between 1995 and 1996, and the clear conclusion was reached that a luminosity upgrade bringing integrated luminosities to the level of 1 fb^{-1} by 2005 would open the possibility for many more exciting measurements.

Given this strong motivation, the HERA machine group, in conjunction with members of the ZEUS and H1 experiments, have studied different alternatives to achieve the desired luminosity upgrade. As described in [13, 14], the solution chosen is to install superconducting combined function magnets in the interaction regions and to rebuild focusing magnets near the interaction regions, thereby significantly reducing the beam cross sections. These upgrades, in addition to other improvements listed in [13], will yield instantaneous luminosities of $7.4 \cdot 10^{31}$ cm^{-2} s^{-1}, leading to delivered integrated luminosities of about 150 pb^{-1} per year per experiment. This design has been reviewed by an internal committee at DESY in July 1997 and no major concerns have been mentioned.

The technical design of components has been started. The design of iron-magnets is well advanced. The first magnets are ready to be built. The present schedule foresees that the new interaction region (IR) will be installed in the six month winter shutdown 2000.

[4] We will postpone the definition and the meaning of these and some other physics quantities in Chapter 2.

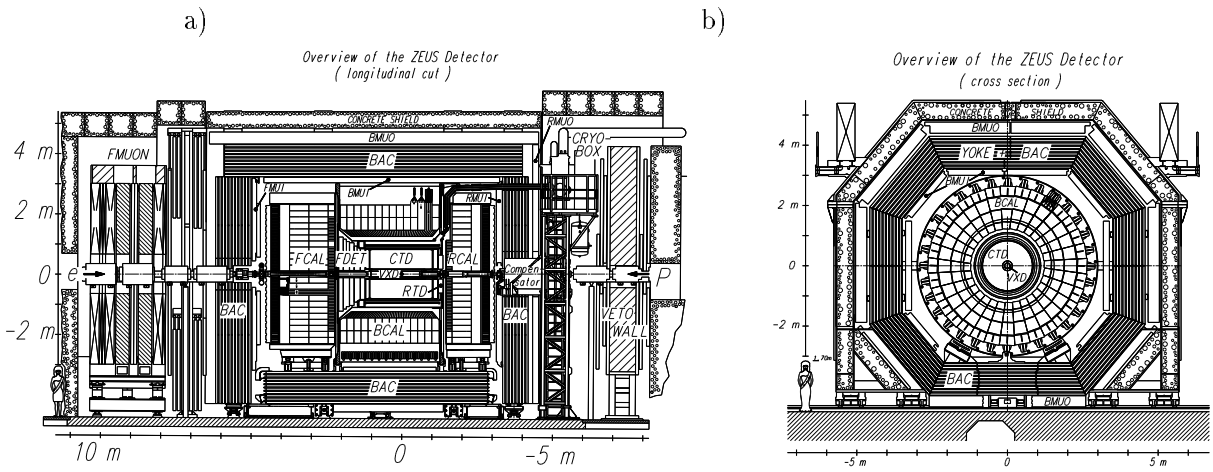

Figure 1.3: Cross sections of the ZEUS detector along (a) and perpendicular to the beam line (b).

In addition to the luminosity upgrade machine elements, more spin rotators will also be installed as planned. This will allow data taking with different electron (or positron) longitudinal polarizations.

The changes in the machine necessitated by the luminosity upgrade lead to some concerns for the experiments. The most serious of these is the synchrotron radiation which must be absorbed. Additionally, some existing components will either have to be modified or removed. We have determined that all of these concerns can be satisfactorily addressed. The impact of the upgrade on the ZEUS detector is described in some detail in the already cited references.

1.3 The ZEUS Detector

The ZEUS detector is an almost hermetic magnetic detector, with a particular emphasis on the hadronic calorimetry.

The detector is able to measure energies from around a hundred MeV up to several hundreds of GeV in the forward region. High energies are well measured with calorimeters (resolutions behave as $\sigma(E)/E \propto 1/\sqrt{E}$), whereas one has to rely on tracking in a magnetic field for lower momenta (with $\sigma(p_T)/p_T \propto p_T$).

Particle identification is needed for electrons in a large momentum range to identify scattered electrons from Neutral Current (NC) DIS events, as well as electrons from semi-leptonic decays of heavy quarks or possibly exotic processes. Muons need to be detected and identified for exotics searches as well as for heavy-quark physics.

To identify Charged Current (CC) DIS events, one needs a hermetic detector

to measure the missing transverse momentum carried by the outgoing neutrino. Also the hadronic final state, consisting of charged as well as neutral particles, needs to be well measured in order to determine the kinematics of events, especially in those events where part of the final state is missing, eg. untagged photoproduction or CC DIS scattering events.

The highly asymmetric energy beams circulating in HERA produce forward-backward asymmetry particle distributions, differently than what happens in typical e^+e^- and $p\bar{p}$ collider experiments. Most of the particles are emitted in the direction of the outgoing protons and this explains why the sub-detectors that build up ZEUS are coaxial but asymmetric with respect to the interaction point. The Figures 1.3 and 1.4 show a longitudinal cross section and an exploded view respectively of the detector. The main detector measures approximately 20 by 11 by 12 meters and has a total weight of about 3600 tonnes. Some additional detectors are located in the HERA tunnel, up to 100 meters away from the interaction point (IP) (see the Figure 1.5 for the definition of the coordinate reference frame).

From the IP the following components are recognizable: the vertex detector (VXD) (that was removed from the beam line at the beginning of the year 1996), the central (CTD), forward (FTD, TRD) and rear (RTD) tracking detectors, the thin superconducting solenoid (COIL), the calorimeters (FCAL, BCAL, RCAL e BAC), the muon chambers (FMUON, BMUON e RMUON). Neither the detector for the measurement of the luminosity (LUMI) nor the leading proton spectrometer (LPS) are shown in Figures 1.3 and 1.4, since they are located several meters away from the interaction point, along the beam line.

1.4 The coordinate system of ZEUS

In the reference frame used in ZEUS the incoming protons move in the direction of positive z. The nominal interaction vertex is the origin of the ZEUS coordinate system. The coordinates x, y, z, θ, ϕ are defined in Figure 1.5. The y-axis points upward, the x-axis is coplanar to the beam orbit plane and directed towards the center of the accumulation ring. The other two are the polar and azimuthal angles, the former is expressed by the following equation:

$$\theta = \arctan\left(\frac{\sqrt{x^2+y^2}}{z}\right), \tag{1.2}$$

the latter as:

$$\phi = \arctan\left(\frac{y}{x}\right). \tag{1.3}$$

We introduce, for our convenience too, other two variables R or ρ, η, the first is the radius and is defined as usual:

$$R = \rho = \sqrt{x^2+y^2}, \tag{1.4}$$

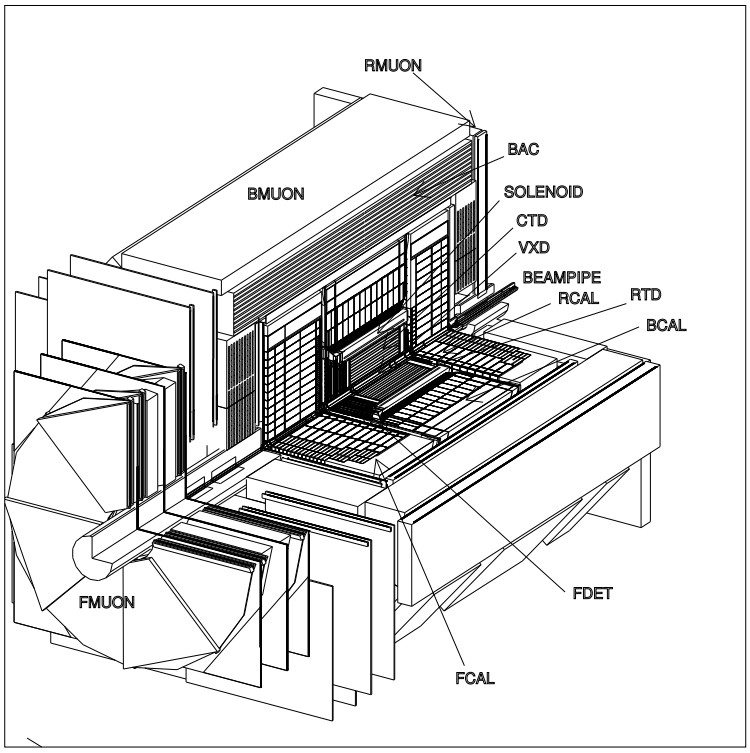

Figure 1.4: Exploded axonometric view of the ZEUS detector with its components. For a description of the parts it is made of see the text. F, R, B have this meaning: F(*forward*) is in the direction of the outgoing proton, R(*rear*) is in the direction of the outgoing electron, B(*barrel*) is central.

the second is called pseudorapidity and is defined in this way:

$$\eta = -\ln(\tan\theta/2)\,. \tag{1.5}$$

1.5 The magnetic system

The momenta of charged particles are determined measuring the deflection of their tracks in an axial magnetic field of 1.43 T produced by a thin superconducting solenoid, placed inside the calorimeters. Measurements of the field have been performed with an accuracy of 0.2% in the central region. The thickness of the solenoid measured in radiation length is limited to 0.9 X_0 (≈ 8 cm of aluminum), to reduce the impact on the energy measurement of particles showering before the calorimeters.

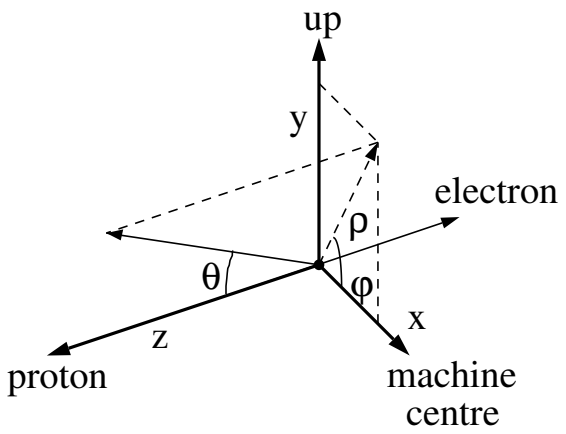

Figure 1.5: Global HERA and ZEUS coordinate system.

The influence of the solenoid magnetic field on the dynamics of the electron beam is canceled by the presence of another small superconducting magnet that acts as a compensator. This magnet is located at about 4 m from the interaction point, in the direction of the negative z-axis, inside the yoke of the main magnet.

The magnetic system is completed by the return yoke that captures the magnetic flux of the solenoid. The yoke acts at the same time as an absorber for the *Backing Calorimeter* (BAC) and, as it is magnetized having a maximum field of 1.4 T, allows the measure of the momentum of muons that cross it.

In the region of the forward muon detector a toroidal magnet provides a magnetic field of 1.7 T.

1.6 Inner tracking devices

The tracking detectors allow to measure the momentum of charged particles, exploiting the track curvature in the magnetic field of the solenoid, and to identify them through the measure of the energy loss, dE/dx. A scheme of this part of the detector is shown in Figure 1.6.

1.6.1 Vertex Detector (VXD)

The Vertex Detector [15] measures the event vertex and possibly secondary vertices, improves the momentum and angular resolution of charged particles as determined by the CTD alone and contributes to the pattern recognition. The VXD is a cylindrical drift chamber with an inner radius of 100 mm and an outer

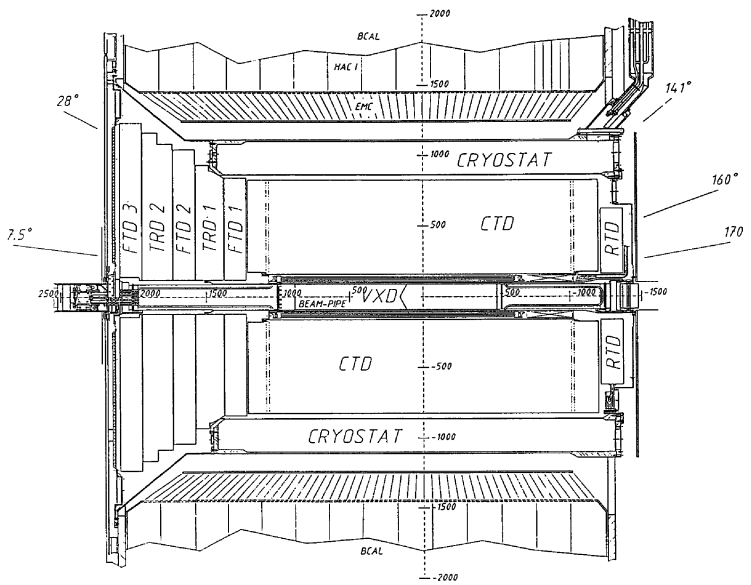

Figure 1.6: Vertical longitudinal cross section of the inner tracking detectors.

radius of 156 mm, it consists of 120 radial cells, each equipped with 12 layers of sense wires of 1.6 m long parallel to the beam line, 3 mm apart, alternated with field wires, organized in 20 sectors in the azimuthal coordinate ϕ.

Unluckily, High Voltage problems caused the VXD to be off from time to time, during the 1993-1995 data taking. So, eventually before the beginning of the 1996 data-taking start up, it was decided to take out this component from the region it was situated. During the next shutdown it will be inserted a new silicon based micro vertex detector [16].

1.6.2 Central Tracking Detector (CTD)

The Central Tracking Detector [17] measures the trajectory and momentum of charged particles with high precision and estimates the energy loss, dE/dx, that is used for particle identification. The CTD is a cylindrical drift chamber with an inner radius of 18.2 cm, outer radius of 79.4 cm and length of 205 cm. It is filled with a gas mixture of Argon, CO_2 and ethane, in the following proportion 0.85:0.05:0.1. 72 layers of wires are organized in nine superlayers with 8 layers of sense wires each. Five superlayers have wires parallel to the beam line; the other four are *stereo* layers, with wires with a small angle with respect to the beam line, which are used to measure the z-coordinate of the hits (Figure 1.7).

With the available calibration of the chamber, the resolution of the CTD is around 180 μm in $r - \phi$. The resulting z position resolution of the stereo layers

Super Layer	Angular (θ) Coverage(°)	Stereo angle (°)
9	36.1-142.6	+0.0
8	33.5-145.2	+5.6
7	30.9-147.9	+0.0
6	27.9-151.0	-5.5
5	24.9-154.0	+0.0
4	21.5-157.3	-5.3
3	18.4-160.7	+0.0
2	14.5-164.8	+5.0
1	11.3-168.2	+0.0

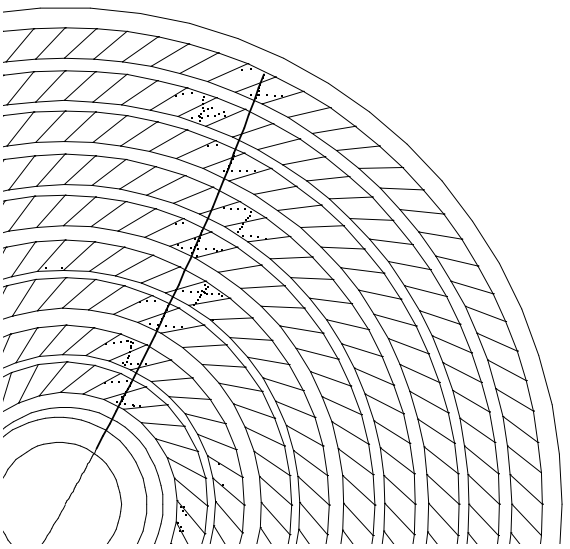

Figure 1.7: (Negatively charged) Track in the CTD; the 'displaced' hits in the even numbered layers show the effect of the stereo angle of the wires. Ghost hits are also displayed.

is about 1.0 mm.

For trigger purposes, three superlayers are additionally equipped with a system that determines the z-position from the arrival time of the electronic pulses, the so-called z-by-timing system (resolution along the z coordinate of 4 cm).

Particles with polar angle in the range $15° < \theta < 164°$ cross at least one CTD superlayer, but tracks with $p_T > 0.150$ GeV/c and $20° < \theta < 160°$($|\eta| < 1.75$) are used in the analysis[5]. Particle with a transverse momentum of more $p_T > 0.1$ GeV/c are already reconstructed with an efficiency larger than 95% (for medium and high energy tracks as those used in the analysis described in this thesis, the efficiency is larger than 99.5%).

For tracks with CTD information, we have reached $\sigma(p_T)/p_T = 0.0058\,p_T \oplus 0.0065 \oplus 0.0014/p_T$ for tracks going through all superlayers [18].

Using the combined data of VXD and CTD, resolutions of ≤ 0.15 cm in z and 0.1 cm in the XY plane were obtained for the primary vertex reconstruction, for medium and high track multiplicity events.

The energy loss, dE/dx, is at present determined with an accuracy of somewhat less than 10% for full length tracks [19]. This will be further discussed in a

[5]Tracks that fail to pass one of these two requirements are hampered by large systematic effects and the 45° inclination of the drift cells introduces an asymmetry between positive and negative charged particle tracks.

following Section 1.6.5.

1.6.3 Rear and Forward Tracking Detector (RTD, FTD)

To get a better coverage at small polar angles, four planar drift chambers are installed, perpendicular to the beam line, three in the forward region (FTD) and one in the rear one (RTD). In particular, the RTD is useful to measure the direction of scattered electrons in events of low Q^2.

The expected momentum resolution is $\sigma(p)/p \sim 0.15 \div 0.2$ while the hit resolution is about 200 μm, for as low as 150 mrad angles with respect to the direction of the beams.

1.6.4 Transition Radiation Detector (TRD)

The identification of electrons, especially if within hadron jets, is improved in the forward region by the Transition Radiation Detector. It has been built and based on the principle that a charged particle irradiates within a cone with an opening angle of $\theta = 1/\gamma$, with $\gamma = E/mc^2$, when moving through the separation boundary between two dielectric materials. This detector allows to identify electrons with an efficiency larger than 90% for momenta between 1 and 30 GeV.

1.6.5 dE/dx determination

The ionization energy loss, dE/dx, of a charged particle in a gas is described by the Bethe-Bloch equation:

$$-\frac{dE}{dx} = 4\pi N_A r_e^2 m_e c^2 z^2 \frac{Z}{A}\frac{1}{\beta^2}\left[\ln\left(\frac{2m_e c^2\gamma^2\beta^2}{I}\right) - \beta^2 - \frac{\delta}{2}\right], \qquad (1.6)$$

for a particle with charge ze passing through material consisting of an element with atomic number Z and atomic weight A. It is a function of $\beta = v/c$, hence of the velocity of the particle. At low β the ionization loss falls rapidly, reaches a minimum around $\gamma = (1-\beta^2)^{-1/2} \sim 3$, and then rises logarithmically to a plateau at very high γ. Relating the ionization loss to the momentum $p = \beta\gamma m$, the energy loss shows bands for the various values of m, i.e. for the various particle types. The dE/dx as a function of p as obtained from the CTD is shown in Figure 1.8.

1.7 The Calorimetry system

The tracking devices are surrounded by the calorimetry system; we can distinguish the high resolution calorimeter (CAL), that is subdivided in an electromagnetic section and two hadronic sections, and the low resolution Backing calorimeter. They cover almost the whole solid angle around the interaction point.

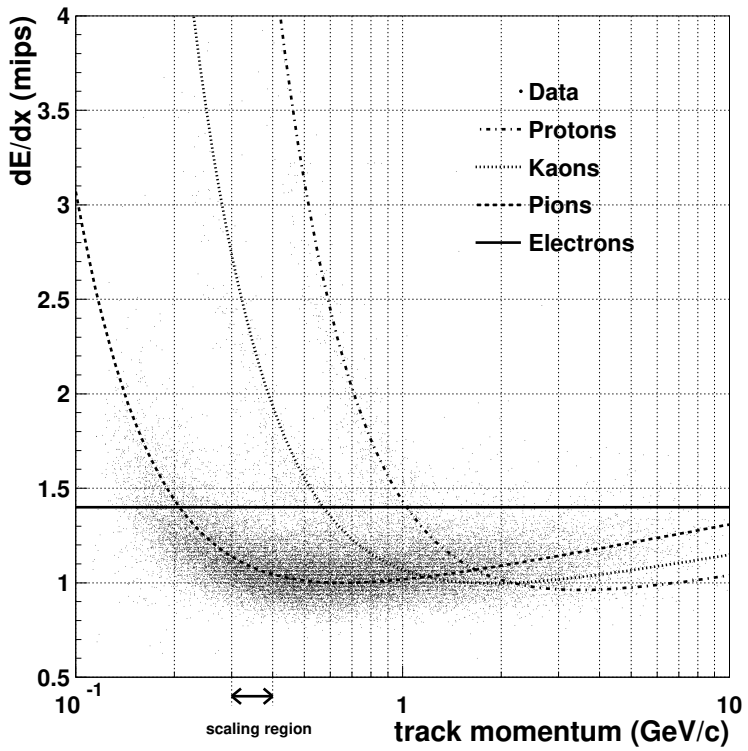

Figure 1.8: The dE/dx versus momentum of tracks reconstructed in the CTD. The curves illustrate the particle types.

The coverage in the forward hemisphere is of 99.8%, while it is of 99.5% in the rear one.

1.7.1 The Uranium-scintillator Calorimeter (UCAL)

The main ZEUS Calorimeter (UCAL or CAL) [20, 21] is a compensating sampling calorimeter built with depleted uranium[6] as absorber and plastic scintillator[7] as active material. The thickness of the plates has been tuned to reach equal response to electrons and hadrons (*compensation*): 3.3 mm thick depleted uranium plates (wrapped in stainless steel) are interleaved with 2.6 mm thick scintillator (wrapped in paper).

The calorimeter consists of three parts: forward (FCAL), barrel (BCAL) and rear (RCAL) calorimeter. Each of these sections is segmented longitudinally in an electromagnetic and one (RCAL) or two (FCAL, BCAL) hadronic sections, called the EMC and HAC respectively, as shown in Figure 1.9. The calorimeter modules are divided into cells, the size of which depends on the type (EMC, HAC) and position, as shown in Table 1.3.

[6] an alloy of 98.4% ^{238}U, 1.4% Nb (which makes the alloy harder) and $\leq 0.2\%$ ^{235}U

[7] SCSN-38

Part	Angular Coverage	Cell size	EMC	HAC
FCAL	$2.2° < \theta < 39.9°$	$x \times y$:	20×5 cm^2	20 x 20 cm^2
RCAL	$36.7° < \theta < 129.1°$	$x \times y$:	20×10 cm^2	20 x 20 cm^2
BCAL	$128.1° < \theta < 176.5°$	$z \times \varphi$:	5.06 cm $\times$ 11.25° (5.06 cm $\times$ 23.4 cm)	20.3 cm $\times$ 11.25°

Table 1.3: Coverage of UCAL calorimeter parts and dimensions of cells.

The BCAL consists of 32 wedge-shaped modules, each covering 11.25° in azimuth. They are 332 cm long. The first (inner) 21 uranium/scintillator layers are read out separately and form the electromagnetic calorimeter (BEMC) of a depth of 22 X_0. The outer 98 layers are divided into two equally sized sections and make up the hadronic calorimeter (HAC1 and HAC2; 2.0 λ each[8]).

The FCAL and RCAL both consist of 23 rectangular modules 20 cm wide, and 220 to 460 cm high (with two half modules above and below the beampipe, leaving a hole of 20×20 cm^2).

The first 25 layers (26 X_0) form the electromagnetic section (FEMC and REMC); the rest forms the hadronic calorimeter, of which the FCAL part is segmented in two longitudinal parts (FHAC1, FHAC2, RHAC1). Every HAC section has 80 layers, i.e. 3.1 λ.

Test beam data show a resolution $\sigma(E)/E = 0.18/\sqrt{E}$ for electromagnetic showers and $\sigma(E)/E = 0.35/\sqrt{E}$ for hadronic showers and a position resolution for impacting electrons of 54 mm$/\sqrt{E}$ in x and 14 mm$/\sqrt{E}$ in y (E measured in GeV).

The light produced in the scintillator is read out via 2 mm thick wavelength shifter (WLS) bars at both sides of the module. Each WLS guides the light to one of the 11386 photomultiplier tubers (PMT), where the light is converted into an electrical signal, which is processed by the readout electronics into energy and arrival time (see below).

The stability of the PMT signals and electronics readout is monitored with laser and charge injection pulses. In addition to this, natural radioactivity of the uranium (Uranium NOise, UNO) provides a small but very stable signal. These signals are equalized (for equal size calorimeter cells) by adjusting the high voltage settings (hence the gain) of the PMTs. The absolute energy scale, i.e. the conversion factor between reconstructed PMT signals (collected charge) and corresponding particle energy has been obtained from test beam data.

Operation experience in ZEUS shows the stability to be within 1%. Bad

[8]The nuclear interaction length λ is defined as the thickness of crossed material by a particle that feels the nuclear strong interaction such that $\lambda = A/(N \times \sigma)$ holds, where N is the Avogadro's number, A is the atomic mass of the substance and σ the absorption cross section in the medium of the impacting particle.

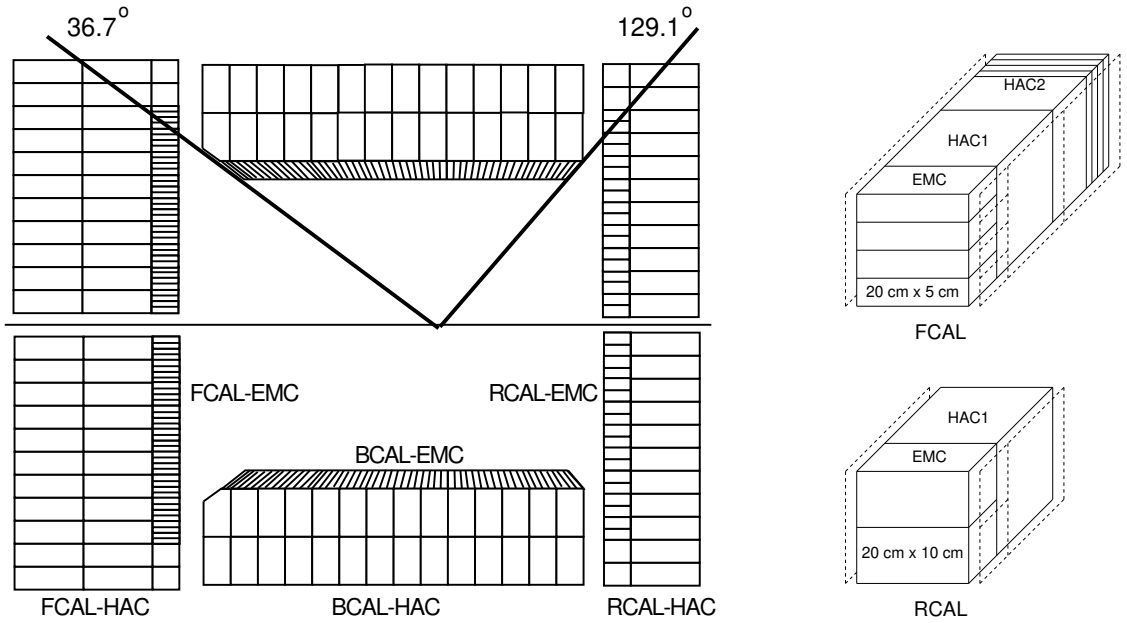

Figure 1.9: a) Schematic view of the ZEUS uranium calorimeter showing the division into three parts: FCAL, BCAL and RCAL. b) Tower structure in FCAL and RCAL; stacked towers together form a module; the BCAL is organized similar to the FCAL, but there EMC cells are projective in the RZ plane and the towers are wedge-shaped.

channels, in general PMTs with electronic readout problems, are below 1% of the total. But since every cell is read out on two sides, this is not very dramatic: only less than 0.5 permille of cells have both PMTs bad, thus making a bad cell or 'hole'.

In addition to energy measurements, the calorimeter also measures the arrival times of energy deposits w.r.t. the bunch crossing time. The timing resolution is a function of the deposited energy, as shown in Figure 1.10. For energy deposits between 200 MeV and 1.2 GeV the timing resolution ranges from 3 to 1 ns. A timing resolution below 1 ns is achieved for energies above 1.2 GeV (we recall the time between two bunch crossing is 96 ns).

It is, indeed, really important that the calorimeter is able to provide timing information: we will see how the time, relative to the HERA clock, when the energy of particles is deposited in the Calorimeter, is a very effective tool for the suppression of background events arising from cosmics or beam-gas interactions.

1.7.2 The Backing Calorimeter (BAC)

The Backing Calorimeter surrounds the main calorimeter, its aim is to improve the measurement of the energy of extended showers leaking out of the UCAL.

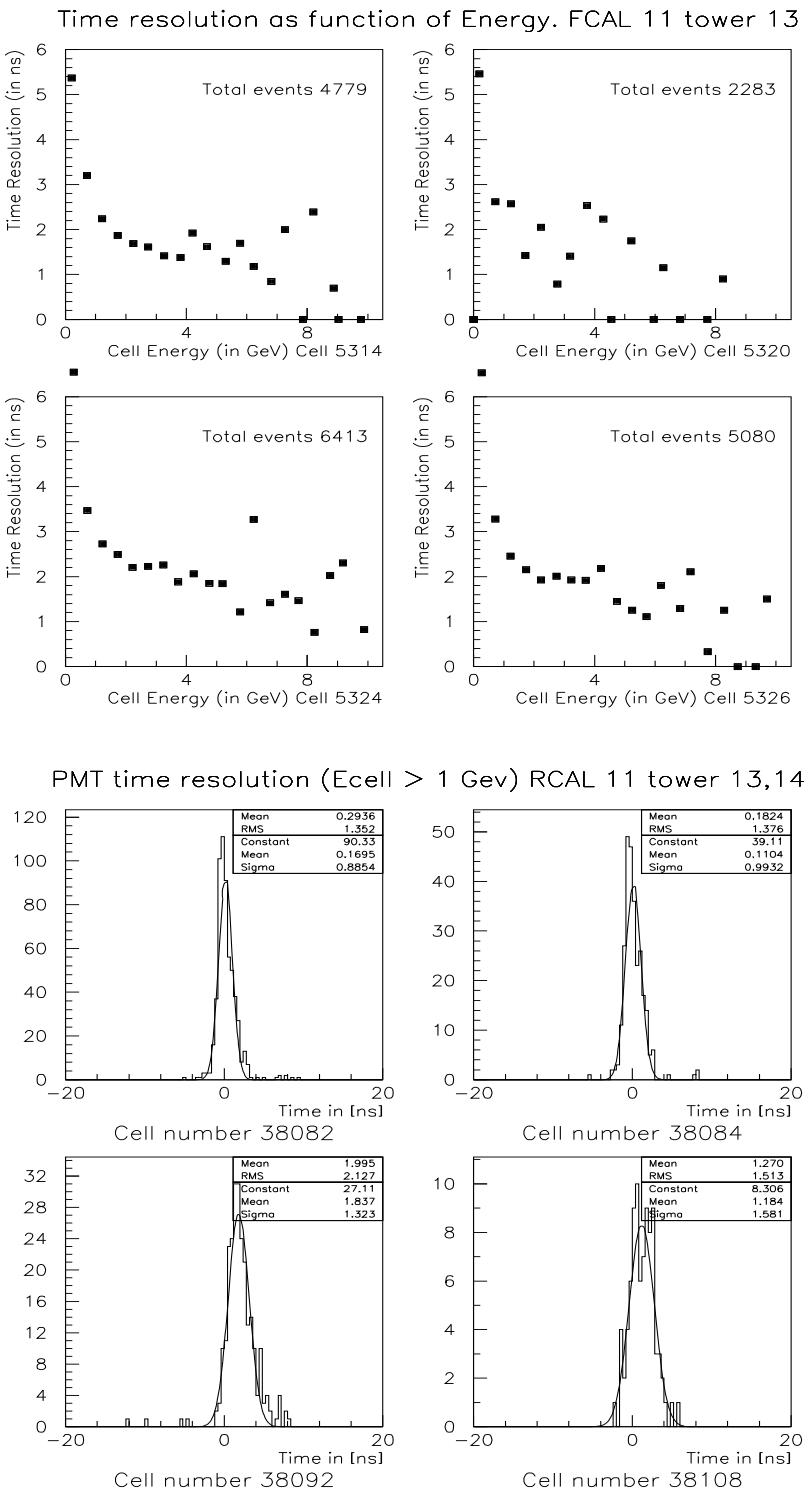

Figure 1.10: Single PMT time resolution as function of energy of a random Calorimeter cell, upper four plots. Single PMT time resolution for events with deposited energy larger than 1 GeV for a random Calorimeter cell, lower four plots. It is to be noted that the timing information is used if both the PMT's of the same cell have given a signal, in this case the time resolution is enhanced, respect the one shown in the plots.

Its presence allows to tag whether or not a shower is completely contained in the high resolution calorimeter.

The BAC is a sampling calorimeter too; this time the absorbing material is the iron of the magnetic yoke (plates of 7.5 cm of thickness) interleaved with proportional tubes. The deposited energy is measured through signals gathered by the wires; the sum of the signals is carried out adding wires in non-projective towers, with a transversal dimension equal to 50×50 cm^2, extend through the entire depth of the calorimeter. The readout system is completed by small rectangular pads put along the wires to read the other coordinate. Even these pads are read summing in tower stripes with equal transverse dimension. This way the position and three-dimensional development of the shower is reconstructed.

The energy resolution of this type of calorimeter is modest: $\sigma(E)/E = 1./\sqrt{E}$.

Using the value of the energy and the spatial distribution of the hit wires and stripes is possible to identify isolated muons coming from inside the apparatus. Nevertheless the efficiency of this method has been discovered to be insufficient for our studies.

1.8 The detection system of muons

The main aim for this kind of detector is to measure tracks of particles coming from the interaction region (*pointing* tracks), capable to cross the calorimeter and magnetic yoke regions (*penetrating* tracks). Such kind of behaviour is characteristic of muons that, losing energy for ionization only, are able to cross remarkable thicknesses of matter. This situation has to take care of the remarkable boost in the direction of incoming protons that produced particles are subject to: while for prompt, forward produced muons a momentum greater to 10 GeV is usual, in the barrel and rear sectors, in most of the non-exotic physics processes, the expected momentum is much smaller. The system is, therefore, made up of two separate modules, designed and realized with different characteristics, the first covers the forward sector (FMUON), the other covers the remaining part of the solid angle (BMUON and RMUON).

1.8.1 The Forward Muon detector (FMUON)

The Forward Muon detector is subdivided into two parts: the first or inner part (FMUI) is located between the FCAL and BAC, the second one outer (FMUO) positioned outside the BAC.

The FMUON detector as shown in Figure 1.11 is composed of the following components:

- a system of four Limited Streamer Tubes [22] trigger planes (LST1 $\div$ LST4) with digital ρ and ϕ readout, that are also called trigger planes;

- two coverage planes of limited streamer tubes with digital (ρ,ϕ) and analog(ρ) read-out (LW1,LW2) in the large polar angle region;
- four planes of drift chambers (DC1 $\div$ DC4)
- two large iron magnets of toroidal shape providing a magnetic field[9] of 1.7 T for the momentum separation and measurement in the angular region $5° < \theta < 16°$.

The FMUI is composed of one drift chamber and by one of the limited streamer tubes chambers. The FMUO is made of the remaining planes.

1.8.1.1 Limited Streamer Tube planes (LST)

The limited streamer tube planes have both the aim to trigger on muon candidates fulfilling certain momentum and direction cuts and the aim to give geometric information on the azimuthal and radial coordinates ϕ, ρ of a track.

Each trigger planes is subdivided into 4 chambers coupled into two pairs to form two separated half-planes. A quadrant is made of two layers of limited streamer tubes (LST), placed horizontally into pairs inside a plastic sheath that allows to substitute singularly each tube in case it becomes needed. The tubes of the two layers are slightly displaced one compared to the other of 0.5 cm to obtain a complete geometric acceptance. Each quadrant is contained in an aluminum air tight box where nitrogen can flow, in case an explosive gas mixture is used for the LST. Signals generated by the LST are induced on copper strips that have a polar geometry and are glued to the sheath of the LST on the outside. There are 132 radial ρ strips, 1.9 cm wide, divided along the bisector of the quadrant so to be able to read out each octant as the simplest unity of the trigger planes. Actually, as a coarser resolution is needed as the polar angle becomes larger, the last 64, further from the beam line, ρ strips are OR'ed two by two. This way the number of channels needed along this coordinate is 96 for each octant. The ϕ strips have a 1.4° spacing and are 32 per octant. The readout is digital for both the kind of strips.

1.8.1.2 The Drift Chambers (DC)

The spatial precision that is needed to reach the desired momentum resolution is obtained by using the information of four drift chamber planes. Each plane of chambers is divided into two half-planes, that are built on a sustain panel on which 4 chambers are fixed. Each chamber is made of 32 cells that form the basic unity of the chamber. A cell is, then, a gas volume where the sense wires are

[9] It is even used the magnetic field produced by the YOKE ($B \sim 1.5$ T), that extends the coverage to a polar angle of $\theta = 32°$, reaching the region where the barrel muon detector starts with its geometric acceptance.

placed and layers that are needed to build up the appropriate electric field. The four sense wires are perpendicular to the beam axis and hence give a measure of the radial coordinate. The gathered signal is sent to a TDC that convert the signal into a time value corresponding to a spatial distance, according to an already known relation. The informations obtained from the wires within a cell are combined to get a segment that reproduce the crossing of the particle.

1.8.1.3 The Large Angle coverage planes (LW)

The two large angle coverage planes are useful to complete the geometric acceptance of the forward spectrometer in the region left uncovered by the toroids ($16° < \theta < 32°$). Each plane is made of 8 aluminum gas tight wrappings that contain a layer of LST. The signals of this tubes are induced on copper strips with polar geometry, with a spacing in the ϕ coordinate of 0.7° (64 per octant) and of 1.8 cm in the ρ coordinate (192 per octant). The readout is digital for the ϕ-strips, while the ρ-strips have an analogous function of the wires of the drift chambers, they reproduce the pseudo-radial geometry and are readout analogically to reach a spatial resolution of $\sim$ 1 mm, that is obtained by using the method of the charge barycentre.

1.8.1.4 The trigger system of FMUON

The trigger planes of FMUON have to distinguish, as much as possible, muons coming from the decay of interesting particles, from tracks produced in background events, that are due to interactions of the beams with the residual gas inside the beampipe, to the synchrotron radiation or to random signals.

In the solid angle covered by the spectrometer it is less important, instead, the background related to the cosmic radiation, that can be eliminated by using the available directional informations and timing measurements.

Another important source of background is the production of muons coming from the decay of light hadrons (π, K). The distinction between these two categories of prompt and non-prompt muons is based mainly on the momentum associated to the track. Muons coming from heavy quarks can have more than $p \simeq 10$ GeV/c.

1.8.2 The Barrel and Rear Muon chambers (BRMUON)

In the case of the barrel and rear sectors [23] the surface that has to be covered is really large (of the order of some thousands squared meters if we consider all the planes of the detector) and it was decided to implement a detector with a modular structure. The basic element of this component is the chamber. The chambers that cover the internal central sector are called BMUI, while those covering the outer sector are BMUO. Likely, the rear chambers are called RMUI or RMUO.

Figure 1.11: A drawing of the Forward Muon Spectrometer.

Generally, the chambers have different shapes and dimensions (Figure 1.12), but the internal structure is kept the same (Figure 1.13). The element that bears the weight of the chamber is made of an aluminum honeycomb frame. On both sides of the frame, 20 cm thick for BMUI, RMUI, RMUO and 40 cm thick for BMUO, two planes of limited streamer tubes [22] are placed. The use of the limited streamer tubes technique is due to the large surface to cover and the good spatial resolution we can get. The limited streamer tubes of the barrel sector are placed parallel to the beam axis and equipped with external metallic readout stripes orthogonal to the wires. In the rear region the detector is equipped by limited streamer tubes parallel to the x-axis in the ZEUS reference frame, and with external readout stripes orthogonal to the wires.

The determination of the position of a particle is done through the reading of the hit wires, with electronic cards called SGS, and reading the induced charge along the stripes, with readout cards called STAR. If in the event a trigger signal from the component is available, the acquisition is of analogic type, on the contrary of a digital kind. The trigger signal follows the identification of a *penetrating*

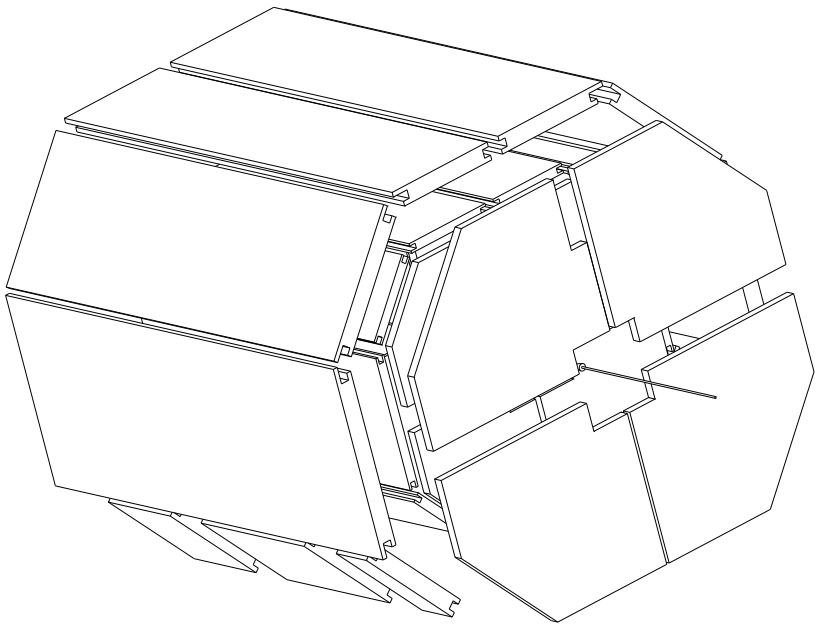

Figure 1.12: Three-dimensional view of the chambers.

track coming from the volume of the inner tracking detectors.

The identification is carried out analyzing the spatial distribution of both hit wires and stripes. The method implemented is this: groups of 16 adjacent wires, within the same chamber, are OR'ed; the same logics is repeated for groups of 16 adjacent stripes and the so produced signals are analyzed again to get informations on the polar and azimuthal position of the wires and stripes that have been hit. By means of specially designed coincidence matrixes, the information coming from the inner chambers is confronted with that coming from the outer chambers. These matrixes have been programmed to select configuration generated by tracks coming from the volume specified by the inner tracking detectors. In the case there is the presence of a trigger signal, the following quantities are recorded: the addresses of the hit wires and the drift time wire by wire, the addresses of the hit stripes and the charge collected by every strip (analogic readout). With the analogic readout the obtainable spatial resolution is of 200 μm for the coordinate perpendicular to the wires and of 700 μm for the coordinate along the wires. In the absence of a local trigger we record the addresses of hit wires and the OR of groups of 4 adjacent strips within the same plane, so called quadruplets (digital readout), only; the resolution of the single point in this case is of $1/\sqrt{12}$ cm perpendicularly to the wires and of $6/\sqrt{12}$ cm in the other coordinate.

The structure of the detector allows to carry out an accurate measurement of the position of the track at the exit of the calorimeter. Then, taking advantage of the magnetization of the yoke, it is possible to measure the correspondent momentum of the reconstructed track too. Once this has been done we are able

a) b)

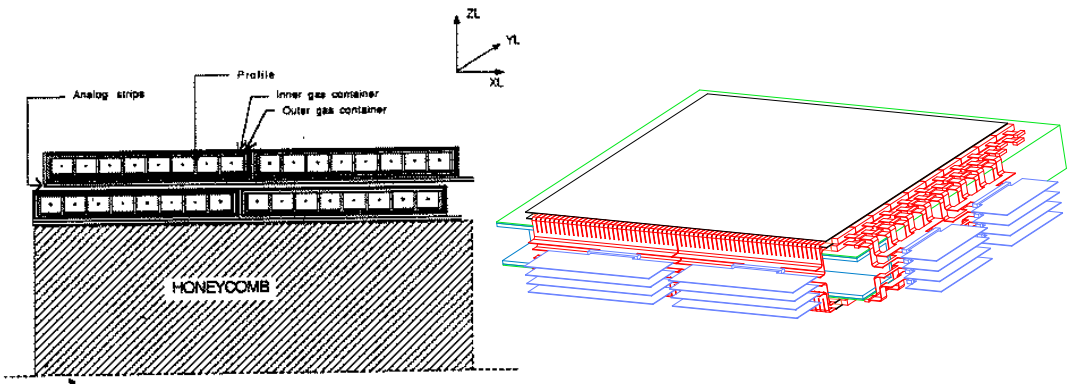

Figure 1.13: (a) Section of a BMUON chamber (we can see the Honeycomb structure). (b) Scheme of a BMUO chamber.

to match the so-obtained track with one reconstructed by the inner detectors.

The compatibility request of the two independent measurement of the momentum (if we take into account the energy loss crossing the CAL) allows to reduce the background from non prompt muons, coming from decay in flight of pions or kaons, in the inner detectors or in the calorimeter. The expected rejection factors, for 10 GeV particles, are of the order of 700 and 3500 for pions and kaons, respectively. To obtain such rejection a spatial resolution of about 1 mm and a momentum resolution[10] of 29% at 10 GeV are needed. Another background of prompt muons is produced by cosmic rays that are not discarded from the first level trigger as their tracks are *pointing* to the interaction vertex. The combined use of the μ chamber with the inner tracking detector allows the selection of muons coming from a predefined limited volume around the interaction point.

1.9 The calorimeters for the measure of the luminosity (LUMI)

The value of the absolute luminosity, provided by the accelerator in the interaction point where ZEUS is situated, is measured by using the process of small angle photon production ($ep \to ep\gamma$). The cross section is described by the Bethe-Heitler formula [24].

The energies of the photon and electron are measured by two lead-scintillator calorimeters, located along the beam line at $z = -106$ m and $z = -35$ m,

[10]Such a resolution is already available with the use of the stand alone μ inner and outer chambers reconstruction, without the use of other components.

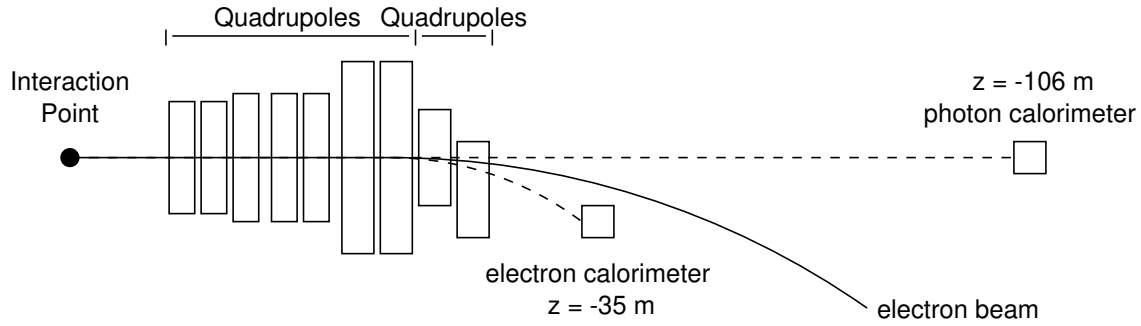

Figure 1.14: The monitor for the measure of the Luminosity (LUMI).

respectively, as it is sketched in Figure 1.14. The calorimeter for the electrons is able to measure even the position of the electron, in such a way to allow the combined determination of the momentum transferred by the electron.

In front of the photon calorimeter a $1.5X_0$ thick carbon filter to absorb the synchrotron radiation is located.

The LUMI-e measures scattered electron at very low angle $\theta_e < 6$ mrad and with energies between $0.2E_e$ e $0.9E_e$, where E_e is the energy of the electron beam. For calibration purposes it is possible to use both the calorimeters. To calculate the luminosity a narrower window is used, $0.35E_e < E'_e < 0.65E_e$, where the acceptance is greater than 70%. The subtraction of the background from the interaction of the electron beam with the residual gas in the vacuum pipeline is done starting from the measured coincidence for the pilot bunches, that is for those electron bunches that have not a paired proton bunch. The electron calorimeter measures scattered electron in photoproduction events in an interval of transferred momentum that goes from 10^{-7} to 2×10^{-2} GeV^2.

1.10 Forward scattered proton detectors (LPS, PRT)

ZEUS has been equipped with two system of detectors to tag at very small angle particles emitted along the direction of outgoing proton.

The Leading Proton Spectrometer (LPS) [25] measures protons scattered at very small angles with respect to the beam line and escaping the central apparatus through the forward beam hole. Such protons carry a substantial fraction x_L of the incoming proton momentum and have a small transverse momentum p_T ($\lesssim$1 GeV). The spectrometer consists of six detector stations located at distances of 23 to 90 m along the proton beam line. In 1994 the three most forward stations S4, S5 and S6 were operational: each of these stations consists of an upper and a lower half, which partially overlap during data-taking. Each half

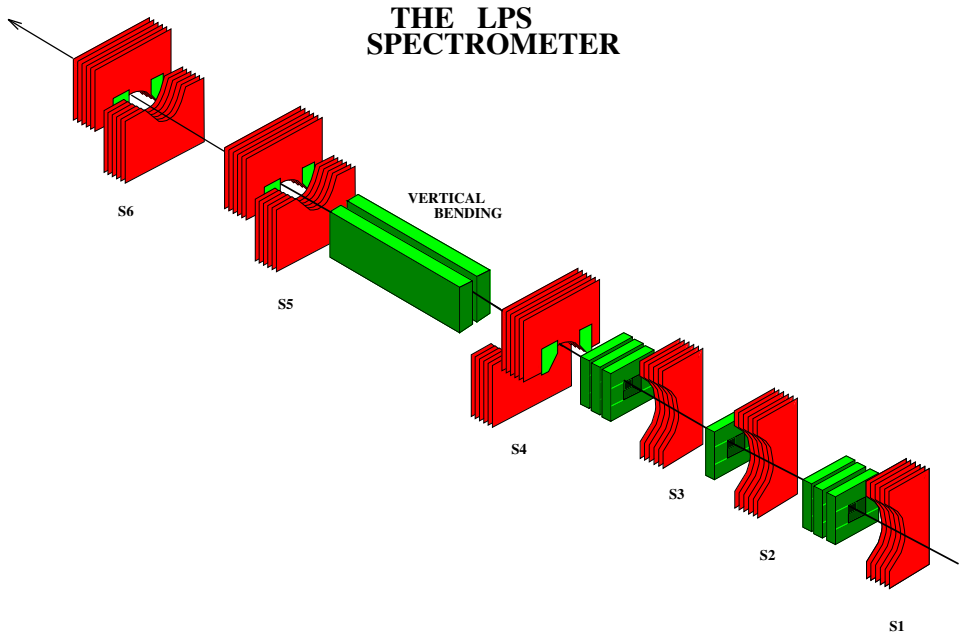

Figure 1.15: Three-dimensional view of the LPS.

is equipped with six rectangular parallel planes of silicon micro-strip detectors. Three different strip orientations (two vertical, two at $+45°$ with respect to the vertical direction and two at $-45°$) are used, in order to remove reconstruction ambiguities. The dimensions of the planes vary from station to station and are approximately 4×6 cm^2; the pitch is 115 μm for the planes with vertical strips and 81 μm for the other planes. The edges of the detectors closest to the beam have an elliptical contour which follows the 10σ profile of the beam, where σ is the standard deviation of the beam spatial distribution in the transverse plane. During data-taking, the planes are inserted in the beampipe by means of re-entrant Roman pots [26] and are retracted during beam dump and filling operations of the HERA machine. The LPS coordinates are reconstructed with a precision of approximately 35 μm, which includes the intrinsic resolution of the coordinate reconstruction and the alignment precision of the detector stations. The track deflection induced by the magnets in the proton beam line is used for momentum analysis of the scattered proton. The x_L resolution was determined using elastic ρ^0 photoproduction events to be better than 0.4% at 820 GeV; the intrinsic p_T resolution is approximately 5 MeV at $x_L = 1$ and is less than the spread introduced by the angular divergence of the proton beam (which is 40 MeV in the horizontal and 90 MeV in the vertical plane).

The second detector is the Proton Remnant Tagger (PRT) [27]. The PRT is made of 7 pairs of scintillator counters located near the vacuum pipeline and subdivided into two stations the first of which is at 5 m (two planes) and the second at 24 m (five planes) from the interaction point in the direction of outgoing

protons. They allow to detect the passage of low angle particles as the angular coverage goes from 6 to 26 mrad and from 1.5 to 8 mrad, respectively. This instrument should permit to distinguish events where the proton undergoes an elastic scattering from those where a diffractive dissociation of the proton take place.

1.10.1 VETOWall, C5, SRTD

The VETOWall is a large iron wall ($8 \times 7.6 \times 0.87$ m^3 with a square hole of 95×95 cm^2 in the center for beampipe and magnets) covered on both sides with scintillation counters, positioned 7 m from the interaction point in the upstream proton direction. It shields the detector against proton beam halo and off-axis particles from beam-gas interactions, and provides a veto signal for beam-gas interactions upstream.

The C5 collimator is positioned around the beampipe at 315 cm from the interaction point in the upstream proton direction (just behind the RCAL), and consists of two horse-shoe shaped planes of scintillator separated by 5 cm of lead. The time information of the C5 counter is crucial to reject proton beam-gas events and it provides the timing *calibration* between the HERA beam crossing and the ZEUS clock.

The Small angle Rear Tracking Detector (SRTD) is a scintillator strip detector located on the front face of the rear calorimeter, just around the beampipe. It measures the impact point of scattered electrons with high accuracy and the electron energy can be corrected using the SRTD as a presampler detector.

1.11 The ZEUS trigger system

The trigger system of ZEUS is designed as a three-stage trigger system [9, 28] (in Figure 1.16 it is possible to see a schematic overview of the ZEUS data-acquisition system). Each level has its own degree of sophistication: moving up in the trigger tree the available processing time increases and the systems allow the use of flexible software instead of fast but more rigid hardware components.

1.11.1 The First Level Trigger (FLT)

The First Level Trigger is designed to handle an event every bunch crossing (every 96 ns) and decide in few μs whether the event is worth keeping or should be discarded. The bunch crossing rate of 10 MHz causes signals in the detector at a rate of 10-200 kHz. The counting rate should be reduced to 1 kHz, which is the design input rate for the Second Level Trigger. To do so, the Global First Level Trigger (GFLT) compares the signals from the component first level trigger processors with (programmable) threshold values. During the 46 crossings, 4.4 μs,

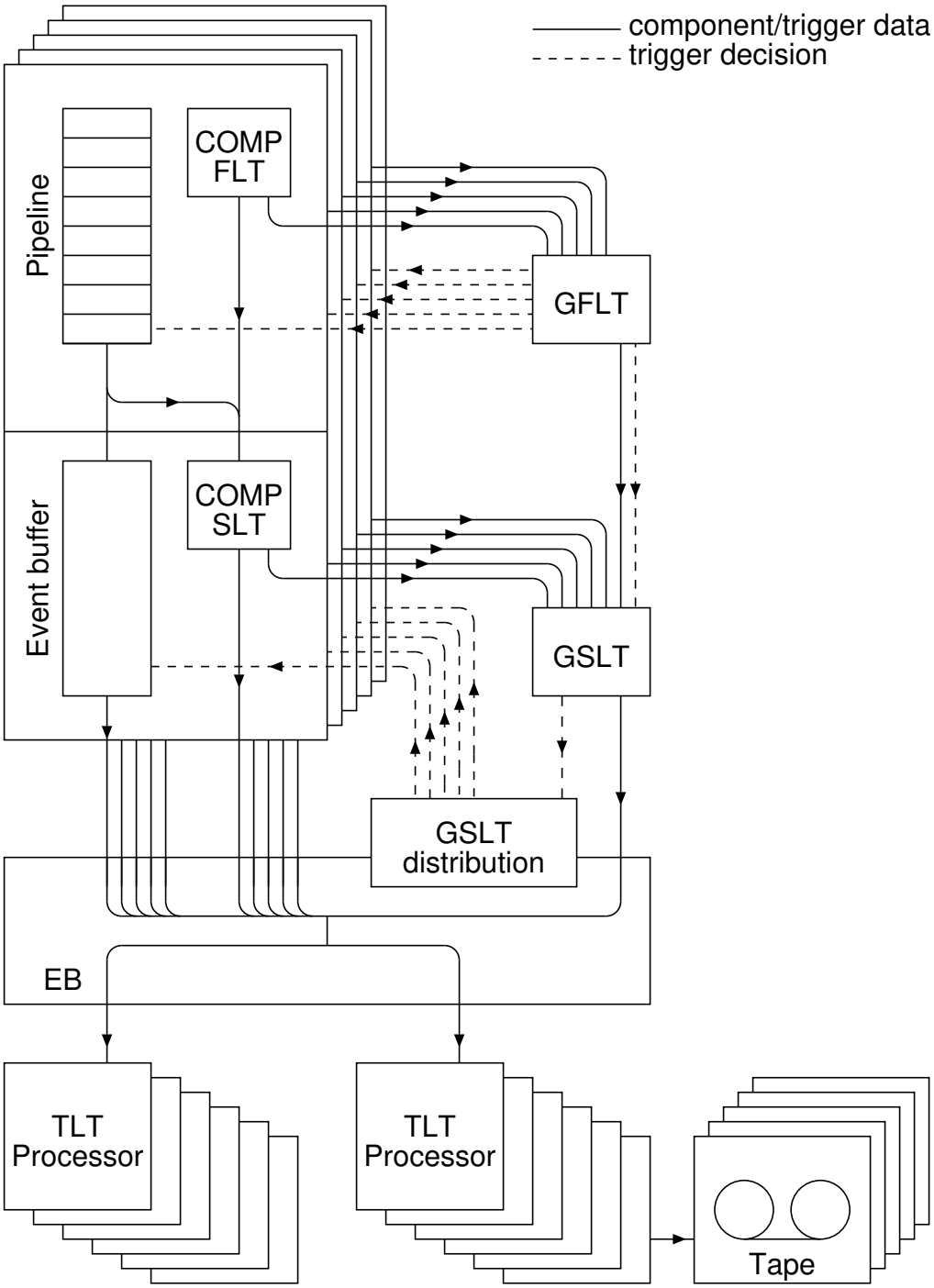

Figure 1.16: Overview of the ZEUS trigger and data-acquisition system. The component trigger systems, pipelines and buffers are shown, together with the global trigger systems.

Hit region	Minimum number of PMT	Energy request
FCAL	4	$E(FCAL) > 2\text{GeV}$
RCAL	2	$E(RCAL) > 1\text{GeV}$
BCAL	2	$E(BCAL) > 1\text{GeV}$
up	2	$E(BCAL - up) > 1\text{GeV}$
down	2	$E(BCAL - down) > 1\text{GeV}$

Table 1.4: List of the minimum requirements that have to be met for the availability of the various calorimeter timing.

that the component and Global First-Level Trigger Box (GFLTB) have available for their processing and decisions, all data are stored in pipelines.

The time of the 46 crossings is shared by the component and global first level trigger: after 26 crossings, the components send their trigger data to the GFLTB, which uses the next 20 crossings to make the final decision. The component/subdetector trigger data is processed and combined in parallel in 8 Trigger Logic Modules of the GFLTB. Logical operations using programmable lookup tables generate 64 individual subtriggers. Some of these are prescaled[11] to reduce the output trigger rate, and finally they are logically-OR'ed to get the final decision.

When the event is accepted by the GFLT, the components have to digitize their data before sending it to the next layer. This operation will take up to 50 μs after the GFLT decision was issued. During this time the Calorimeter data can be processed by the Fast Clear (FC) processors. Here the data from the three calorimeter parts are processed in parallel and global sums and cluster quantities are calculated. Based on this, the FC can decide to recommend the GFLT to reject the event after all. The GFLT issues an ABORT to all components and the event is discarded ('fast-cleared').[12]

At this level it has been discarded most of the background caused by proton beam-gas, halo and cosmic rays interactions.

1.11.2 The Second Level Trigger (SLT)

Every event accepted by the GFLT is passed to the Second Level Trigger [29, 30] processors. Again all components have a local processor, some of them having access to the full data, some to a pre-processed set only. They have more processing time available than at the first level, up to a few milliseconds. Many

[11] We call a trigger prescaled by a factor k if only a fraction $1/k$ of the all events satisfying the trigger requirements are kept and readout.

[12] This last feature is available only from the shutdown between the years 1998-1999.

components have built transputer [31] networks[13] allowing for a relatively simple, straightforward way of parallelization and programming by the use of a high-level programming language: OCCAM [32] or parallel-C.

The SLT component data is sent over transputer links to the input modules of the Global Second Level Trigger Box (GSLTB). From there the data are broadcast to up to five subtrigger modules, VME-modules with 2 transputers developed at NIKHEF-H.

Different algorithms are running on these subtrigger transputers in parallel. The results are sent to a master processor over the VME-bus, where all subtrigger results are combined into a final decision.

This way, the Global Second Level Trigger gets more, and also more accurate information than the GFLT, allowing a further reduction of the event rate, down to 100 Hz.

We now describe the vetoes that are available and applied to all the events.

The most important veto is the cut on the event timing: the timing is calibrated in such a way that a physics event that took place in the interaction point has zero time in the whole calorimeter once the produced particles arrive at it. An event that has been originated upstream of the detector (as a proton-beam gas interaction can be) hits RCAL first, and FCAL at the same time of the physics event (Figure 1.17). In this way the RCAL timing is about 10 ns early than a physics event, a time that is double compared to the time of flight from the nominal interaction point to RCAL. As the timing can be determined with an accuracy that is better than one nanosecond this criterium has a good discrimination power. The same reasoning goes for the FCAL timing when interactions due to the electron beam and the residual gas in the beampipe occur. The timing helps to reduce not only the number of events due to beam gas but also the one of cosmic induced and electronic noise induced interactions, since both appear asynchronous to the HERA timing.

The values of the calorimeter timing are available if at least one cell, with at least an energy of 200 MeV, has both the PMT's that have given signal. The times are calculated doing a weighted average of the values read over all the cells above threshold, region per region, where the weight is such to give more importance to cells with greater energy. For the timing be useful to veto an event it is also requested that the minimum number of cells interested by the energetic deposit be greater than a certain prefixed value (see Table 1.4). Both the value of the minimum energy per cell and the minimum number of above-threshold cells vary region per region of the calorimeter.

Let's list the requests that have to be met:

[13] A transputer, for what deals with the use done in our experiment, is a microprocessor obtained through photolitography on a single chip where four serial ports are integrated, called *link*, that are driven by the microprocessor and are used to make the connections among different transputers.

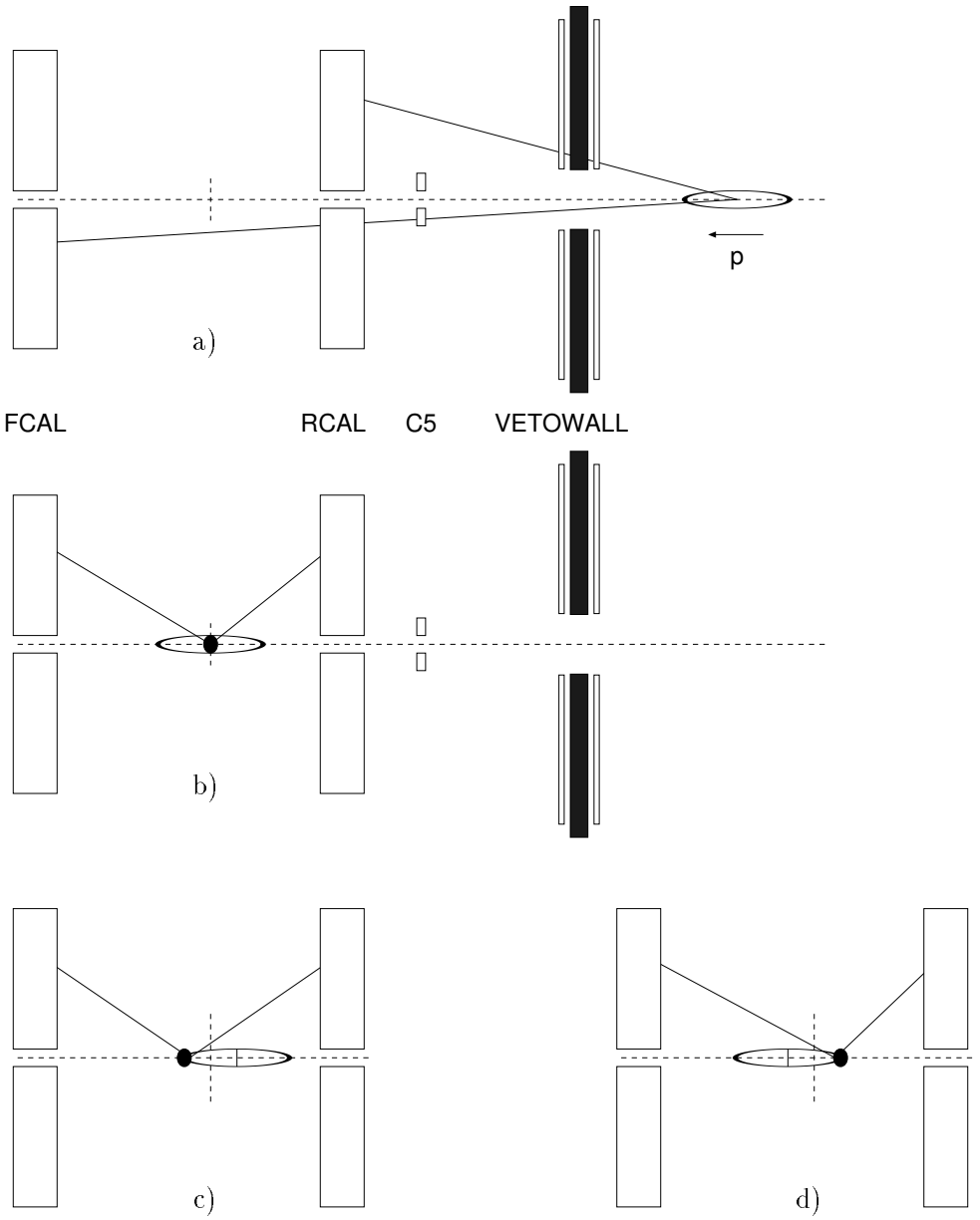

Figure 1.17: Timing: a) upstream proton beam-gas interactions produce events which (might) hit the VETOWall, the C5 scintillator counter and the calorimeter: the C5 time determines the exact passing time of the p-beam and is used to correct for run-by-run vertex deviations from the nominal position; the RCAL is hit earlier than the time of the beam crossing and earlier than the FCAL; moreover the time difference $T_{\mathrm{FCAL}} - T_{\mathrm{RCAL}}$ is independent of the proton bunch size;
b) events from the nominal interaction point result in time 0 in FCAL and RCAL;
c) and d) the FCAL time varies because of the length of the proton bunch but the RCAL time is less sensitive to that; in c) the FCAL time is early, in d) the FCAL time is late.

- **RCAL Timing**. Triggered events that are due to interactions of the proton beam with the residual gas in the vacuum pipeline are acknowledged as the RCAL timing is early: events are rejected making the following request:

$$|T_{RCAL}| > 8 \text{ ns}$$

- **FCAL Timing**. Muonic events due to cosmics and interactions of electrons with the residual gas in the pipeline cause FCAL times inconsistent with being ep interactions: cosmics happen anytime and the e-gas events come early. The event is discarded using the FCAL time if

$$|T_{FCAL}| > 8 \text{ ns}$$

- **F-RCAL Timing**. Not only the single FCAL or RCAL time, but even their difference F-RCAL is suitable to discriminate interactions of the gas with the proton beam when these happen upstream in comparison with real ep interactions: while for the latter ones the time difference is near zero, for the beam-gas events it is of about 11 ns. We discard the event that has

$$T_{FCAL} - T_{RCAL} > 8 \text{ ns}$$

- **Up-down Timing**. The cut on the up-down Timing is efficient for removing events caused by cosmic muons. Such events are characterized having a big value of the difference between the timing of the upper and lower half of BCAL. The events are discarded if both the halves have a valid timing, if FCAL and RCAL haven't signaled the presence of energetic deposit and if

$$T_{up} - T_{down} < -10 \text{ ns}$$

- $\mathbf{E - P_z}$. The maximum observable value of the difference between[14] E and P_z is imposed by the kinematics and is equal to the double of the electron beam energy. Those events having $E - P_z > 75$ GeV are rejected.

- **Global calorimetric timing**. If at least one of the calorimeter time is valid and if the same is, in absolute value, greater than 10 ns, the event is discarded.

[14]We define the total energy of the event E as the sum of the deposited energies in the calorimeter cells, and the component of the momentum along the beam axis P_z as the sum of the products $E_i \cos\theta_i$, where E_i and θ_i are the deposited energy and polar angle of the i^{th} cell above threshold.

1.11.3 The Third Level Trigger (TLT)

The GSLT sends its decision to the Event Builder (EVB), which broadcasts it to all components participating in the run. If the GSLT decides to keep the event, all components ship their data to the EVB, which takes care of putting them in a standard format (tables of ADAMO [33], definition of structures of memorization and data manipulation) and passes the full data to the Third Level Trigger (TLT).

The Third Level Trigger is formed by algorithms[15] written in FORTRAN, running on a farm of SGI workstations[16], where a rather complete event reconstruction is done. The TLT has all *raw* data available, allowing more sophisticated calculations than is possible on the lower trigger levels, especially when combining data from different components (e.g. matching tracks with calorimeter deposits).

The TLT reduces the event rate to 3-10 Hz, and sends the data via an optical link to the DESY computer center, where the data are stored on tape in a large cartridge robot.

[15] In Section 5.2.3 the TLT algorithm we used during the data taking as a physics filter to select events with at least two jets will be illustrated.

[16] The TLT is made of 14 SGI Challenge-S using MIPS R4400 CPU's of 150MHz, 250MHz clocks and 3 SGI Origin200 using MIPS R10000 CPU's with dual processor.

Chapter 2

Physics at HERA

2.1 ep Processes

The kinematic description of the interactions between electrons (positrons) and protons is done through particular variables defined by the four-momenta of final and initial state particles.

To define these kinematic variables let's consider the process:

$$e(p_e) + p(P) \rightarrow l(p_l) + X(P') : \tag{2.1}$$

where we indicate the outgoing lepton with l. The symbols that indicate the four-momenta of the particles are written in brackets.

The electroweak interaction between the incoming lepton and proton happens via the exchange of an intermediate vector boson, γ or Z^0 in neutral current interactions (NC) and $W^{\pm}$ in charged currents (CC), as shown in Figure 2.1.

We define:

$$q^2 = (p_e - p_l)^2 = -Q^2, \tag{2.2}$$

$$W^2 = (q + P)^2 \approx sy - Q^2, \tag{2.3}$$

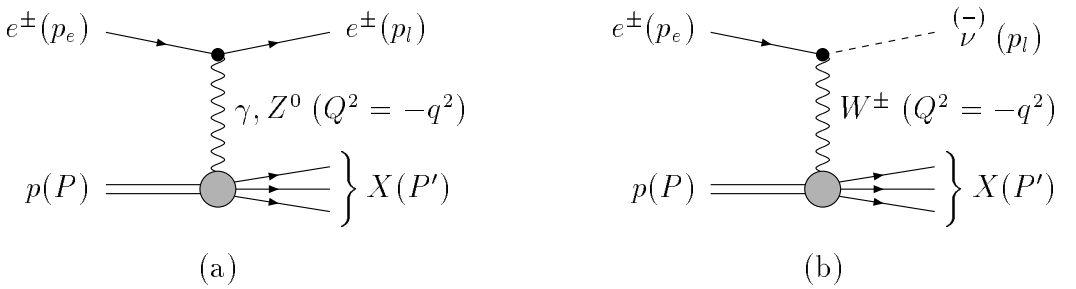

Figure 2.1: Lepton-proton scattering. Figure (a) represents neutral-current DIS, while figure (b) displays charged-current DIS. The four-momenta are indicated in brackets.

that represent the square of the transferred momentum at the lepton vertex and the centre of mass energy squared of the intermediate boson-proton system.

We will, often, prefer to use, instead of the variables W^2 and Q^2, the below defined quantities that are relativistic a-dimensional invariant:

$$x = \frac{Q^2}{2(P \cdot q)} \qquad (0 \leq x \leq 1), \tag{2.4}$$

$$y = \frac{P \cdot q}{P \cdot p_e} \qquad (0 \leq y \leq 1). \tag{2.5}$$

In the parton model these can be interpreted as the fraction of four-momentum of the incoming proton carried by the parton participating to the hard scattering, evaluated in the so-called *infinite momentum frame*[1] and the fraction of the energy lost by the electron and gained by the proton evaluated in the reference frame where the latter is at rest.

The square of the total energy available in the center of mass frame can be written as:

$$s = (p_e + P)^2 \simeq 2p_e \cdot P \simeq 4E_e E_p.^{\dagger} \tag{2.6}$$

In our case ($E_e = 27.5$ GeV and $E_p = 820$ GeV) $s \simeq 10^5$ GeV^2, which corresponds to a fixed target experiment with a beam of electrons of about 50 TeV energy.

From the definitions of s, x, y we see that:

$$Q^2 \simeq sxy, \tag{2.7}$$

therefore the maximum value that can be reached for the square of the transferred momentum is $Q^2_{max} \simeq 10^5$ GeV^2, that is achieved when $x = 1$ and $y = 1$.

Some particles of the final state are subject to strong nuclear force, and these are called *hadrons*, consist at an elementary level of quarks and gluons. The gluons are the propagator of the strong force, they have no electric charge but they possess color. Analogously to Quantum Electrodynamics (QED), which describes electromagnetic interactions, the strong force is described by Quantum

[1] We call the *infinite momentum frame* that class of reference frame systems were the proton has a very large three-momentum, in the limit *infinite*; in this kind of frame the proton can be visualized as a parallel stream of particles and, since all momenta are large, masses and transverse momenta can be neglected. Another characteristic of this system is that the following relations hold (Bjorken limit):

$$Q^2 \to \infty,$$
$$\nu = P \cdot q/M \to \infty,$$
$$\omega = \frac{2M\nu}{Q^2} \quad \text{is finite.}$$

[†] We can neglect the values of the masses of incident particles, as they are much smaller than the beam energies.

ChromoDynamics (QCD) which is the field theory of quarks, gluons and their interaction. The coupling constant of the strong force, α_s[‡], increases with distance due to an anti-screening effect. As gluons can couple to each other, then a gluon can fluctuate into a gluon-gluon pair, which causes the anti-screening effect.

HERA, as a collider, provides an opportunity for tests of QCD. When performing QCD calculations the presence of larger momentum scale yields more reliable results. This momentum scale, referred as the *hard scale*, is achieved in the analysis we will deal with, through the production of jets above a certain transverse energy threshold and through the study of heavy quarks.

2.2 Structure Functions

In an electromagnetic interaction between a lepton and a proton (or an hadron) we can write the cross section as a product of two tensors $L_{\mu\nu}$ and $W_{\mu\nu}$, the former describes the leptonic vertex, the latter the hadronic vertex. We know perfectly the functional dependence of $L_{\mu\nu}$, if we restrict ourselves to the Leading Order QED. The same thing is not true for the protonic tensor, but $W_{\mu\nu}$ describes all that happens at the hadronic vertex of the propagator. We can still subdivide this same tensor, according to the functional dependencies towards the relativistic invariant quantities involved (the metric matrix $g^{\mu\nu}$, the momenta p and q), into its parts[4]:

$$W^{\mu\nu} = -W_1 g^{\mu\nu} + \frac{W_2}{M^2} p^\mu p^\nu + \frac{W_4}{M^2} q^\mu q^\nu + \frac{W_5}{M^2} \left(p^\mu q^\nu + q^\mu p^\nu\right). \tag{2.9}$$

We can impose current conservation laws at the hadronic vertex and doing so we see that only two out of the five W_i quantities are independent; we usually choose them to be W_1 and W_2. We just need to rename these quantities, that are usually called structure functions, as

$$F_1(x, Q^2) \equiv M W_1(x, Q^2),$$

$$F_2(x, Q^2) \equiv \frac{p \cdot q}{M} W_2(x, Q^2),$$

[‡]We call α_s or α_{strong} the coupling constant of the strong interaction that is usually expressed in the following form (i.e. at the Leading Order):

$$\alpha_s(Q^2) = \frac{12\pi}{(33 - 2N_f) \ln Q^2/\Lambda^2}, \tag{2.8}$$

where Λ, Q^2 e N_f are: a residual scale after the renormalization of the theory (it is measurable through a fit and indicates, in some way, the application limit of the perturbative theory to the theoretical model), the scale at which the interaction takes place and the number of *active quark* flavours in the model. This type of description comes from the Renormalization Group equation [34].

[4]Remembering we are dealing with unpolarized cross section measurement.

where: Q^2 indicates the four-momentum transferred from the incoming electron, x the fraction of the momentum carried by the parton in the initial state.

To include the possibility of the exchange of an electroweak boson we just have to introduce another structure function we call $F_3(x, Q^2)$. This quantity is proportional to the propagator of the exchanged vector boson, i.e. a $W^{\pm}$ for charged current interactions and a Z^0 for neutral current events; in both the cases this extra structure function contains a dependence like

$$P_{W/Z} = \frac{Q^2}{(Q^2 + M^2_{W/Z})}.$$

where $M_{W/Z}$ is the mass of the $W^{\pm}$ or Z^0 boson.

The differential cross section for processes with neutral current (NC) exchange can, therefore, be written through these three quantities $F_2(x, Q^2)$, $F_L(x, Q^2)$, $F_3(x, Q^2)$:

$$\frac{d^2\sigma_{NC}(e^{\pm})}{dxdQ^2} = \frac{4\pi\alpha^2}{xQ^4}\left[\left((1-y) + \frac{y^2}{2}\right)F_2(x,Q^2) - \frac{y^2}{2}F_L(x,Q^2) \mp \left(y - \frac{y^2}{2}\right)xF_3(x,Q^2)\right] \tag{2.10}$$

where [5]; $F_L = F_2 - 2xF_1$ is the longitudinal structure function, xF_3 is proportional to the propagator of the Z^0 boson $P_z = Q^2/(Q^2 + M_Z^2)$ and α is the fine structure constant.

We can express in a similar way the charged current interaction cross section:

$$\frac{d^2\sigma_{CC}(e^{\pm})}{dxdQ^2} = \frac{G_F^2}{4\pi x}\left(\frac{M_W^2}{Q^2 + M_W^2}\right)^2\left[Y_+(y)F_2(x,Q^2) - y^2F_L(x,Q^2) \mp Y_-(y)\,xF_3(x,Q^2)\right], \tag{2.11}$$

where G_F is the Fermi constant and can be expressed as

$$G_F = \frac{\pi\alpha}{\sqrt{2}\sin^2\theta_W M_W^2}$$

and $Y_{\pm}(y)$ are helicity functions defined by

$$Y_{\pm}(y) = 1 \pm (1-y)^2.$$

[5] We want to notice that in the *infinite momentum frame* the *Bjorken limit* should hold and

$$F_1(x,Q^2) \xrightarrow{\text{Bjorken limit}} F_1(x),$$

$$F_2(x,Q^2) \xrightarrow{\text{Bjorken limit}} F_2(x).$$

a behaviour known as *scale invariance* or scaling.

In the quark parton model [35] in the *Bjorken limit*

$$F_2(x, Q^2) = F_2(x) = \sum_i e_i^2 x f_i(x), \tag{2.12}$$

$$F_1(x, Q^2) = F_1(x) = \frac{1}{2x} F_2(x), \tag{2.13}$$

and so the relation $F_2 = 2xF_1$ (Callan-Gross [36]) holds and hence F_L would be identically zero. This same function, F_L, is one of the largest systematic uncertainties in the determination of the proton structure function F_2 in DIS events.

2.3 QCD Improved Parton Model

The Callan-Gross relation holds on the hypothesis that the proton is composed only of charged particles with spin 1/2, the quarks. This means that if we sum all the contributions of the densities f_i and integrate over the momenta of the charged partons inside the proton the relation

$$\sum_i \int_0^1 dx f_i(x) x = 1 \tag{2.14}$$

should hold.

Experimentally, this value was found to be ≈ 0.5 [37], the implication being that the proton also consists of neutral particles. Evidence for the existence of these neutral particles, gluons, was provided in 1979 via the observation of 3-jet events in e^+e^- annihilation at DESY [38].

The QPM approach where the proton consists only of quarks was then modified to include gluons. This then became QCD, where quarks interact via the exchange of gluons. Gluons, themselves, can split into quark pairs or gluons. The radiated gluons result in the quarks having a component of transverse momentum. Coupling to longitudinally polarized photons is then possible, thereby violating the Callan-Gross relation.

As a result of the gluon radiation, exact scaling of the structure functions (i.e. dependence only on x) is violated and a logarithmic dependence on Q^2 is introduced. The photon at low Q^2 is then interpreted as resolving the valence quark substructure. At high Q^2 a quark may have radiated a gluon and consequently having a fraction of momentum, x, less than its original value, or alternatively, it may have arisen from gluon splitting.

At large values of x, where the valence quarks dominate, the quark density (and hence F_2) falls with increasing Q^2 whereas at low x, the number of "sea" quarks and gluons is larger, so F_2 increases with Q^2. This dependence of F_2 with Q^2 has been demonstrated at HERA [39].

2.4 The Evolution of Partonic Densities

The logarithmic Q^2 dependence of the structure functions can be predicted by accounting for the qqg vertex and modifying Equation (2.12) to

$$\frac{F_2(x,Q^2)}{x} = \left| \quad \right|^2 + \left| \quad + \quad \right|^2$$

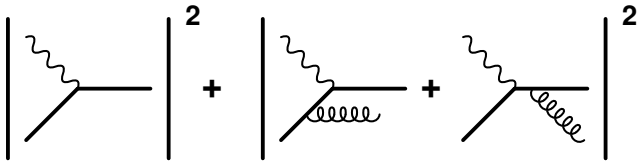

$$= \sum_q e_q^2 \int_x^1 \frac{dy}{y} q(y) \left(\delta\left(1-\frac{x}{y}\right) + \frac{\alpha_s}{2\pi} P_{qq}\left(\frac{x}{y}\right) \log\frac{Q^2}{\mu^2} \right) \quad (2.15)$$

where $q(y) = f_q(y)$ is the quark structure function, μ is a lower limit on the transverse momentum to regularise divergences which occur as the transverse momentum squared tends to zero and $P_{qq}(z)$ represents the probability of a quark emitting a gluon and then having a momentum fraction z and it is called a splitting function. The second term of Equation (2.15) can be re-written as

$$\Delta q\left(x,Q^2\right) \equiv \frac{\alpha_s}{2\pi} \log\frac{Q^2}{\mu^2} \int_x^1 \frac{dy}{y} q(y) P_{qq}\left(\frac{x}{y}\right). \quad (2.16)$$

At some $Q^2 \sim Q_0^2$, the photon starts to resolve the point-like valence quarks within the proton. QCD then predicts that with increasing Q^2, such that $Q^2 \gg Q_0^2$, the resolution power increases and the quark itself (surrounded by a sea of partons) is "seen". The quark structure function can be calculated for any value of Q^2, given some reference value $q(x,Q_0^2)$ by considering the change in $\Delta q(x,Q^2)$ for a small change in $\log Q^2$:

$$\frac{dq(x,Q^2)}{d\log Q^2} = \frac{\alpha_s}{2\pi} \int_x^1 \frac{dy}{y} q\left(y,Q^2\right) P_{qq}\left(\frac{x}{y}\right). \quad (2.17)$$

By then considering a quark evolved from a gluon in a pair production process, the evolution of the quark density distribution can be modified further. The same procedure can also be applied to the evolution of the gluon density distribution by considering gluons resulting from quarks or gluons. The resulting equations describe partonic evolution and are called the Dokshitzer-Gribov-Lipatov-Altarelli-Parisi equations [40]:

$$\frac{dq_i(x,Q^2)}{d\log Q^2} = \frac{\alpha_s}{2\pi} \int_x^1 \frac{dy}{y} \left[q_i\left(y,Q^2\right) P_{qq}\left(\frac{x}{y}\right) + g(y,Q^2) P_{qg}\left(\frac{x}{y}\right) \right] \quad (2.18)$$

$$\frac{dg(x,Q^2)}{d\log Q^2} = \frac{\alpha_s}{2\pi} \int_x^1 \frac{dy}{y} \left[\sum_i q_i\left(y,Q^2\right) P_{gq}\left(\frac{x}{y}\right) + g(y,Q^2) P_{gg}\left(\frac{x}{y}\right) \right] \quad (2.19)$$

where $q_i(x,Q^2)$ is the quark density function, for each quark flavour i and $g(x,Q^2)$ is the gluon density function. There are now several splitting functions $P_{jk}(x/y)$

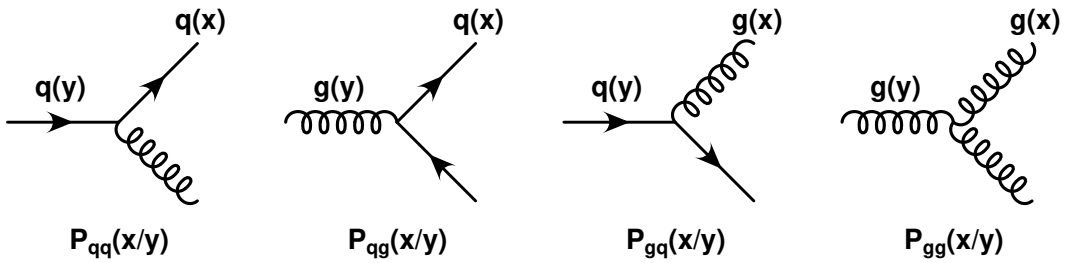

Figure 2.2: The first order splitting functions $P_{jk}\left(\frac{x}{y}\right)$ used in the DGLAP equations.

which are shown in Figure 2.2. They represent the probability of a parton k of momentum fraction y emitting a parton j of momentum fraction x.

The parton evolution can be seen as the sum of ladder diagrams where each "ladder" corresponds to a gluon emission as in Figure 2.3. Each diagram with n gluon emissions of momentum $k_{T_i}^2$ represent a term in $(\alpha_s \log Q^2)^n$, where $\alpha_s \log Q^2 \sim 1$, which is dominant at large x and Q^2. In this regime, each contribution is ordered in transverse momentum such that,

$$k_{T_1}^2 \ll k_{T_2}^2 \ll ... \ll k_{T_{n-1}}^2 \ll k_{T_n}^2 \ll Q^2.$$

With the knowledge of the x dependence at a minimum Q^2, Q_0^2, the evolution equations can be solved to give the parton distributions as a function of x for all Q^2. This minimum value Q_0^2, cannot presently be calculated so relies on experimental determination.

As was stated these evolution equations describe the physics at high x and Q^2 ignoring terms of $\log(1/x)$ whose importance arises at low x. The terms at low x have been taken into account by summing $(\alpha_s \log(1/x))^n$ gluon emission terms which are now not ordered in transverse momentum resulting in the Balitsky-Fadin-Kuraev-Lipatov (BFKL) equation [41].

A unification of the two methods leading to a complete description of the parton distribution function's x and Q^2 dependence is an obvious goal, but is experimentally as well as theoretically challenging.

2.5 The Deep Inelastic Scattering (DIS) Regime

Within the single-photon exchange approximation, we can view deep inelastic electron scattering (DIS) as photoproduction by *virtual*, really *off-shell*, photons. As the virtuality, q^2, of the photon that is its effective mass is variable the exchanged photon may have longitudinal as well as transverse polarization.

The Equations 2.10 and 2.11 are useful to describe the NC and CC interactions, respectively, in the whole plane x, Q^2, that we can divide into regions where

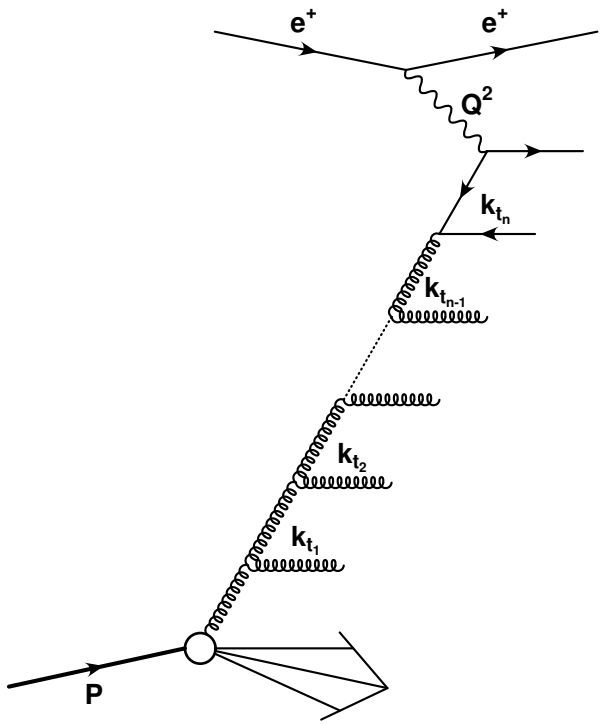

Figure 2.3: Parton evolution diagram showing the k_t ordered gluon emissions.

some aspects of the kinematics are peculiar. At least two of these regions exist, the first is the one where the Deep Inelastic scattering regime is applicable, and we will give here a short description of some characteristics of its. The second one is that where the momentum transferred at the leptonic vertex Q^2 is small and that we call of photoproduction. We will describe it starting from the next section.

We can speak of DIS when the incoming lepton has undergone a large scattering and the transferred four-momentum Q^2 is much greater of the mass of the proton. In this kind of events a virtual photon can be exchanged (but also an electroweak vector boson) between the lepton and the proton of the initial state. Several are the characteristics of this regime that become important as the virtuality increases:

- the photon can acquire a longitudinal polarization, so both the transverse and longitudinal cross section are important[6];
- the flux of the virtual photons is not uniquely defined, and require a convention. The Hand is normally chosen [42];
- the photon probes smaller transverse distances. The order of the scale

[6] We call transverse or longitudinal cross section the square of the modulus of the amplitude to scatter the initial state particles through transversally or longitudinally polarized bosons.

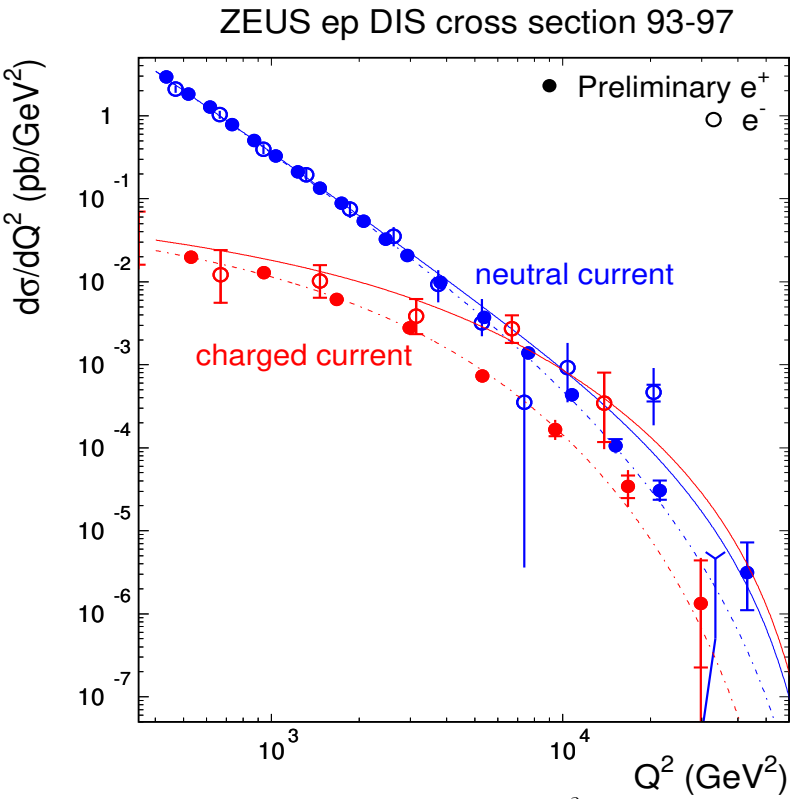

Figure 2.4: The differential cross section versus Q^2 for neutral and charged current scattering as measured by ZEUS in the 1993-1997 data sets. The results are compared to Standard Model expectations separately for e^+p and e^-p scattering. The cross sections all become comparable near $Q^2 = 10000$ GeV^2,as expected from electroweak unification [43].

probed is given by

$$d \approx \frac{0.2}{\sqrt{Q^2}(\text{GeV})} \text{ fm.}$$

For $Q^2 > 1$ GeV^2, transverse distances at the level of a fraction of the proton radium are probed;

- the greater is the transferred momentum the less the difference between NC and CC interactions (see Figure 2.5).

It is in this regime that the scattering of the incoming electron on the proton is visible as an incoherent sum of elastic diffusion of the electron on *free* partons inside the proton.

It is still in this regime that both the ZEUS and H1 experiments [39] have studied the structure function F_2 and its scaling violation to calculate the gluon density of the proton.

However, in most of the kinematic region available at HERA, the single-photon exchange dominates by far, and as can be seen in Figure 2.5 the cross

section at low values of Q^2 is much larger than in the other cases.

2.6 The Photoproduction Regime

In the photoproduction regime the momentum transferred at the leptonic vertex Q is small ($Q^2 \sim 0$) so the exchanged particle is an almost real photon.

At these low Q^2 values the contribution of the weak interaction can be neglected since the Z^0 and $W^{\pm}$ propagators $P_{W/Z} = Q^2/(Q^2 + M^2_{W/Z})$ are essentially zero and also the longitudinal component of the cross section can be ignored ($\sigma_L \simeq 0$). As a consequence, we can restrict ourselves to the exchange of photons. We can thus consider the electron beam as a source of photons and factorize the cross section of electron on proton in the following way:

$$\sigma_{e-p} = \phi_{\gamma/e} \times \sigma_{\gamma-p}. \tag{2.20}$$

The expression links the electro-production cross section with the photoproduction one through a factor, the photon flux $\phi_{\gamma/e}$.This is known as the *equivalent photon approximation* (EPA) and can be written as (see [44, 45] and reference therein):

$$\phi_{\gamma/e} = \frac{\alpha}{2\pi} \int_{y_{min}}^{y_{max}} \left[\frac{1+(1-y)^2}{y} \ln\left(\frac{Q^2_{max}(y)}{Q^2_{min}(y)} \right) + \frac{2(y-1)}{y} \left(1 - \frac{Q^2_{min}(y)}{Q^2_{max}(y)} \right) \right] dy : \tag{2.21}$$

where:

$$Q^2_{min}(y) = m_e^2 \frac{y^2}{1-y} = \mathcal{O}(10^{-9}\mathrm{GeV}^2),$$

while the median of the distribution of Q^2 is $\mathcal{O}(10^{-3}\mathrm{GeV}^2)$. This flux can be interpreted as the probability to find a photon in the electron of energy $E_\gamma = yE_e$.

As can be seen, one of the important variables in the real-photon induced interactions is clearly the photon virtuality Q^2, that is both above and below limited. In the HERA environment the upper limit of variability is usually lower than some unit in GeV^2 ($Q^2_{max} \approx 1\ \mathrm{GeV}^2$), as we have already anticipated, if we use the capability of the main calorimeter to anti-tag the scattered electron (positron). The value of the transferred momentum is, on the contrary, below $10^{-2}\ \mathrm{GeV}^2$ if the outgoing lepton is detected in the luminosity monitor (LUMI).

Another important variable that can be noticed in Equation (2.21) is y. It is linked to the energy available in the center of mass frame of the reaction $\gamma - p$ by the Equation (2.3).

Photoproduction processes allow to carry on studies and controls on the validity of the Quantum ChromoDynamics in strong interactions with photons, studies carried out through the structure function of the proton and photon, that can be extracted from the interaction of the photon.

Following [46], as an example, the photon can be seen as a superposition of different states and the state function can be written as:

$$|\gamma\rangle = c_{bare}|\gamma_{bare}\rangle + \sum_{V=\rho,\omega,\phi,J/\psi} c_V|V\rangle + \sum_{q=u,d,s,c,b} c_q|q\bar{q}\rangle + \sum_{l=e,\mu,\tau} c_l|l^+l^-\rangle, \qquad (2.22)$$

where:

- $|c_{bare}|^2 = 1 - \sum_V |c_V|^2 - \sum_q |c_q|^2 - \sum_l |c_l|^2$;
- $c_V = em_V^2/g_V$: this is the part of Vector Dominance Model (VDM) [47] and correspond to the interval of fluctuation of $q\bar{q}$ below k_0 and is thus μ-independen (if we assume $\mu > k_0$);
- $c_q \approx \frac{\alpha}{2\pi} 2e_q^2 \ln \frac{\mu^2}{k_0^2}$;
- $c_l \approx \frac{\alpha}{2\pi} \frac{2}{3} \ln \frac{\mu^2}{m_l^2}$;

  where:

  - k_0 is a *cutoff* that separates $q\bar{q}$ fluctuations with high and low virtuality,
  - μ^2 is the scale used to probe the photon,
  - e_q is the electromagnetic charge of the quark.

The first term describes the photon in its bare state and the probability for the photon to remain in such a state is approximately of 99.5%. Nevertheless the event rate at high energy is dominated by the other components, due to their higher cross sections.

The contribution due to the second term is the one that correspond to the VDM part such that the photon couples directly to hadrons as the vector mesons and behaves thoroughly as an hadron. In this way the process of photoproduction coincides with the one of hadro-production.

The third term describes the quantistic oscillations of the photon in $q\bar{q}$ pairs and it is calculable within the domain of perturbative QCD. This type of processes is a novelty of HERA and can be distinguished from the precedent ones by the different value that k_0 assumes, even called scale of the extracted parton by the photon. We think, as a matter of fact, it to be larger than in the case of the VDM model.

We note that all the relevant processes we dealt with so far and present in the Equation (2.22) have the same order of magnitude in terms of the coupling constants ($\mathcal{O}(\alpha\alpha_s)$).

Photoproduction can be studied at HERA at energies that are one order of magnitude higher than what was possible in previous experiments. Mainly the photon can interact with the proton in two ways (we can investigate both of these); according to the behaviour of the photon we have the so-called "direct" and "resolved" photon interactions.

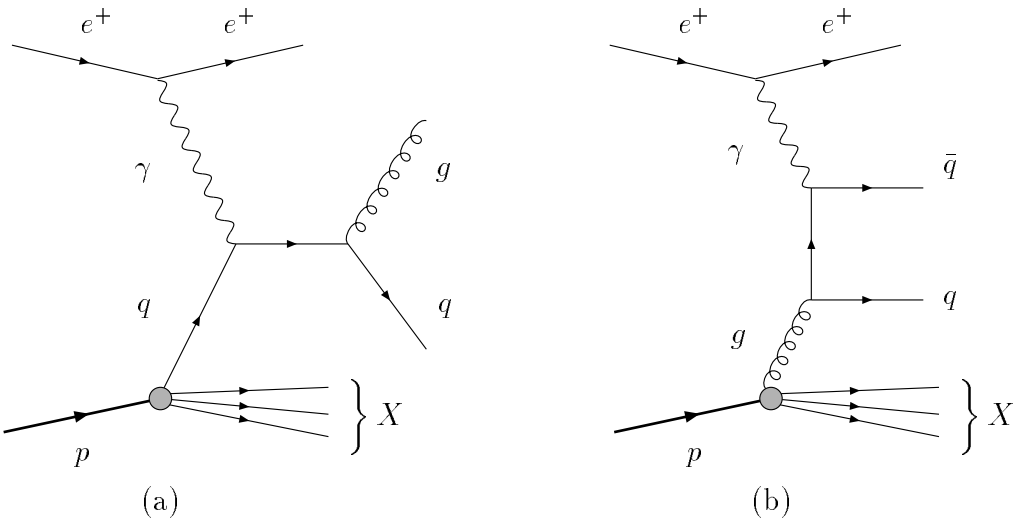

Figure 2.5: Leading order direct processes; (a) QCD Compton and (b) Boson gluon fusion.

2.7 Direct Photoproduction

Direct photoproduction is so-called because in this process the photon can be thought of interacting *directly* in the hard sub-process. The photon acts as a pointlike object interacting with the partons from the proton; a property which distinguishes photon-proton from hadron-hadron scattering. As all the photon's energy couples to the parton, the final state of the process is expected to be of higher transverse momentum than for hadronic (or resolved) type interactions in which only part of the photon's energy participates. The two LO direct photoproduction diagrams can be seen in Figure 2.5. The QCD Compton process in Figure 2.5a shows the photon coupling to a quark within the proton which then radiates a gluon before hadronisation. In Figure 2.5b, the photon couples to a quark coming from a "split" gluon in the proton which produced a quark-antiquark pair. This process is termed boson-gluon fusion. Both have final states consisting of two high transverse energy jets where, in the case of the QCD Compton process, one is a quark and the other a gluon jet and in boson-gluon fusion both are quark jets.

2.8 Resolved Photoproduction

In resolved photon processes, the photon acts as a source of partons one of which interacts with a parton from the proton in the hard sub-process. In the case of a resolved photon, only a fraction of the photon's energy participates to the hard interaction. Examples of resolved photoproduction diagrams at LO can be seen in Figure 2.6. In Figure 2.6a, a gluon from the photon interacts with a gluon from

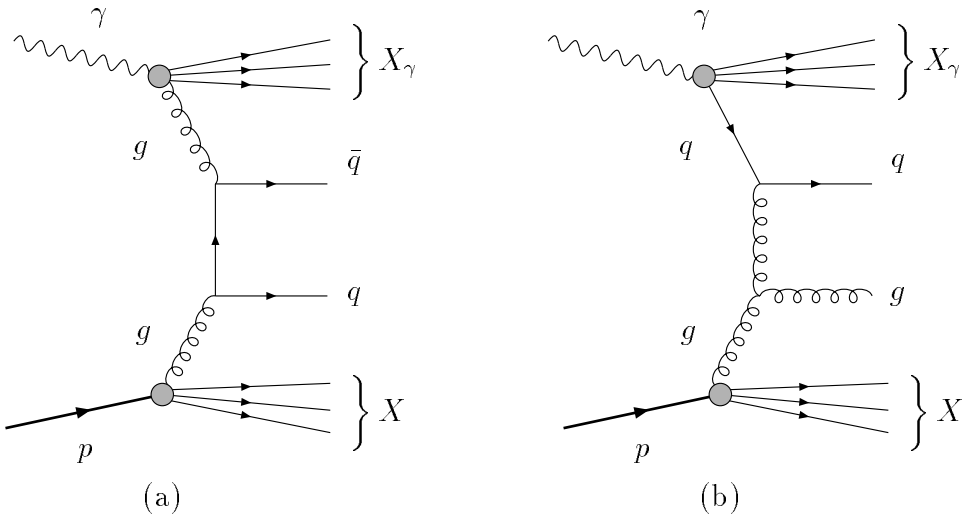

Figure 2.6: Examples of leading order resolved processes.

the proton in what is termed gluon-gluon fusion. However, in Figure 2.6b it is a quark from the photon which interacts with the gluon from the proton. Again these two processes differ in that the final state consists of two quark jets in the case of Figure 2.6a and one quark and one gluon jet in the case of Figure 2.6b. Therefore it seems to possess the same final state as direct processes. This, however, is not true as in addition to the two jets, proton remnant and scattered electron, there is a photon remnant (X_γ).

2.9 Generalised Photoproduction Model

Direct and resolved processes at LO and the diagrams shown in Figures 2.5 and 2.6 can be generalised and are shown in Figure 2.7 for jet production. The dotted lines in the figure represent the cut-offs between the hard process which can be calculated perturbatively and the non-perturbative parton distribution functions. The factorisation scales μ_P and μ_γ are arbitrary, but are chosen to be $\sim p_T$, the transverse energy of the jet, allowing the incoming parton a large region of phase space in which to evolve. As the hard sub-process is independent of the factorisation scale, a variation of the scale would only effect the parton distribution functions.

The differential cross-section for the generalised model can be separated into direct and resolved components;

$$d\sigma_{\gamma p \to cd} = d\sigma^{dir}_{\gamma p \to cd} + d\sigma^{res}_{\gamma p \to cd} : \tag{2.23}$$

where the two separate components can be written as,

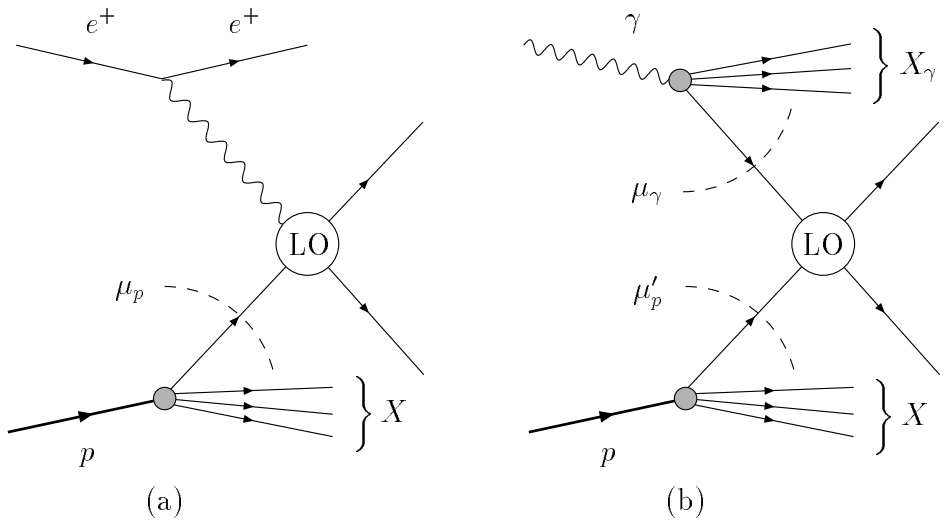

Figure 2.7: General Leading Order picture for resolved and direct processes.

$$d\sigma^{dir}_{\gamma p\to cd} = \sum_b \int_{x_p} dx_p f_{p\to b}\left(x_p, \mu_p^2\right) d\hat{\sigma}_{\gamma b\to cd} \tag{2.24}$$

and

$$d\sigma^{res}_{\gamma p\to cd} = \sum_{ab} \int_{x_p} dx_p \int_{x_\gamma} dx_\gamma f_{p\to b}\left(x_p, {\mu'_p}^2\right) f_{\gamma\to a}\left(x_\gamma, \mu_\gamma^2\right) d\hat{\sigma}_{ab\to cd}. \tag{2.25}$$

The $d\hat{\sigma}$'s represent the perturbatively calculable $2 \to 2$ scattering matrix element and $f_{p\to b}$ and $f_{\gamma\to a}$ the density functions of the proton and photon, respectively.

At Next-to-Leading Order (NLO), there are also contributions from $2 \to 3$ parton scattering, which are dependent on the factorisation scale. By varying μ_γ, the amount of $2 \to 3$ processes at NLO and the amount which are in fact simply LO processes varies. More specifically, an ambiguity between NLO direct and LO resolved arises and is dependent on μ_γ. The advantage of NLO over LO therefore lies in the reduction of the dependence on the factorisation scale.

2.10 The Structure of the Photon

Consider deep inelastic $e\gamma$ scattering as in Figure 2.8 which is formally analogous to deep inelastic ep scattering. The cross-section for a probing photon with virtuality $Q^2 \equiv -q^2$ scattering off a real target photon with virtuality $P^2 \approx 0$ producing a final state eX is given by,

$$\frac{d^2\sigma_{e\gamma\to eX}}{dxdy} = \frac{2\pi\alpha^2 s}{Q^4}\left\{\left[1+(1-y)^2\right] F_2^\gamma(x_\gamma, Q^2) - y^2 F_L^\gamma(x_\gamma, Q^2)\right\} \tag{2.26}$$

where $x_\gamma \equiv Q^2/(2p \cdot q)$.

The beauty of the $e\gamma$ cross-section is that unlike in ep scattering, the structure functions can be computed in the Quark Parton Model. Unfortunately the result depends on the mass of the constituent quarks which are not well defined in field theory.

Analogously to ep scattering the structure function F_2^γ can also be written in terms of the quark densities in the photon, $q_i^\gamma(x_\gamma, Q^2)$, such that (in LO)

$$F_2^\gamma(x_\gamma, Q^2) = 2x_\gamma \sum_i e_{q_i}^2 q_i^\gamma(x_\gamma, Q^2), \tag{2.27}$$

where the sum runs over all quark flavours, i, of charge e_{q_i} and the factor of two accounts for quarks and antiquarks.

We can then compute the photonic parton densities Q^2 dependence [48];

$$\frac{dq_i(x_\gamma, Q^2)}{d\log Q^2} = a(x) + \frac{\alpha_s(Q^2)}{2\pi}\int_{x_\gamma}^1 \frac{dy}{y}\left[P_{qq}\left(\frac{x_\gamma}{y}\right) q_i(y, Q^2) + P_{qg}\left(\frac{x_\gamma}{y}\right) g(y, Q^2)\right], \tag{2.28}$$

$$\frac{dg(x_\gamma, Q^2)}{d\log Q^2} = \frac{\alpha_s(Q^2)}{2\pi}\int_{x_\gamma}^1 \frac{dy}{y}\left[P_{gq}\left(\frac{x_\gamma}{y}\right) 2\sum_i^f q_i(y, Q^2) + P_{gg}\left(\frac{x_\gamma}{y}\right) g(y, Q^2)\right], \tag{2.29}$$

where,

$$a(x_\gamma) = 3e_i^2 \frac{\alpha}{2\pi}\left[{x_\gamma}^2 + (1 - x_\gamma)^2\right]$$

represents the $\gamma \to q\overline{q}$ splitting and the P_{jk} are the splitting functions[49, 50, 51].

At large values of x_γ, the production of quarks comes predominantly via the $\gamma \to q\overline{q}$ splitting. As this coupling is electromagnetic, the number of u quarks produced is four times that of the d quarks due to their relative electric charge. At low values of x_γ however, the quarks are produced from the gluon splitting process and here there is an equal number of u and d quarks as the strong force does not differentiate between charge.

There is currently a large number of photon parton density parametrisations and they usually involve some fits to data. Because of the large errors on F_2^γ additional assumptions need to be made. These assumptions differ in different models and involve the treatment of heavy quarks, the choice of the scale Q_0^2 and the methods of deciding the form of the input densities. HERA could provide interesting information that would allow the testing of these different parametrisations.

2.10.1 Dijet Photoproduction Results at HERA

As was shown previously, the distinction between resolved and direct photon processes at LO is theoretically defined whereas at higher orders the distinction

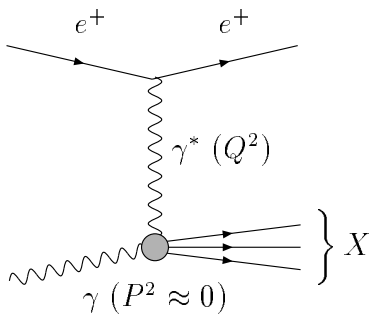

Figure 2.8: Diagram for $e\gamma$ diagram with a virtual photon, γ^*, probing an on-shell photon, γ.

between the two becomes ambiguous. The relevant contributions from the two processes in the photoproduction of jets were compared to fixed target experiments in 1979 [52]. The contribution from the resolved photon processes was found to be small. With the advent of HERA, the contribution from resolved processes becomes large and consequently their observation possible. From the knowledge of their properties an experimental distinction and observation can be made.

The observation of resolved photon processes was achieved in the early stages at HERA [53] via the observation of large energy deposits in the rear (electron) direction consistent with a photon remnant. A distinction between the resolved and direct photon processes was also seen [54] and an experimental separation of the two processes can be performed. This separation is based on the knowledge of the fraction of the photon's momentum, x_γ, participating in the interaction. For the LO QCD diagrams shown in Figures 2.5 and 2.6, energy and momentum conservation in a $2 \to 2$ parton scatter yield:

$$x_\gamma^{LO} = \frac{\sum_{partons} E_T^{partons} e^{-\eta^{partons}}}{2yE_e}, \tag{2.30}$$

where yE_e is the initial photon energy. For direct events, this value is one and for resolved events it is less than one. Translating this into an experimentally measurable quantity, we sum over jets instead of partons. Equation (2.30) then becomes, in terms of our new variable, $x_\gamma^{\rm obs}$ [55],

$$x_\gamma^{\rm obs} = \frac{\sum_{jets} E_T^{jet} e^{-\eta^{jet}}}{2yE_e}, \tag{2.31}$$

where the sum runs over the two highest transverse energy jets. Due to effects of hadronisation and/or higher order effects, the value of $x_\gamma^{\rm obs}$ is not one for direct events, but the events do populate the higher regions of $x_\gamma^{\rm obs}$. By fitting the Monte Carlo simulations of resolved and direct processes to the data measured,

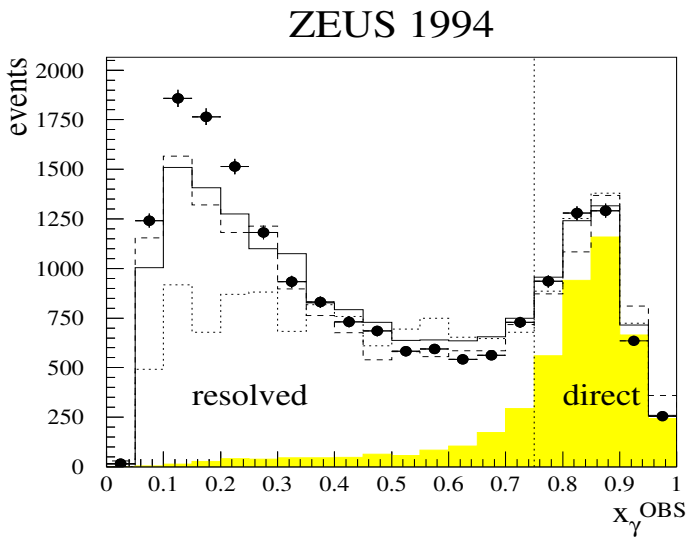

Figure 2.9: The $x_\gamma^{\rm obs}$distribution in dijet events for data (black dots) compared with HERWIG with and without MPI (solid line and dotted line), and PYTHIA with MPI (dashed line) Monte Carlo generators. The shaded area represents direct only events as generated by HERWIG and the vertical line is the experimental cut to separate direct and resolved processes.

the two processes can be separated. This is shown in Figure 2.9 [56] where the experimental cut-off of $x_\gamma^{\rm obs} = 0.75$ to divide the sample into a direct enriched and resolved enriched one is also shown.

The agreement in shape between data and Monte Carlo is good except below $x_\gamma^{\rm obs}= 0.3$, even when a MultiParton Interaction (MPI) model is included. The description of this region without MPI is poor using both generators.

Having proved the existence of the two types of processes, the next question to then ask is of their form. In Figure 2.6, there are two examples of LO resolved processes and it is reasonable to ask if one dominates over the other. This can be determined by studying the dijet angular distribution which is dependent on the propagator of the process. The angle θ^* between the jet-jet axis and the beam axis, in the dijet centre of mass system, can be calculated in terms of measurable quantities such that,

$$\cos\theta^* = \tanh\left(\frac{\eta^{jet1} - \eta^{jet2}}{2}\right), \tag{2.32}$$

where η^{jet1} is the pseudorapidity of the highest and η^{jet2} the pseudorapidity of the second highest jet in transverse energy. At LO, direct processes involve a quark as a propagator (see Figure 2.5) whereas resolved processes can have quark (Figure 2.6a) or gluon (Figure 2.6b) propagators. A quark propagator, with spin-1/2, leads to an angular dependence which is $\propto (1 - |\cos\theta^*|)^{-1}$ and a gluon, with spin-1, gives an angular dependence which varies $\propto (1 - |\cos\theta^*|)^{-2}$. QCD

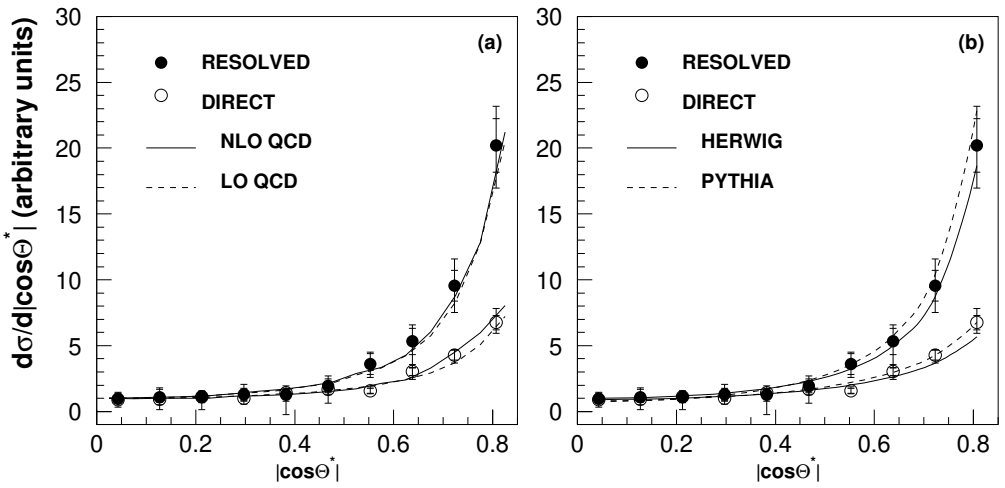

Figure 2.10: Dijet angular cross-sections for resolved (black dots) and direct (open dots) compared to LO and NLO QCD predictions and HERWIG and PYTHIA Monte Carlo.

predicts that in the case of resolved photon processes the angular distribution will rise rapidly in line with the gluon being the dominant process. This was confirmed in dijet photoproduction at ZEUS [57] by measuring the dijet angular cross-section for resolved and direct events where the direct-resolved separation was achieved by a cut on $x_\gamma^{\rm obs}$ at 0.75 as previously mentioned. The result is shown in Figure 2.10.

These and other results from HERA are for inclusive dijet photoproduction. As the analysis in this thesis also tags heavy quarks in dijet photoproduction, the phenomenology of heavy quarks is discussed and is the subject of the next part of this chapter. The results shown so far, however, provide an interesting baseline for comparison with future results so the effect of a charm or beauty quark can be seen. The questions to answer are amongst others:

- Is there direct and resolved charm and beauty photoproduction at HERA?
- What are the dominant resolved and direct diagrams?
- Is there any charm or beauty in the photon?

These points will be discussed and some of them answered in the following pages.

2.11 The Physics of Heavy quarks

The study of heavy quarks yields the opportunity of studying perturbative QCD with an additional hard scale, the quark mass, to that of the transverse energy of the jets. The charm mass is approximately that of the hadronic scale and is at the (lower) limit of applicability for perturbative QCD. This implies the study of semi-perturbative effects may be better performed through measurements of the charm rather than the beauty quark. The mass of the beauty quark lies well above this value ($m_b \sim 3m_c$) so it would theoretically provide the better tests of perturbative QCD.

Hadro-production and photoproduction data from fixed target experiments agree qualitatively with QCD predictions but quantitative deviations remain. This prompts the question as to whether simple non-perturbative models such as fragmentation effects and intrinsic transverse momentum are sufficient to explain the deviations. The new possibilities provided by HERA are the wide kinematic range for photoproduction allowing the study of the photon and proton structure functions and the study of heavy quark jets.

2.12 Heavy Quark Production at Fixed Target Experiments

Heavy quark production has been extensively studied at a number of fixed target experiments at centre-of-mass energies of about 10 - 40 GeV. At this energy the cross-section for beauty quarks is low so most studies concentrated on the charm quark.

If one considers the photoproduction data for the total charm production cross-sections at fixed target experiments compared to pQCD calculations, qualitative agreement but quantitative deviations can be clearly seen (see Figure 2.11).

Looking at a data set from one experiment in isolation, one can see that the E687 data is consistent with a charm mass of 1.2 GeV and inconsistent with a value of 1.8 GeV whilst the E691 data is inconsistent with $m_c = 1.2$ GeV, but consistent with $m_c = 1.8$ GeV. These results from γN collisions clearly show a broad agreement with QCD predictions, but no consistent value of charm mass or renormalisation scale can be obtained from the comparison. To constrain the physical parameters, the (sometimes large) discrepancies between experiments need to be resolved.

Single inclusive distributions have also been measured at fixed target experiments and compared to QCD calculations. The effect of non-perturbative phenomena coupled to the pQCD predictions have also been studied by, for example, introducing an intrinsic transverse momentum for the incoming partons (the so-called "k_T kick") and introducing a hadronisation for the charm quark. Figure 2.12 shows the inclusive p_T^2 distribution of charmed hadrons in γN colli-

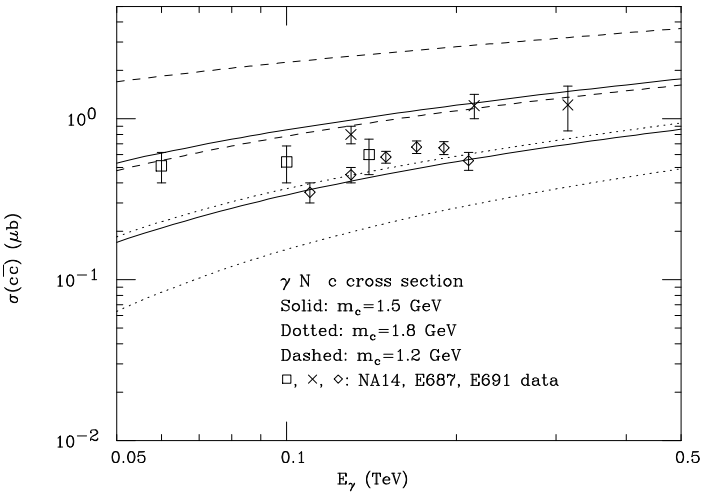

Figure 2.11: Total pair cross-section for c production in γN collisions from the NA14 [58], E687 [59] and E691 [60] collaborations compared to QCD predictions. The bands represent (for a given charm mass) the variation due to the choice of the renormalisation scale, where the limits shown here are, $\mu_R = m_c/2$ and $\mu_R = 2m_c$ (from [61]).

sions from the E687 (Left) and E691 (Right) collaborations. By comparing the data with theoretical predictions, it can be seen that some non-perturbative component is needed to describe the data, although it is reasonably insensitive to the value of the "k_T kick" chosen. The convolution of the pQCD prediction with a fragmentation function is however necessary.

Correlations between charmed quarks have also been studied in photoproduction data; namely $\Delta\phi$, the angle between the momenta projections of the pair onto the transverse plane, and the transverse momentum of the pair $p_T(Q\bar{Q})$. These values are again thought to be sensitive to non-perturbative effects such as the "k_T kick". Photoproduction data has been compared to NLO QCD calculations with an added "k_T kick" [61]. Both distributions indicate a sensitivity to "k_T kick" but the value which gives the best description of the data is dependent on experiment and distribution.

2.13 Heavy Quark Production at HERA

There are two theoretical advantages to the study of heavy rather than light quarks in photoproduction. As mentioned at the beginning of Section 2.11, the large mass ($m_q \gg \Lambda_{\rm QCD}$) ensures that perturbative calculations are more reliable although corrections $\propto (\Lambda_{\rm QCD}/m_q)^n$ might be non-negligible for the charm quark. With accurate values of m_q and $\Lambda_{\rm QCD}$, reliable total cross-sections could be predicted. Secondly, the study of heavy quarks also reduces the number of

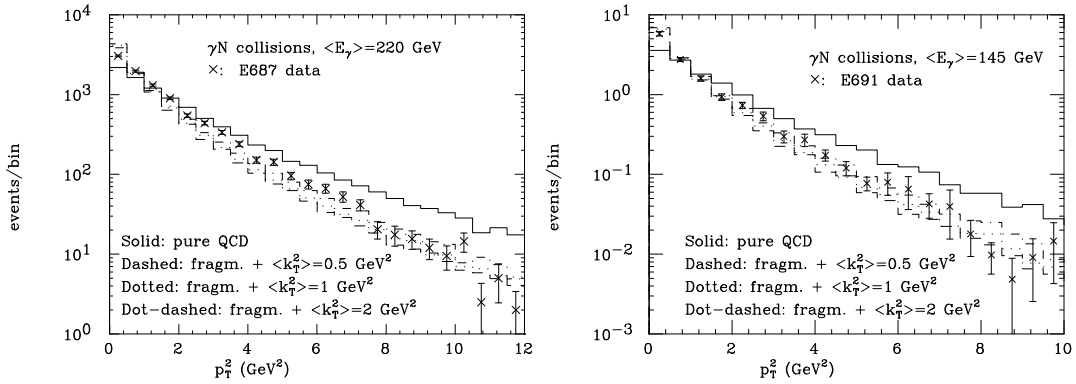

Figure 2.12: Distribution in p_T^2 for charmed hadrons from the E687 [59] (left) and E691 [60] (right) collaborations compared to NLO pQCD (m_c = 1.5 GeV) and NLO pQCD with non-perturbative effects (from [61]).

contributing partonic processes, such that the boson-gluon fusion (Figure 2.5b) process

$$\gamma g \to Q\bar{Q},$$

is the only direct photon process at LO. To LO this process is directly sensitive to the gluon content of the proton. The question of the relative contribution of LO resolved processes is less clear. Heavy quark "excitation" processes

$$Qg \to Qg,$$

(the charge conjugate being implied), where the heavy quark comes from the photon, may contribute. The size of the contribution relative to the gluon-gluon fusion process

$$gg \to Q\bar{Q},$$

is a question that studies at HERA hope to answer. It is addressed in this thesis. Coupled to the unexplored kinematic region in photoproduction available at HERA, the study of heavy quarks promises to yield interesting results.

At LO, heavy quark production, like light quark production, is considered as the sum of direct (pointlike) and resolved (hadronic) components. Therefore, the general photoproduction description given by Equations (2.23 - 2.25), also describes photoproduction for heavy quarks. However, we must remember that approximations such as $p_T^2 \gg m_Q^2$ are not necessarily valid and the mass must be included. We should also consider that the pseudorapidity is a massless approximation of the rapidity, y, which is given by

$$y = \frac{1}{2}\log\left(\frac{E + p_z}{E - p_z}\right).$$

The subsequent treatment of what constitutes direct and resolved and in which proportions, is where differences occur in theoretical models. For example, the

"excitation" process, mentioned in the previous paragraph, can be considered, at sufficiently high transverse momenta, as a LO resolved process or alternatively a NLO direct process.

2.13.1 Perturbative Formalism of Heavy Quark Photoproduction

The inclusive photoproduction of a heavy quark, Q, with momentum p and energy E in the process

$$\gamma(p_1) + p(p_2) \to Q(p) + X$$

has been calculated to $\mathcal{O}(\alpha\alpha_s^2)$ [62]. The total cross-section at a photon-proton centre-of-mass energy, W, is given by

$$\begin{aligned}\sigma(W) &= \sum_j \int dx \hat{\sigma}_{\gamma j}(xW, m^2, \mu^2) F_j^p(x, \mu) \\ &+ \sum_{i,j} \int dx_1 dx_2 \hat{\sigma}_{ij}(x_1 x_2 W, m^2, \mu^2) F_i^\gamma(x_1, \mu) F_j^p(x_2, \mu), \end{aligned} \quad (2.33)$$

where F_j^p and F_i^γ are the parton densities of the proton and photon respectively, m is the heavy quark mass and μ is the factorisation scale. The short distance cross-section, $\hat{\sigma}$, for a photon-parton collision is given by

$$\hat{\sigma}_{\gamma j}(\hat{s}, m^2, \mu^2) = \frac{\alpha\alpha_s(\mu^2)}{m^2} f_{\gamma j}(\rho, \mu^2/m^2), \quad (2.34)$$

where $\rho = 4m^2/\hat{s}$ and $\hat{s}$ is the partonic centre of mass energy. The second term in Equation (2.33) is simply the cross-section for the hadro-production process of heavy quarks, where one of the hadron parton density functions is replaced by the photon parton density function. This has been calculated to $\mathcal{O}(\alpha_s^3)$ [63], where the short-distance cross-section is given by

$$\hat{\sigma}_{ij}(s, m^2, \mu^2) = \frac{\alpha_s^2(\mu^2)}{m^2} f_{ij}(\rho, \mu^2/m^2). \quad (2.35)$$

The dimensionless function $f_{\gamma j}$ has the following perturbative expansion,

$$f_{\gamma j}(\rho, \mu^2/m^2) = f_{\gamma j}^{(0)}(\rho) + g^2(\mu^2) \left[f_{\gamma j}^{(1)}(\rho) + \bar{f}_{\gamma j}^{(1)}(\rho) \log(\mu^2/m^2) \right] + \mathcal{O}(g^4), \quad (2.36)$$

and the function f_{ij}, the following,

$$f_{ij}(\rho, \mu^2/m^2) = f_{ij}^{(0)}(\rho) + g^2(\mu^2) \left[f_{ij}^{(1)}(\rho) + \bar{f}_{ij}^{(1)}(\rho) \log(\mu^2/m^2) \right] + \mathcal{O}(g^4). \quad (2.37)$$

Details of the forms of the lowest order functions $f_{\gamma j}^{(0)}$ and $f_{ij}^{(0)}$ are given in [62] and [63]. The higher order corrections, $\bar{f}^{(1)}$ are the coefficients of $\log(\mu^2/m^2)$

and are determined by renormalisation group arguments and use the explicit forms [64, 65] of the Altarelli-Parisi kernels, P_{ij}. The quantities $f_{\gamma j}^{(1)}$ and $f_{ij}^{(1)}$ can be obtained by performing a complete $\mathcal{O}(\alpha\alpha_s^2)$ and a complete $\mathcal{O}(\alpha_s^3)$ calculation respectively or from numerical (physically motivated) fits. Results for both $\bar{f}^{(1)}$ and $f^{(1)}$ are again given in [62] and [63].

From our perturbative expansions in Equations (2.36) and (2.37), we see that the expansion parameter is the mass of the heavy quark, m. Here we see clearly for the first time the reasoning behind statements about the mass being important in perturbative expansions. The above expansions are the origin of the question whether the mass of the charm is "big enough" ($m_c \gg \Lambda_{\rm QCD}$) for reliable perturbative calculations. Correspondingly, the equations demonstrate why the beauty quark with a larger mass provides a more reliable perturbative expansion. Furthermore there is an uncertainty in the actual quark mass, which then feeds into the perturbative expansion.

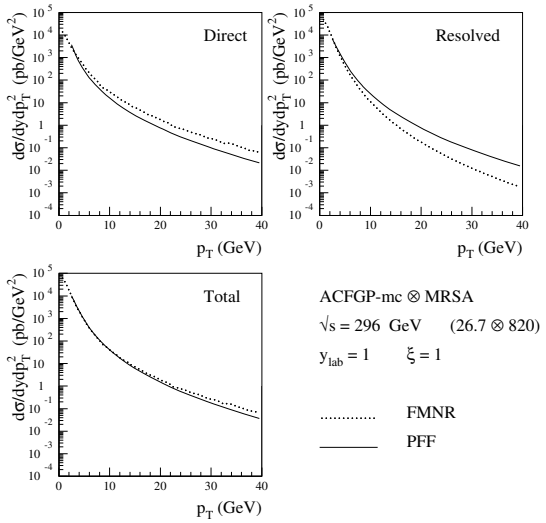

Figure 2.13: Comparison between the massive (FMNR) and massless (PFF) calculations for charm photoproduction p_T distribution (from [66]).

The above perturbative calculation (and in [67] we can find another independent calculation) is for single particle inclusive cross-sections. This has been extended in [68] to provide fully exclusive cross-sections allowing more detailed comparisons with the data. This was extensively done in [61], a few examples of which appeared in Section 2.12 of this chapter. This benchmark calculation uses what is referred to as the *massive* scheme [69], with certain extensions thereof called the *massless* scheme [70, 71, 72]. These schemes will now be discussed in turn.

2.13.2 Massive Scheme

The massive scheme assumes the gluons and light quarks (u, d, s) to be the only active partons in the photon, the heavy quarks not contributing to the evolution of the running coupling constant or the structure functions of the proton or photon. The heavy quark is produced dynamically in the hard sub-process. Therefore we have only two LO resolved processes,

$$gg \to Q\bar{Q}, \quad q\bar{q} \to Q\bar{Q},$$

where the former process is expected to dominate over the latter by significant factors of approximately three or four depending on the parametrisations used [73, 74].

The massive calculation for photoproduction [75] is heavily based on the hadro-production calculations [68, 76]. The calculation is implemented as an effective "parton Monte Carlo" generator and can be used widely.

We can see the problem with the perturbative calculation: that of the mass in the perturbative expansion. Only when the coefficients of the coupling constant remain small will our expansion be reliable. However, a limitation of the method arises at high p_T, where terms of the form $\log(p_T^2/m^2)$ become large, forcing the series to diverge. In the massive scheme soft and collinear divergences are treated by generating sequences of correlated events such that cancellation of the divergences occurs. This method developed in [77] removes the need for artificial regularisation required when a light parton accompanies the heavy quark pair. Alternatively, these logarithms need to be resummed by treating the heavy quark as massless and leading to a reduced sensitivity to the renormalisation and factorisation scale. The scale at which the resummation of these logarithms becomes important is as yet uncertain, but a phenomenological analysis shows that it happens at large p_T of about 20−25 GeV [66].

2.13.3 Massless Scheme

The massless scheme treats the charm quark as an additional active flavour above some threshold. Below this threshold, $\mu^2 \sim m_c^2$, the quark reverts to an inactive flavour, the light quarks and gluons being the only active partons as for the massive scheme. This massless scheme allows the resummation of the logarithms in p_T^2/m^2 providing perturbative fragmentation functions for the heavy quark containing the logarithmic dependence. However, the method is not reliable at $p_T^2 \sim m^2$ [78] and so total cross-sections cannot be calculated. As a result of the method, we have extra LO resolved processes;

$$gQ \to gQ, \quad qQ \to qQ,$$

which are termed flavour excitation processes. An example is depicted in Figure 2.6. These processes which are present in the massless scheme as part of the structure of the photon, in some proportion also contribute in the massive scheme but only in the hard sub-process.

The fragmentation functions, D_k^Q, can be evaluated in perturbative QCD at a scale of the heavy quark mass and evolved up to the factorisation scale through the Altarelli-Parisi equations. They are given by the following,

$$D_Q^Q(x,\mu^2) = \delta(1-x) + \frac{\alpha_s(\mu)C_F}{2\pi}\left[\frac{1+x^2}{1-x}\left(\log\frac{\mu^2}{m^2} - 2\ \log(1-x) - 1\right)\right]_+, \tag{2.38}$$

$$D_g^Q(x,\mu^2) \;=\; \frac{\alpha_s(\mu)T_F}{2\pi}\left(x^2+(1-x)^2\right)\log\frac{\mu^2}{m^2}, \tag{2.39}$$

where the massive logarithms are contained in the fragmentation functions as stated previously. The QCD color factors are $C_F = 4/3$ and $T_F = 1/2$. The splitting functions from light quarks to heavy quarks are zero.

Comparison of the two schemes, massive and massless, has been performed for charm by one of the groups [66] and the two schemes found to yield similar results. The comparison of the (unphysical) direct and resolved processes however shows differences but the (physical) sum of the two demonstrates good agreement as is shown in Figure 2.13.

The two descriptions can be used for comparison with HERA data for heavy quarks like c, b. The quantity of data for the production of heavy quarks at HERA has so far been rather small but it is increasing. Serious comparisons have so far been made between data and the two schemes above described. In the next section we will discuss the methods for tagging heavy quarks at HERA and then discuss some results with respect to comparisons with the above schemes.

2.13.4 Heavy Quark Results from HERA

Recent results on the production of D^* mesons [79, 80] have allowed an extensive comparison with massive and massless calculations [69, 70]. In [79], inclusive cross-sections for the D^* meson were measured and the properties of dijet events with a tagged D^* meson were investigated. Before discussing the measurements and comparisons with data we first discuss how the NLO calculations are interfaced to be directly comparable with a cross-section in terms of a hadron and not the quark itself.

For the massive calculation, the MRSG [81] structure function for the proton and the GRV-G HO [82] structure function for the photon were used. The renormalisation scale was set to $\mu_R = \sqrt{m_c^2 + p_T^2}$ and the factorisation scale twice this value, where the value for the charm mass, $m_c = 1.5$ GeV was used. The charm is then fragmented into a D^* meson using the Peterson fragmentation function [83], $f(z) \propto [z(1-1/z-\epsilon/(1-z))^2]^{-1}$, where z is the fraction of the momentum of the charm quark taken by D^* meson. A cross-section in terms of the D^* meson is then obtained by convoluting the partonic cross-section with the fragmentation function. The value of ϵ was initially chosen to be $\epsilon = 0.06$ from [69] as to be the central recommended value for D mesons [84]. Recent fits to e^+e^- data [72] have suggested that a lower value of $\epsilon = 0.02$ is more appropriate and so it was also used.

In the case of the massless calculations, the CTEQ4M [85] structure function for the proton and the GRV-G HO [82] structure function for the photon were used by both sets of authors. The renormalisation and factorisation scales and the charm mass are the same as before. The non-perturbative component of the

fragmentation is fitted to the Peterson function [83], the perturbative fragmentation has the forms as in Section 2.13.3. The fit to the Peterson function was performed using recent e^+e^- data [86] on D^* production to extract the ϵ parameter. The two fitted values for the specific calculations are $\epsilon = 0.116$ [70] and $\epsilon = 0.02$ [72]. Alternative fitting functions, besides the Peterson form, for the description of the e^+e^- data were also used, yielding similar results.

The decays of the D^* meson and the experimental techniques are discussed in [87]. In [79] D^* mesons were reconstructed through the decay channels $D^* \rightarrow D^0\pi \rightarrow (K\pi)\pi_s$ and $D^* \rightarrow D^0\pi \rightarrow K3(\pi)\pi_s$. For the inclusive cross-section measurements, candidates were selected with $p_\perp(D^*) > 2$ GeV/c in the pseudorapidity region, $|\eta(D^*)| < 1.5$. Photoproduction events were defined by a photon virtuality, $Q^2 < 1$ GeV^2 and a photon-proton centre of mass energy, $130 < W < 280$ GeV.

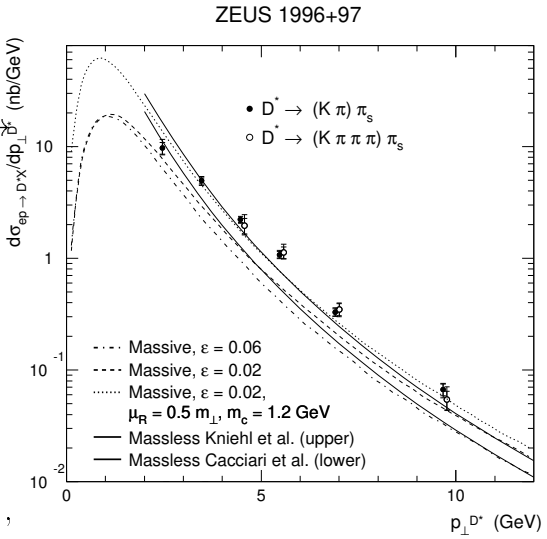

Figure 2.14: Differential cross-section, $d\sigma/dp_\perp^{D^*}$, for D^* photoproduction for two decay channels. The data is compared to massive calculations and the two massless calculations.

The differential cross-section, $d\sigma/dp_\perp^{D^*}$, is shown in Figure 2.14. The displayed data are for the two decay channels and they are compared to the massive and massless calculations. The two lowest massive curves lie consistently below the data for all $p_\perp(D^*)$. The two curves are for the different ϵ parameters, $\epsilon = 0.06$ (dot-dashed line) and $\epsilon = 0.02$ (dashed line), with the nominal values for the scales and charm mass. Choosing extreme values of the scale and charm mass (dotted line) displays reasonable agreement but still lies too low for the three central points in $p_\perp(D^*)$. The massless calculations (solid) also generally lie below the data. Of significance is the disagreement in normalisation between the two massless calculations, the shapes being similar. Also of significance is the comparison between the massless and massive calculations as a function of $p_\perp(D^*)$. The low $p_\perp(D^*)$ data is better described by the massless than the massive calculations, with the two converging at higher $p_\perp(D^*)$. However, as it was mentioned previously, the massive calculation is supposed to be more relevant at $p_\perp \sim m_Q$ and the massless at $p_\perp \gg m_Q$, which does not appear to be the case in Figure 2.14. The hardening of the massive calculation relative to the massless calculation as we increase the $p_\perp$ is however expected (see Figure 2.13). Before making firmer statements we will move onto the cross-sections as a function of $\eta(D^*)$ in Figure 2.15.

In Figure 2.15 the differential cross-sections, $d\sigma/d\eta^{D^*}$, are shown for four minimum $p_\perp(D^*)$ values. The massive and massless curves are again displayed

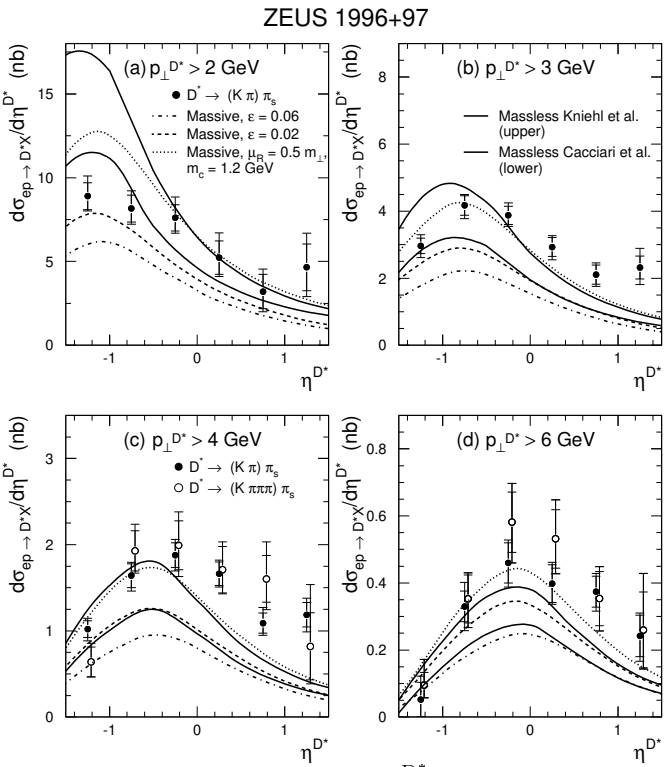

Figure 2.15: Differential cross-section, $d\sigma/d\eta^{D^*}$, for D^* photoproduction for two decay channels in ranges of $p_\perp^{D^*}$. The data is compared to massive calculations and the two massless calculations.

as for the $p_\perp(D^*)$ cross-section. For the nominal scale and charm mass values, the massive calculations generally lie below the data. By choosing the extreme values we again obtain a higher cross-section but this lies below the data in the forward region. As it was done when comparing to the fixed target data, a "k_T kick" was folded into the massive calculation. This had little effect, increasing the cross-sections by about 10%. In the case of the massless calculations, we again see a difference in the overall normalisation. The calculations agree generally in shape, but lie below the measured data particularly at high $p_\perp(D^*)$ and (forward) $\eta(D^*)$.

The above results represent the most significant comparison of data with massive and massless NLO calculations for charm production published at HERA. Clearly more measurements and hence comparisons to theory are needed for a more complete understanding of charm quark production. Measuring the beauty quark would also be of benefit providing us with a more rigorous test of QCD, being less dependent on non-perturbative factors. A measurement of Υ production has been performed by the ZEUS collaboration [88]. The measured elastic Υ photoproduction cross-section was found to lie above QCD predictions. However, a more recent calculation [90] shows good agreement between the data and the

QCD prediction. Open beauty production has been observed at HERA by the H1 collaboration and a cross-section measured [91]. The cross-section was found to be higher than calculations based on LO QCD models. Also, results from hadron colliders have caused much speculation as reviewed in the next section.

2.14 Beauty Production at Hadron Colliders

The beauty quark differential p_T spectrum has been measured at hadron colliders by integrating over a rapidity range, y_{max}, above a given momentum threshold p_T^{min}, such that

$$\sigma(p_T^{min}) = \int_{|y|<y_{max}} dy \int_{p_T>p_T^{min}} dp_T \frac{d^2\sigma}{dy dp_T}. \tag{2.40}$$

NLO QCD calculations exist for this distribution [93, 94] and the cross-section has been measured by the UA1 experiment at CERN and the CDF and D0 experiments at the TEVATRON. The UA1 measurement restricted the rapidity to $|y| < 1.5$ with a centre of mass energy, $\sqrt{s} = 630$ GeV [95]. The experiment measured four different decay channels, but all with a muon in the final state, finding reasonable agreement between the data and QCD calculation. Through extensive study of many decay channels, the CDF experiment has also measured the cross-section in Equation (2.40), for a rapidity limit, $|y| < 1$ and a centre of mass energy, $\sqrt{s} = 1800$ GeV [96]. Similarly, the D0 collaboration has also produced results in the above rapidity region for the same centre of mass energy [97]. The results from the three collaborations have all been compared to the NLO QCD calculations and collected together in [61]. We show the comparison with the NLO calculations for the CDF collaboration as an example in Figure 2.16. From Figure 2.16 we see that the data lies consistently above the central theoretical prediction, whilst being compatible with the upper limit predictions for extreme values of the beauty mass and scale as detailed in the caption.

A more revealing comparison was performed in [61], in which the ratio of the measured data to the theoretical prediction was analyzed as a function of p_T^{min} for the results from all three collaborations. The results are shown in Figure 2.17. The dotted line is a constant fit to the data points, the value given in the top right-hand corner for each experiment, and the solid lines are the upper, central and lower theoretical predictions. From Figure 2.17, we see that the three experiments differ in the factor they lie above the theoretical prediction, the CDF data being particularly high and having a large spread especially at low p_T^{min}. The general shape of the data is predicted by perturbative QCD, the upper limit reproducing the magnitude in the case of the UA1 and D0 data.

The results from hadro-production shown are reasonably provocative representing an "upper limit" of pQCD predictions and question what the results in

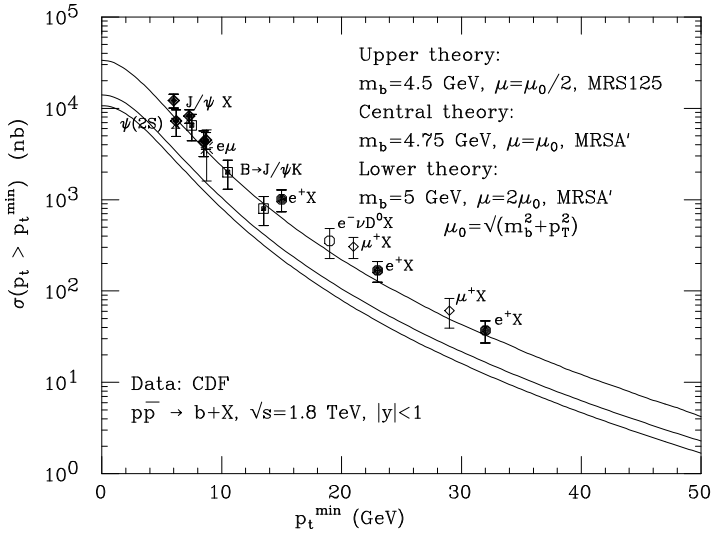

Figure 2.16: CDF data on the integrated b-quark p_T distribution compared to NLO QCD (from [61]).

photoproduction would be. As was said, no measurements or even observations of open beauty production had so far been published at HERA and the comparison of results with NLO calculations was an obvious goal.

2.15 Identification of Open Beauty Production at HERA

Identification of open heavy quarks at HERA has so far primarily been achieved through the tagging of decay products of the $D^*(2010)$ meson as a means of selecting charm. Most currently published data on open heavy quark production in photoproduction and DIS from both ZEUS and H1 have used the D^* tagging method. For the most recent publications on charm production from both collaborations see [79] and [98].

Published data on open beauty production from H1 currently exists [91], where results from an analysis on dijet photoproduction of beauty with a semi-leptonic decay to muons is exposed. The ZEUS collaboration [92], instead, is following methods to tag beauty production through the leptonic decays of heavy flavours both to electrons and to muons.

There are several predictions of massive calculations for the total $ep \to b\bar{b}X$ cross section. The first calculation for all $2 \to 2$ and $2 \to 3$ processes in photoproduction, barring virtual corrections, was published and integrated for HERA in [74]. The first full next-to-leading order calculation was given in [93] and was cross-checked by Smith and van Neerven in [94]. Another calculation based on

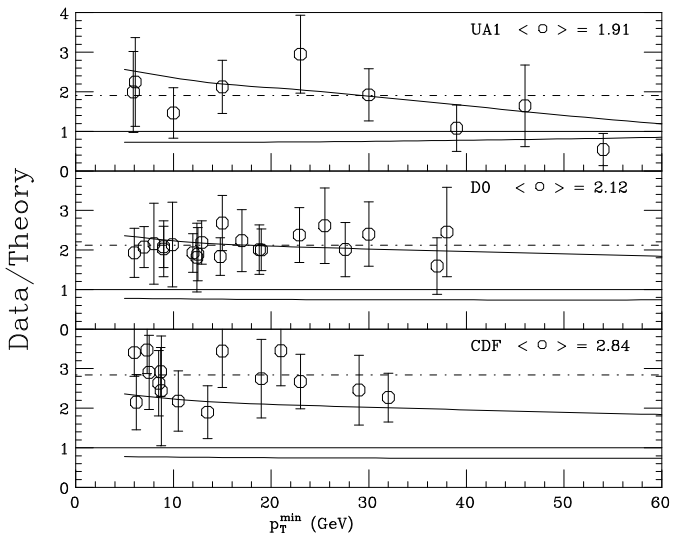

Figure 2.17: Comparison between experimental data and theory for the integrated b-quark p_T distribution (from [61]).

the work of Ellis and Nason was done by Frixione *et al.* in [75]. The predictions of these calculations are given in Table 2.1, where m_b indicates the mass of the beauty quark.

The variation given for Frixione *et al.* is due to different choices of the mass of the b-quark and contains in addition different choices for the parton density functions (PDF's) of the proton and the photon. Table 2.2 provides a detailed overview of the dependence of the open b cross section on various parameters, such as the b-mass, the PDF's, and the factorization and renormalization scales [75]. The sensitivity to scale variations is, in beauty production, much smaller than for charm production. It should be noted that the uncertainty due to the choice of the PDF is typically smaller than that from scale variation. By far the largest dependence is observed in the variation of the b-mass.

2.16 Fragmentation of Heavy Quarks

The description of heavy quark production provided by perturbative QCD is valid at short distances only. At long distances, the effective coupling gets too large and perturbative theory breaks down. In this confinement regime, the colored heavy quarks are transformed into colorless hadron in a process called *fragmentation*. This process is not yet understood from first principles , but is currently described in several models.

The Lund string fragmentation model [100], implemented in PYTHIA 6.1 [101], assumes that a color flux tube is stretched between two partons as they move apart. The energy density along the tube is assumed to be uniform, which auto-

Reference	$\sigma(ep \to b\bar{b}X)$ (nb)	μ_F	Scheme	μ_R	m_b (GeV/c^2)
Eichler & Kunszt [74]	8.0	$\sqrt{\hat{s}}/2$	—		5.27
Ellis & Nason [93]	4.9	m_b	$\overline{\text{MS}}$	m_b	5.0
	7.1	m_b	$\overline{\text{MS}}$	m_b	4.5
Smith & van Neerven [94]	6.12	$2m_b$	$\overline{\text{MS}}$	$2m_b$	4.75
	8.77	$m_b/2$	DIS	$m_b/2$	4.75
Frixione *et al.* [75]	4.8	m_b	$\overline{\text{MS}}$	m_b	5.0
	9.9	m_b	$\overline{\text{MS}}$	m_b	4.5

Table 2.1: Predictions for the total $ep \to b\bar{b}X$ production cross section by several next to leading order calculations (the calculation of Eichler and Kunszt does not contain virtual correction), m_b is the mass of the beauty quark. The column denoted "Scheme" indicates the renormalization scheme used.

matically leads to a confinement picture with a linearly rising potential. As the potential energy stored in the string increases, the string may break up into a $q\bar{q}$ pair, which may attach to the original partons. The process goes on if the invariant mass of either of the resulting strings is large enough. The iterative process continues until only *on-mass-hadrons* remain.

The fraction z of the energy of the original quark transferred to the (heavy) hadron in this process is given by a fragmentation function $f(z)$ which is parameterized using phenomenological models. Standard PYTHIA 6.1 (or JETSET 7.4) settings choose the Lund symmetric fragmentation function

$$f(z) \propto \frac{1}{z}(1-z)^a \exp\left(-bm_\perp^2/z\right).$$

Heavy quark fragmentation is often described by the Peterson's function [83],

$$f(z) \propto \frac{1}{z\left(1-\frac{1}{z}-\frac{\epsilon_Q}{1-z}\right)},$$

where ϵ_Q is a free parameter expected to scale between flavours like $\epsilon_Q \propto 1/m_Q^2$. This last functional form can be motivated by observing that the attachment of a light anti-quark $\bar{q}$ to a heavy quark Q, to form a hadron, decelerates Q only slightly. The parameters ϵ_Q have been determined by fits to data measured at e^+e^- experiments like ARGUS and OPAL [86] and for the c and b quarks they have these values:

$$\epsilon_c = 0.06, \epsilon_b = 0.008.$$

		μ_R		μ_F		μ_γ		m_b (GeV)	
	Default	$m_b/2$	$2m_b$	$m_b/2$	$2m_b$	$m_b/2$	$2m_b$	4.5	5.0
Point-like component									
MRSA	4.640	5.332	4.098	4.391	4.773			5.541	3.917
CTEQ2MF	4.814	5.469	4.283	4.554	4.958			5.720	4.079
MRSD'_	4.856	5.580	4.288	4.649	4.963			5.839	4.073
CTEQ2ML	5.123	6.110	4.418	4.728	5.290			6.113	4.325
Hadronic component (with MRSA for the proton PDF)									
GRV-HO	1.115	1.510	0.851	1.077	1.146	1.018	1.177	1.408	0.892
LAC1	2.842	3.947	2.142	2.861	2.840	3.067	2.675	3.792	2.157

Table 2.2: Dependence of the open quark b production cross section, expressed in nb, on different parameters. The default parameter setting corresponds to $\mu_R = \mu_F = m_b = 4.75$ GeV [75].

2.17 Semi-leptonic Decays of Heavy Quarks

Hadrons containing a b-quark or a $c-$quark have typical lifetimes of $\sim 10^{-12}$ s. Roughly 20% of the decays of these heavy quarks proceed through a semi-leptonic channel into three final-state particles. The semi-leptonic decay amplitude of a meson X into meson Y is described by the product of a leptonic and a hadronic current analogously as in Section 2.2: $\langle Y|J_\mu|X\rangle\langle\nu|\gamma^\mu(1-\gamma_5)|l\rangle$. Whereas the leptonic is easily calculable, the hadronic piece requires modeling. The momentum transfer between X and Y can be taken as the only parameter of the hadronic current in terms of form factors that are Lorentz-invariant function of this variable. In the limit of massless leptons, which is a good approximation dealing with electrons and muons, only one form factor is necessary to describe the decay of a pseudo-scalar meson P into another pseudo-scalar meson. For the decay $P \to Vl\nu$, where V is a vector meson, three form factors are needed.

Various models are used to describe form factors and there are simplifications of these if the limit $m_Q \to \infty$ can be used.

In both Monte Carlo event generators used, PYTHIA and HERWIG, semi-leptonic decays of heavy hadrons are simplified to the point of neglecting form factors altogether. The momenta of the decay products are, hence, distributed according to the simple $V-A$ matrix element and all lepton masses are assumed to be negligible except for the τ lepton to reduce the branching ratios.

	DIS			$\overline{MS}$		
	$Q = m_b/2$	$Q = m_b$	$Q = 2m_b$	$Q = m_b/2$	$Q = m_b$	$Q = 2m_b$
α_s	0.237	0.190	0.162	0. 237	0.190	0.162
$\sigma_{\gamma g} O(\alpha_s)$	4.94	4.60	4.36	4. 30	4.16	4.02
$\sigma_{\gamma g} O(\alpha_s^2)$	1.92	1.62	1.72	1. 71	1.54	1.68
$\sigma_{\gamma q} O(\alpha_s^2)$	0.92	0.15	-0.21	0. 98	0.20	-0.17
$\sigma_{qq} O(\alpha_s^2)$	0.14	0.12	0.11	0. 15	0.12	0.11
$\sigma_{gg} O(\alpha_s^2)$	0.85	0.64	0.53	0. 73	0.57	0.48
σ_{tot}	8.77	7.13	6.51	7. 87	6.59	6.12

Table 2.3: Partial and total cross sections (measured in nb) for the process $\sigma(ep \to b\bar{b}X)$ at HERA ($\sqrt{s} = 314\ GeV$) within the renormalization schemes of DIS and $\overline{MS}$, the value of the mass of the b-quark is $m_b = 4.75\ GeV$ (as in ref. [99]).

2.18 Heavy Quark Jets

The study of jets containing heavy quarks, should allow us to test perturbative QCD predictions more thoroughly than inclusive measurements. The transverse energy distribution of a jet containing a heavy quark should be more reliable than the transverse momentum of the heavy quark. As we have seen previously, at large quark momentum, we have large logarithms of the form $\log(p_T^2/m^2)$ in the perturbative expansion due to the emission of collinear gluons. However, in the measurement of E_T of the jet, these collinear gluons are included in the jet along with the heavy quark, so large logarithms do not appear.

The limitation in statistics so far achieved at HERA prevented the study of heavy quark jets until [79]. In [79] the $x_\gamma^{\rm obs}$ distribution for dijet events with a tagged D^* meson was measured.

The use of jets is also essential for the study of direct and resolved processes and for the identification of beauty quarks.

2.19 Summary

From this chapter we can see that the knowledge of heavy quark production, both experimentally and theoretically, in photoproduction is somewhat mixed and limited. Some characteristics of charm production have been measured but do not reveal a consistent picture, whilst little information exists on beauty production. The aim of this thesis is to make measurements of heavy quark production and provide us with at least the start of a coherent picture at HERA.

Chapter 3

Event Reconstruction

Event and jet kinematics are reconstructed from measured quantities and we can use Monte Carlo programs to deconvolute these quantities to the true values through evaluation of the detector resolution. We discuss, hereafter, the reconstruction of the relevant event variables, y and Q^2, and the jet variables, E_T^{jet}, η^{jet} and ϕ^{jet}. Having defined these kinematic variables we then discuss the reconstruction of cross-section related quantities, $x_\gamma^{\rm obs}$ and p_T^{rel}.

3.1 Reconstruction of y and Q^2

There are many ways to reconstruct the variables, y and Q^2 [102], two of which are here discussed. The two used in this thesis are the so-called "electron-method" and the "Jacquet-Blondel method" and are described in the following sections.

3.1.1 Electron Method

The electron method is theoretically simple and relies only on the knowledge of the energy of the scattered lepton, E'_e and the angle of the scatter, θ_e. For a given initial lepton energy, E_e, we can write our variables, y and Q^2 as the following:

$$y_e = 1 - \frac{E'_e}{2E_e}(1 - cos\theta_e)\,, \tag{3.1}$$

$$Q^2_e = 2E_e E'_e (1 + cos\theta_e)\,. \tag{3.2}$$

Photoproduction events are defined by seeing no scattered lepton in the calorimeter, that is, high values of θ_e. At ZEUS, the angles through which the lepton scatters when it is not seen in the calorimeter are greater than $\sim 177°$. From Equation (3.2), we can see that this corresponds to low values of the photon virtuality, Q^2. In this thesis (and for ZEUS photoproduction analysis in 1996 and 1997 in general) Q^2 is limited to be less than 1 GeV^2. The region of photoproduction

then allows us to approximate y_e to be,

$$y_e \approx \frac{E_e - E'_e}{E_e} = \frac{E_\gamma}{E_e}, \tag{3.3}$$

where E_γ is the energy of the incoming photon. We can therefore interpret y_e to be the fraction of the incoming lepton's energy carried by the photon. In Monte Carlo simulations where we know all about the scattered lepton, the above formulae can be used. However, in the data, we have an effective *anti-tag* on the lepton as it is scattered down the beam-pipe. Consequently, we consider another method of reconstructing our kinematic variables.

3.1.2 Jacquet-Blondel Method

The Jacquet-Blondel method [103] calculates the variables y and Q^2 from the hadronic final state. The hadronic final state is all particles except the scattered lepton and summing over these gives:

$$y_{JB} = \frac{\sum_i (E_i - p_{z_i})}{2E_e}, \tag{3.4}$$

$$Q^2_{JB} = \frac{(\sum_i p_{x_i})^2 + (\sum_i p_{y_i})^2}{1 - y_{JB}}. \tag{3.5}$$

Obviously, the above sum cannot experimentally be done over hadrons, but is for calorimeter cells. If the scattered lepton is found in the calorimeter, then the cluster of cells associated with it are eliminated from the calculation. The identification of the scattered lepton is not 100% efficient, so its energy deposit will sometimes enter into the above summations. This will yield high values of $y_{JB} \sim 1$, which are removed in the case of photoproduction events as DIS contamination. Before calorimeter cells can be used for the calculation of y_{JB} and Q^2_{JB}, their positions are first corrected for the position of the event vertex. This process is essential before any quantity can be reconstructed from calorimeter cells such as islands and jets which are discussed in the next section.

3.2 Jet Reconstruction

Within the ZEUS Collaboration, use is made of two types of jet algorithm for photoproduction analysis. These are the "cone" and the "cluster" algorithms. Two variants of the cone type are used - EUCELL [104] and PUCELL [105] - wheras the used cluster algorithm is the so called "k_T" algorithm [106] implemented in the KTCLUS library of routines [107].

Detailed discussions of each of these can be found elsewhere [108], so only a brief discussion of these will be included here.

3.2.1 Cone Algorithms

Two cone algorithms are used, defined in a standard form by the Snowmass Convention [109]. The Snowmass Convention defines the transverse energy and the coordinates of a jet as;

$$E_T^{jet} = \sum_i E_{t,i}$$

$$\eta^{jet} = \frac{1}{E_T^{jet}} \sum_i E_{t,i}\eta_i \tag{3.6}$$

$$\phi^{jet} = \frac{1}{E_T^{jet}} \sum_i E_{t,i}\phi_i$$

where the sum runs over all hadron or calorimeter cells within the cone defined by a given prescribed radius, R, in $\eta - \phi$ space.

PUCELL is an adaptation of the jet algorithm used at CDF. Both it and EUCELL use the concept of pre-clustering, but then diverge in the method of combination.

In PUCELL, a pre-cluster is formed by combining all objects within a radius, R, with the highest E_T object. This is done until all objects are assigned to a pre-cluster. The centre of the pre-clusters are then recalculated and the process repeated until some stable situation (or some maximum number of iterations) is reached. The formation of clusters is then complete and those that have a transverse energy above a certain threshold are considered jets.

In EUCELL, clusters are determined using a grid in $\eta - \phi$ space. The size of the cells that make up the grid is determined such that $\Delta\eta^{gridcell} \approx \Delta\phi^{gridcell} \approx R/2$. By then sliding a 3×3 cell window over the grid, a potential pre-cluster is then formed. To be called a pre-cluster, it must be above some prescribed transverse energy. A cone of radius R is then placed around the pre-cluster and an iterative process as in PUCELL is performed. The first jet is defined as the cone with the highest transverse energy. Successive jets are then determined from the remaining objects by the same procedure until there exist no more cones above a certain energy threshold.

3.2.2 Clustering Algorithm

The use of the aforementioned cone algorithms leads to ambiguities. The treatment of overlapping jets is *not defined* within the Snowmass convention, nor is the question of seed finding for the initial jets. This leads to theoretical ambiguity with respect to jet merging in the final state and the process is not infra-red safe at NNLO without modification [110].

These problems are avoided by the use of the k_T algorithm, as the merging criterion is completely defined for any given final state. As such, in this analysis

we avoid the problems inherent in the use of the cone algorithm and use only the k_T algorithm.

The k_T algorithm was initially designed for use in e^+e^- annihilation, wheras the presence of hadron remnants in hadron-hadron, DIS or photoproduction events means that it must be used in a modified form which maintains the property of factorisation of initial state radiation [107].

For a cluster algorithm we must specify some distance measure which determines *which* particles will be merged, together with a recombination scheme which defines *how* they will be merged. In photoproduction we run the algorithm in the laboratory frame using the inclusive recombination scheme of Ellis and Soper [111] in a mode which is invariant under longitudinal boosts, the recombination scheme being similar to that of the Snowmass Convention (the so-called "*pt*" mode). The algorithm scheme depends on a parameter R and is analogous to a cone radius.

To decide which particles should be merged, for each particle i we form the quantity,

$$d_i = E_{T,i}^2$$

and for each pair of particles, ij, we form the quantity

$$d_{ij} = \min(E_{T,i}^2, E_{T,j}^2) \left[(\eta_i - \eta_j)^2 + (\phi_i - \phi_j)^2\right] / R^2.$$

The d_i is the limiting case of small angles of the "distance" between particle i and a large mass remnant traveling along the z direction.

If the smallest of all the d values is a d_{ij}, then particles i and j are merged into a single object, k. If however, the smallest value is a d_i then this particle is considered "complete" and is removed from further clustering. This process is then repeated until all the objects have been removed, producing an E_T ordered list of objects.

The scheme for merging the objects is similar to the Snowmass Convention, and is,

$$E_{T,k} \equiv E_{T,i} + E_{T,j} \tag{3.7}$$

$$\eta_k \equiv \frac{E_{T,i}\eta_i + E_{T,j}\eta_j}{E_{T,k}} \tag{3.8}$$

$$\phi_k \equiv \frac{E_{T,i}\phi_i + E_{T,j}\phi_j}{E_{T,k}}. \tag{3.9}$$

Therefore the scheme assigns objects to jets in a well-prescribed manner, and as each quantity $E_T, \Delta\eta, \Delta\phi$ in the distance parameter is invariant under longitudinal boosts, so the property of boost invariance of the jet finding itself is retained.

3.3 μ Reconstruction

To reconstruct the global trajectory of muons in the detector we use two matching packages that have been developed to this aim. We will now describe them, a wider explanation of the way they work can be found in Appendix B.

3.3.1 The Bremat matching package

The main purpose of the BREMAT [112] algorithm[1] is to find out candidate muons associating inner detector tracks to segments in the Barrel and Rear chambers and to provide the resulting matching χ^2.

The parameters and error matrix of a candidate track at the exit of the inner tracking detector are extrapolated through the UCAL, up to a reference surface on the inner muon chambers, where the matching is done.

The track extrapolation is done outward, starting from the inner region. This has been chosen for the best treatment of low momentum muons, which suffer non-negligible energy losses compared to their initial energy. Indeed, knowledge of the momentum, as measured by the inner tracking, is helpful in the extrapolation, with no particular problem in dealing with many track complex events.

The algorithm uses as main inputs the table [113] of the reconstructed B/RMU segments and of the reconstructed inner tracks [18]. If there is an entry in the former, it looks for candidate tracks in the latter, which might be associated to it. This loose track pre-selection requires:

- momentum of the track $p > 1$ GeV
- polar angle of the track $\theta > 20°$
- the track has to start from CTD superlayer 1 and extend at least to superlayer 3
- impact parameter of the track $|D_H| < 10$ cm
- z coordinate at the point of minimum approach $|Z_H| < 75$ cm
- $\chi^2_{\rm track}/n.d.f. < 5$
- $\Delta \leq 150$ cm

The last cut is done on the distance Δ between a central point in the B/RMU segment, and the straight line obtained by extrapolating the track at the UCAL entrance.

The requirement of the hits on the third CTD superlayer has been introduced in the pre-selection to use only tracks from the region where the CTD acceptance

[1] Barrel and Rear Extrapolation MATching.

is well under control. In the rear angular region it could be relaxed if the track is well measured by the RTD.

Track passing this pre-selection are then extrapolated using the GEANE package [114].

The GEANE extrapolation is terminated when the fiducial surface described at the beginning of the section is reached. Here the output track parameters and error matrix are usually referred to as *prediction*. The predicted variables and error matrix are finally obtained in a convenient Cartesian parameterization.

Naming ξ_{Mi} and ξ_{Pi} respectively the measured and the predicted track parameters at the reference surface, the residuals are: $\delta_i = \xi_{Mi} - \xi_{Pi}$. The used Cartesian parameterization is written as $(x, y, x', y', Q/p)$. The matching χ^2 is given by:

$$\chi^2 = \sum_{i,j} S_{ij}^{-1} \delta_i \delta_j = \delta S^{-1} \delta^T$$

where the summation goes from 1 to $n = 4$ or 5, depending whether momentum is included or not in the χ^2, $\delta = (\delta_1, ..., \delta_n)$ and S^{-1} is the inverse of the covariance matrix of the residuals:

$$S_{ij} = \sum_{k,l} T_{ik} (\sigma^2_{track})_{kl} T^T_{lj} + (\sigma^2_{random})_{ij} + (\sigma^2_{BRMU})_{ij}$$

with $k, l = 1, ..., n$. Here T is the so called transport matrix, between the start and the stop of the *swim*, σ^2_{track} is the error matrix of the inner detector track, σ^2_{random} the error matrix due to the random processes of multiple scattering and energy loss and σ^2_{BRMU} the error matrix of the B/RMU segment. The first two terms are calculated by steps during the GEANE extrapolation using the detailed geometry of the ZEUS detector and the magnetic field map.

3.4 The Mpmatch matching package

Mpmatch is a package which connects FMUON reconstructed tracks with FTD segments and/or CTD tracks [115].

The attempt to make a match starts from an FMUON reconstructed track; a θ and ϕ road is opened around a track and a search for segments or track, belonging to central detectors, inside the road is done. The FMUON track is then back extrapolated to the z of the next detector measurement and a fit between the extrapolated FMUON track and the detector parameters is performed by means of Kalman filtering [116]. The procedure is then repeated for all available tracks or segments. After having considered all the combinations if a match is found a vertex fit is performed. The track is extrapolated towards the z coordinate of the reconstructed vertex, a fit is done with the x and y coordinates of the vertex and with the direction and momentum of the track as measured by the tracking chambers, the resulting track parameters are eventually available.

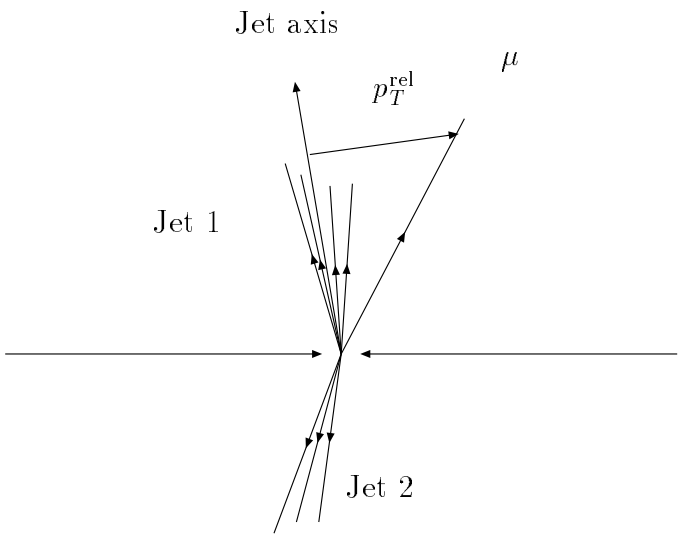

Figure 3.1: Geometric meaning of the $p_T^{\rm rel}$ variable.

3.4.1 Definition of a FMUON track

The FMUON track is defined by 5 parameters in the usual ZEUS reference frame, see Figure 1.5: x, y, dx/dz, dy/dz, Q/p (the z coordinate is the arc-coordinate)[2]. In order to perform a match, the track parameters and their covariance matrix are extrapolated to the z where further measurements are available. The track to be reconstructed by the FMUON has to have hit at least 4 planes in the ρ coordinate and three planes in the ϕ coordinate, see Section 1.8.1.

3.5 Reconstruction of $x_\gamma^{\rm obs}$ and $p_T^{\rm rel}$

Having discussed how we reconstruct jets and y, the formation of $x_\gamma^{\rm obs}$ as in Equation (2.31), is then reasonably trivial. We simply replace y with y_{JB} and we then have our value for $x_\gamma^{\rm obs}$ from calorimeter quantities. In the Monte Carlo, we measure y directly so can use Equation (2.31) with no further adaptation.

The quantity $p_T^{\rm rel}$ is reconstructed from the muon momentum and the jet axis and is simply given by,

$$p_T^{\rm rel} = |\mathbf{p}_\mu \times \hat{\mathbf{p}}_\mathbf{j}|,$$

where $\mathbf{p}_\mu$ is the muon momentum and $\hat{\mathbf{p}}_\mathbf{j}$ is the unit jet axis, simply being $\hat{\mathbf{p}}_\mathbf{j} = \mathbf{p}_\mathbf{j}/|\mathbf{p}_\mathbf{j}|$, where $\mathbf{p}_\mathbf{j}$ is the jet momentum, see Figure 3.1.

[2]In this only instance Q is the charge of the particle we are considering.

Chapter 4

The Monte Carlo simulation

To make comparisons with theories the analysis of physics results relies on the use of Monte Carlo techniques in order to correct the obtained measures as a function of the response of the detector allowing the study of ep processes at their origin, that is, typically, following the original variables at the interaction vertex.

The Monte Carlo simulation allows to evaluate two kinds of correction: one is relative to the geometric acceptance of the detector, and the second relative to the identification efficiency of tracks left by the passage of particles within ZEUS.

The initial procedure is the simulation of the actual physics events themselves. We therefore rely on the Monte Carlos to describe in some way the physics presented in Chapter 2 till Section 2.11. These Monte Carlos use principles of pQCD to simulate LO hard sub-processes and use phenomenological methods to simulate soft physics processes such as parton density functions and hadronisation.

Following this, we then produce a collection of events for a certain physics process we are interested in and simulate their path through the ZEUS detector.

To make a common platform available to the whole ZEUS collaboration some programming tools have been created, they are flexible and easy to use.

The chain that forms the ensemble of the simulation has as the first ring a software program called AMADEUS[1]. Within this program all supported simulators of interaction processes are gathered, these are packages that are called generators; many programs belong to this category among which PYTHIA [101], HERWIG [117], DIPSI and many others. The way we employ these is independent from the code that we choose to use.

The produced data are then passed to MOZART[2] [9], that is the program that has the task to simulate the behaviour of our detector (ZEUS) when the same is crossed by particles produced in the ep interaction.

The architecture MOZART is based on is given by the GEANT program [118] (of the CERN library) that describes the characteristic parameters of the devices

[1] Before it was called ZDIS: Zeus interface to Deep Inelastic Scattering.

[2] MOnte Carlo for Zeus Analysis Reconstruction and Triggering.

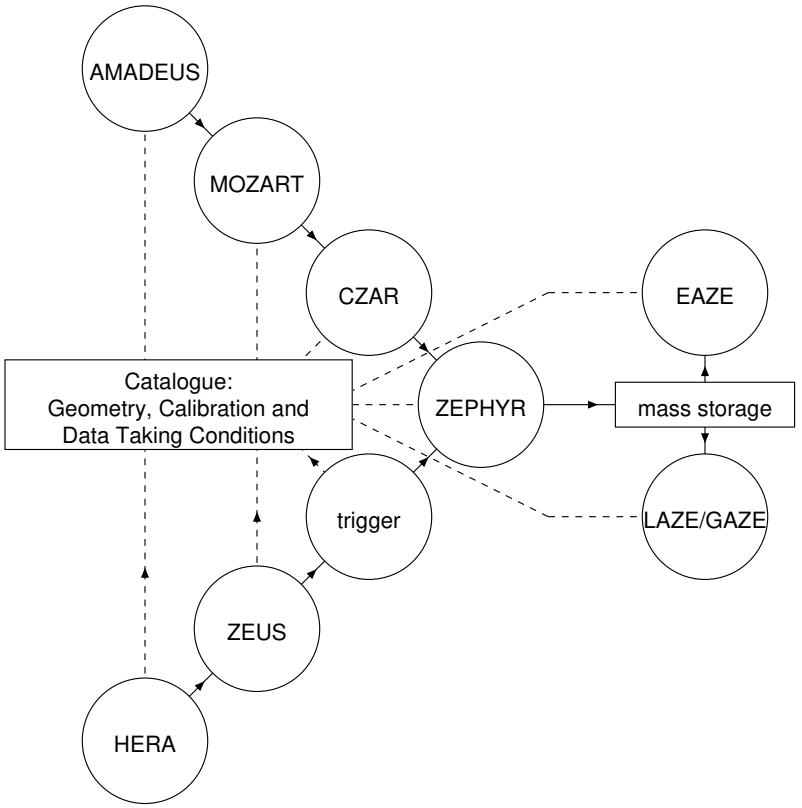

Figure 4.1: ZEUS Data and Reconstruction chain with Offline and Analysis Programs; full lines with arrows indicate the data flow; dashed lines indicate the communication with the catalogue; for details see text.

the detector is made of (geometry, materials, ...) and simulate the passage and interactions of particles in such devices. To simulate the development of electromagnetic and hadronic showers other software products can be used and these have been created on purpose for the ZEUS detector.

The simulated events pass, then, through the CZAR[3] package [119] that simulates the logic of the triggers employed during the data-taking.

Finally the samples are elaborated by ZEPHYR[4] that reconstruct the events independently from the fact that they come from simulation programs or from the acquisition of real data.

All data structures are defined using the ADAMO data management system and are described in the Data Definition Language (DDL). The ADAMO system (Aleph DAta MOdel) [33] is used in ZEUS event reconstruction and analysis for the design of data structures, for their storage in memory and on external media

[3]Complete Zgana Analysis Routines.
[4]ZEus PHYsics Reconstruction.

(tape or disk), and for their documentation.

ADAMO is based on the Entity Relationship Model (ERM) of data [120] and provides a description of the data in terms of entities (e.g. hits or tracks), their attributes (e.g. position or momentum) and their relationships (e.g. a hit lies on a track).

The data are organized in interrelated tables, which –for real data taking– are built by the Event Builder from the raw data provided by the components.

4.1 Generators

4.1.1 HERWIG Generator

The HERWIG (Hadron Emission Reactions With Interfering Gluons) Monte Carlo [117] is a general purpose generator with a large predictive power and a relatively small number of free parameters. Particular attention is paid to being as independent as possible from non-perturbative parameters.

The factorisation scale for the hard sub-process, μ^2, is given by,

$$\mu^2 = \frac{2\hat{s}\hat{t}\hat{u}}{\hat{s}^2 + \hat{t}^2 + \hat{u}^2},$$

where, $\hat{s}, \hat{t}$ and $\hat{u}$ are the Mandelstam variables. The resultant cross-section is divergent in the limit of transverse momentum of the outgoing partons, $\hat{p}_T^2 \to 0$, so we introduce a minimum transverse momentum cut, $\hat{p}_T^{min}$. The value chosen, $\hat{p}_T^{min} > 2.5$ GeV should not bias our results as we measure jets of $E_T^{jet} > 6$ GeV.

The incoming and outgoing partons go through a process of showering in which hadrons are formed from the partons. The showering is initiated by each single parton splitting into many partons. Logarithms of the form $(\alpha_s \log(\mu^2/\mu_0^2))^n$ are resummed and the partons ordered in terms of their opening angle. The ordering is continued until the hadronisation scale is of the order of the lightest mesons.

Parton showers from the initial hadrons to the partons of the hard sub-process are treated differently. Backward evolution from the hard sub-process proceeds until some cut-off is reached and is matched to the parton density parametrisations of the initial hadrons.

Resolved photoproduction has an initial photon spectrum as generated by the EPA. The backward evolution in HERWIG allows at each stage the possibility for a $\gamma \to q\bar{q}$ vertex in resolved events. For direct events, the LO matrix elements for $2 \to 3$ scattering are used.

The transition from partons to hadrons after the parton shower then proceeds via a non-perturbative model called the *cluster* model, which groups the partons into color neutral objects. The gluons are split into $q\bar{q}$ pairs and these are subsequently clustered into colorless objects via the color connections generated in the parton shower. Each cluster is then fragmented into two hadrons or the

lightest hadron for its flavour if the cluster is not massive enough. Finally the decay of unstable particles is simulated.

For the evolution of heavy quarks in the hard sub-process back to the photon, there are three possibilities. A heavy quark pair can result from the photon splitting directly, $\gamma \to Q\bar{Q}$, from a gluon splitting, $g \to Q\bar{Q}$, or be present when the evolution terminates. The latter represents heavy quark excitation below the factorisation scale as shown in Figure 2.6b. As the factorisation scale is set to be at the hard sub-process, the question of whether excitation processes occur is dependent on whether $p_T^2 > m_Q^2$. We can then see that with sufficiently high p_T jets, we will have "bottom excitation".

HERWIG version 5.9 is used throughout this thesis.

4.1.2 PYTHIA Generator

The PYTHIA Monte Carlo [101] is also a general purpose generator, sharing many common features with HERWIG , but also significant differences. There are two main differences in the perturbative phases of the respective models. For photoproduction events, the photon spectrum in PYTHIA is generated using the WWA for both direct and resolved photon processes. Secondly, the factorisation scale, μ^2, used is the transverse mass of the two outgoing partons, m_T^2, given by,

$$\mu^2 = m_T^2 = \frac{1}{2}\left(m_1^2 + p_{T_1}^2 + m_2^2 + p_{T_2}^2\right).$$

The parton shower is conceptually the same in both generators, but in PYTHIA the evolution is ordered in the virtuality of the radiated partons. The partons are hadronised using the Lund Symmetric String Fragmentation model [100]. In the Lund model, partons are connected by "strings", the strength of which is about 1 GeV/fm. As the partons move away from each other, the strings become more energetic, finally breaking to produce $q\bar{q}$ pairs. When the energy of a string is too small to enable further separation of the partons, hadrons are formed. Finally the unstable hadrons are forced to decay as in HERWIG .

PYTHIA version 6.1 is used throughout this thesis.

4.2 Monte Carlo Samples Generated

For the analysis performed in this thesis different sets of Monte Carlo events were required. Consequently, HERWIG and PYTHIA Monte Carlo samples were generated, for all of them these values for the masses of the heavy quarks were used:

- $m_c = 1.35$ GeV/c^2,
- $m_b = 4.5$ GeV/c^2.

Requirements on jets	
Number of jets in the event	$\# \geq 2$
Transverse energy of the jet	$E_T \geq 4.0$ GeV
Pseudorapidity of the jet	$\eta \leq 3.0$
Requirements on μ	
Number of muons in the event	$\# \geq 1$
Momentum of the muon	$p \geq 1.5$ GeV
Polar angle of the muon	$0.08723 < \theta < 3.0543$

Table 4.1: List of the cuts applied on each event in the samples generated with the PYTHIA 6.1 program for heavy flavour photoproduction of charm and beauty quarks.

Requirements on jets	
Number of jets in the event	$\# \geq 2$
Transverse energy of the jet	$E_T \geq 4.0$ GeV
Pseudorapidity of the jet	$\eta \leq 3.0$
Requirements on μ	
Number of muons in the event	$\# \geq 1$
Momentum of the muon	$p \geq 2.0$ GeV
Polar angle of the muon	$0.1047 < \theta < 3.0543$

Table 4.2: List of the cuts applied on each event in the samples generated with the HERWIG 5.9 program for heavy flavour photoproduction of charm and beauty quarks.

We choose these structure functions:

- GRV-LO for the photon [144],
- CTEQ-4L for the proton [85].

All the analyzed samples have an equivalent integrated luminosity larger than that of the data studied in this thesis. For what it concerns the production of heavy flavours this means that the following samples were generated and used:

- PYTHIA 6.1 heavy quark production, $b\bar{b}$ massive, 240 k events, equivalent to $\mathcal{L} = 778$ pb^{-1};
- PYTHIA 6.1 heavy quark excitation in the photon, $b\bar{b}$ massless, 100 k events, equivalent to $\mathcal{L} = 618$ pb^{-1};

- PYTHIA 6.1 heavy quark excitation in the proton, $b\bar{b}$ massless, 40 k events, equivalent to $\mathcal{L} = 1236$ pb^{-1};
- PYTHIA 6.1 heavy quark production, $c\bar{c}$ massive, 420 k events, equivalent to $\mathcal{L} = 387$ pb^{-1};
- PYTHIA 6.1 heavy quark excitation in the photon, $c\bar{c}$ massless, 360 k events, equivalent to $\mathcal{L} = 404$ pb^{-1};
- PYTHIA 6.1 heavy quark excitation in the proton, $c\bar{c}$ massless, 100 k events, equivalent to $\mathcal{L} = 708$ pb^{-1};
- HERWIG 5.9 heavy quark production, $b\bar{b}$ direct photon, 220 k events, equivalent to $\mathcal{L} = 1241$ pb^{-1};
- HERWIG 5.9 heavy quark production, $b\bar{b}$ resolved photon, 160 k events, equivalent to $\mathcal{L} = 2954$ pb^{-1};
- HERWIG 5.9 heavy quark production, $c\bar{c}$ direct photon, 250 k events, equivalent to $\mathcal{L} = 421$ pb^{-1};
- HERWIG 5.9 heavy quark production, $c\bar{c}$ resolved photon, 140 k events, equivalent to $\mathcal{L} = 435$ pb^{-1};

Each event in the samples where a particular heavy quark is produced has at least 2 jets of transverse energy greater than 4 GeV and pseudorapidity less than 3.0, and at least a muon with a momentum greater than a minimum cut and a polar angle comprised in an interval that is larger than the geometrical acceptance of the muon detectors, see the Tables 4.1 and 4.2 for details. For the generation of light flavours or inclusive dijet photoproduction sample with five active flavours, that means all the quarks that can be produced at HERA, only a jet cut has been applied, because in this case we are generating mostly background events. These can be events where a muonic signal is caused not by a real muon in the event but by particles punching through the detector and escaping the calorimeters.

All these samples have been generated with a minimum cut on the transverse momentum, $\hat{p}_{min} = 2.5$ GeV, of the final state quark with respect to the direction of the incoming partons; this is necessary in the case we use a massless calculation to get rid of the singularity at $\hat{p} = 0$ GeV. This cut was applied even in the case of the use of massive calculation to have a faster generation of large samples.

In the generation of light flavour we have decided to have tighter cuts in order to obtain a higher efficiency and even faster generation. This is needed in order to have samples equivalent to large integrated luminosities and not to have to generate and simulate through the ZEUS detector a number of events too large to be handled. Nonetheless we have generated Monte Carlo samples for long periods of time, more than six months.

Requirements on jets	
Number of jets in the event	$\# \geq 2$
Transverse energy of the jet	$E_T \geq 5.25$ GeV
Pseudorapidity of the jet	$\eta \leq 2.8$
Requirements on y	
For direct photon processes	$0.075 < y < 1.0$
For resolved photon processes	$0.15 < y < 1.0$

Table 4.3: List of the cuts applied on each event in the samples generated with the PYTHIA 5.9 program for *light* flavour photoproduction of dijet events.

We have used small samples to study specific cuts to get reduction factors as high as possible without biasing the generation. This means, at first, a higher cut on the quantity $\hat{p}_{min}$, that was risen to 4.0 GeV (for the resolved photon process). Then we decided to put a tighter requirement on the jets, that is a higher generated transverse energy, $E_T^{\rm jet} \geq 5.25$ GeV, and a more strict pseudorapidity interval, $\eta \leq 2.8$.

In addition, we have introduced a restriction on the values of the variable y as defined in Equation (2.5):

- PYTHIA 6.1 light flavour direct photoproduction $0.075 < y < 1.0$;
- PYTHIA 6.1 light flavour resolved photoproduction $0.15 < y < 1.0$.

This has not been enough and we have decided to select in a more stringent way the sample. If something has to reach the outer chambers or planes of BRMUON and FMUON it is likely that an *energetic particle* is present in the event. If at least one particle[5], that is sufficiently stiff, is in the shower of the final state partons we keep the event. The actual definition of this *energetic particle* is based on an algorithm that has been tailored to minimize the chance to discard a good event and its details can be seen in Table 4.4.

Eventually the following samples have been generated, simulated and analyzed with the programs developed on purpose for the study that we illustrate in this thesis:

- PYTHIA 6.1 light quark production, direct photon, 1.7 M events, equivalent to $\mathcal{L} = 75$ pb^{-1};
- PYTHIA 6.1 light quark production, resolved photon, 4.0 M events, equivalent to $\mathcal{L} = 72$ pb^{-1}.

[5] We indicate as final state particles those that are treated as stable by the generator, that is those that have not decayed within the generator.

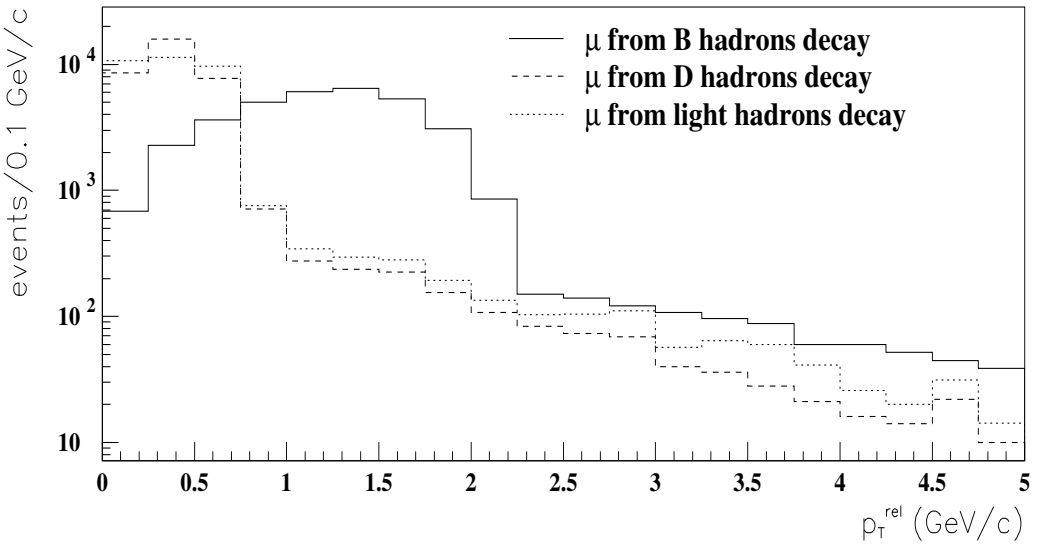

Figure 4.2: Hadron level Monte Carlo predictions for p_T^{rel} in the cross-section region to be measured.

We use our HERWIG Monte Carlo as a systematic check for our unfolding procedure and so was not used as completely as the PYTHIA Monte Carlo. We therefore only generated decays from heavy quarks whose generation is fast. The generation procedure for light quarks is extremely time consuming and was therefore thought not necessary because the shapes of the "μ from D hadrons decays" and "μ from light hadrons decays" p_T^{rel} distributions are similar as can be seen in Figure 4.2.

When we display a distribution in p_T^{rel} for Monte Carlo we classify it into and refer to it as three different samples; beauty, charm and other Monte Carlo. How the classification is performed is important because by using this classification we determine the amount of beauty production in the data. We consider the outgoing partons in the hard sub-process. If one or both partons are beauty quarks then this is termed "beauty Monte Carlo". If one or both partons are charm quarks, then it is termed "charm Monte Carlo". If the two partons are neither beauty nor charm, then this is termed "other" Monte Carlo.

Comparison of physical quantities between data and Monte Carlo will be reserved for the analysis chapter.

4.3 Jet Energy Corrections

4.3.1 Jet Resolutions

The measurement in the calorimeter of the jet parameters - transverse energy, E_T^{jet}, pseudorapidity, η^{jet} and azimuthal angle, ϕ^{jet} - deviates from the true values

of the hadron jets. This is due to dead material in front of the calorimeter, the resolution of the calorimeter and particles which do not deposit energy in the calorimeter such as muons and neutrinos. Monte Carlo events are studied to account for these systematic effects. In the following sections we use PYTHIA to evaluate the corrections.

Jet finding is performed on the final hadronic state and on the calorimeter cells. The calorimeter jets and hadron jets are then matched in $\eta - \phi$ space. A pair is considered matched when,

$$\Delta R(\eta, \phi) = \sqrt{(\eta^{CALjet} - \eta^{HADjet})^2 + (\phi^{CALjet} - \phi^{HADjet})^2} \tag{4.1}$$

is a minimum and $\Delta R(\eta, \phi) < 1$. For these matched jets, resolutions in η and ϕ and the energy ratio between hadron and calorimeter jets were considered.

By considering Figure 4.3, the dependence of the jet parameters and comparison between calorimeter and hadronic jets is reported. Direct and resolved processes are displayed separately and the error shown is the spread of the mean. We can clearly see that the jets measured in the calorimeter have a smaller transverse energy than the hadron jets. The value of E_T^{CALjet} is typically 40% too low. Considering the dependence on η^{CALjet}, we see that this energy loss exhibits a dependence, ϕ^{CALjet} and η^{CALjet} itself showing almost no dependence compared to the errors; all variations or non-variations are the same for both direct and resolved processes. We also see a non-dependence of all variables on ϕ^{CALjet} and so we seek a correction as a function of E_T^{CALjet} and η^{CALjet}. These results are consistent with previous dijet analyses; for example, see [108].

4.3.2 Correction of Jet Energy

The transverse energy of the jets is corrected using the Monte Carlo such that the average energies of the hadron jets and those in the calorimeter are equal.

As was said previously, the transverse energy of the jet varies with the jet pseudorapidity and jet energy. Therefore a correction function of the form $C(E_T^{CALjet}, \eta^{CALjet})$ was determined such that:

$$E_T^{CORjet} = C(E_T^{CALjet}, \eta^{CALjet}) \cdot E_T^{CALjet} \tag{4.2}$$

where E_T^{CORjet} is the corrected transverse energy of the jet.

Figure 4.4 shows the variation of $E_T^{HADjet}/E_T^{CALjet}$ as a function of E_T^{CALjet} in bins of η^{CALjet} for matched calorimeter and hadron jets. The curves for the resolved and direct are shown separately and are consistent with those of the combined curves. For a bin, i, in η^{CALjet}, the correction function fitted, $C(E_T^{CALjet}, \eta^{CALjet})$, is of the form:

$$C\left(E_T^{CALjet}, \eta^{CALjet}\right) = a_1\left(\eta_i^{CALjet}\right) + \exp\left(a_2\left(\eta_i^{CALjet}\right) + a_3\left(\eta_i^{CALjet}\right) \cdot E_T^{CALjet}\right) \tag{4.3}$$

Requirements on the polar angle of a track $0.105 < \theta < 3.054$	
Requirements on a track in a sector	
Requirements on a forward track	
$0.105 < \theta_f < 0.54$	$p_T > 1.25$ GeV/c
Requirements on a barrel track	
$0.405 < \theta_b < 2.695$	$p_T > 2.50$ GeV/c
Requirements on a rear track	
$1.8375 < \theta_r < 3.054$	$p_L > 2.00$ GeV/c
Requirements on a track on adjacent sectors	
Requirements on a forward or barrel track	
$0.105 < \theta_f < 0.54$ $0.405 < \theta_b < 2.695$	$p_T > 2.75$ GeV/c $p_T > 1.50$ GeV/c
Requirements on the minimum momentum of a track on adjacent sectors	
$0.105 < \theta_f < 0.54$	$0.405 < \theta_b < 2.695$
$\min(p_T\{\text{forward}\}) + \min(p_T\{\text{barrel}\}) > 2.25$ GeV/c	
$0.405 < \theta_b < 2.695$	$1.8375 < \theta_r < 3.054$
$\min(p_T\{\text{barrel}\}) + \min(p_L\{\text{rear}\}) > 2.00$ GeV/c	

Table 4.4: List of the cuts applied on each final state particle to define an *energetic particle* in events generated with the PYTHIA 5.9 program for *light* flavour photoproduction of dijet events, polar angles are measured in radians, p_T and p_L are the transverse and longitudinal momentum with respect to the beam axis. It is to be noted that the forward, barrel and rear sectors overlap geometrically. If no track satisfy any of these cuts the event is discarded.

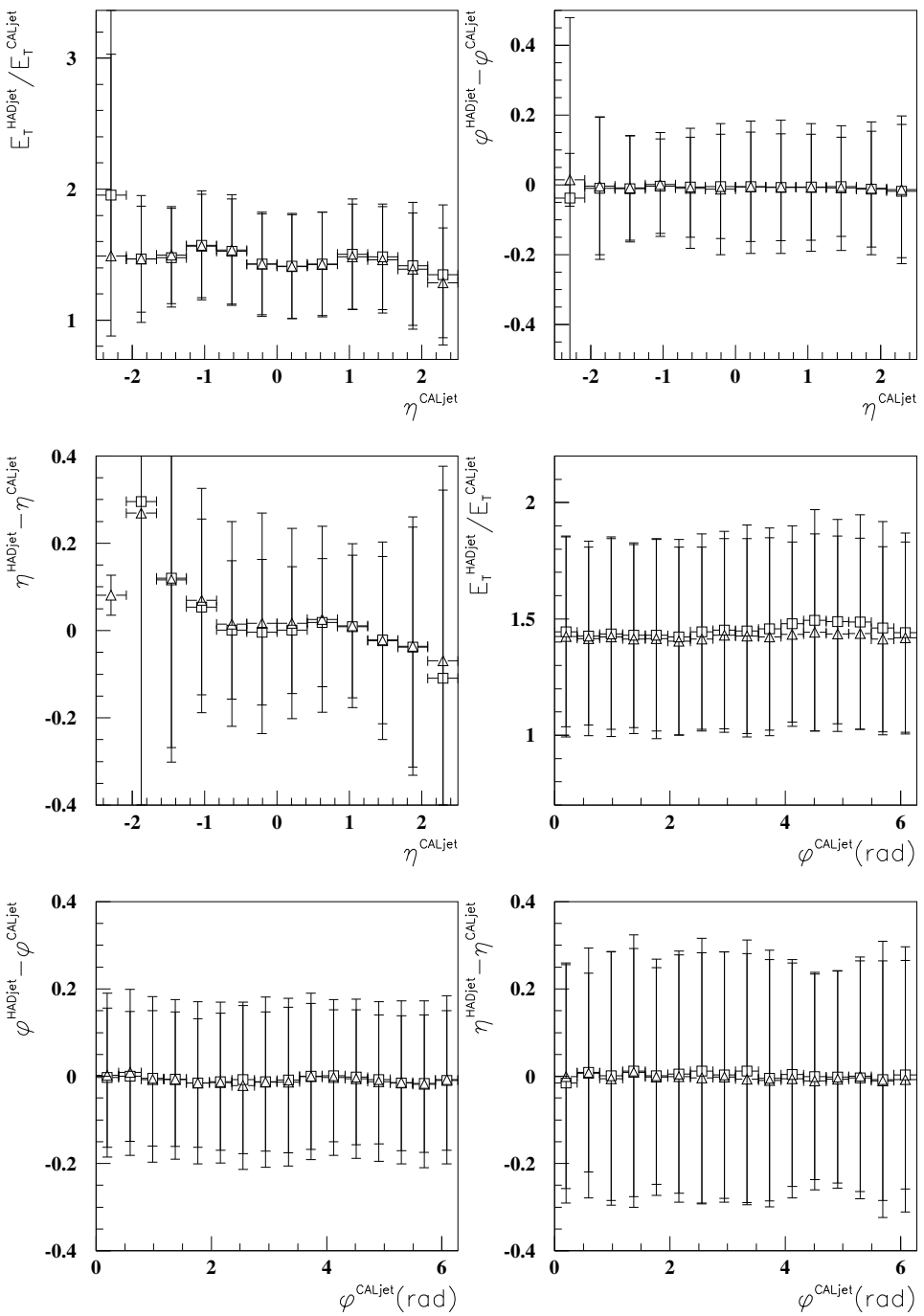

Figure 4.3: Jet resolutions. The dependence of jet parameters on each other is shown separately for direct (open squares) and resolved (open triangles). The dependence of $E_T^{HADjet}/E_T^{CALjet}$, $\phi^{HADjet}-\phi^{CALjet}$ and $\eta^{HADjet}-\eta^{CALjet}$ on η^{CALjet} and ϕ^{CALjet} is shown.

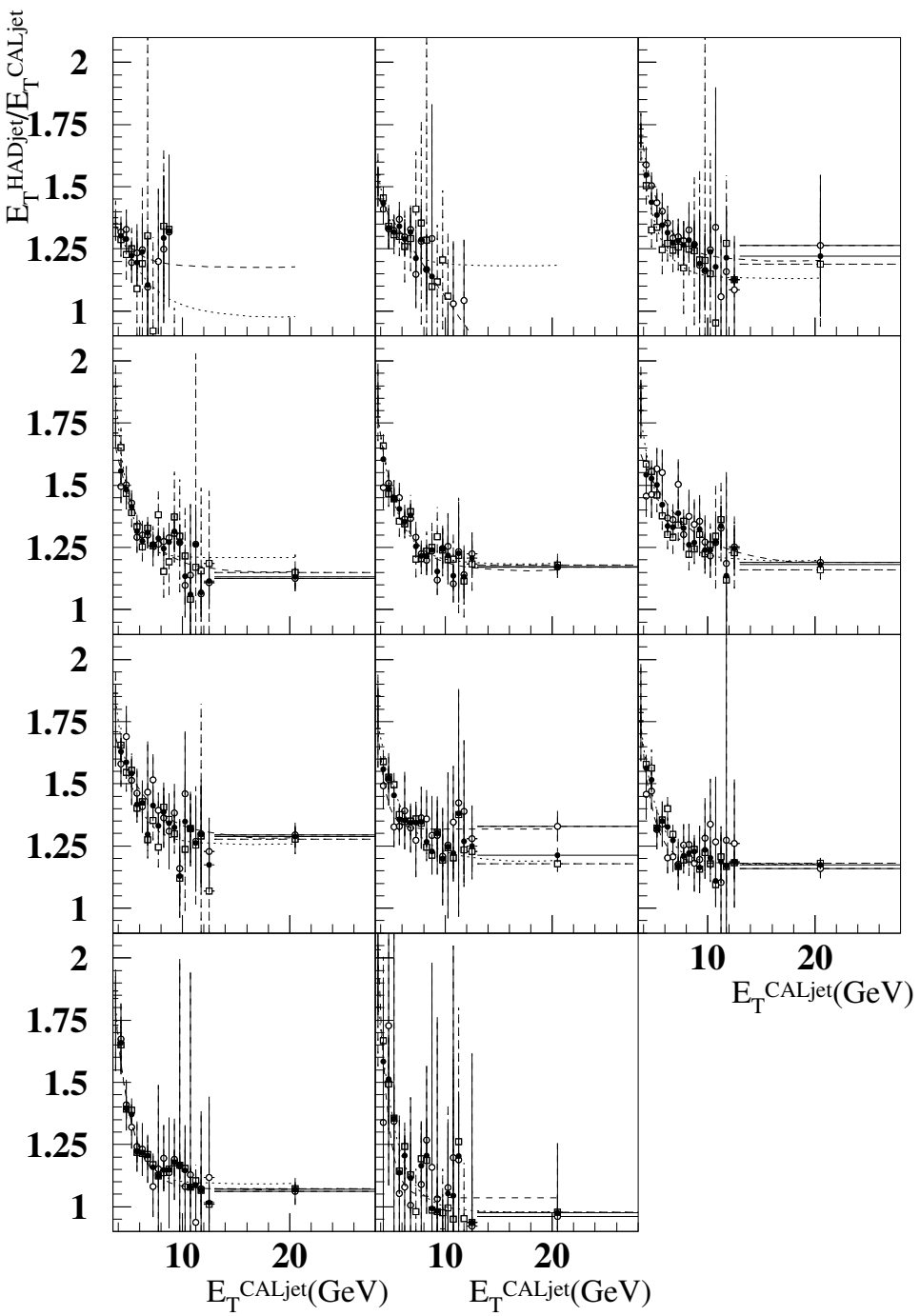

Figure 4.4: The ratio of E_T^{HADjet} and E_T^{CALjet} versus E_T^{CALjet} in bins of η. The points and fit lines are shown for direct (open squares, dashed line), resolved (open triangles, dotted line) and resolved and direct combined (solid dots, solid line). The fit parameters shown are for the fit to the combined sample using the correction function, $C(E_T^{CALjet}, \eta^{CALjet})$

With a maximum correction factor of about 1.48 for low E_T^{CALjet}, a cut of $E_T^{CORjet} > 6$ GeV for the lowest transverse energy jet is justified, see Chapter 6.

The result of using these combined correction factors can be seen by applying them back to the Monte Carlo. This is achieved by plotting the ratio of the hadron level values and the corrected calorimeter values of transverse energy and values as a function of η^{CALjet} and ϕ^{CALjet}, Figure 4.5.

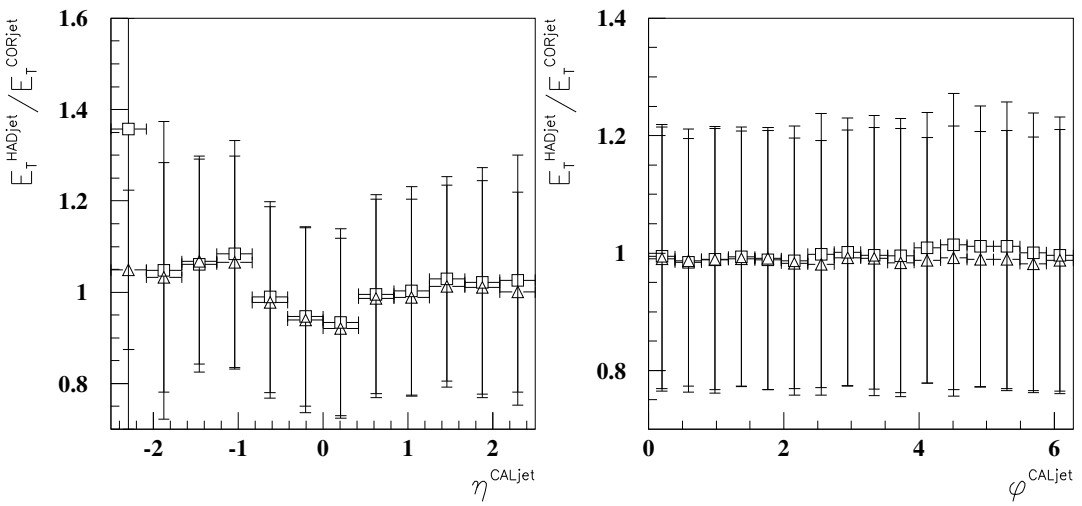

Figure 4.5: Result on the jet energy resolutions when applying the jet energy corrections. The resolutions are shown again for direct (open squares) and resolved (open triangles) separately.

As can be seen in Figure 4.5, the mean value is about 1 and not 1.40 and the pseudorapidity dependence is removed. The high values in the first bins in η^{CALjet} arise from a lack of statistics in the rear direction. The same correction factor was used for the first three bins, with the result that the third bin dominates the first two. This was chosen because by using three bins in the rear direction would be unreliable due to the inadequate statistics caused by the large boost in the proton direction. By applying the overall correction on direct and resolved separately, one can see the justification of using a combined correction factor. The resolution of E_T remained roughly the same after as before correction.

4.4 Correction of y_{JB}

The value of y as calculated from the Jacquet-Blondel method, y_{JB}, clearly deviates from the true value of y, y_{true} (see Figure 4.6).

The value of y_{JB} is systematically lower than y_{true}, as expected, due to energy losses as particles pass through dead material in front of the calorimeter or are lost down the rear beam-pipe. The resulting shift in y_{JB} is about 20%. This dependence can be corrected by studying the ratio of y_{JB}/y_{true} as a function of $x_\gamma^{\rm obs}$, as the shift is dependent on the presence of the photon remnant. The

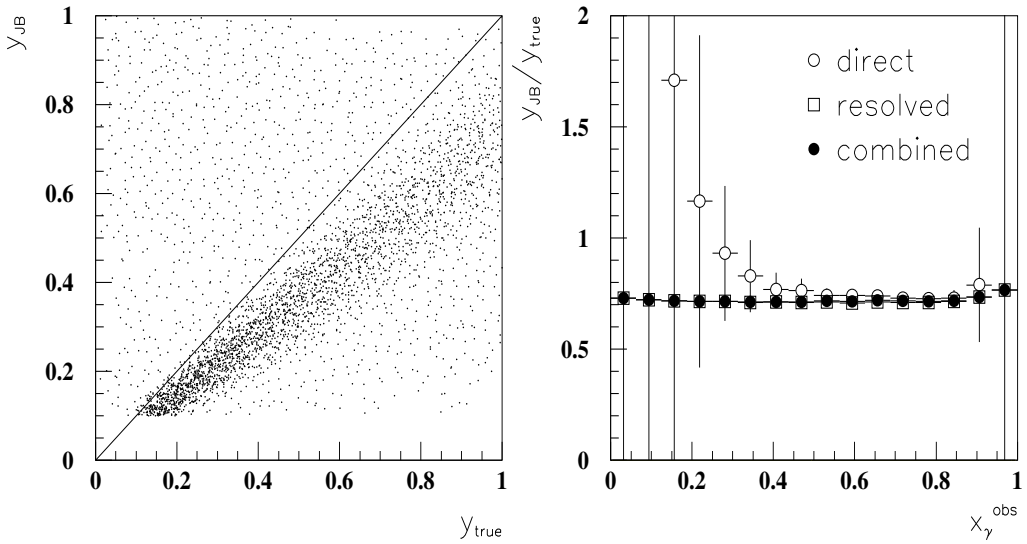

Figure 4.6: Correction of the measurement of y. The correlation of y_{JB} and y_{true} (Left) is shown. Also displayed is the dependence of y_{JB}/y_{true} on $x_\gamma^{\rm obs}$ for direct (open circles) and resolved (open squares) and the combined sample (solid points) with the polynomial fit.

dependence on y_{JB} itself, E_T^{jet} and η^{jet} were also studied and found not to be significant. A dependence of y_{JB}/y_{true} on $x_\gamma^{\rm obs}$ can clearly be seen.

A polynomial was fitted to the sum of the direct and resolved components. The polynomial correction factor, $P(x_\gamma^{\rm obs})$ has the following form:

$$y_{corr} = y_{JB}/P(x_\gamma^{\rm obs}); \quad P(x_\gamma^{\rm obs}) = p_1 + p_2 x_\gamma^{\rm obs} + p_3 x_\gamma^{\rm obs^2}. \tag{4.4}$$

The correction to y_{JB} was then applied back onto the calorimeter level Monte Carlo. As the correction factor was determined from the combined direct and resolved samples, then its effect on direct and resolved separately was considered. As can be seen in Figure 4.7 the results of applying separately to resolved and direct yield similar results. There is an improvement in the resolution for both direct and resolved; the previous rms values were 0.2 and 0.15 for direct and resolved respectively. The value of $y_{JB}^{\rm corr}$ is now closely correlated to y_{true} with a mean difference of about zero. This justifies the use of the overall correction factor even when applying it to direct and resolved samples separately.

4.5 Corrections for the Presence of a Muon in the Event

Then presence of a muon in the jet may require modifications to the above described jet correction algorithm. However since the same procedure has been

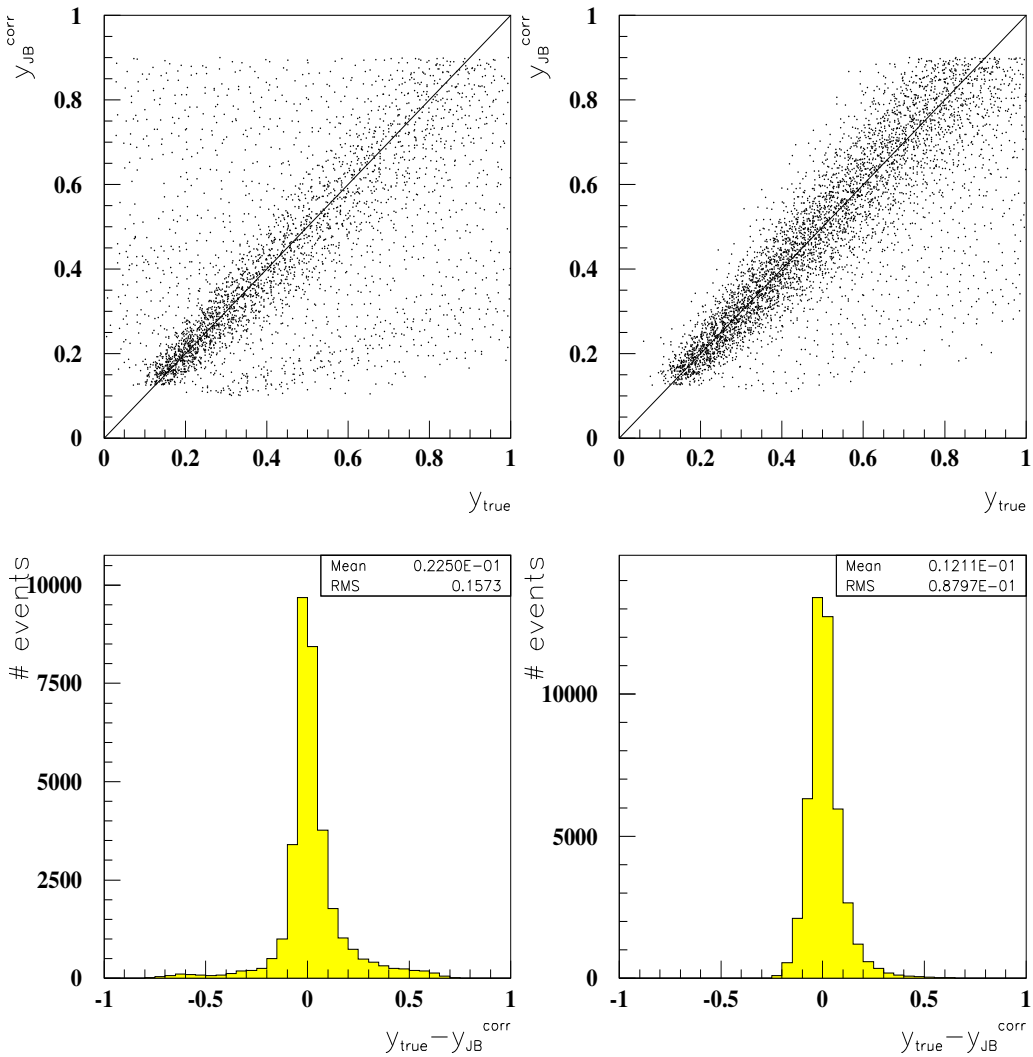

Figure 4.7: Effect of the y_{JB} correction for direct (right) and resolved (left) separately on the correlation (top) and projection (bottom).

applied to data and Monte Carlo events, in first approximation, the effect should not modify the final result. More detailed studies are presently in progress.

Chapter 5

Analysis and data Selection

The present analysis is searching for open beauty photoproduction in events with two jets tagged through the semi-leptonic decays to muons. In particular in this chapter we will describe the selection procedures that define the final samples we will use to measure the signal and cross sections.

5.1 The data sample

Data were used from the years 1996 and 1997 giving a combined integrated luminosity of $36.9 \pm 0.5 \text{pb}^{-1}$: 10.7pb^{-1} from 1996 and 26.2pb^{-1} from 1997. For the FMUON region the useful luminosity is somewhat lower, i.e. 33.7 pb^{-1}. These two years only were used as no change in the trigger or significant change in the detector occurred.

The selection procedure can be separated into two parts - the selection using the First, Second and Third level online triggers and a tighter offline selection on quantities after full reprocessing of the data where calibration constants are applied.

5.2 The Trigger chainfor dijet event selection

In the following section we will illustrate the definitions of the trigger chain that constrains the data acquisition filters for dijet events.

5.2.1 Jet First Level Trigger (FLT)

To pass the slot used at the first level trigger, slot 42, one of four thresholds at the Calorimeter FLT (CFLT), five vetoes and a good track quality demand must be satisfied.

- The four CFLT thresholds are:

  - Total calorimeter energy > 14.968 GeV,
  - Total Electromagnetic Calorimeter (EMC) Energy > 10.068 GeV.

  The "total" energies are calculated by excluding the 3 inner rings around the FCAL and the inner ring around the RCAL beampipe, corresponding to a region in pseudorapidity of approximately $-3.66 < \eta < 2.2$.

  - RCAL EMC energy > 2.032 GeV.

  This also excludes the inner ring around the RCAL beam-pipe.

  - BCAL EMC energy > 3.404 GeV.

- The criteria for the event to pass the vetoes are:

  - The timings observed in the two C5 counters should match with physics timing, but not with that of the beam gas.
  - Two vetoes requiring that no coincidence of the inner and outer veto wall is detected.
  - The timing in the SRTD should match with physics events and not with beam-gas events.
  - Events should have `TrKclass>2`. These are events with a relatively high ratio of vertex to total number of tracks. The exact value of the ratio is dependent on the number of vertex and non-vertex tracks, but is approximately $> 25 - 30\%$.

- The tracking demand requires the event to have at least one track found by the CTD-FLT coming from the nominal interaction region, -50 cm $< z_{vtx} <$ 80 cm.

5.2.2 Jet Second Level Trigger (SLT)

The SLT used, the so-called "high-E_T" trigger, designed for hard photoproduction, has selection criteria that ensures high transverse energy events are accepted (whence the name). The following requests are made:

- -60 cm $< z_{vtx} < 60$ cm.
- there must be at least 1 vertex track found by the CTD-SLT.
- $E - P_z > 8.0$ GeV, where E is the energy sum of calorimeter cells and P_z the vector sum of longitudinal momentum of all cells;

- $E_T(\text{box}) > 8.0$ GeV, where $E_T(\text{box})$ is the sum of transverse energy, E_T in all calorimeter cells excluding the first ring around the FCAL beampipe (outside a value of about $\eta = 3$)

- $(E - P_z > 12.0$ GeV) or $(p_z/E < 0.95)$.

5.2.3 Jet Third Level Trigger (TLT)

At the TLT, more time is available and a software trigger is used. There are essentially two *independent* TLT's that could be used for the analysis; one based on tracking and the finding of muon candidates (bit40/41) and the other on calorimeter quantities and the finding of dijet events (bit77). The μ trigger relies on a modified version of the offline tracking reconstruction package to identify μ candidates. We will describe the dijet trigger first.

In order to pass the "dijet" TLT the following criteria must be satisfied:

- -60 cm $< z_{vtx} < 60$ cm;

- number of bad tracks is less than 6 where a bad track is so defined if it does not meet the following:

  - the number of degrees of freedom should be > 20,
  - $p_T \geq 0.2$ GeV,
  - $-0.35 < \eta < 3.13$,
  - the number of hits used in CTD axial superlayers > 5,
  - the number of hits used in CTD stereo superlayers > 5,
  - the distance of closest approach in z to the vertex must be ≤ 75 cm.

- 5.0 GeV $< E - P_z <$ 75.0 GeV which is equivalent to a y_{JB} demand: $0.09 < y_{JB} < 1$, see Equation (3.5);

- $E_T(10°\text{cone}) > 5.0$ GeV, where $E_T(10°\text{cone})$ is the sum of all the E_T in the calorimeter cells outside a 10° cone ($\eta < 2.44$) around the FCAL beampipe;

- $p_z/E < 1.0$;

- a simplified version of the EUCELL jet cone algorithm is run at the TLT and there must be at least two jets with the following:

$$E_T^{\text{jet}} > 4 \text{ GeV};$$

$$\eta^{\text{jet}} < 2.5.$$

5.3 Efficiency of Trigger Chain for jet selection

The efficiency of the above three stage trigger chain has been extensively studied in previous dijet analysis by means of independent triggers [108, 121]. We will therefore include only a brief summary of the method and conclusions.

5.3.1 Jet FLT

The FLT slot was studied [108] by choosing an independent trigger which subsequently fed into the SLT and TLT as described. A LUMI branch of the FLT was chosen which required the observation of a scattered positron in the LUMI detector with some low energy calorimeter thresholds. The fraction of events passing the LUMI branch which also pass the calorimeter triggers was found to agree reasonably well between data and Monte Carlo.

5.3.2 Jet SLT

Similarly an independent trigger was used to test the efficiency of the SLT. The LUMI SLT was studied [108], which has events from the FLT which then pass the TLT. The LUMI SLT has the same requirements as the LUMI FLT with the additional criterion that the energy in the LUMI is more than 5 GeV. Reasonable agreement between data and Monte Carlo was again seen.

5.3.3 Jet TLT

The TLT has been studied extensively in [121] by considering an independent sample of events which have passed the charm TLT (bit 27). The overall efficiency of the trigger was found to be good and increases with the value of the transverse energy E_T, such that for $E_T > 6$ GeV, the efficiency is almost 100%. The Monte Carlo models the efficiency reasonably well.

5.4 The Trigger chain for Muon selection

In the following sections we will describe the online trigger chain of the selection of muons in the barrel and rear region of the detector. We need to consider this chain in order to have the complete analogic readout of the signals from the chambers that is requested by the offline reconstruction and matching programs to identify muons in these sectors of the experiment. There are not such requirements in the forward region were the only requirement is the offline reconstruction of a FMUON stand-alone track, see Section 3.4.1.

5.4.1 First Level Trigger for Muons in the BR Regions

We are interested in the semi-leptonic decay of beauty quark in the muonic channel that is to the process:

$$e\ p \rightarrow e\ b\ \bar{b}\ X \rightarrow e\mu^{\pm}\text{dijet}X \tag{5.1}$$

Hence the events, we are interested in, have at least one muon that can go in the barrel or in the rear sector, in a certain percentage of cases. The polar angular coverage of the muon chambers in these sectors is in the range $34° < \theta < 177°$. As we have seen in the Section 1.8.2 to have a muonic signal from the chambers for the detection of μ we have to require the presence of a local trigger. In our analysis we are dealing with events with muons that have momenta large enough to cross both the inner and outer chambers with a sufficiently high efficiency. Hence we are able to require the trigger of the outer chambers that has requirement on energy deposits in the calorimeter and on the quality of the tracks in the central tracking device. At the first level trigger many informations are available from the calorimeter (CAL), these can be global, regional or local quantities referred to elementary unities constituted by the trigger towers (see Figure 5.4.1). The typical tower has transverse dimensions of 20×20 cm^2 and is formed by four electromagnetic cells (two if in RCAL) followed by two hadronic cells. Its definition does not usually coincide to the one of calorimetric towers that have been described in Section 1.7 because these are not projective. The trigger towers, instead, are defined in such a way to be as projective as possible. In each of them we are able to evaluate the energetic deposits in the electromagnetic and hadronic parts, and these deposits are then analyzed through programmable thresholds.

For what it concerns the central tracking detector, the FLT receives from it the total number of tracks and the number of those coming from the vertex. Analyzing the arrival time of signals from the wires, the CTD is able to determine whether tracks are produced near an ep collision or tracks are out of time. Conditions on the track multiplicity and on the signal arrival time are synthesized by the request of a minimum *class* of the event, that is equivalent to impose the fraction of tracks recognized by the CTD to come from the vertex to be larger than a certain value.

The FLT is subdivided in 64 parallel branches, the inner and outer muon chambers correspond to the slots 14 and 15. The former covers the central region of the detector, while the latter covers the backward region. The trigger we use is the OR of both these branches and is globally defined as:

$$\begin{aligned} & [(CAL_E > 464\ \text{MeV} * BMU)\ or\ (RCAL_E > 464\ \text{MeV} * RMU)] \\ * \ & [TRK_q95b] * vvv \end{aligned} \tag{5.2}$$

where:

- BMU e RMU indicate the request of the presence of a trigger signal in the inner and outer chambers in the barrel and rear zones, respectively;

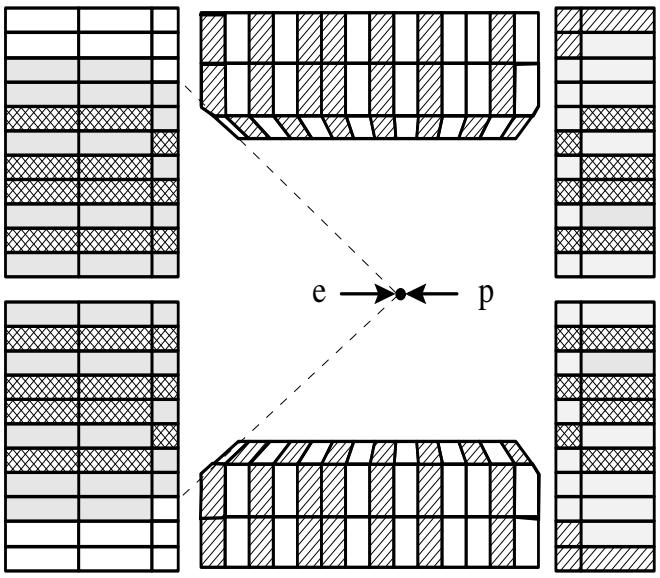

Figure 5.1: Disposition of the towers of the first level of trigger of the CAL along the beam axis.

- CAL_E indicates the sum of the energies in all the trigger towers, except for those near by the beampipe in FCAL and RCAL; for an event to be accepted, CAL_E has to be larger than 464 MeV;
- $RCAL_E$ is satisfied if an analogous to the previous condition applies, taking into account the towers of the rear calorimeter only;
- TRK_q95b indicates the quality of tracks at the CTD level: this condition requires at least a track coming from the vertex to be present;
- vvv indicates the absence of veto signals.

In this way we select all the ep collisions where a muons is able to reach the B(R)MUO outer chambers.

The numerical values for the calorimeter trigger so far quoted are such because the used processors are able to supply digital values. In this case the condition to be satisfied for an event to be accepted is that at least one trigger tower has an energy deposit equal or greater than 464 MeV. This value correspond to the threshold energy that the calorimeter electronics is able to detect: a particle that deposits an energy smaller than 464 MeV cannot be detected. In this case, the energy request is at the minimum because the trigger branch we are looking into has as its aim to select those events where muons are produced, and these particles deposit in the calorimeter small quantities of energy. The energetic

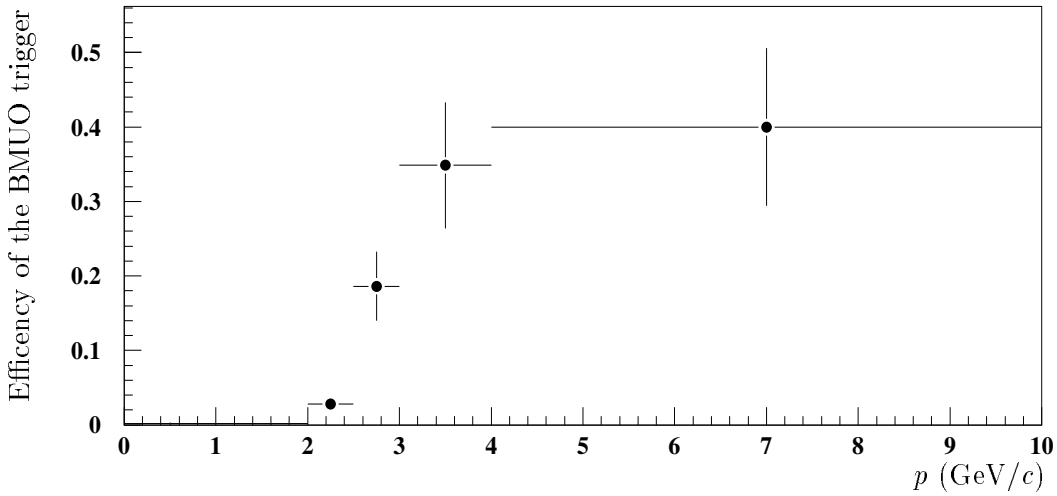

Figure 5.2: Trigger efficiency of the outer muon chamber in the barrel region ($34° < \theta < 140°$) in the data as a function of the momentum p of the muon; the FLT branch taken in consideration is the 14 (see Section 5.4.1).

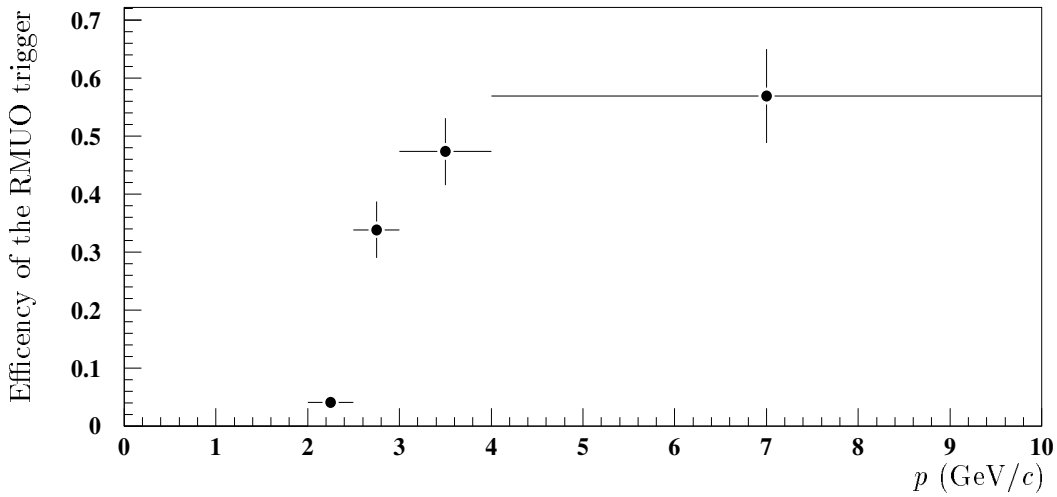

Figure 5.3: Trigger efficiency of the outer muon chamber in the rear region ($140° < \theta < 177°$) in the data as a function of the momentum p of the muon; the FLT branch taken in consideration is the 15 (see Section 5.4.1).

request of the CAL has in this case just the aim to signal that a crossing of a minimum ionizing particle has taken place.

5.4.2 Second Level Trigger for Muons in the BR Regions

No other request is done at the second level trigger to select events with large momentum muons. Simply the SLT imposes the events timing conditions to suppress cosmics events and beam-gas interaction as we have already described in Section 1.11.2.

5.4.3 Third Level Trigger for Muons: GLOEXO

One of the selection programs of the TLT has been designed to recognize and accept *ep* collision with a final state that contains at least a muon measured by the B(R)MUI chambers. Most of the events of this kind that reach the TLT come from the branch of the FLT that we have described in Section 5.4.1 and they have passed the general veto cuts applied at the second level trigger of the data acquisition chain. The selection program has been developed to recognize these particular events and is called GLOEXO. In Appendix A we will describe the algorithms deployed in the GLOEXO program in a somewhat detailed way. Its aims are listed shortly here:

- to reconstruct the position of the muon within the hit B(R)MUI chamber;
- to select tracks reconstructed in the CTD that can be associated to the muon identified with the B(R)MUI chambers;
- to combine the informations obtained from the B(R)MUI chamber and from the CTD to identify the global trajectory of the muon inside ZEUS.

5.5 Efficiency of Trigger Chain for BRMUON selection

The efficiency of the first two stages of the above three stage trigger chain has been extensively studied and tested in previous muon analysis [122] where analogous inner first level muonic trigger was used[1]. We will describe in the next section the studies that were done to measure the efficiency of the outer chamber trigger.

[1]In those cases the *inner chamber trigger* or the *low multiplicity trigger* were used. The logics of both requires the local trigger of the B(R)MUI chambers, which is similar to the one that is inserted in the outer slots 14 and 15 of the FLT, that are the ones we need.

5.5.1 Muon FLT

Different kind of samples, both of data and of Monte Carlo, were used to study the efficiency of this trigger filter. The trigger itself has not displayed any problem of stability during the data taking, the only thing that the study has enlightened is the difference between the efficiency of the online trigger and of its offline implementation in the ZGANA simulation program. What we mean with *efficiency* is the convolution of the trigger itself with the geometric acceptance, the BRMUON detector inefficiency (due to hit inefficiency) and the trigger tower efficiency:

$$\begin{aligned}\text{Trigger Efficiency } 14/15 = \text{Slot-14/15 Efficiency} \otimes \text{Geometrical Acceptance} \\ \otimes \text{ BRMUON Detector Efficiency} \otimes \text{Trigger Tower Efficiency.}\end{aligned} \quad (5.3)$$

Using events of elastic photoproduction of J/ψ decaying in two muons it was possible [123] to check the efficiency of the trigger requiring the events to pass an independent first level trigger slot. An event of elastically photo-produced J/ψ vector meson is a two tracks event with no energetic calorimetric deposit except for those linked to the muons coming from the decayed particle. The final state is composed of two muons with a large angle between them, because of the mass of the produced state and of the kinematics of the accelerator. We select those events where one of the two muons goes towards the barrel sector and the other in the rear sector. The BRMUON detector gives a local trigger that is divided in independent zones and so if we tag as trigger muon, for example, the muon that has caused the *low multiplicity trigger* to fire in the rear region, we can look at the other muon in the barrel chambers and see whether a *outer chamber trigger* of the barrel exists or not. So if we calculate a ratio of this kind:

$$\epsilon = \frac{\#\text{ of events with a rear low mult trigger and a barrel outer trigger}}{\#\text{ of events with a rear low mult trigger}}$$

as a function of the polar angle and momentum of the muons we can evaluate the trigger efficiency in the barrel sector. In a symmetrical way it has been studied the rear outer trigger. In Figures 5.2 and 5.3 we can see the behaviour of the two slots in the data as a function of the momentum p of the associated muon track, that is the only interesting quantity.

5.5.2 Muon SLT

We do not explain here the tests that have been done to study the second level trigger because the muon selection is composed just by vetoes that are common to the ZEUS detector and they do not cause any bias or inefficiency.

5.5.3 Muon TLT

The GLOEXO TLT was used [124] as a cross check of the selection in the BRMUON sectors and showed that when the momentum of the muon is large

enough to pass the applied cut the dijet online filter does not loose a statistically significant number of events and the samples defined by the two trigger chains almost overlap.

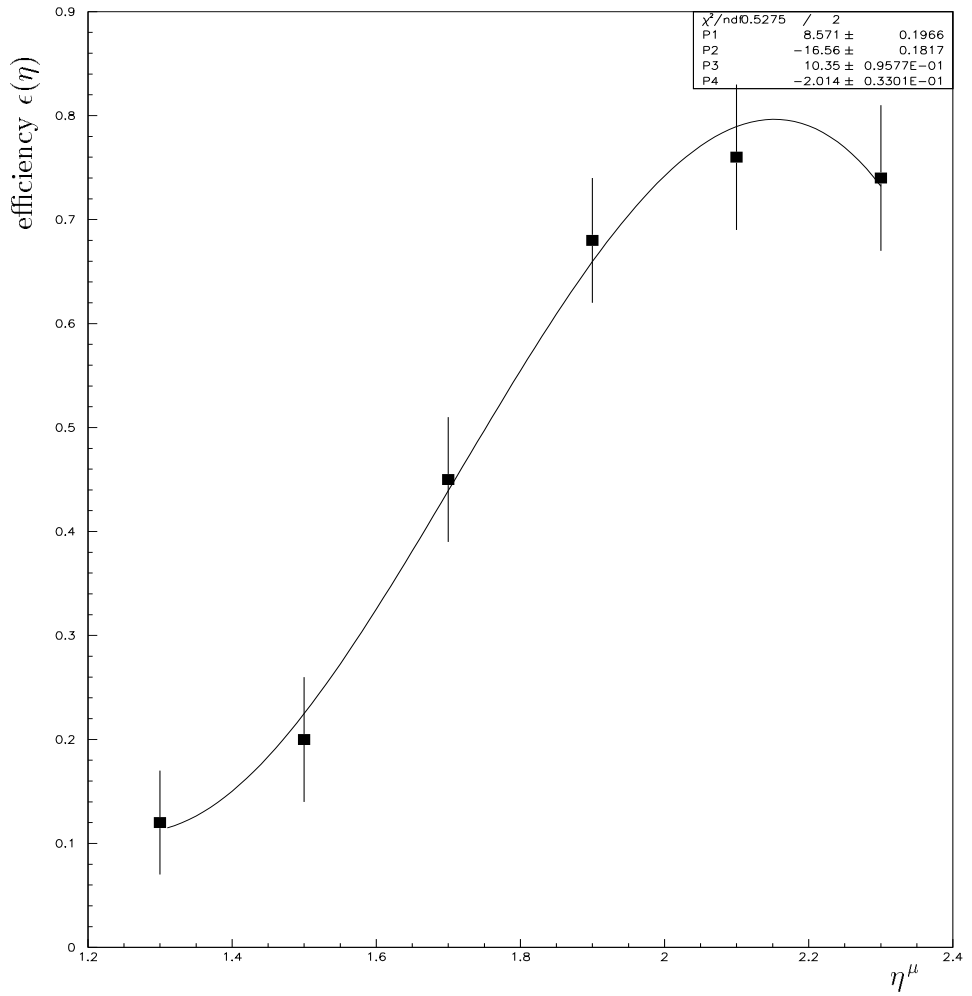

Figure 5.4: FMUON efficiency values $\epsilon(\eta)$ as a function of the pseudorapidity η^{μ} of the muon, the black squares are the measured data points, the solid line is the polynomial fit with the parameters as shown in the top right corner.

5.6 Efficiency of the Online Chain for FMUON selection

The only online efficiency we have to study for the forward sector is the hit efficiency, that basically is the efficiency of the planes that compose the FMUON

spectrometer and of the electronics of the data acquisition chain. The spectrometer is composed of three kind of planes LST/LW and DC, as it has been said in Section 1.8.1. Both the LST and DC planes have been thoroughly studied every year with the use of halo muon events, that in a small percentage are stored during the data taking periods, and their efficiencies have been known since a long time and have been implemented in the official Monte Carlo simulation of the detector. The LW planes, instead, have been object of investigation only since the year 1996 [125]. Because these efficiency values are not included in the Monte Carlo we have reweighted the events with a muon in the forward sector with a function $\epsilon(\eta^{\mu})$ (Figure 5.4) that has been obtained [126] comparing the ratio

$$R = \frac{(\text{Mpmatch tracks})}{(\text{CTD tracks})} \tag{5.4}$$

in data and Monte Carlo. This is the ratio of the number of tracks found in by the central tracking detector that are pointing in the direction of the forward detector and that have been matched by the Mpmatch algorithm, described in Section 3.4, over the total number of tracks reconstructed by the CTD.

5.7 Offline Selection

5.7.1 Jet and Photoproduction Selection

Before cuts on quantities based on calorimeter values can be made, corrections for noise and the energy scale are implemented. Within the calorimeter, a number of cells are described as being "noisy". The effect is corrected by using standard routines for each year [127]. The correction falls into distinct categories; the removal of noisy cells according to lists provided each year in [127], a cut on the relative cell imbalance[2], and the removal of isolated EMC and HAC cells with energies below 80 and 140 MeV respectively. The noise associated with the imbalance and isolation cuts arises predominantly due to sparks in the PMT's, whereas the noisy cells are mainly from electronic malfunctions.

Differences in the energy scale of the calorimeter exist between data and Monte Carlo. Studies have shown that the calibration of the CAL (BEMC, BHAC, RCAL, FEMC) is (6%, 7.5%, 2.5%, 4%) lower (FHAC is 4.5% higher) in the data than in the Monte Carlo. Consequently the energies of each cell in the CAL are scaled up by +6% (BEMC), +7.5% (BHAC), +2.5% (RCAL) and 4% (FEMC), scaled down by −4.5% (FHAC) in the data [128, 129].

After the trigger selection and calorimeter corrections, a tighter offline selection was applied with the cuts detailed below:

[2] We recall that each cell of the calorimeter is read at both sides with a photomultiplier. The imbalance is defined as the fractional difference of the two independent measures.

- $0.2 < y_{JB} < 0.8$;
- No positron as found by the electron finder SINISTRA [130] satisfying requirements on y_e and the energy, E_e;
  - $y_e < 0.7$, $E_e > 5$ GeV.
- The event must contain at least two jets as found by KTCLUS with:
  - $E_T^{\rm jet} > 5$ GeV;
  - $\eta^{\rm jet} < 2.4$.

The effect of the cut on y_{JB} is two-fold. The rejection of low values eliminates proton-beam gas background. At high y_{JB}, there is a large DIS background due to the positron entering into the sum with the result that $E - p_z \rightarrow 2E_e$. The cut on y_e using the electron finder SINISTRA is also to eliminate DIS candidates. The effect of this cut on the scattered electron can be seen as applied to a combined resolved and direct Monte Carlo sample (Figure 5.5). A sample of heavy flavour events having only loose requirements on the presence of a muon is shown. There are, however, jet cuts applied; requiring two jets with $E_T^{\rm jet} > 4$ GeV and $|\eta^{\rm jet}| < 2.5$. These cuts lead to an enhancement at high Q^2 in the "generated" sample because the scattered positron can form one of the jets. When the cut on the scattered positron is applied (dashed line), it can be seen that a large number of high Q^2 events are removed. Applying the cut on y_{JB} (dash-dotted line) further reduces the number of high Q^2 events. At a value of $Q^2 \approx 1$ GeV^2, as indicated by the dotted line at $\log_{10}(Q^2) = 0$, and above, the number of events surviving the cut is really small. This justifies the value of $Q^2 < 1$ GeV^2 as used in the cross-section estimate.

The demand on the pseudorapidity of the jets is slightly harder than that for the trigger by 0.1 units. The requirement for the transverse energy of the jets is effectively higher also because of the different jet finder used. As was mentioned in Section 5.2.3, the jets are found at the TLT with a modified version of the EUCELL cone jet finder. This has a cone radius, $R = 1$, compared to the effective cone radius for KTCLUS of $R = 0.7$ [131], see Figure 5.6 . Therefore, the jets found by KTCLUS are, on average, lower in energy than the jets found by EUCELL.[3]

5.7.2 Muon selection

We want to select events where the muon, which we reconstruct as a global trajectory through the use of the CTD and the muon detection system, is coming from the decay of a heavy quark. The beauty quark, for its large mass, will have energetic decay products and the muon coming from it will have a larger

[3] A cut of the same value is therefore harder for the jets found by KTCLUS.

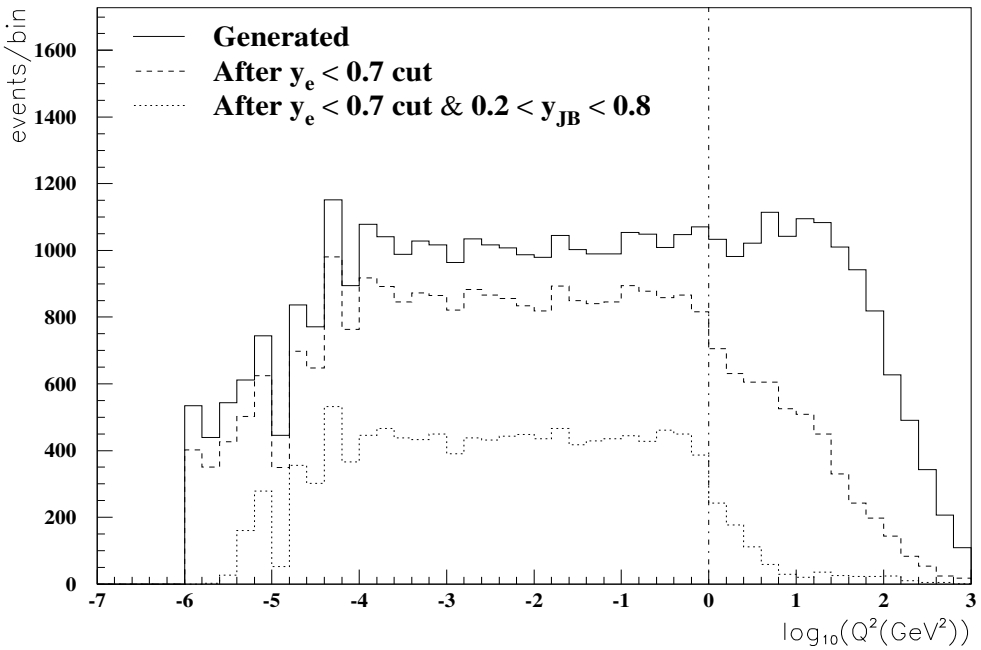

Figure 5.5: Effect of the cut to remove DIS electrons on Q^2 (Q in GeV) for the event simulated using the PYTHIA Monte Carlo.

momentum compared with the cases when it is produced by a charm or a lighter quark, see Figure 5.7. We want to use this characteristic to reject as much as possible the events where the muon is not coming from the beauty quark.

5.7.2.1 Muon selection in the FMUON region

In the forward region of the detector we have to consider the presence in the FMUON spectrometer of signals caused by the fact that the accelerated beams are really near the apparatus and spurious signals can be caused by the beam backgrounds. These effects, like photons caused by electron *bremsstrahlung* and secondary particles emitted by the proton beam are not described by the Monte Carlo and we are, therefore, not able to simulate them. These problem causes the presence in the detector of spurious hits that can be randomly associated to a FMUON-track.

To solve this kind of problems we want to restrict ourselves to those cases where the Monte Carlo is able to describe the data.

To have the values of the kinematic parameters of the muons emitted in the forward direction from the vertex and to be able to evaluate these quantities at the interaction vertex we have used a matching package Mpmatch, which we describe in somewhat more detailed way in Section 3.4. This algorithm is able to exploit the informations coming from the central tracking detectors (CTD and FTD) and from the forward muon spectrometer (FMUON) and do a position and

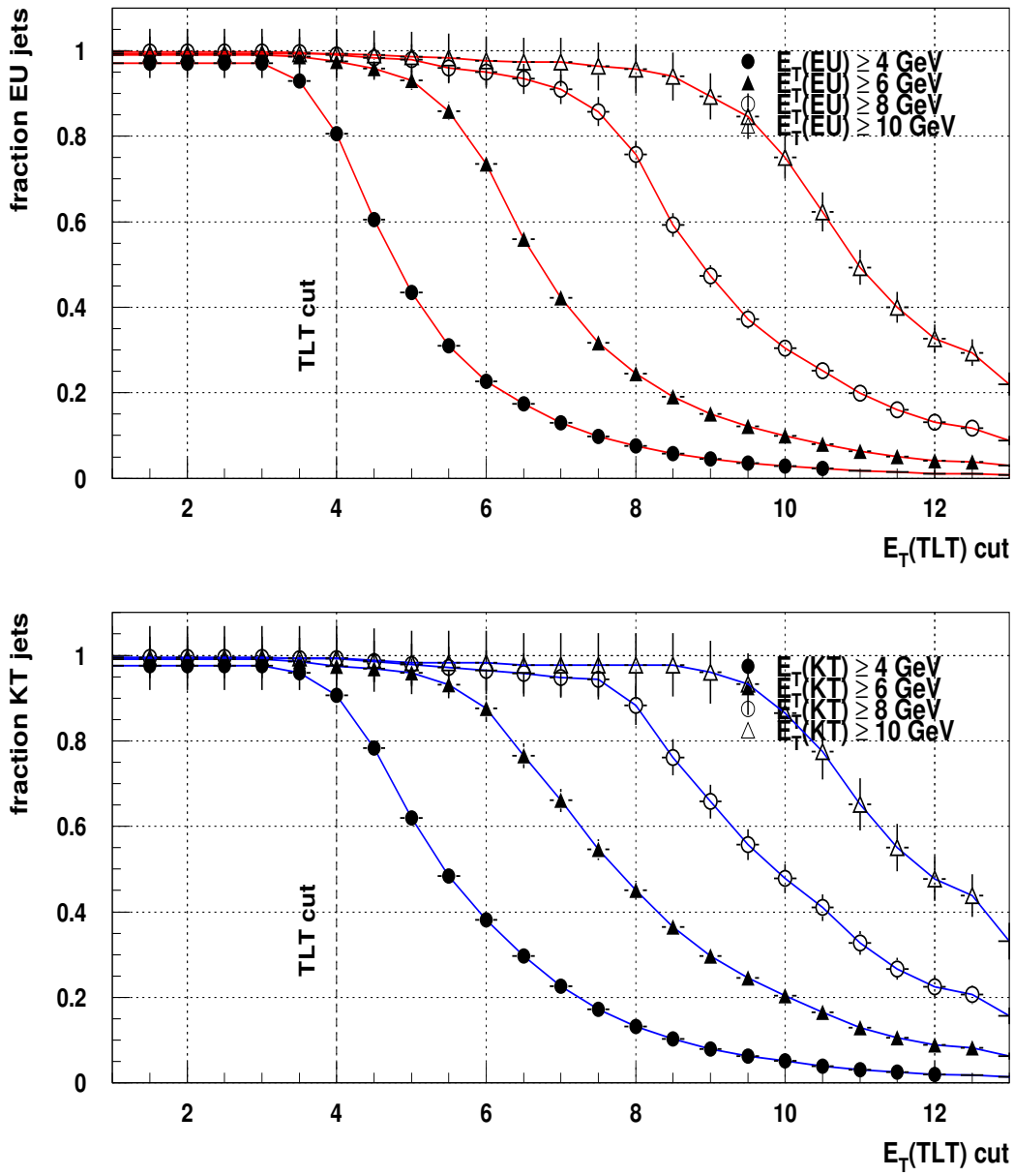

Figure 5.6: The efficiency of the Dijet TLT as a function of TLT jet E_T threshold for offline thresholds 4, 6, 8 and 10 GeV. The dashed line shows the actual TLT threshold of 4 GeV [131]. Top plot, jets reconstructed off line using EUCELL, bottom, jets reconstructed using KTCLUS.

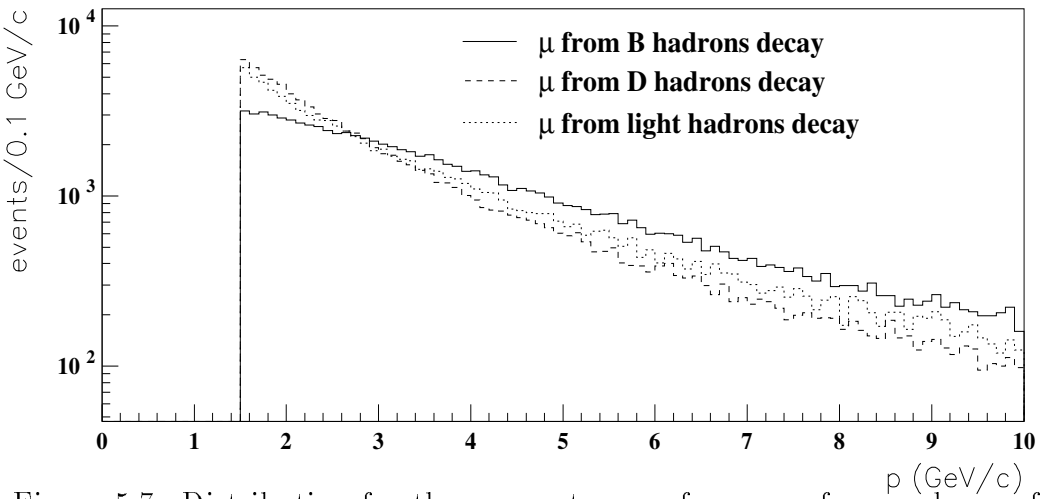

Figure 5.7: Distribution for the momentum p of a muon from a decay of a B meson (solid line), D meson (dashed line) and a light hadron (dotted line).

momentum matching of the tracks reconstructed in the central trackers [18] and the tracks measured by FMUON as a stand alone detector [115].

At first we want to check whether or not the matching package is able to improve the knowledge of the kinematic variables of the reconstructed muons. To do so we have used a sample of elastically produced J/ψ, where the vector meson decays in the muonic channel and one of the two muons goes in the direction of the FMUON detector. In this way we put ourselves in a situation where we know that the tracks in the detector are muons and we do not have to care of mis-tag. And moreover we exactly know which is the mass of the state we want to reconstruct, and it is a narrow one. As we can see Figure 5.8 the use of the matching algorithm improves the accuracy of the determination of the value of the $M_{J/\psi}$ invariant mass, that is shown as $M_{\mu\mu}$ on the abscissa axis of the plots, both for the case of the use of the CTD only reconstruction and the use of the CTD plus FMUON-stand-alone reconstruction methods. Being this the situation we can relax the usual requirement on the CTD track to be at $\eta < 1.75$[§] and have a wider kinematical range. This means we can accept a forward track up to a pseudorapidity of 2.4 and be still able not to worsen the resolution on the momentum of matched tracks.

To define a matching in the forward region we require that the Mpmatch algorithm finds a position and momentum matching with a probability greater than 0.05.

We then try to define the cuts that allow also in inelastic events to have a Monte Carlo that is able to describe the data. As in the data there are much

[§]That is, more or less, a requirement that the outer superlayer associated to a track be at least the third, that is the cut recommended by the tracking group for standard analysis within ZEUS.

more tracks with few planes associated, we require that a FMUON track has to have at least 4 planes (LST/LW/DC planes) associated with it. This cut is able to reject those tracks where the random presence of spurious hits in the chambers makes the reconstruction software of FMUON to identify a track that does not correspond to any actual particle.

When we look at some control quantities having imposed the number of planes cut, we notice that the situation is on average good but the transverse momentum spectrum of Monte Carlo is softer than the one in the data.

To improve the agreement between the simulation and the reality we require that a candidate global track has a high transverse momentum with respect to the beam axis and put a cut at $p_T \geq 1.5$ GeV/c, that is also equivalent to the presence of an hard μ. If we do so the comparison of Monte Carlo and data, Figure 5.9, is much improved and is sufficient for the purpose of our study.

After having applied the before mentioned cuts the final sample with a good forward matched muon and at least two jets contains 283 events.

5.7.2.2 Muon selection in the BRMUON region

Also in this region we require the presence of a hard muon in the event and this means a muon with a large momentum and able to reach the outer chambers in the barrel and rear sectors. This requirement is also able to discard low energy tracks coming from decay in flight of light particle or from punch through, that we will define in a more thorough way in Section 5.8.

Infact we measure the ratio of the number of events that have both the inner and outer chamber tag over the number of events that have just the inner chamber tag:

$$R = \frac{\#\text{ events with outer \& inner chambers}}{\#\text{ events with inner chambers}}. \tag{5.5}$$

We can see in Table 5.1 that, although in the case of heavy flavours the samples are reduced, in the case of light flavours, that is mostly background, the reduction is much more powerful. We will require henceforth the presence of signals in the outer chambers to define a μ-tag in the BRMUON regions.

As we can see in Appendix B the BREMAT reconstruction package has within itself a minimum cut on the momentum of the candidate muons, this is the minimum logical cut that we can impose to a particle in order that it is able to reach the inner muon chamber. We want to decide which is the minimum momentum a BREMAT matched muon has to have so that it is able to reach the outer chamber and we need to take into consideration not only the geometric acceptance of the detector[5] but also the efficiencies of the chambers and trigger themselves. To get an insight of the situation we look at the trigger efficiencies of the outer chambers, that are shown in Figures 5.2 and 5.3. From these we can see

[5]Geometrical arguments would make us decide for a momentum cut at $p = 2$ GeV/c.

Sample	R
Monte Carlo PYTHIA $b\bar{b}$	0.39
Monte Carlo PYTHIA $c\bar{c}$	0.39
Monte Carlo PYTHIA light flavour	0.15
Data	0.11

Table 5.1: Ratio of the number of events that have both the inner and outer chamber tag over the number of events that have just the inner chamber tag, for the samples described in the text. It is shown for comparison the same ratio in the case of data.

that the more correct thing to do is to put a cut at $p = 3$ GeV/c over the entire range of variation of the polar angle for the matched μ. As the pseudorapidity of the muon is concerned it is included in the $-1.75 < \eta < 1.3$ interval, that corresponds to a value of the polar angle included in the interval $30° < \theta < 160°$, to ensure a good track parameter evaluation.

There is another cut to fix: BREMAT identifies a CTD-chamber matching if the χ^2 of the matching between the tracks is less than a maximum value set at $\chi^2 = 100$. We can see in Appendix B that BREMAT is able also to carry on a momentum-matching, when the particle is able to reach the outer chambers and hence it is possible to measure its momentum with the BRMUON detector alone. We impose that the probability of such a momentum-matching[6] be larger than 0.01 (that corresponds more or less to a cut like $\chi^2 \lesssim 20$) to ensure a good match CTD-BRMUON.

We summarize, hence, the cut on the muon-candidates we have introduced at the offline level:

- momentum of track as measured by the CTD ≥ 3 GeV/c;
- pseudorapidity of the track $-1.75 \leq \eta \leq 1.3$. as measured by the CTD;
- probability of the position and momentum-matching ≥ 0.01.

In this way we have completed the list of the cuts that define a good muon candidate. At this level the sample in the BRMUON region has been reduced to 595 events.

[6] It is implicit the position matching.

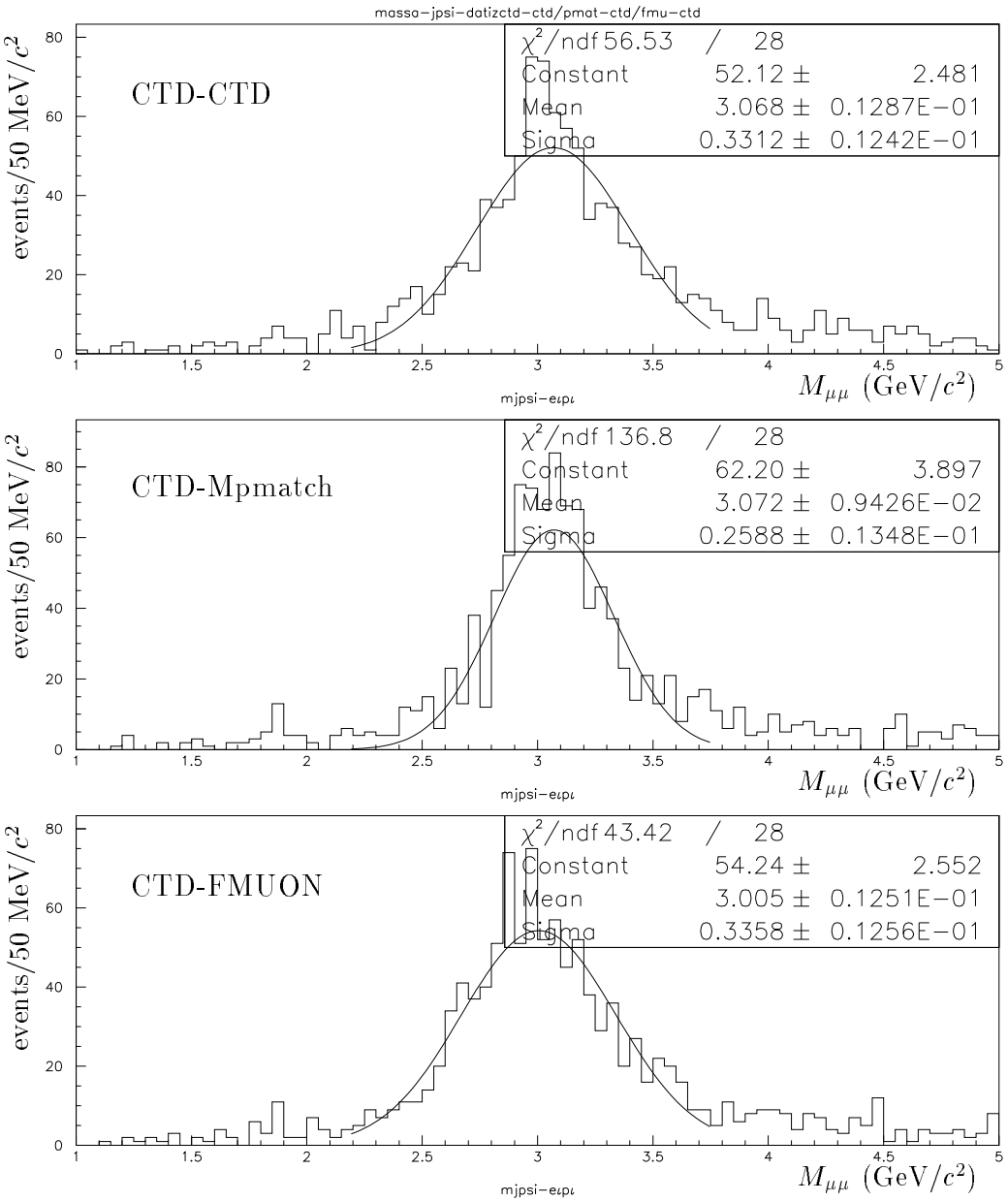

Figure 5.8: In the plots it is visible the resolution on the value of the J/ψ mass that can be reached with the use of the central tracking detector and the forward muon spectrometer: at the bottom there is the mass spectrum as it is obtained using the FMUON plus CTD detectors, in the middle the one using the informations coming from the FMUON and CTD component and using the Mpmatch algorithm, at the top the resolution of the CTD only reconstruction. It is to be noted that the use of the Mpmatch package improves the mass resolution as can be seen from the middle plot, the fit is a Gaussian one.

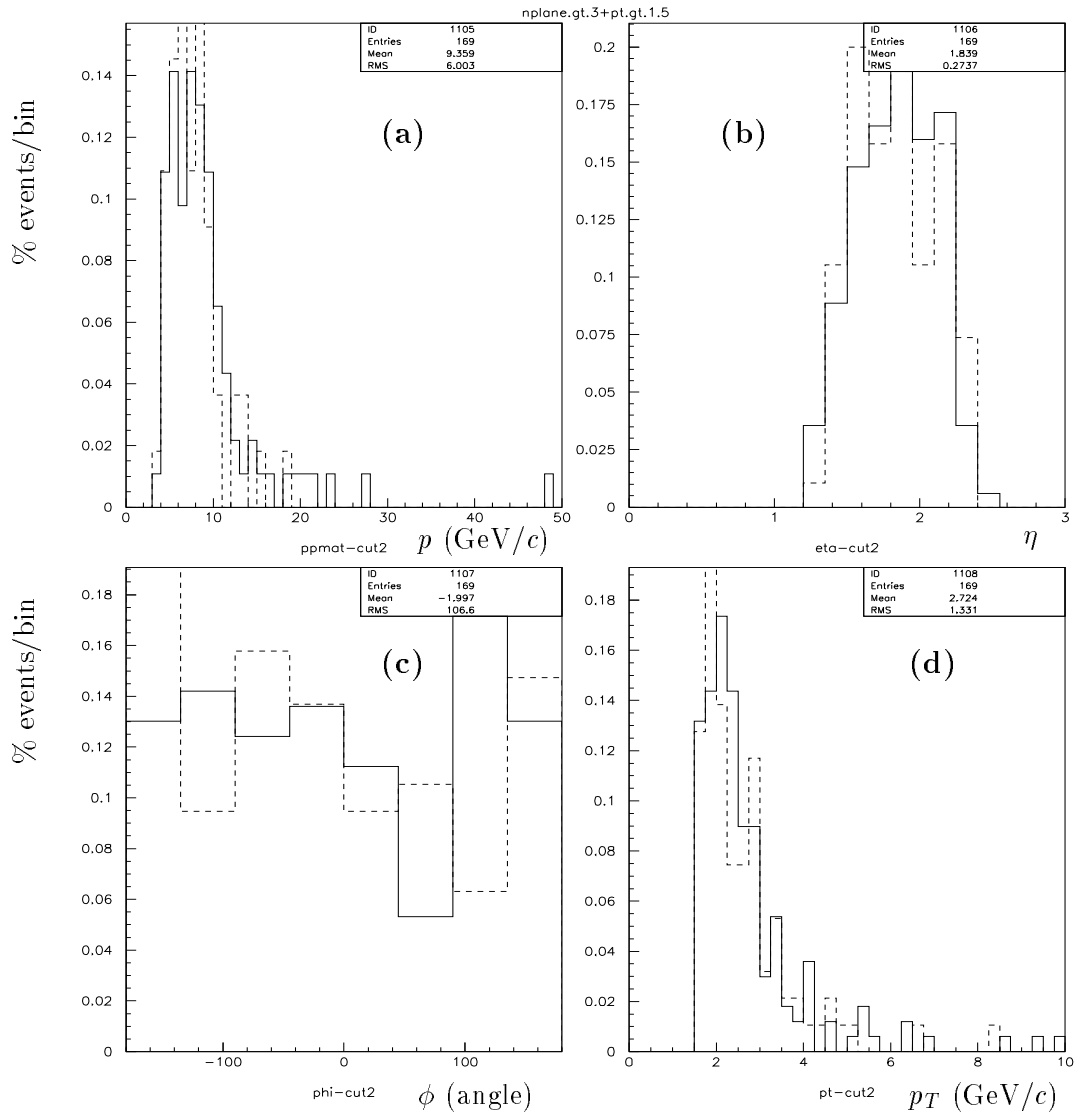

Figure 5.9: In the plots it is visible the comparison between Monte Carlo (dashed line) and data (solid line) using control variables for dijet events where a Mp-match exists. A much improved agreement can be seen. We have applied a cut requiring at least a FMUON-track with 4 or more associated planes and a transverse momentum larger than 1.5 GeV/c. (a) Momentum p of the matched track, (b) pseudorapidity η of the matched track, (c) azimuthal angle ϕ of the matched track, (d) transverse momentum to the beam axis p_T of the matched track; the histograms are normalized, so that we can compare the differences in the shapes of the distributions.

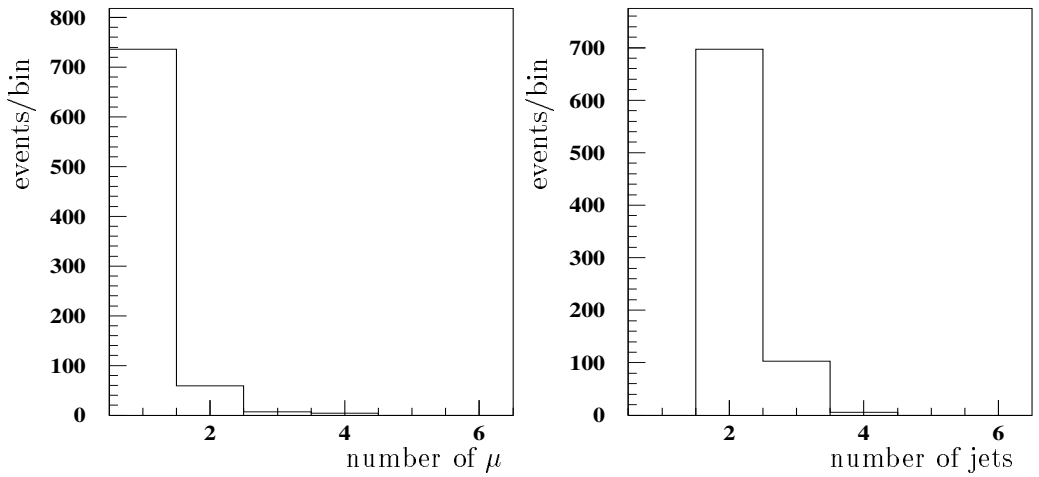

Figure 5.10: Muon (a) and jet (b) multiplicities in the data for events that satisfy all the introduced cuts.

5.7.3 Association μ-jet

After having applied all the cuts, in each event we find two or more jets reconstructed at the detector level, and one or more muons reconstructed by the BREMAT or Mpmatch packages. In Figure 5.10 we can see the muon and jet multiplicities for those events that survive our cuts. We can see that most of the events have just one selected muon. Now we focus our attention on this accepted muon alone and on the two jets. We have to establish to which of the two jets the muon is associated; to this purpose we have to find a variable that in some way defines the angular distance of the muon from the jet. A quantity that can be useful in this sense is the angular separation in the plane (η, ϕ):

$$\delta r = \sqrt{(\eta^{\rm jet} - \eta^{\mu})^2 + (\phi^{\rm jet} - \phi^{\mu})^2}. \tag{5.6}$$

We calculate therefore the distance δr among the muon and the two jets, and we choose the jet that is nearer to the muon according to the values of the distance δr. Moreover, with the aim to avoid contaminations from events with a muon that is rather far from the nearest jet, and hence it does not come from the decay of the beauty quark, or from events where a particle is misidentified as a muon, we impose a condition on the maximum angular distance between the muon and the jet. It has to hold:

$$\delta r < 1.5. \tag{5.7}$$

We can see in Figure 5.11 that the angular distance between a decayed beauty particle and a μ that comes from it is almost always less than 1.5, while the directions of the muon and of the *nearest jet* are less correlated.

When two or more muons are present in the event and they satisfy all the described cuts, we calculate for each one the angular separation δr with respect to both the jets and we select the μ-jet pair that has the minimum value of δr.

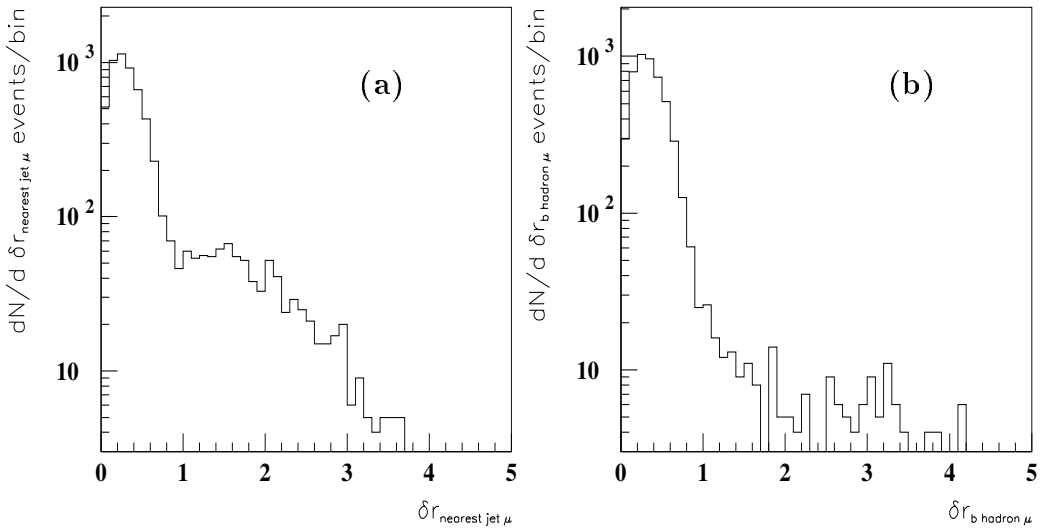

Figure 5.11: Distribution of the angular distance between a muon and its nearest jet in a beauty production event (a). Distribution of the angular distance between a decayed beauty hadron and its muon (b).

When more than two jets are present in the event we try to associate all the jets with all the muons.

In the case that two muons have distances less than the δr cut to a jet, only the one with smaller δr is considered.

After we have decided which muon is nearest to which jet, we are able to define and calculate the transverse momentum of the muon $p^{\mu}_{T\mathrm{rel}}$ with respect to the jet axis.

The list of cuts is complete and we have our final samples that are composed by the events summarized in Table 5.2.

region	# of events
BRMUON (BREMAT)	513
FMUON (Mpmatch)	253

Table 5.2: Number of events that compose the final sample, for the forward (FMUON) and barrel-real (BRMUON) regions.

5.8 Background analysis

One of the problems we have to face when developing an analysis like this one is the determination and elimination, as much as possible, of the background sources.

Let us see, hence, where the background events come from mainly. We have said that in each event we require the presence of at least two jets that satisfy the condition listed in Section 5.7.1. Beside this, we want a track in the muon detectors to be found in every event. Such track may come from an interaction we are interested in, however it is possible for the matching packages to reconstruct and identify as a muon a particle that actually is not a μ. As an example, light hadrons that are able to reach the outer detectors could cause a signal and therefore erroneously be identified as muons: we talk in this case of *fake muon* or *mistag*.

Another important contribution to the background comes from those events in which a pair of charm quarks is produced and afterward decays semi-leptonically in the μ-channel. The pair of heavy quarks yields two jets and the muon can be detected in the chambers, as in the case of the b quark (see Table 5.1): we will therefore have to use the large difference in mass between the two quarks to get a method to distinguish events with a c quark and those with a b quark.

5.8.1 Determination and subtraction of the background from light quark events

The background from light quarks is composed by events where a minimum of two jets is found and with a signal in the muon-chamber that can be due to various mechanisms and processes:

- decay in flight like: $\pi^{\pm} \rightarrow \mu^{\pm}\nu$, or $K^{\pm} \rightarrow \mu^{\pm}\nu$, with a detection of the muon coming from the decay;
- *punch-through*, that is the interaction of hadrons in the calorimeter, that give way to secondary particles that, on their turn, can hit the muon detectors;
- *sail-through*, that is the passage of an hadron through the calorimeter and its subsequent identification by the μ chambers.

The probability for these processes to give signals in the outer detectors is really low compared to the one for true muons to be detected; nonetheless we have to take into account that the cross section of inclusive production of pions and kaons is much higher than the one of the processes we are interested in, and therefore the above described phenomena actually represent the most important contributions to the background.

To quantify these effects a large sample of Monte Carlo events has been generated ($\mathcal{O}(10M\text{events})$) like we have described in Chapter 4. The analysis program has been run over the whole sample to see which are the characteristics of the background events that get in the final sample. To quantify the fraction of events in the final sample that are due to light flavour production we have followed the same procedure that we have used to determine the charm induced background.

5.8.2 Determination of the background coming from charm events

The dynamics of the production of charm and its subsequent semi-leptonic decay are totally analogous to those of the beauty. The only distinction is the large mass difference of the produced quarks, and the consequences of this difference will give us a handle to distinguish the two categories of events.

As the beauty quark is heavier, the kinematics of the particles that come from its decay is different from the kinematics of those from charmed particles. In particular, we expect the transverse momentum relative to the jet axis[7] of particles from hadrons with beauty to be on the average larger than in the cases of decay of the charmed particles and light quarks. This is true also for the muon that is one of the products of the fragmentation of the decaying particle.

In Figures 5.12 and 5.13 we can see the $p_T^{\rm rel}$ distributions, at the detector level, that we can find after having applied all the cuts to the three Monte Carlo samples for the barrel-rear and forward sectors respectively. As we will see in the following pages, we will be able to determine the relative composition in light quarks, charm e beauty of our data samples with a fit of the $p_T^{\rm rel}$ distribution of the data themselves with the analogous distributions for the three different Monte Carlo sources.

5.9 Comparison of Data and Monte Carlo

Before converting our data to a cross-section, we compare event properties and look at resolutions in the Monte Carlo.

Most of the considerations we can draw holds for both the Barrel and Rear muon sample and for the Forward muon sample. The only case in which we have to distinguish between the two samples is for what it concerns the tracking resolution.

We first consider the resolution in pseudorapidity and transverse momentum of tracks which are our candidate muons. The resolution distributions are shown in Figure 5.14 for all tracks associated by the BREMAT package. Both the distributions in pseudorapidity and transverse momentum show no average shift and both have good resolutions. Of particular interest is the resolution of the transverse momentum which is,

$$\frac{\sigma(p_T)}{p_T} = 0.028.$$

This represents an upper limit as we have assumed $p_T = 1.2$ GeV/c, which is the lower cut-off value.

[7] In Figure 3.1 it is shown the geometrical meaning of the $p_T^{\rm rel}$ variable.

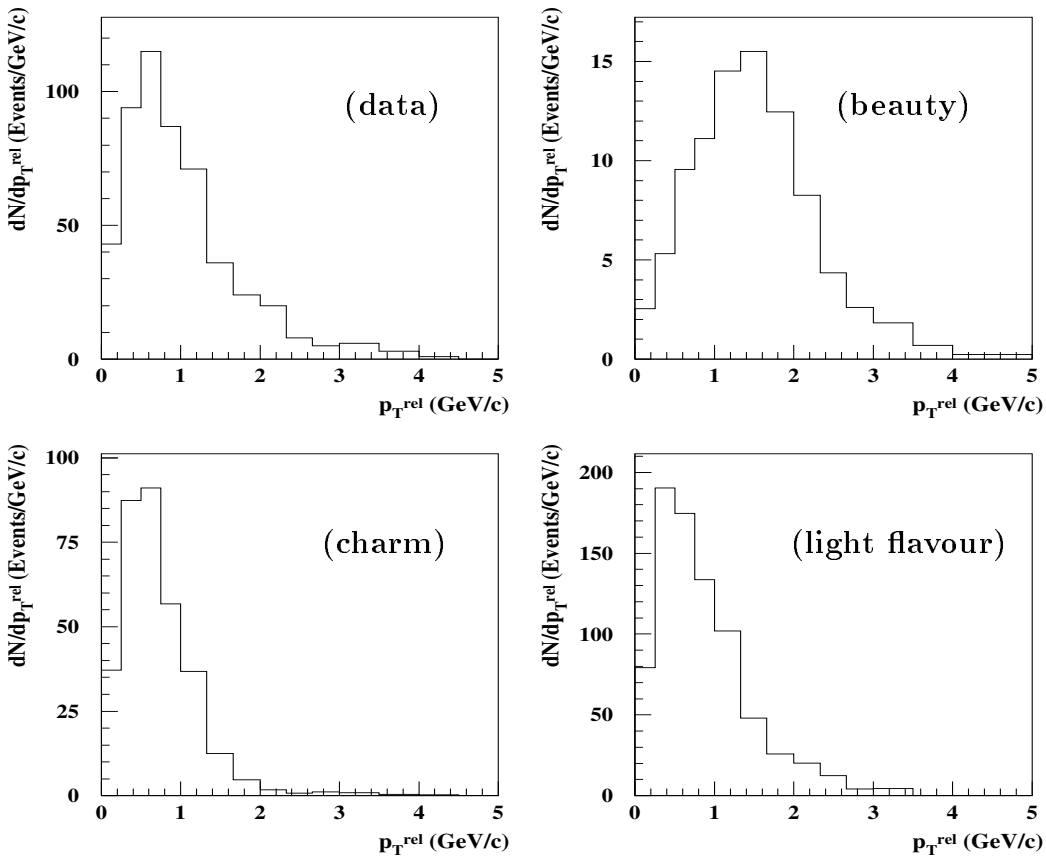

Figure 5.12: $p_T^{\rm rel}$ distributions in the data, beauty, charm and light flavour Monte Carlo, for the sectors covered by the BRMUON detector. We can notice how, while the distributions for charm and light flavours are rather similar, the one of the beauty is characterized by the presence of much more events having large values of $p_T^{\rm rel}$.

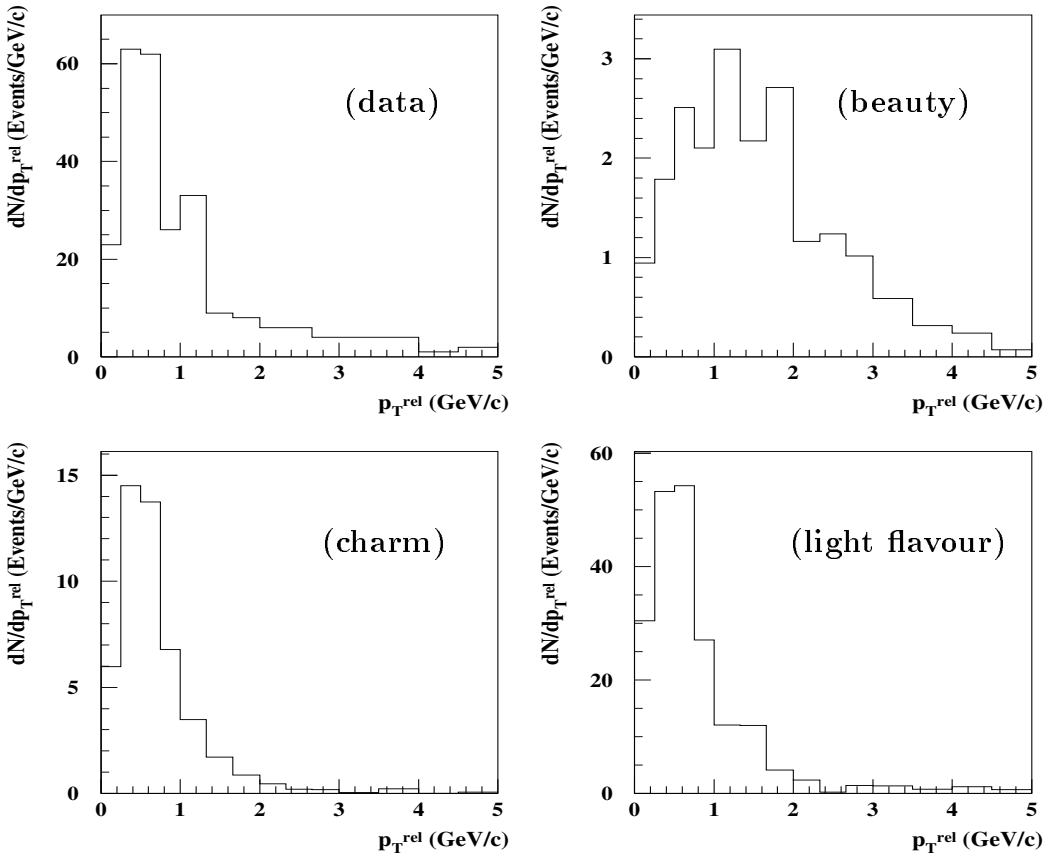

Figure 5.13: $p_T^{\rm rel}$ distributions in the data, beauty, charm and light flavour Monte Carlo, for the sectors covered by the FMUON spectrometer. We can notice how, while the distributions for charm and light flavours are rather similar, the one of the beauty is characterized by the presence of much more events having large values of $p_T^{\rm rel}$.

If we now take into consideration the sample where a good Mpmatch is found we see that the transverse momentum resolution is changed and it is about 12%. In this case the width of the distribution, see Figure 5.15, is much larger, but the mean value is well peaked at zero value, so we have decided not to correct this quantity. The resolution in pseudorapidity of the matched muon is almost as good as in the barrel and rear regions. The width of the distribution is twice as large as in the previous case, $\sigma_{\rm Mpmatch} = 0.78\ 10^{-2}$ compared to $\sigma_{\rm BREMAT} = 0.41\ 10^{-2}$, but here the absolute values are larger, $(1.4 \div 2.4)$ instead of $(-1.75 \div 1.3)$, so the percentual spread is the same. The mean value of the difference between the measured and true value is not peaked at zero, but, if we consider the values of the position of the maximum of the distribution 0.006 or the mean value obtained through the fit (that is shown in Figure 5.15 (Left)) 0.012, we can notice that the average displacement is between the 0.4% and the 0.7% of the measured value,

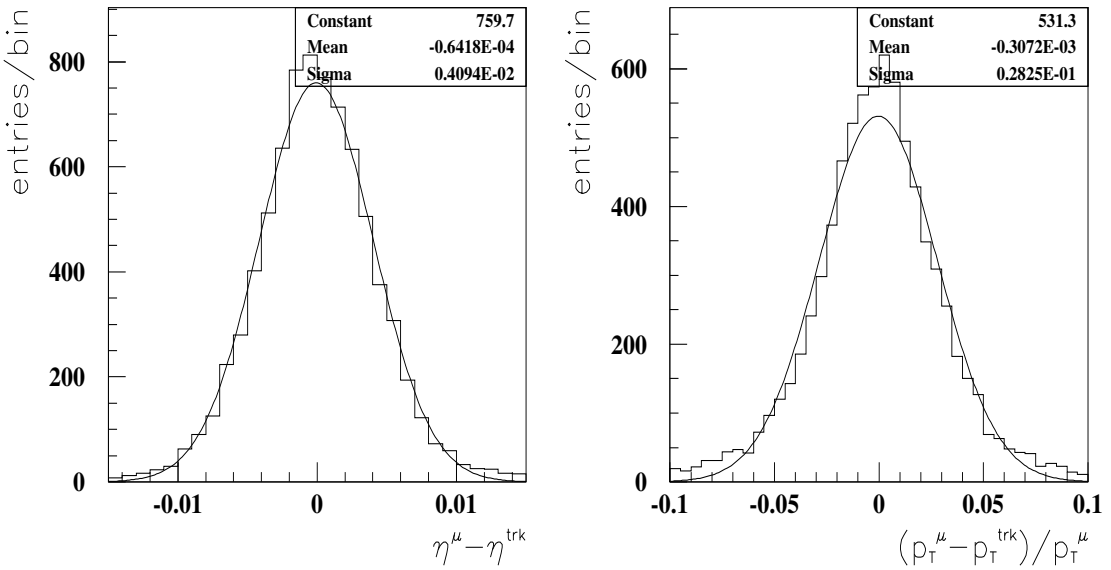

Figure 5.14: Pseudorapidity (Left) and transverse momentum (Right) resolutions of the tracks from semi-leptonic decays to muons in the barrel and rear sector of the detector tagged by the BREMAT package.

and we have, therefore, decided not to correct for this tiny effect[8].

The jet resolutions (Figure 5.16) show that the jets we are measuring are reasonable jets. They exhibit no mean shift in pseudorapidity and have a resolution of 0.1 unit in η. The transverse momentum of the jets is shifted by 35% with respect to the true jets, due to energy loss in the dead material and the presence in the jet of a particle, the muon, that does not deposit all its energy in the calorimeter, with a resolution of 20%. Due to this energy shift, we correct our jets before proceeding further to a evaluation of the cross-section. We correct our jet transverse energies and y_{JB} using the methods detailed in Chapter 4. Again we then have to redefine our cuts for jet transverse energy and y_{JB} such that,

$$E_T^{COR}(jet1, jet2) > 7.0, 6.0 \text{ GeV},$$

$$0.2 < y_{JB}^{\text{corr}} < 0.8.$$

Finally, we can compare the resolutions of our main variables, x_γ^{obs} and p_T^{rel}. These are shown in Figure 5.17. We see that considering x_γ^{obs} there is no shift in the absolute value and the fit gives a resolution of ~ 0.09. This resolution is commensurate with the bin width and previous jet results [79]. For p_T^{rel}, the shift is less than one third of a standard deviation and the resolution is of the 40%: the bin width was chosen accordingly.

We now compare data and Monte Carlo predictions for some important quantities in the analysis. In all the presented plots the Monte Carlo histograms have

[8] We are investigating the causes of this.

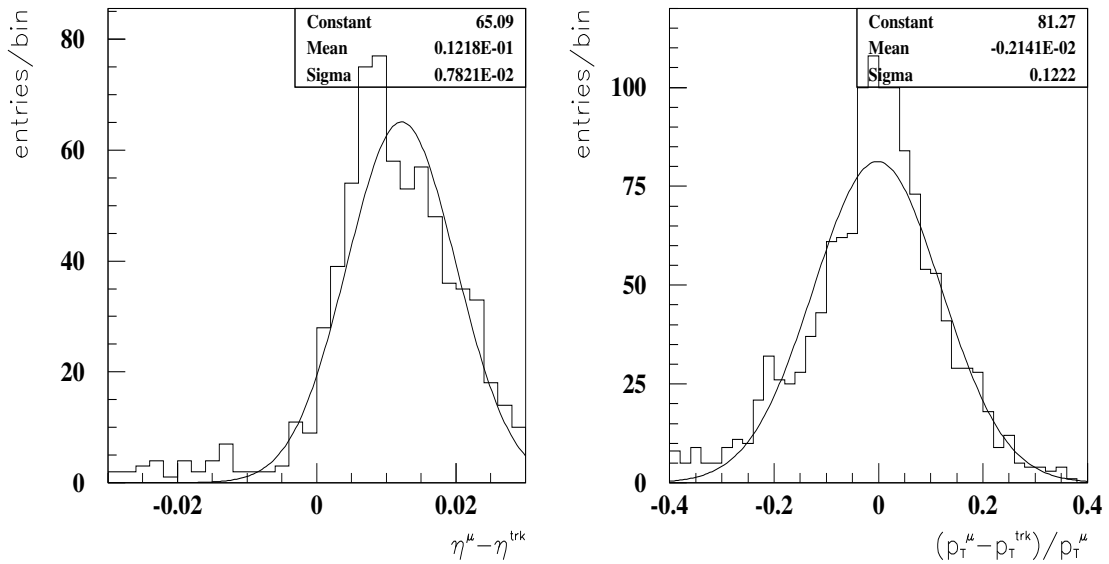

Figure 5.15: Pseudorapidity (Left) and transverse momentum (Right) resolutions of the tracks from semi-leptonic decays to muons in the forward sector of the detector tagged by the Mpmatch package.

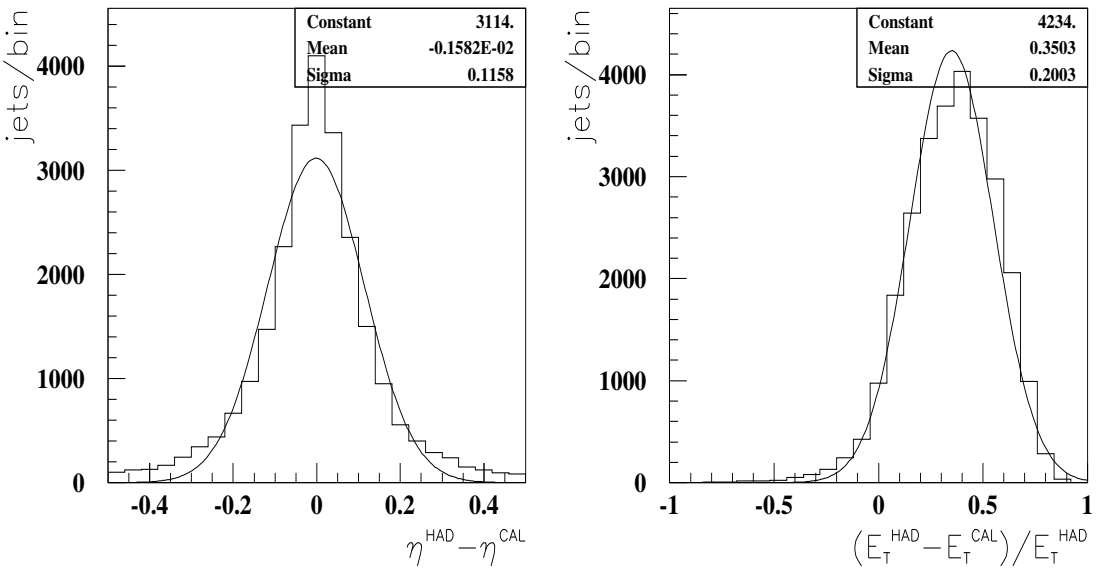

Figure 5.16: Pseudorapidity (Left) and transverse energy (Right) resolutions of the two highest E_T jets in events containing a semi-leptonic decay to a muons.

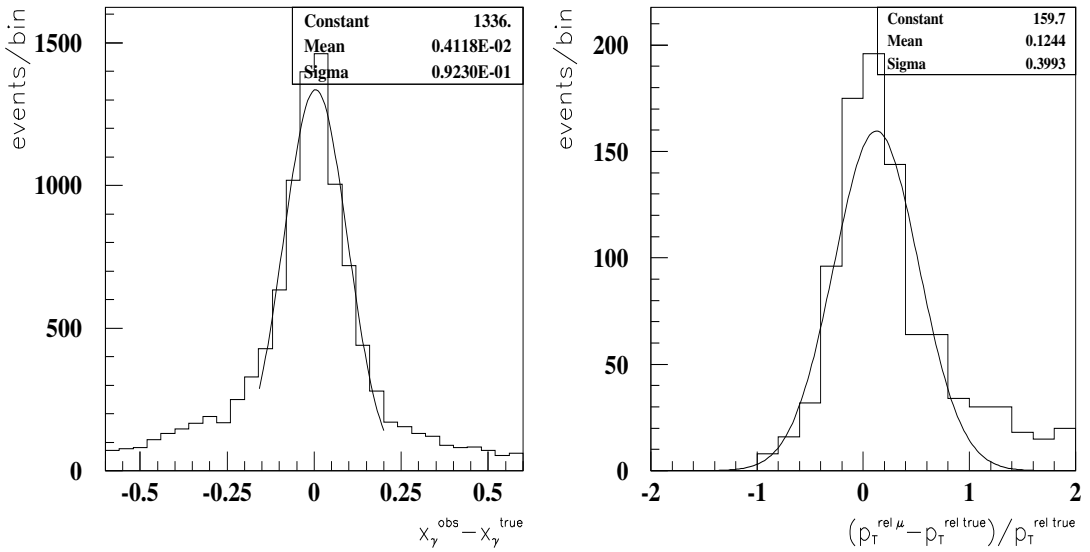

Figure 5.17: Resolutions of $x_\gamma^{\rm obs}$ and $p_T^{\rm rel}$ of events containing a muon in the final state.

been obtained as sums of b and c + light quarks PYTHIA samples weighted according to the percentage of beauty that has been measured with a fit of the distribution of the variable $p_T^{\rm rel}$ as it is described in the following Chapter.

In the figures of pages 122 and 123, we compare a number of jet, event and track properties between data and Monte Carlo, where the Monte Carlo is area normalized to the data so no conclusion should be drawn except for differences in the shape of the distributions. Now we can proceed to consider one by one each of the plots commenting them shortly.

- *Muon:*
  In Figures 5.18b and 5.18d (Figures 5.20b and 5.20d) it is plotted the comparison data-Monte Carlo for the transverse momentum and pseudorapidity of the muon. As can be seen the agreement is good for the p_T^μ, not so well for the η^μ. It should be noticed that the latter variable is sensitive to the gluon density used in the Monte Carlo; a tuning of this gluon density has not been attempted.

- *Jets:*
  We quote the comparison data-Monte Carlo for the distributions regarding the *selected* jet, the one we use to calculate the $p_T^{\rm rel}$. The quantities to which we refer are the transverse energy $E_T^{\rm jet}$ (the one measured at calorimeter level and then corrected) and the pseudorapidity $\eta^{\rm jet}$, see Figures 5.18a, 5.18c (Figures 5.20a and 5.20c). The general agreement is good. We notice that the chosen jet is bounded in a narrower angular zone with respect to jets in general: we can see that no jet is chosen with large pseudorapidity in the case of the sample in the barrel and rear regions, this is a consequence of

the fact that the muon can be detected only in the central and rear regions and that we have put a cut on the maximum angular distance we accept between the muon and the jet, Equations (5.6) and (5.7). A similar case happens in the forward sector, in this case there are few events having the pseudorapidity of the associated jet at small values, in most of the cases the value of $\eta^{\rm jet}$ is larger than $1.2 \div 1.4$.

- *Matching muon-jet:*
  The matching distance $\delta r = \sqrt{\delta\eta^2 + \delta\phi^2}$ is reported in Figure 5.19b (Figure 5.21b). We can notice the good agreement.

- *General quantities:*
  We show in Figure 5.21a (Figure 5.18a) the quantity y corrected as seen in Section 4.4. The maximum and minimum values 0.2 and 0.8 correspond to the cuts we have applied.

We will see in Figures 6.1b and 6.2b the comparison for the variable $x_\gamma^{\rm obs}$, that is calculated with Equation (2.31), and in the next Chapter we will comment on the shapes and peculiarities of the distributions.

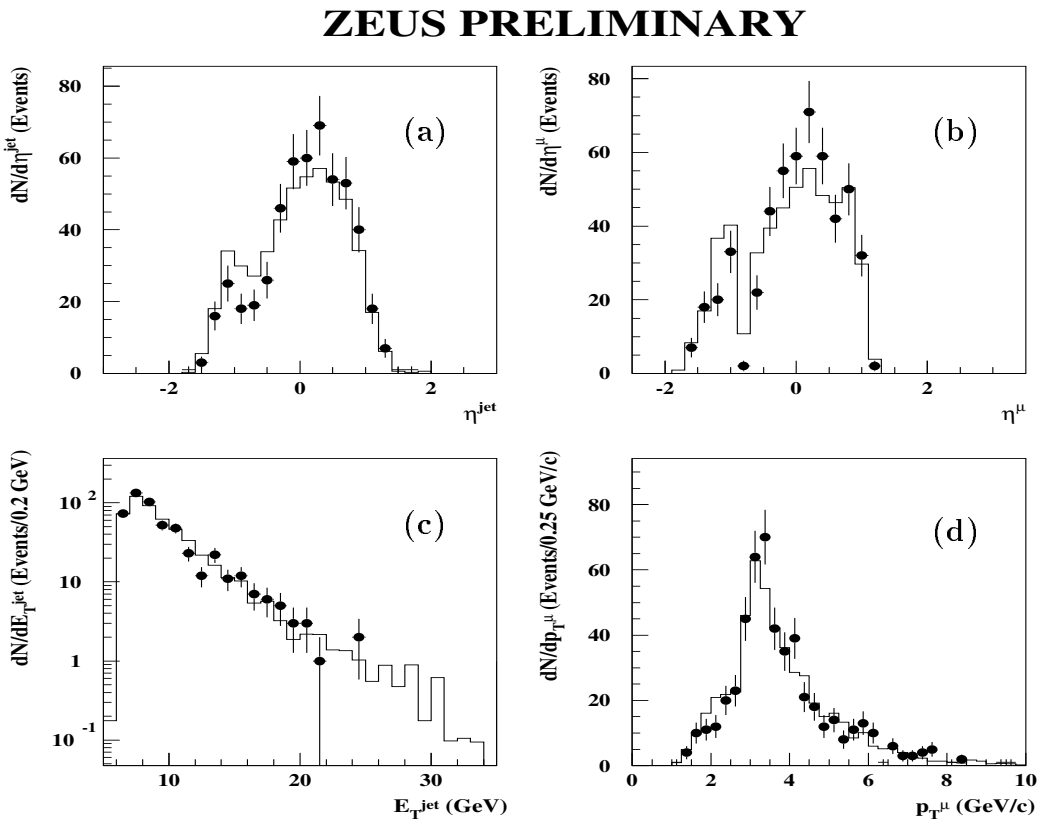

Figure 5.18: Data (dots) and MC (solid line) for the samples of events selected in the BRMUON regions. The MC is a mixture of beauty, charm and light quark contributions according to the percentage given by the fits. The pseudorapidities of the associated jets are shown in (a), the pseudorapidities of the associated μ in (b), the transverse energies of the associated jets in (c) and the transverse momenta of the associated μ (d).

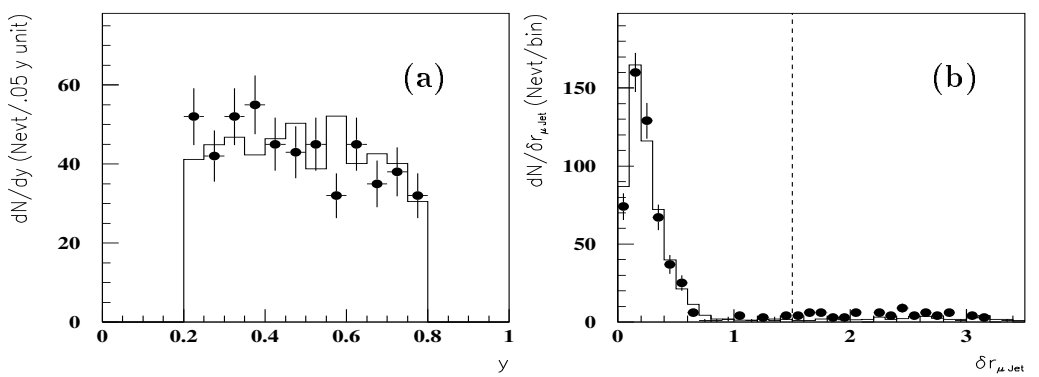

Figure 5.19: Data (dots) and MC (solid line) for the samples of events selected in the BRMUON regions. The MC is a mixture of beauty, charm and light quark contributions according to the percentage given by the fits. The quantity y ($y_{JB}^{\rm corr}$) of the event (left) and the angular distance between the associated muon and jet (right) are drawn, for the latter the dots and line show the distributions of Data and Monte Carlo before the $\delta r < 1.5$ cut is applied.

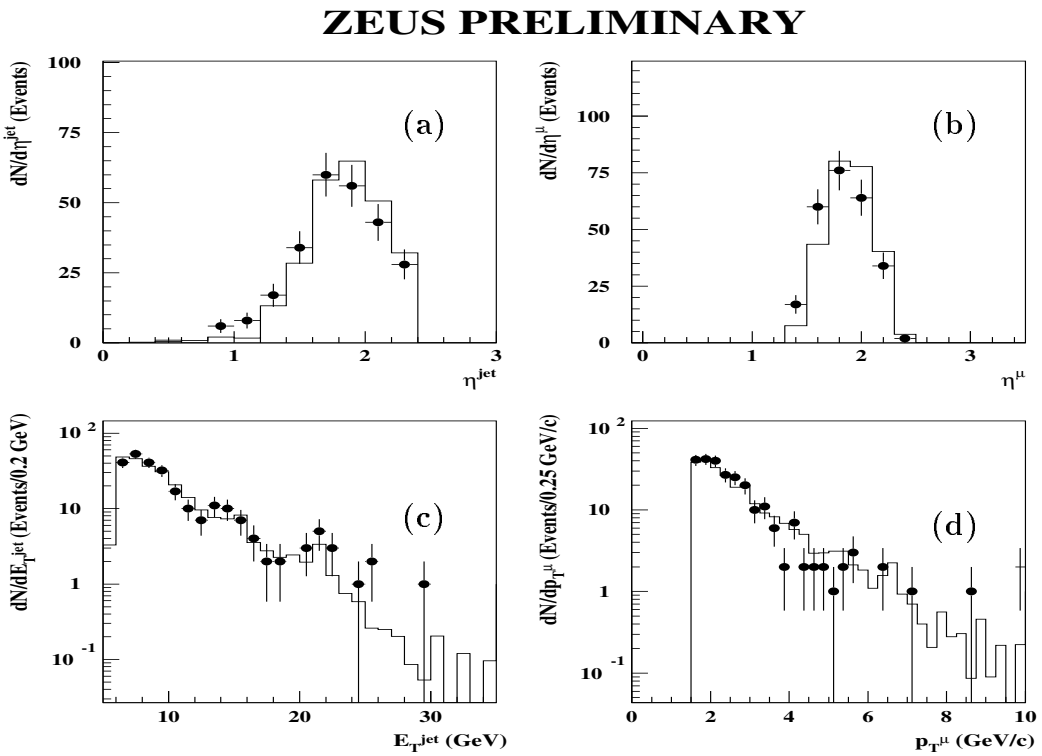

Figure 5.20: Data (dots) and MC (solid line) for the samples of events selected in the FMUON regions. The MC is a mixture of beauty, charm and light quark contributions according to the percentage given by the fits. The pseudorapidities of the associated jets are shown in (a), the pseudorapidities of the associated μ in (b), the transverse energies of the associated jets in (c) and the transverse momenta of the associated μ (d).

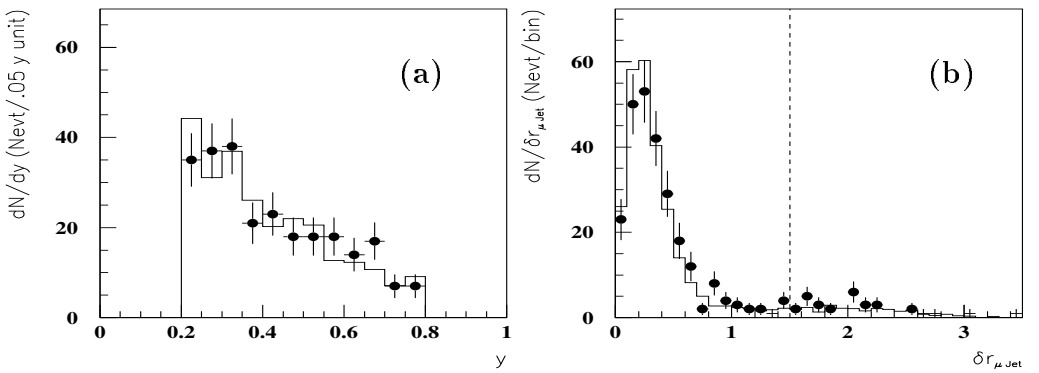

Figure 5.21: Data (dots) and MC (solid line) for the samples of events selected in the FMUON region. The MC is a mixture of beauty, charm and light quark contributions according to the percentage given by the fits. The quantity y ($y_{JB}^{\rm corr}$) of the event (left) and the angular distance between the associated muon and jet (right) are drawn, for the latter the dots and line show the distributions of Data and Monte Carlo before the $\delta r < 1.5$ cut is applied.

Chapter 6

Results

6.1 The final sample

To summarize the discussion done in the previous chapter, the final sample selects events from the reaction

$$e^+p \rightarrow e^+\mu^\pm + \text{dijets} + X,$$

with the following cuts

$$\begin{gathered} 0.2 < y < 0.8 \\ Q^2 < 1 \text{ GeV}^2 \\ E_T^{jet1,jet2} > 7,6 \text{ GeV} \\ \eta^{\text{jet}} < 2.4 \\ p_T(\mu^\pm) > 1.5 \text{ GeV}/c \qquad p(\mu^\pm) > 3.0 \text{ GeV}/c \\ 1.4 < \eta(\mu^\pm) < 2.4 \qquad -1.75 < \eta(\mu^\pm) < 1.3. \end{gathered} \tag{6.1}$$

6.2 p_T^{rel} Fit and Determination of the Beauty Fraction

The fraction of events with beauty in the final sample has been obtained fitting the data with the three contributions already discussed: light flavours, charm and beauty.

Now we will explain the procedure we have followed to obtain the value of the percentage of beauty quark contained in the sample.

To this purpose the p_T^{rel} distribution of the data has been fitted with the function

$$\mathcal{N}_i = \frac{p_b \cdot \mathcal{N}_i^{\text{beauty}} + p_c \cdot \mathcal{N}_i^{\text{charm}} + p_l \cdot \mathcal{N}_i^{\text{ light}}}{p_b + p_c + p_l} \tag{6.2}$$

where $\mathcal{N}_i^{\rm beauty}$, $\mathcal{N}_i^{\rm charm}$ and $\mathcal{N}_i^{\rm light}$ are the contents of the bin i of the three Monte Carlo histograms of beauty, charm and light flavour, and p_b, p_c and p_l some weights that can be directly interpreted as percentages if the sum of these three quantities is equal to one. The fitting procedure will allow us to determine the values of p_b, p_c and p_l that approximate the distribution of data in the best possible way.

To perform the fit we have built a χ^2 function, through a FORTRAN program, in the following way:

$$\chi^2 = \frac{\sum_i \frac{(\mathcal{N}_i^{\rm data} - \mathcal{N}_i)^2}{\sigma_i^2}}{d.o.f.}, \tag{6.3}$$

where $\mathcal{N}_i$ is given by the Equation (6.2), $\mathcal{N}_i^{\rm data}$ is the content of the bin i of the distribution of data and σ_i is the square root of the content of the bin i if it is greater than 5 other way it is given by the Poisson statistics. The free parameters of the program are the three values of p_b, p_c and p_l, that are bound to have sum equal to unity. The algorithm varies the values of these parameters to look for the values of the percentages of beauty, charm and light quarks that give the minimum χ^2 fit. It loops over all the possible percentage of b, c and light flavours and for each triplet calculates the value of the χ^2 given by the Equation (6.3).

The problem we have faced in trying to understand and interpreting the results from the fit is that if we compare the plots of the $p_T^{\rm rel}$ distribution of the charm and light flavours component, we are not able to catch any difference large enough to distinguish between the two through a fit, while the $p_T^{\rm rel}$ distribution of beauty differs drastically from those of charm and light quarks. We have therefore decided to make use of two instead of three Monte Carlo samples as inputs to the fit and eventually to add this to the systematics of the measurement; the first sample is the b sample as it is, the second is a mixture of charm and light flavours mixed together according to their respective cross sections, as given by the generator. Once we have obtained these two input distributions we have proceeded to perform the fit again and used the result as the central value of the percentages.

$$\begin{aligned} \text{Percentage of beauty} \quad p_b \quad \text{in the BRMUON sample} &= 28.0 \pm 5.0 \ \% \\ \text{Percentage of beauty} \quad p_b \quad \text{in the FMUON sample} &= 22.0 \pm 7.0 \ \% \end{aligned} \tag{6.4}$$

In Figures 6.1a and 6.2a are shown the $p_T^{\rm rel}$ distributions of data (dots), beauty (dotted line) and the mixture charm plus light flavours (dashed line) and finally the sum of the components of beauty and charm plus light flavours (solid line). The errors shown are statistical only. We notice that the solid line, the result of the fit, describes the distribution of the data in both cases. The values of the minimum χ^2 obtained with the two samples are:

$$\chi^2 = 4.7/13 \quad \text{BRMUON}$$

$$\chi^2 = 20.3/13 \quad \text{FMUON}$$

6.2.1 Systematic errors to the p_T^{rel} fit

Now we will consider the sources of systematic errors that give a non negligible contribution to the measurement of the beauty percentage of our samples through the above described fit. We will enumerate and describe the other error sources that affect only the cross section determination afterwards, see Section 6.5.

We performed three alternative fitting procedures:

- fit with beauty, charm, light flavours separately;
- fit with only beauty and light flavours;
- fit with only beauty and charm.

The variation of the value of p_b obtained in the three cases is shown in Table 6.1. We can see that the differences are small, all below the 9% of the central value in both the regions taken in consideration.

BRMUON sample	
fit with beauty, charm, light flavours separately	< 0.1
fit with only beauty and light flavours	-1.7
fit with only beauty and charm	$+1.7$
FMUON sample	
fit with beauty, charm, light flavours separately	< 0.1
fit with only beauty and light flavours	-1.0
fit with only beauty and charm	$+2.0$

Table 6.1: Systematic errors on the determination of the percentage of beauty events p_b in the final samples as obtained by changing the composition of the Monte Carlo data. The values that are shown are the deviation from the central value.

We have then varied the number of bins and their width contributing to the fit. First we have re-binned the distributions to have equally spaced intervals of 0.25 GeV/c and redone the fit, this procedure has the disadvantage that in this way there are some bins containing less than 10 events each.

Then we eliminate the last point, that has the disadvantage of lower statistics, or the first one or two bins of the spectra, that are mostly populated by events with light parton produced jets, from the fit.

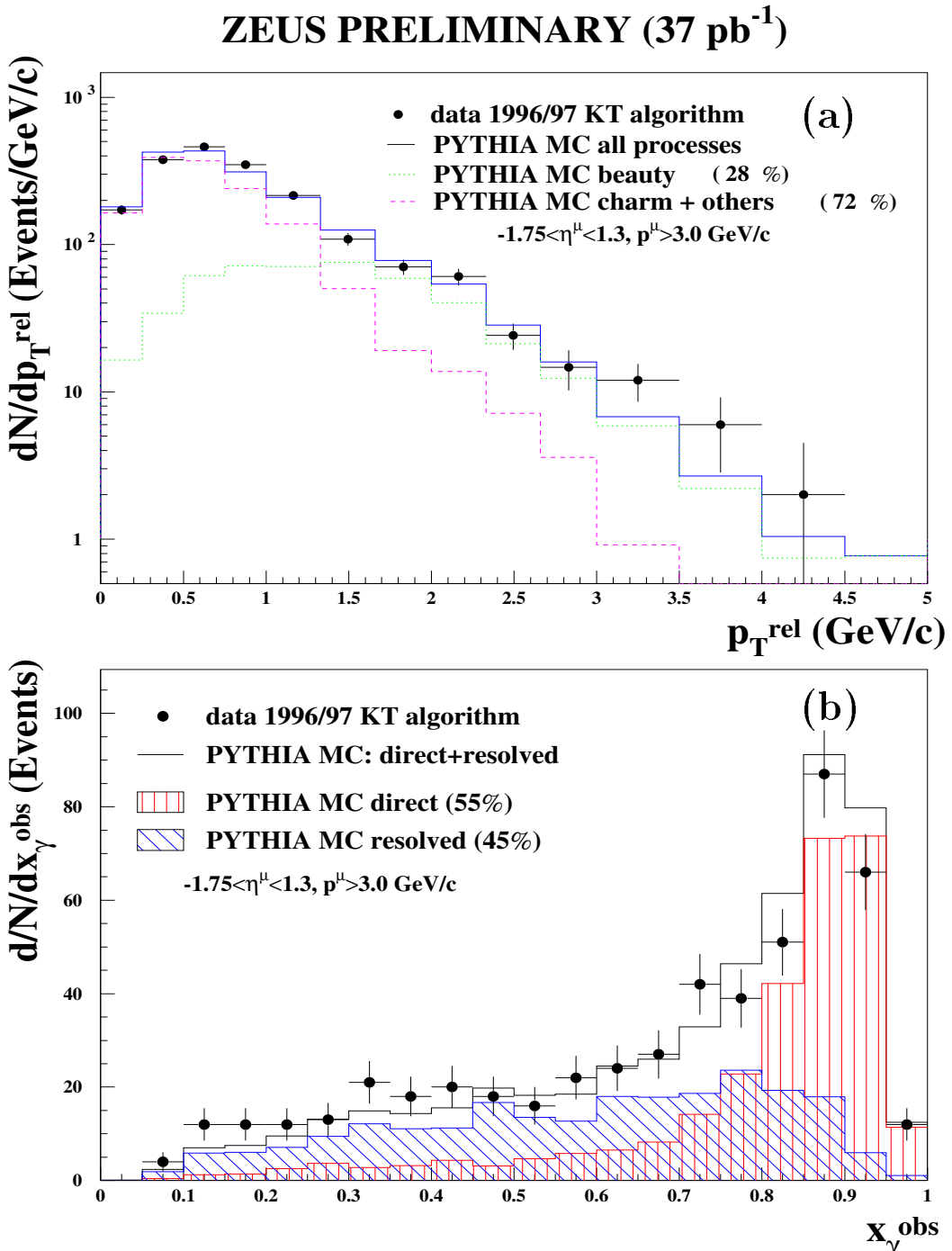

Figure 6.1: (a) Distribution of the number of events in $p_T^{\rm rel}$ in the BRMUON region. The experimental data (dots) are compared to a PYTHIA MC (solid line) prediction which has been normalized to the data. The beauty component (dotted line) and the charm plus light quark component (dashed line) are shown according to the percentages given by a fit. (b) Distribution of the number of events in $x_\gamma^{\rm obs}$in the BRMUON region. The experimental data are compared to PYTHIA MC (open histogram) with a mixture of beauty and charm plus light quark components according to the percentage given by the fit. The components from direct processes (vertically hatched area) and from resolved processes (diagonally hatched area) are shown separately.

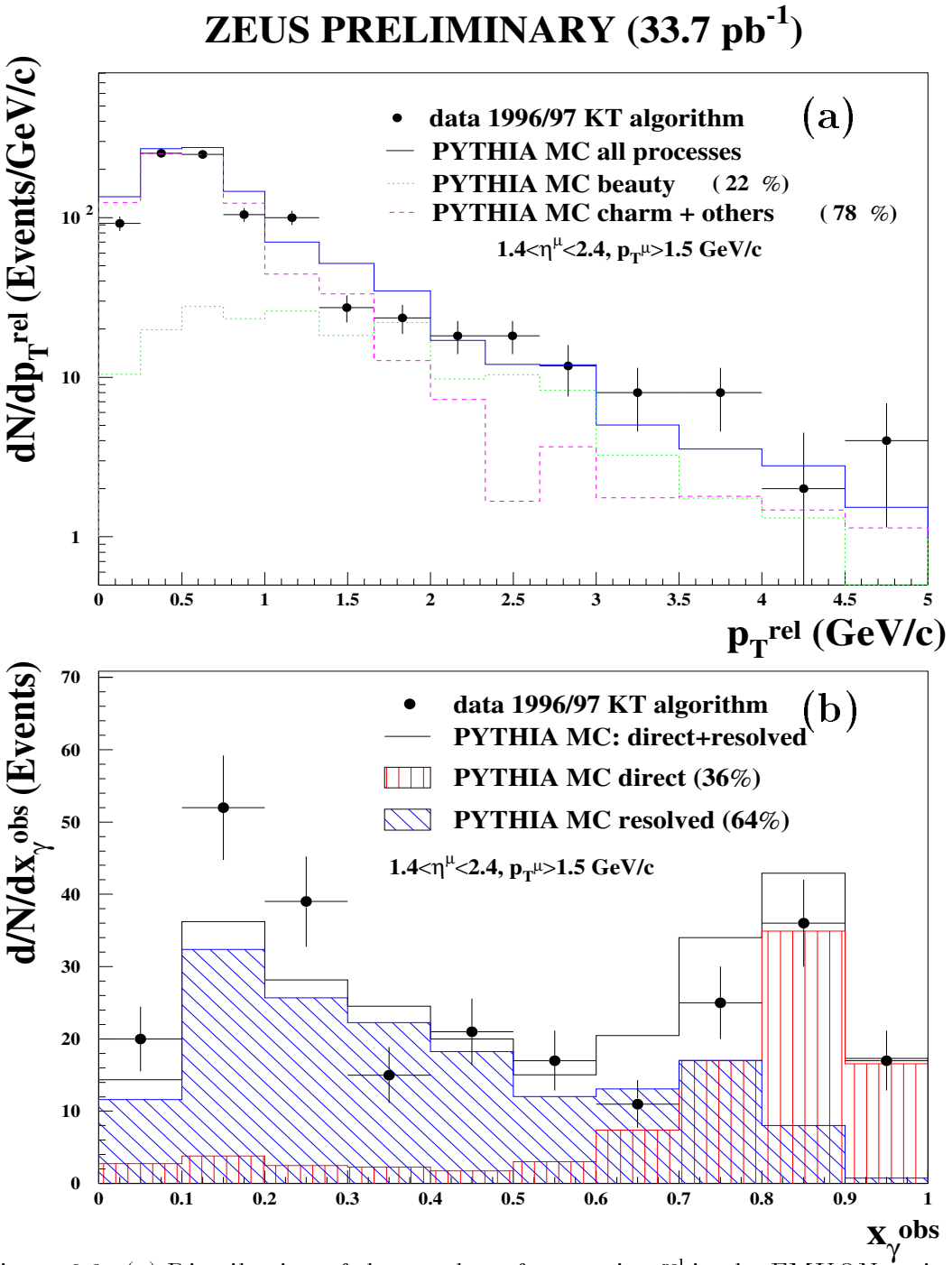

Figure 6.2: (a) Distribution of the number of events in $p_T^{\rm rel}$ in the FMUON region. The experimental data (dots) are compared to a PYTHIA MC (solid line) prediction which has been normalized to the data. The beauty component (dotted line) and the charm plus light quark component (dashed line) are shown according to the percentage given by a fit. (b) Distribution of the number of events in $x_\gamma^{\rm obs}$in the FMUON region. The experimental data are compared to PYTHIA MC (open histogram) with a mixture of beauty and charm plus light quark components according to the percentage given by the fit. The components from direct processes (vertically hatched area) and from resolved processes (diagonally hatched area) are shown separately.

BRMUON sample	
fit with equal binning	± 1.7
fit without last/first point(s) in the spectrum	< 0.1
FMUON sample	
fit with equal binning	-1.0
fit without last/first point(s) in the spectrum	< 0.1

Table 6.2: Systematic uncertainties on the determination of the percentage of beauty events p_b in the final samples as obtained by changing the binning or the range involved in the measure. The values that are shown are the deviation from the central value.

Both these systematic factors are summarized in the Table 6.2 and are small.

If we now add in quadrature the values of the cited systematic errors we obtain:

p_b (BRMUON)	$28.0 \pm 5.0\ (stat) \pm 2.3\ (syst)\%$
p_b (FMUON)	$22.0 \pm 7.0\ (stat)^{+2.0}_{-1.5}\ (syst)\%$

We want to stress that a fit carried on without any beauty component but with the charm and light flavour spectra gives us a really bad description of the $p_T^{\rm rel}$ distribution of the data, the minimization procedure gives in this case:

$$\begin{aligned} \chi^2 &= 49.8/13 \quad \text{BRMUON} \\ \chi^2 &= 31.7/13 \quad \text{FMUON} \end{aligned}$$

6.3 $x_\gamma^{\rm obs}$ distribution

We want to comment on the $x_\gamma^{\rm obs}$ distributions of the final samples. First we take into consideration the sample obtained in the barrel and rear regions. We can see the spectrum of the experimental data in Figure 6.1b (dots) superimposed to the LO Monte Carlo prediction (solid line), the histogram is obtained as a mixture of beauty and charm plus light quark components according to the percentage given by the fit algorithm. The simulation shows a good description of the data even without modification in the relative contribution of direct and resolved photon processes. In fact the curve is obtained just adding the contributions of direct, resolved and beauty excitation as predicted by the cross section in the Monte Carlo and similarly in the case of charm and light flavour: the only free parameter is the fractional beauty content in the sample that has been fixed with the $p_T^{\rm rel}$ fit.

We note the presence of an important peak due to the direct photon process at $x_\gamma^{\rm obs}$ values near 0.9 (vertically hatched area) and a long tail at low values caused by the resolved photon processes and the presence of excitation processes (diagonally hatched area).

In the case of the sample selected through the presence of a muon in the forward sector, shown in Figure 6.2b, we can see that the Monte Carlo (open histogram) still describes the data (dots) but not in a as good a way as in the previous case. The direct photon induced peak is less prominent both in the spectrum of the experimental data and in the one predicted by the PYTHIA Monte Carlo. The low $x_\gamma^{\rm obs}$ tail is much more enhanced and the Monte Carlo in this case somewhat undershoots the data, even if the errors of the data points are too large to draw any strong conclusion.

In both cases, in the barrel and rear regions or in the forward sector, if we neglect the processes of excitation of charm and beauty flavours, we obtain that the Monte Carlo no longer describes the shape of the experimental distributions and the simulated distribution deviates from the measured one at values of $x_\gamma^{\rm obs}$ as high as 0.7. This deviation, in the case of the barrel and rear regions, is of almost an order of magnitude in the range of $x_\gamma^{\rm obs}$ less than 0.6 and of about a factor of two till 0.8.

6.4 Cross sections

At this point we have measured the percentage of events in the final samples that have been produced by the decay of a beauty hadron. We can therefore extract the number of events due to the beauty photoproduction that populate our samples. If we propagate quadratically the errors on the percentage and on the number of observed events we obtain:

$$\boxed{\begin{array}{l}\mathcal{N}^{\text{beauty in data}}\,(\text{BRMUON}) = 143.6 \pm 26.4(stat) \\ \mathcal{N}^{\text{beauty in data}}\,(\text{FMUON}) = 55.7 \pm 18.1(stat)\end{array}}$$

where $\mathcal{N}^{\text{beauty in data}} = p_b \cdot \mathcal{N}^{\text{data}}$ and the errors are statistical only.

As we have seen in Chapter 5 and in Sections 6.2 and 6.3, the Monte Carlo samples we have obtained after the fit describe the data in a good way and so we can relay on the Monte Carlo itself to extract the cross section of the process of open beauty photoproduction.

To calculate the cross sections we apply the usual formula:

$$\sigma(e^+p \to e^+\, b\bar{b}\, X \to e^+\,\text{dijet}\,\mu\, X)^{\text{vis}} = \frac{\text{N}_{\text{ev}}}{\epsilon \cdot \mathcal{L} \cdot Br} \tag{6.5}$$

where

- N_{ev} in our case is $\mathcal{N}^{\text{beauty in data}}$;

- ϵ is the convolution of the detector acceptance and efficiency of:
  - the online trigger chain,
  - the data acquisition system,
  - the offline selection algorithms;
- $\mathcal{L}$ is the value of the integrated luminosity to which the data sample refers;
- Br is the branching fraction of the process, in this case an *inclusive* measurement is carried on and it is not needed to be considered (it can be taken as equal to 1).

At the moment we know everything except the value of ϵ.

In the case of the BRMUON sectors this quantity can be split in the product of two other independent variables. The first of these is the acceptance and can be calculated through the Monte Carlo at our disposal. It is defined as the ratio of the number of generated events that pass the online and offline selection over the ensemble of the events that are generated in a specified kinematical range defined by cuts at the generator level:

$$\text{acceptance} = \frac{N^{\text{sel}}}{N^{\text{gen}}}, \tag{6.6}$$

In the BRMUON kinematic regions the acceptance has the following value:

$$\text{acceptance(BRMUON)} = 0.138. \tag{6.7}$$

The second quantity that we have to introduce is due to the fact that the detector simulation is not so faithful as we need and there is a discrepancy[1] between the behaviour of the first level trigger of the outer chambers as it is in the reality and the implementation of it in the simulation programs. We have to correct for this difference and we introduce an overall factor to get the cross section. This factor is the ratio of the efficiencies of the real and simulated trigger logic evaluated as an unique number, above the momentum cut imposed by the analysis[2]. This global quantity has been determined with a large error because some of the data samples used to extract it are statistically limitedand this same uncertainty will be one of the largest systematic error in this measurement. The constant that we have used to renormalize the measure is

$$\frac{\epsilon(\text{FLT data})}{\epsilon(\text{FLT Monte Carlo})} = 0.77 \pm 0.11. \tag{6.8}$$

[1] Part of this discrepancy is due to hit inefficiencies of the chambers and to the presence of single LST's or groups of LST's that have temporary or permanent malfunctions. These effects have not been implemented in the Monte Carlo.

[2] The ratio has been determined using various samples including elastic two muon track events like described in Section 5.5.1

We concentrate now on the forward sector. In this case the values of the detector efficiencies of the LST and DC planes are already included in the Monte Carlo simulation, while the efficiencies of the LW planes are not. These were measured with the data and their influence on the reconstruction of the tracks of the forward spectrometer as a stand alone tracking detector were summarized in a re-weighting function, see Section 5.6 and Figure 5.4. This depends on the pseudorapidity of the track alone. We use this re-weighting function in this way. To calculate the acceptance we apply the formula in Equation (6.6), but, instead of using in the numerator the bare number of selected events, we re-weight each event with the function in Figure 5.4, that is we use an expression like:

$$\text{acceptance} = \frac{\sum_{\text{sel}} \epsilon(\eta^{\mu})_i \cdot N_i^{\text{sel}}}{N^{\text{gen}}}, \tag{6.9}$$

where $\epsilon(\eta^{\mu})_i$ are the values of the re-weighting function calculated for each event according to the pseudorapidity of the matched μ and the sum of the quantities $\epsilon(\eta^{\mu})_i$ at the numerator is performed over all the events that pass the selection cuts. In this way we obtain the following global factor:

$$\text{acceptance(FMUON)} = 0.0808. \tag{6.10}$$

We can now apply the formula in Equation (6.5) and obtain the values of cross sections in the two kinematic ranges.

In the BRMUON sectors we measure:

$$\sigma_{b\bar{b}}^{\text{vis}}(e^+p \to e^+\text{dijet} + \mu + X) = 36.4 \pm 5.2\ (stat)^{+10.4}_{-9.1}\ (syst)\ \text{pb} \tag{6.11}$$

where the first error is statistical only, the second is obtained adding in quadrature all the systematic uncertainties listed in Table 6.3.

In the FMUON sector we have:

$$\sigma_{b\bar{b}}^{\text{vis}}(e^+p \to e^+\text{dijet} + \mu + X) = 20.5 \pm 6.5\ (stat)^{+6.3}_{-5.7}\ (syst)\ \text{pb} \tag{6.12}$$

where the first error is statistical only, the second is obtained adding in quadrature all the systematic uncertainties listed in Table 6.4.

The LO Monte Carlo generator PYTHIA in the kinematic range defined by the cuts in Equation (6.1) predicts for $\sigma_{b\bar{b}}^{\text{vis}}(e^+p \to \text{dijet} + \mu + X)$ 30 pb and 9.6 pb, for the BRMUON and FMUON regions, while HERWIG predicts 12 pb for the BRMUON sector and 4.1 pb for the FMUON sector. For both Monte Carlo programs, the masses of b and c quarks have been set to $m_b = 4.5$ GeV/c^2 and $m_c = 1.35$ GeV/c^2 while for the proton and photon structure functions CTEQ-4L and GRV-LO, respectively, were used.

In the following sections we will explain the various sources of systematic errors.

6.5 Study of Systematic Uncertainties

We have now to consider the sources of *uncorrelated* systematic uncertainties in the determination of the value of the cited cross sections. We can somewhat arbitrarily categorize the changes into classes:

- Variation of the kinematic cuts used to define the analysis. This was done by varying the reconstructed variables, E_T^{jet} and y_{JB} both in the data and the PYTHIA Monte Carlo samples.

- Variation of the kinematic cuts and quantities used to define the muon selection. This is again done by varying the cut values in the data and reconstructed Monte Carlo.

- Errors due to the limited knowledge of the muon detector efficiencies. This is due to the limited statistics of the samples we have been able to use to measure the behaviours of both the BRMUON trigger and FMUON planes. Even these are therefore expected to systematically increase or decrease the cross-section.

- We also consider the systematic effect due to the uncertainty on the absolute calorimeter energy scale between the data and Monte Carlo. This is done by varying the calorimeter quantities (E_T^{jet}, y_{JB}) by some factor in the Monte Carlo only, while the data remain at the nominal value. This is therefore expected to systematically increase or decrease the cross-section.

- Uncertainties arise from the dependence of the model used to obtain the cross-section. It was therefore used another Monte Carlo generator to quantify the effect.

6.5.1 Uncertainties Arising From the Kinematic Cuts

We vary the y_{JB}^{corr} by changing the lower and upper limits separately to:

$$0.18 < y_{JB}^{\text{corr}} < 0.8, \quad 0.2 < y_{JB}^{\text{corr}} < 0.88.$$

As the purpose of the lower and upper cuts on y_{JB} is different they have been varied separately, rather than choosing one extended window. The cut on the transverse energy of the jets has been varied by considering the resolution (Figure 5.16) and varying the central values by $\pm 1\sigma$. We therefore have the following cuts,

$$E_T^{CORjet1,2} > 8,7 \text{ GeV}, \quad E_T^{CORjet1,2} > 6,5 \text{ GeV},$$

Systematic errors due to the analysis selection	
$\eta^{\rm jet} < 2.5$	-3.6%
$\eta^{\rm jet} < 2.3$	$+0.8\%$
$E_T > 8,7$	$+15\%$
$E_T > 6,5$	-4%
y resolution $0.18 < y < 0.8$ $(+10\%)$	-2.8%
y resolution $0.2 < y < 0.88$ (-10%)	-3.6%
Systematic error due to the muon selection	
p_μ threshold effect	-4% $+0.5\%$
Systematic errors due to energy scale uncertainty	
E_T scale $(+5\%)$	-8%
E_T scale (-5%)	$+11\%$
y scale $(+5\%)$	$+2\%$
y scale (-5%)	-2%
preliminary energy correction to account for μ in jet	-14%
Systematic errors due to model dependency	
fit only $b + lf$	-6%
fit only $b + c$	$+6\%$
equal/unequal binning	$\pm 6\%$
HERWIG	-3%
Systematic error due to limited knowledge of detector efficiency	
muon chamber and trigger efficiency	-15% $+20\%$

Table 6.3: BRMUON sample, summary of the systematic errors on the cross section, the values are fractional variations on the central value (see Equation (6.13)).

Systematic errors due to the analysis selection	
$\eta^{\text{jet}} < 2.5$	-1.5%
$\eta^{\text{jet}} < 2.3$	$+3.0\%$
$E_T > 8,7$	$+13\%$
$E_T > 6,5$	-4%
y resolution $0.18 < y < 0.8$ $(+10\%)$	$+0.5\%$
y resolution $0.2 < y < 0.88$ (-10%)	-0.5%
Systematic error due to the muon selection	
$p_{T\mu}$ threshold effect	-3.5%
Systematic errors due to energy scale uncertainty	
E_T scale $(+5\%)$	-10%
E_T scale (-5%)	$+14\%$
y scale $(+5\%)$	-1%
y scale (-5%)	-3%
preliminary energy correction to account for μ in jet	-19%
Systematic errors due to model dependency	
fit only $b + lf$	-5%
fit only $b + c$	$+9\%$
equal/unequal binning	-5%
HERWIG	$+16\%$
Systematic error due to limited knowledge of detector efficiency	
muon chamber efficiency	-15% $+15\%$

Table 6.4: FMUON sample, summary of the systematic errors on the cross section, the values are fractional variations on the central value (see Equation (6.13)).

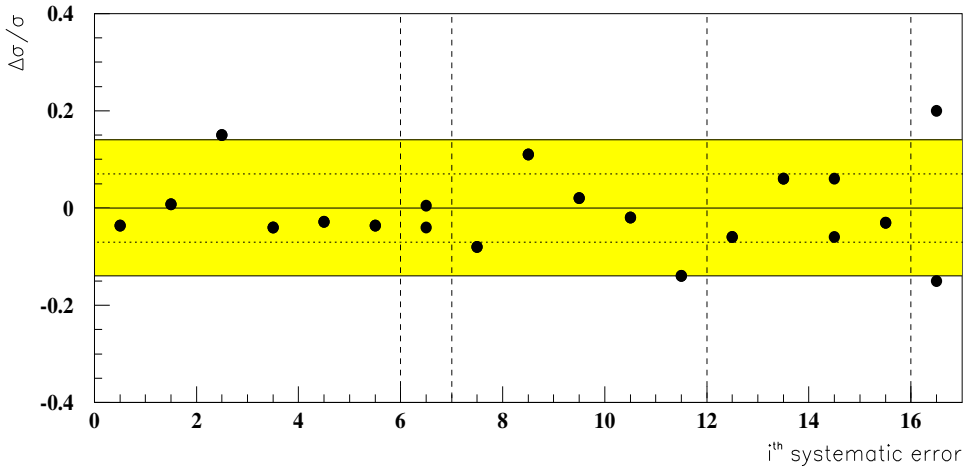

Figure 6.3: BRMUON sample, summary of the systematic errors on the cross section, the values are fractional variations on the central value see Equation (6.13). The order of the plotted points is the same as the one of the listed errors in Table 6.3.

where our resolution for low transverse energy jets is $\approx 15 \div 20\%$. The same method has been pursued for the cut of the pseudorapidity of jets where the standard deviation is $\sigma_\eta = 0.1$:

$$\eta^{\text{jet}} < 2.3 \quad \eta^{\text{jet}} < 2.5.$$

The effect of these six kinematic changes on the cross-section can be seen in the first rows of Table 6.3 for the BRMUON sectors and of Table 6.4 for the FMUON region where on the right column the fractional variation on the cross section can be read:

$$\frac{\Delta\sigma}{\sigma} = \frac{\sigma_{syst} - \sigma_{nominal}}{\sigma_{nominal}}, \tag{6.13}$$

where σ_{syst} and $\sigma_{nominal}$ are our varied and central cross-sections respectively. Figures 6.3 and 6.4 show plots of the same fractional variation of the cross-section, see Equation (6.13). The statistical error on the central cross-section value is shown as the shaded band. Some of the absolute shifts are of the order of the statistical error.

The effect of varying the cuts on the transverse energy is more marked. If the cuts are increased by 1σ on the transverse energy absolute shifts of significant size appear. However, this variation is caused more by the limitation of the statistics than by the cuts themselves. Changing to these higher values of jet transverse energy results in a $30 \div 40\%$ reduction in events and so we are using correction factors of almost twice the size as the nominal ones and hence a large Monte Carlo extrapolation. Lowering the transverse energies by 1σ results in another situation. Here the resultant shifts from the central values are not so large, but

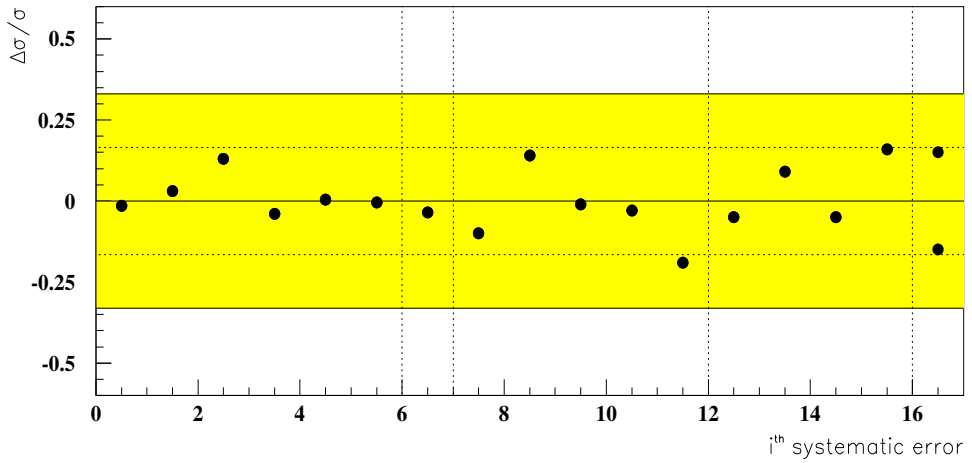

Figure 6.4: FMUON sample, summary of the systematic errors on the cross section, the values are fractional variations on the central value see Equation (6.13). The order of the plotted points is the same as the one of the listed errors in Table 6.4.

by requiring jets with a corrected jet transverse energy of 5 GeV, we are using jets that can have measured energies at the calorimeter level as low as ~ 3.4 GeV. Jets of this value are poorly modeled and we are relying on extrapolation from the Monte Carlo as the trigger requires jet energies to be greater then 4 GeV.

The cross-section in both the forward and barrel-rear case is almost unaffected by the the changes in y_{JB} and η^{jet}. The percentage changes are less than one forth of the statistical error.

6.5.2 Uncertainties Arising From the Muon Selection

We have chosen to consider just the effect of the momentum selection cut. That is we have checked for threshold effects on the requirement of the track associated to the matched muon. We have varied the cut on the data and the reconstructed Monte Carlo of a quantity equal to plus and minus one standard deviation, for the barrel and rear detector on the momentum of the muon and for the forward detector on the transverse momentum of the matched particle. The results of this control can be seen in the second group of entries of the Tables 6.3 and 6.4.

The difference in the cross-sections when changing the minimum momentum cut of the track is small, even here the magnitude of the variation is far less than the statistical error.

6.5.3 Uncertainties Arising From the Limited Knowledge of Detector Efficiency

As we have already said the methods we have at our disposal to obtain an estimate of the detector and trigger inefficiencies are limited by the statistical samples we can use to measure them. For both cross section measurements these errors are one of the largest sources of systematic uncertainties, in the BRMUON case even larger than the statistical error. Being multiplicative factors they automatically change the measured values (last row of Tables 6.3 and 6.4).

6.5.4 Uncertainties Arising From the Energy Scale

When we say uncertainties arising from the energy scale we mean an uncertainty in our knowledge of the calorimeter energy scale *between* data and Monte Carlo. In all of our systematic checks so far studied, a change in a quantity corresponded to the same change in both the data and the Monte Carlo. However, as the energy scale could be different between data and Monte Carlo, we apply a change to it in one and not the other. The Monte Carlo has been shown to reproduce the absolute energy scale of the calorimeter to within $\pm 5\%$ [133], for low energies. We therefore increase the calorimeter quantities, y_{JB} and cell energies, by $\pm 5\%$ in the Monte Carlo *only*, the data remaining in the nominal situation. However, jets are also measured via the calorimeter so they must also be subsequently changed as for y_{JB} and cell energies. The scale uncertainty attributed to our relatively low energy jets is $\pm 5\%$ [56] and so the jet energies are scaled by $\pm 5\%$, also here only in the Monte Carlo.

The presence of a muon in one of the jets has been taken into consideration using a different jet energy correction algorithm and the use of this causes a systematic error on the cross section that is reported in Tables 6.3 and 6.4.

The effects of the uncertainty of our knowledge in the energy scale between data and Monte Carlo are shown in the before mentioned tables and figures (Tables 6.3 and 6.4 third group of entries, Figures 6.3 and 6.4 third group of columns).

6.5.5 Uncertainties Arising From the Model Dependency and Fitting Procedure

In this category of sources of error we find mainly two branches:

- errors introduced by the fitting procedure;
- errors introduced with the choice of the Monte Carlo generator.

The first of these contains the systematic deviations from the central value of the percentage of beauty content in the samples as obtained with the fit, which we

have described in Section 6.2. These changes in the value of p_b automatically and proportionally reflect in a higher or lower cross section measurement(Tables 6.3 and 6.4 and Figures 6.3 and 6.4).

The second kind of error was evaluated with the use of the HERWIG generator to calculate the acceptance. In the case of the forward sector this method has shown that this quantity has a large variation that causes the second largest systematic error. The amount of the systematic shift for this change is reported in the same tables and figures.

6.6 Comparison with other measurement

6.6.1 Semi-leptonic Decay of b to Electrons

A measurement of the cross section of the semi-leptonic decay of beauty in the electronic channel has already been published as preliminary result of the ZEUS collaboration [92, 134]. The observed process is the following

$$e^+ + p \rightarrow e^- + dijets + X \tag{6.14}$$

in the kinematic range

- $Q^2 < 1\ GeV^2$, $0.2 < y < 0.8$;
- $E_T^{jet1,jet2} > 7,6$ GeV and $\mid \eta \mid < 2.4$;
- an electron (e^- only) with $p_T > 1.6$ GeV/c and $\mid \eta \mid < 1.1$ in the final state.

The corrected x_γ and $p_T^{\rm rel}$ distributions have been analyzed. As in the muonic case the high $p_T^{\rm rel}$ spectrum should be mostly populated by electrons coming from b decay. It has been found that in the cited region the visible cross section value of beauty production is:

$$\sigma_{b\bar{b}}^{vis}(e^+ + p \rightarrow e^- + dijets + X) = 39 \pm 11^{+23}_{-16}\ pb \tag{6.15}$$

In Figure 6.5 the corrected distribution as a function of the transverse momentum of the electron with respect to the nearest jet can be seen.

A cross check was done on the measurements in the electronic and muonic channels. An extrapolation procedure was applied using Monte Carlo simulations (both HERWIG and PYTHIA generators were used) and, starting from the cross section measured in the BRMUON sectors, a comparison was done with the direct measurement done with the electron analysis.

The extrapolation to the electron analysis region yields:

- With Pythia $41.1 \pm 5.9\ (stat)^{+11.8}_{-10.3}\ (syst)$ pb,
- With Herwig $40.8 \pm 5.8\ (stat)^{+11.6}_{-10.2}\ (syst)$ pb.

The values obtained were found compatible within the statistical errors.

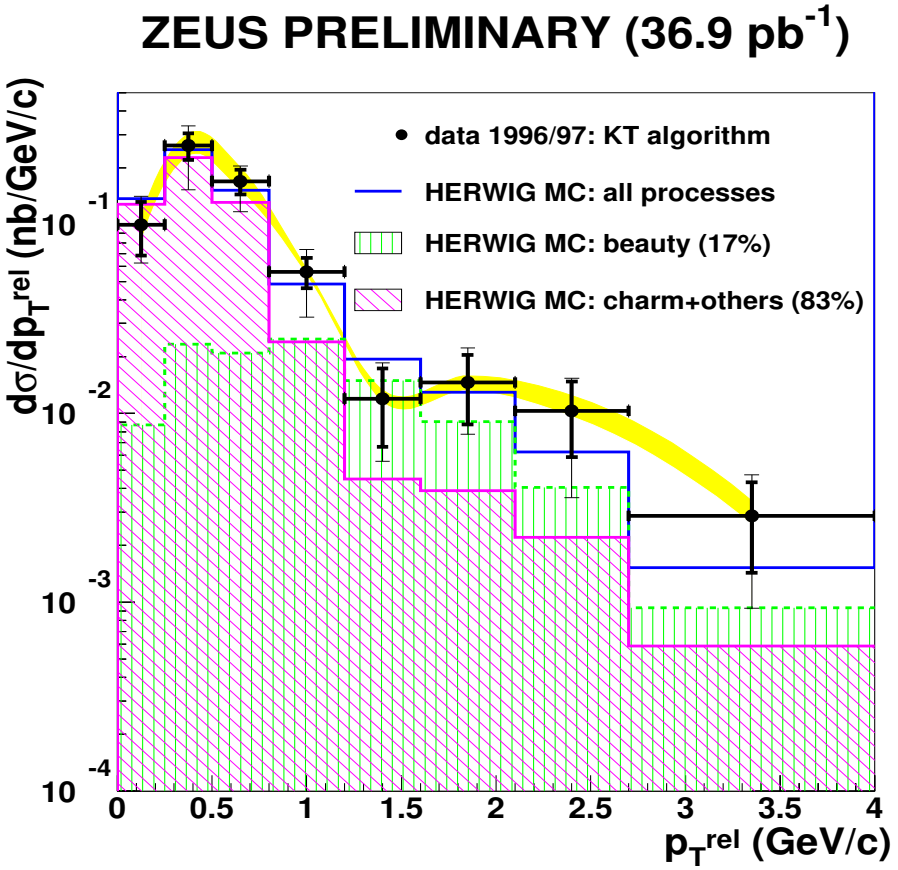

Figure 6.5: Cross section in $p_T^{\rm rel}$, where the data points are shown with statistical (inner bars) and statistical and systematical errors added in quadrature (outer bars). The energy scale uncertainty is shown as the shaded band. The experimental data is compared to HERWIG MC (open histogram) predictions, which have been scaled up by a factor of 3.7. The components from beauty processes (vertically hatched histogram) and from charm plus light quark processes (diagonally hatched histogram) are shown separately [92].

Conclusions

A study of open beauty photoproduction at the HERA accelerator with the ZEUS detector has been performed. Using the 1996/97 data-sample (about 37 pb^{-1}) it has been possible to measure the visible cross section of the following process:

$$e^+p \to e^+b\bar{b} + X \to e^+\mu^\pm + \text{dijets} + X.$$

in the kinematic regions defined by the following cuts:

$$0.2 < y < 0.8$$

$$Q^2 < 1 \text{ GeV}^2$$

$$E_T^{jet1,jet2} > 7,6 \text{ GeV}$$

$$\eta^{\text{jet}} < 2.4$$

$$p_T(\mu^\pm) > 1.5 \text{ GeV}/c \qquad p(\mu^\pm) > 3.0 \text{ GeV}/c$$

$$1.4 < \eta(\mu^\pm) < 2.4 \qquad -1.75 < \eta(\mu^\pm) < 1.3.$$

Muons have been identified with the muon detectors in the Forward, Barrel and Rear sectors. Jets have been reconstructed through the energy deposits in the main calorimeter.

This work has extended the pseudorapidity range of all previous measurement.

To extract the percentage p_b of beauty in the data a fit of the transverse momentum of the muon with respect to the associated jet axis, p_T^{rel}, has been performed and has given as a result:

$$p_b(\text{BRMUON}) = 28.0 \pm 5.0\ (stat) \pm 2.3\ (syst)\%$$

$$p_b(\text{FMUON}) = 22.0 \pm 7.0\ (stat)^{+2.0}_{-1.5}\ (syst)\%.$$

The visible cross sections in the Forward and Barrel-Rear sectors have been measured to be:

$$\text{(BRMUON)} \qquad \sigma^{\text{vis}}_{b\bar{b}}(e^+p \to \text{dijet} + \mu + X) = 36.4 \pm 5.2\ (stat)^{+10.4}_{-9.1}\ (syst) \text{ pb},$$

$$\text{(FMUON)} \qquad \sigma^{\text{vis}}_{b\bar{b}}(e^+p \to \text{dijet} + \mu + X) = 20.5 \pm 6.5\ (stat)^{+6.3}_{-5.7}\ (syst) \text{ pb}$$

where the first errors are statistical only, the second are obtained adding in quadrature all the systematic uncertainties.

Even if with large errors the measured cross sections are higher than those predicted by the LO Monte Carlo HERWIG and PYTHIA .

The PYTHIA Monte Carlo do describe the data in all the relevant quantities, including the percentages of direct and resolved photon processes seen in data. The $x_\gamma^{\rm obs}$distributions enlightened the necessity to take into account the production of heavy quarks through the flavour excitation processes, in particular way for the FMUON selected sample. In both cases neglecting the flavour excitation Monte Carlo has the consequence that it is not possible anymore to describe the experimental $x_\gamma^{\rm obs}$distributions.

Appendix A

The third level trigger for μ: GLOEXO

One of the programs of selection on the TLT has been designed to recognize and accept ep collision with a final state that contains at least a muon measured by the B(R)MUI chambers. The events of this kind that reach the TLT come from, most of them, from the branch of the FLT that has been described in the Section 5.4.1 and that at the second level trigger have passed the general veto cuts applied at this level of the data acquisition. The selection program developed to recognize these particular events is called GLOEXO. In the next few pages we will describe the algorithms deployed in the GLOEXO program shortly. The purposes of the filtering program are:

- to reconstruct the position of the muon within the hit B(R)MUI chamber;
- to select tracks reconstructed in the CTD that can be associated to the muon identified with the B(R)MUI chambers;
- to combine the informations obtained from the B(R)MUI chamber and from the CTD to identify the global trajectory of the muon inside ZEUS.

A.1 The reconstruction of muons within the B(R)MUI chambers

To reconstruct the position of muons in the inner chambers a simpler version of the final reconstruction has been developed. In the Section 1.8.2 we have seen that each chamber is build out of two pairs of LST layers and in every event the address of hit wires and quadruplets are readout. The reconstruction algorithm is able to identify the chambers crossed by a particle looking for those planes where wires and quadruplets have been hit.

The reconstruction of the position and direction of the particle in the hit chamber is carried out initially in a local reference frame with the x axis along the wires, the y axis along the quadruplets and the z axis perpendicular to the chamber. The algorithm calculates, plane by plane, the barycenter of the hit wires and quadruplets identifying in this way the point where the particle has crossed (the probability that two particles cross the same chamber can be neglected at this level). If both the layers of the inner (outer) pair have been hit the barycenter of wires and quadruplets are averaged out. The two points so far reconstructed in the local reference frame, one for each pair of layers, are then transformed into the reference frame of ZEUS. From the coordinates of the two points the direction of the track within the crossed chamber is calculated.

A.2 The Selection of reconstructed tracks inside the CTD

As we have already seen in Section 1.11.3 the reconstruction program of the TLT supplies to the filters the parameters of the tracks that have been reconstructed in the CTD. The parameters used to select the CTD tracks that can be associated to a muon identified with the B(R)MUI chambers and the CTD are:

- the minimum distance between the projection of the track in plane x y, a circumference arc, and the beam-axis, the axis z, called D_H. The space point so identified is called of maximum approach;
- the position along the z axis of the point of maximum approach, called Z_H;
- the transverse momentum of the track if this gets out of the CTD from a point of the cylindrical surface of the drift chamber. In this case the track is called central. If the track gets out in the forward direction but its polar angle is not smaller than 20° or if it is in the rear direction the algorithm uses the momentum of the track. Tracks with a polar angle at the origin less than 20° are discarded as they cannot reach the B(R)MUI chambers.

CTD tracks that can be associated to the muon identified through the B(R)MUI chambers have to verify:

$$D_H < 2 \text{ cm} \tag{A.1}$$

$$-60 < Z_H < 60 \text{ cm} \tag{A.2}$$

$$\text{for central tracks } p_T > 3 \text{ GeV/c} \tag{A.3}$$

$$\text{for rear tracks } p > 1 \text{ GeV/c} \tag{A.4}$$

The conditions A.1 and A.2 reduce cosmics events that have D_H and Z_H distributions more or less flat, while ep collisions produce track that are characterized

by:

$$D_H \simeq 0 \text{ cm} \tag{A.5}$$

$$Z_H \simeq 0 \text{ cm}. \tag{A.6}$$

The condition on the p_T of central tracks A.3 is useful to select events with a μ with a large momentum, while the cut on the p quantity in the rear region is kept low to limit the losses due to a poor resolution of the CTD at the TLT for tracks with a low angle.

A.3 Identification of the global trajectory of a muon in the BR regions

The GLOEXO algorithm, to identify the global trajectory of a muon in the barrel or rear region, has to associate two different kind of objects:

- a track reconstructed inside the CTD with the characteristics described in the previous section:
- a track segment reconstructed in a B(R)MUI chamber.

To explain how the association takes place we call (see Figure A.1): P_1 the exit point of the muon from the CTD, $\vec{p}_1$ the momentum of the muon in the point P_1, P_2 the point where the muon reaches one of the B(R)MUI chambers and $\vec{u}_2$ the versor that gives the direction of the track segment reconstructed within the hit chamber.

If the magnetic field outside the CTD were null, if the muon would not be subject to the multiple scattering inside the CAL and if the spatial resolution of the detectors were infinite the points P_1 and P_2 would be aligned and the two vectors $\vec{p}_1$ and $\vec{u}_2$ parallel. The GLOEXO algorithm identifies the global trajectory of the muon looking for the kind of configuration we have so far illustrated.

As the magnetic field at the exit of the CTD is not negligible, the GLOEXO algorithm extrapolates[1] the preselected tracks till a optimal cylindrical surface, that contains the CTD, beyond which the magnetic field can be neglected, practically the tracks are extrapolated to the internal surface of the CAL. Hence P_1 becomes the point beyond which the muon trajectory is no longer influenced by the magnetic field.

We define: φ_1 (θ_1) the azimuthal (polar) angle of the vector $\vec{p}_1$ and φ_2 (θ_2) the azimuthal (polar) angle of the versor $\vec{u}_2$. If both the point P_1 and P_2 are

[1]Starting from the parameters of the tracks at the origin that are made available from the TLT reconstruction program.

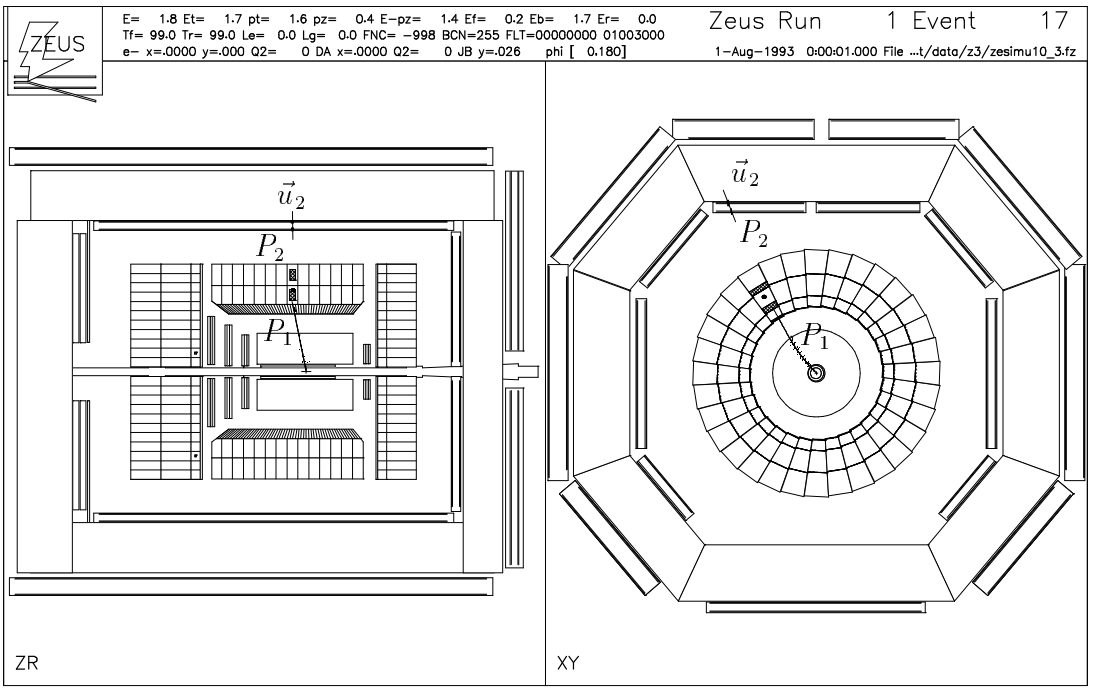

Figure A.1: Simulation of the global trajectory of a muon.

more or less aligned and the vectors $\vec{p}_1$ and $\vec{u}_2$ more or less parallel, the following relations have to hold:

$$\varphi_i \simeq \varphi_j \quad \forall\, i,j = 1,2 \tag{A.7}$$

$$\theta_i \simeq \theta_j \quad \forall\, i,j = 1,2 \tag{A.8}$$

The algorithm imposes this condition calculating:

$$\langle\varphi\rangle = \frac{\sum_{i=1,2}\ \varphi_i/\sigma^2_{\varphi_i}}{\sum_{i=1,2}\ 1/\sigma^2_{\varphi_i}} \tag{A.9}$$

$$\langle\theta\rangle = \frac{\sum_{i=1,2}\ \theta_i/\sigma^2_{\theta_i}}{\sum_{i=1,2}\ 1/\sigma^2_{\theta_i}} \tag{A.10}$$

and requiring that:

$$\begin{aligned}\Delta &= \sum_{i=1,2}\left(\frac{\langle\varphi\rangle - \varphi_i}{\sigma_{\varphi_i}}\right)^2 + \sum_{i=1,2}\left(\frac{\langle\theta\rangle - \theta_i}{\sigma_{\theta_i}}\right)^2 \\ &\leq \Delta_o\end{aligned} \tag{A.11}$$

where σ_{φ_i} (σ_{θ_i}) is the expected resolution on the azimuthal angle φ_i (polar θ_i) and Δ_o is a constant quantity.

The identification phase of the GLOEXO algorithm starts from the list of reconstructed segment in the inner chambers and the list of the CTD reconstructed tracks that have been selected as we have illustrated in the Section A.2. The algorithm tries to associate each segment with each track applying for all the possible combinations the Equation A.11. An event with $n_{B(R)MUI}$ segments and n_{CTD} preselected tracks needs, hence, to calculate $n_{B(R)MUI} \times n_{CTD}$ different combinations. But $n_{B(R)MUI}$ is almost never a large number (events where $n_{B(R)MUI} = 3$ are rare) and the pre-selection of the CTD reconstructed tracks is really important to keep n_{CTD} equal to values that are not too high, hence the identification phase does not require a too long time, on the average.

An event is accepted by the GLOEXO algorithm and taken by the TLT if:

- it is accepted by the FLT branch described in Section 5.4.1;
- it is accepted by the SLT branch described in Section 5.4.2;
- at least a segment–track combination exists that verifies the condition: $\Delta \leq \Delta_o$.

The latest request allows to identify the global trajectory of the muon. In the 1996/97 data taking period it has been chosen:

$$\Delta_o = 20. \tag{A.12}$$

The imposed cut is not but a cut on a χ^2 quantity, and it fixes a condition the matching has to undergo so the matching itself is recognized as a good one.

Appendix B

The Bremat matching package

The main purpose of the BREMAT [112] algorithm[1] is to find out candidate muons associating inner detector tracks to segments in the Barrel and Rear chambers and to provide the resulting matching χ^2.

The parameters and error matrix of a candidate track at the exit of the inner tracking volume are extrapolated through the UCAL, up to a reference surface on the inner muon chambers, where the matching is done. This surface is shaped as a prism with octagonal section, where one base corresponds to the rear chambers' plane at $Z_{\rm ZEUS} = -310.53$ cm and the side faces to the barrel chamber sectors. The other base is defined to lie over the forward end of the barrel chambers at $Z_{\rm ZEUS} = +450.0$ cm. The reference surface coincides with the entrance face of the first layer of LST's.

The track extrapolation is done in an unusual way: outward, starting from the inner region. This has been chosen for the best treatment of low momentum muons, which suffer non-negligible energy losses compared to their initial energy. Indeed, knowledge of the momentum, as measured by the inner tracking, is helpful in the extrapolation, with no particular problem in dealing with many track complex events.

The algorithm uses as main inputs the table MBXYSG [113] of the reconstructed B/RMU segments and VCTRHL for the reconstructed inner tracks [18]. If there is an entry in MBXYSG, it looks for candidate tracks in VCTRHL, which might be associated to it. The loose track preselection requires:

- $p > 1$ GeV
- $\theta > 20°$
- track starting from CTD superlayer 1 and extending at least to superlayer 3
- impact parameter $|D_H| < 10$ cm

[1] Barrel and Rear Extrapolation MATching.

- $|Z_H| < 75$ cm
- $\chi^2_{\rm track}/n.d.f. < 5$
- $\Delta \leq 150$ cm

The last cut is done on the distance Δ between a central point in the B/RMU segment, and the straight line obtained by extrapolating the CTD track at the UCAL entrance. It has been set safely with a study on inclusive muon data samples to accept most of the low energy muons.

The requirement of the hits on the third CTD superlayer has been introduced in the preselection to use only tracks from the region where the CTD acceptance is well under control. In the rear angular region it could be relaxed if the track is well measured by the RTD.

Track passing this preselection are then extrapolated using the GEANE package [114], which intimately relates to the GEANT one [118].

Two possibilities are allowed. The first one starts from VCATCAL table. There is a transformation of the VCATCAL covariate matrix into a form suitable to GEANE, suitable expression are available in the literature [112] and in the reference therein [138]. The VCATCAL covariance matrix includes contributions from multiple scattering on the CTD, FTD and RTD walls and on the COIL with some approximation [18].

The second method (the most rigorous one) takes as input the information stored in the VCYPCO common block filled during the VC reconstruction. It contains the track parameters and covariance matrix near the outermost hit used in the trajectory fit. If the track is fully contained in the CTD the used track parameterization is a cylindric-polar one, otherwise if FTD, RTD or SRTD hits are used it is a Cartesian parameterization. Unfortunately the common block VCYPCO is not written out to any table, so one needs to run VCEAZE, that is the tracking reconstruction package, and hence to have the tracking raw data. However these have not been stored in the MDST since 1997 data.

The GEANE extrapolation is terminated when the fiducial surface described at the beginning of the section is reached. Here the output track parameters and error matrix are usually referred to as *prediction*. The predicted variables and error matrix are finally obtained in a convenient Cartesian parameterization. This is related to the local Cartesian frame specific of each sector, with the x and y axes being respectively the coordinates measured by LST wires and strips and z an axis perpendicular to the chamber and pointing outside of the detector. On each view the direction is expressed by the slope: $x' = dx/dz$, $y' = dy/dz$. It may be useful to add that in the barrel $y \equiv Z_{\rm ZEUS}$ while in the rear $x \equiv Y_{\rm ZEUS}$, $y \equiv X_{\rm ZEUS}$ ($z \equiv -Z_{\rm ZEUS}$).

The B/RMU measurement is taken from the MBTS table instead of MBXYSG, since there it is already given in the local sector frame, while MBXYSG gives it in the LAB frame. This would be wrong in principle to use the *Kalman-filtering*

option to reconstruct the momentum (obviously when the muon goes through the outer chambers), as the position and slopes are slightly changed by the filtering. The exact procedure would be to start always from the MBXYSG variables and then rotate them back into the local sector frame. However the difference is tiny. The measured coordinates are propagated through the chamber depth down to the reference surface by a simple linear extrapolation (inward).

If the prediction does not fall on the same sector of the measurement it does not mean that there should be no matching: measurement and prediction could just be on opposite sides of the boundary between nearby sectors. In this case there is no loss of efficiency for BREMAT. The prediction is projected on the same reference plane of the measurement and then matching is done normally. Note that on a purely technical basis a standard GEANE backward extrapolation would not have these complications but, as we already said, we prefer a forward extrapolation. Another particular case occurs when a candidate track is predicted to loose all of its energy in the material before getting to the muon chambers. In this case GEANE stops the tracking and the track is abandoned: it will not give any spurious matching.

Naming ξ_{Mi} and ξ_{Pi} respectively the measured and the predicted track parameters at the reference surface, the residuals are: $\delta_i = \xi_{Mi} - \xi_{Pi}$. The used Cartesian parameterization is written as $(x, y, x', y', Q/p)$. The matching χ^2 is given by:

$$\chi^2 = \sum_{i,j} S_{ij}^{-1} \delta_i \delta_j = \delta S^{-1} \delta^T$$

where the summation goes from 1 to $n = 4$ or 5, depending whether momentum is included or not in the χ^2, $\delta = (\delta_1, ..., \delta_n)$ and S^{-1} is the inverse of the covariance matrix of the residuals:

$$S_{ij} = \sum_{k,l} T_{ik} (\sigma^2_{track})_{kl} T^T_{lj} + (\sigma^2_{random})_{ij} + (\sigma^2_{BRMU})_{ij}$$

with $k, l = 1, ..., n$. Here T is the so called transport matrix, between the start and the stop of the *swim*, σ^2_{track} is the error matrix of the inner detector track, σ^2_{random} the error matrix due to the random processes of multiple scattering and energy loss and σ^2_{BRMU} the error matrix of the B/RMU segment (from MBXYSG). The first two terms are calculated by steps during the GEANE extrapolation using the detailed geometry of the ZEUS detector and the magnetic field map.

Bibliography

[1] HERA, A Proposal for a Large Electron-Proton Colliding Beam Facility at DESY, DESY HERA 81-10 (1981); B. H. Wiik, Electron - Proton Colliding Beams, The Physics Program and the Machine, Proc. 10^{th} SLAC Summer Institute, ed. A. Mosher, 1982, p. 233, and Proc. XXVI Int. Conf. High Energy Physics, Dallas, 1992; G. - A. Voss, Proc. First Euro. Acc. Conf., Rome, 1988, p. 7;
G. -A. Voss, B. H. Wiik, *The electron-proton collider HERA*, Ann. Rev. Nucl. Part. Sci. **44** (1994), 413.

[2] R.E. Taylor, H.W. Kendall and J.I. Friedman, *Deep inelastic scattering,* Rev. Mod. Phys. 63 vol. 3 (1991) 573-629.

[3] S. Dasu et al., SLAC, *Precision measurement of $R = \sigma_L/\sigma_T$ and F_2 in deep inelastic electron scattering,* Phys. Rev. Lett. **61** (1988), 1061-1064;
A. Whitlow et al., SLAC, *A precise extraction of $R = \sigma_L/\sigma_T$ from a global analysis of the SLAC deep inelastic e–p and e–d scattering cross sections,* Phys. Lett. **B250** (1990), 193-199 and references therein.

[4] BCDMS Collaboration, A.C. Benvenuti et al., *A high-statistics measurement of the proton structure functions $F_2(x, Q^2)$ and R from deep inelastic muon scattering at high Q^2,* Phys. Lett. **B237** (1990) 592; idem, *Test of QCD and a measurement of Λ from scaling violations in the proton structure function $F_2(x, Q^2)$ at high Q^2,* Phys. Lett. **B223** (1989) 490; idem, *A comparison of the structure functions F_2 of the proton and the neutron from deep inelastic muon scattering at high Q^2,* Phys. Lett. **B237** (1990), 599.
EMC Collaboration, J.J. Aubert et al., *Measurement of the proton structure function F_2 in muon-hydrogen interactions at 120 GeV and 280 GeV,* Phys. Lett. **B105** (1981), 315; idem, *QCD analysis of the structure function F_2 in muon nucleon scattering,* Phys. Lett. **B 114** (1982), 291; idem, *A detailed study of the proton structure functions in deep inelastic muon-proton scattering,* Nucl. Phys. **B 259** (1985), 189.
NMC Collaboration, P. Amaudruz et al., *Proton and deuteron F_2 struc-*

ture functions in deep inelastic muon scattering, Phys. Lett. **B295** (1992), 159-168.

[5] CDHSW Collab., P. Berge et al., *A measurement of differential cross sections and nucleon structure functions in charged-current neutrino interactions on iron,* Z. Phys. **C49** (1991) 187-224.
WA25 Collaboration, D. Allasia et al., *Measurement of the neutron and proton structure functions from neutrino and anti-neutrino scattering in deuterium,* Phys. Lett. **B135** (1984) 231-236.
WA59 Collaboration, K. Varvell et al., *Measurement of the structure functions F_2 and xF_3 and comparison with QCD predictions including kinematical and dynamical higher twist effects,* Z. Phys. **C36** (1987) 1-14.

[6] E665 Collaboration, M.R. Adams et al., *Extraction of the ratio $F_2(n)/F_2(p)$ from muon-deuteron and muon-proton scattering at small x and Q^2,* FERMILAB-PUB-95-017-E; idem, *Measurement of the ratio $\sigma(n)/\sigma(p)$ in inelastic muon-nucleon scattering at very low x and Q^2,* Phys. Lett. **B309** (1993) 477-482.

[7] C. Foudas et al., CCFR Collaboration, *Neutrino production of opposite-sign dimuons at Fermilab Tevatron energies,* Phys. Rev. Lett. **64** (1990) 1207-1210.

[8] H1 Collaboration, I. Abt et al., *The H1 Detector at HERA,* DESY 93-103.

[9] ZEUS Collab.; The ZEUS Detector, Status Report, DESY (1993).

[10] K. Ackerstaff et al., The HERMES Collaboration, "The HERMES Spectrometer", Nucl. Instr. & Meth. **A417** (1998) 230-265.

[11] HERA-B Collaboration, E. Hartouni et al., *HERA-B – An experiment to Study CP Violation in the B System Using an Internal Target at the HERA Proton Ring – Design Report*, DESY-PRC 95/01, January 1995.

[12] A. A. Sokholov, M. Ternov, Sov. Phys. Doklady **8** (1964) 1203.

[13] The ZEUS Collaboration, *HERA Luminosity Upgrade Report for Funding Agencies*, October 28, 1997.

[14] The HERA-ZEUS Upgrade Group, *ZEUS Interaction Region Upgrade*, ZEUS Note 97-035.

[15] C. Alvisi et al., Nucl. Instr. & Meth. **A305** (1991) 30.

[16] ZEUS Collaboration, "A Microvertex Detector for ZEUS", ZEUS Note 97-006 (01/97)

[17] N. Harnew et al., Nucl. Instr. & Meth. **A279** (1989) 290; C. B. Brooks et al., Nucl. Instr. & Meth. **A283** (1989) 473; B. Foster et al., Nucl. Phys. B, Proc. Suppl. **B32** (1993) 181; B. Foster et al, Nucl. Instr. Meth. & Meth. **A338** (1994) 254. C. B. Brooks et al., Nucl. Instr. Meth. **A283** (1989) 477.

[18] G. F. Hartner, Y. Iga, J. B. Lane, N. A. McCubbin, "VCTRAK (3.06/20): Offline Output Information", ZEUS Note 96-013, 02/96.
G. F. Hartner, Y. Iga, J. B. Lane, N. A. McCubbin, M. Wing, "VCTRAK (3.07/04): Offline Output Information", ZEUS Note 97-064, 09/97.

[19] G. F. Hartner, "VCTRAK Briefing: Program and Math", ZEUS Note 98-058, 08/98.

[20] M. Derrick et al., Nucl. Instr. & Meth. **A309** (1991) 77; A. Andersen et al., Nucl. Instr. & Meth. **A309** (1991) 101; A. Bernstein et al., Nucl. Instr. & Meth. **A336** (1993) 23; A. Caldwell et al., Nucl. Instr. Meth. **A321** (1992) 356.

[21] Jan Straver, *Design, Construction and Beam Tests of the High Resolution Uranium Scintillator Calorimeter for ZEUS,* PhD Thesis, University of Amsterdam, March 1991.
Jürgen Krüger, *The Uranium Scintillator Calorimeter for the ZEUS Detector at the Electron-Proton Collider HERA — The Heart of ZEUS —,* Internal Report DESY F35-92-02, January 1992.

[22] E. Iarocci et al., Nucl. Instr. Meth. **A217** (1983) 30.

[23] G. Abbiendi et al., Nucl. Instr. & Meth. **A333** (1993) 342; F. Gasparini et al., Nucl. Instr. Meth. **A267** (1988) 87.

[24] H. Bethe, W. Heitler, Proc. Roy. Soc. **A146** (1934) 83; H. A. Bethe, Phys. Rev. **89** (1953) 1256.

[25] ZEUS Collaboration, M. Derrick et al., Z. Phys. **C73** (1997) 253.

[26] U. Amaldi et al., Phys. Lett. **B43** (1973) 231.

[27] K. Desler, U. Schneekloth, ZEUS-Note 95-61 (1995).

[28] W. H. Smith et al., "The ZEUS Trigger System", ZEUS Note 89-084.

[29] F. Chlebana, ZEUS-Note 94-102 (1995).

[30] H. A. J. R. Uijterwaal, "The Global Second Level Trigger", Ph.D. Thesis, University of Amsterdam, 1992.

[31] INMOS Limited, *The Transputer Databook,* 2^{nd} edition (1989).

[32] *OCCAM Programming Manual,* Prentice-Hall International (1984).

[33] S. M. Fisher and P. Palazzi, *The ADAMO Data System Programmer's Manual.*

[34] Close, Physica Scripta **25** (1982) 86.

[35] R. P. Feynman, Phys. Rev. Lett. **23** (1969) 1415.

[36] C. Callan, D. Gross, Phys. Rev. Lett. **22** (1969) 156.

[37] T. Eichten et al., Phys. Lett. **B46** (1973) 274.

[38] TASSO Collab., R. Brandelik et al., Phys. Lett. **B86** (1979) 243.

[39] H1 Collab., I. Abe et al., Nucl. Phys., **B407** (1993) 515.
ZEUS Collab., M. Derrick et al., Phys. Lett., **B316** (1993) 412.

[40] V. N. Gribov, L. N. Lipatov, Sov. J. Nucl. Phys., **15** (1972) 438.
L. N. Lipatov, Sov. J. Nucl. Phys., **20** (1975) 96.
Y. L. Dokshitzer, Sov. Phys. JETP, **46** (1977) 641.
G. Altarelli, G. Parisi, Nucl. Phys., **B126** (1977) 298.

[41] Y. Balitsky, L. N. Lipatov, Phys. Rev. Lett., **28** (1978) 822.
E. A. Kuraev, L. N. Lipatov, V. S. Fadin, Phys. Rev. Lett. **44** (1976) 443.
E. A. Kuraev, L. N. Lipatov, V. S. Fadin, Phys. Rev. Lett. **45** (1977) 199.

[42] F. Halzen, A. D. Martin, *QUARKS AND LEPTONS: An introductory course in modern particle physics*, Wiley, 1984.

[43] H. Abramowicz, A. Caldwell, *HERA Collider Physics*, DESY 98-192, December 1998, hep-ex/9903037.

[44] L. Stanco, *Photoproduction at HERA and the behaviour of the photon*, Proceeding of the *Workshop on Two-Photon Physics at LEP and HERA*, Lund, 26-28 May, 1994, 104.

[45] C. F. Weizsäcker, Z. Phys. **88** (1934) 612;
E. J. Williams, Phys. Rev. **45** (1934) 729.

[46] G. Schuler, Proceedings of the Workshop *Physics at HERA*, vol. 1, Hamburg 1992, 461;
Nucl. Phys. **B407** (1993) 539.

[47] J.J. Sakurai, Ann. Phys. **11** (1960) 1.

[48] R. J. De Witt, L. M. Jones, J. D. Sullivan, D. E. Willen, H. W. Wyld, Phys. Rev. **D19** (1979) 2046.

[49] V. N. Gribov, L. N. Lipatov, Sov. J. Nucl. Phys., **15** (1972) 438.
L. N. Lipatov, Sov. J. Nucl. Phys., **20** (1975) 96.
Y. L. Dokshitzer, Sov. Phys. JETP, **46** (1977) 641.
G. Altarelli, G. Parisi, Nucl. Phys., **B126** (1977) 298.

[50] B. R. Martin, G. Shaw, "Particle Physics", Wiley 1992.

[51] D. H. Perkins, *Introduction to High Energy Physics*, Addison Wesley (1987)

[52] J. F. Owens, Phys. Rev. **D21** (1980) 52.

[53] H1 Collab., T. Ahmed et al., Phys. Lett. **B297** (1992) 205.
ZEUS Collab., M. Derrick et al., Phys. Lett. **B297** (1992) 404.

[54] ZEUS Collab., M. Derrick et al., Phys. Lett. **B322** (1994) 287.

[55] ZEUS Collab., M. Derrick et al., Phys. Lett. **B348** (1995) 665.

[56] ZEUS Collaboration; J.Breitweg et al. The European Physical Journal **C1** (1998) 109-122.

[57] ZEUS Collab., M. Derrick et al., Phys. Lett. **B384** (1996) 401.

[58] NA14/2 Collab., M. P. Alvarez et al., Z. Phys., **C60** (1993) 53.

[59] G. Bellini, Proc. of Les Rencontres de Physique de la Vallée d'Acoste, La Thuille, 1994.

[60] E691 Collab., J. C. Anjos et al., Phys. Rev. Lett., **62** (1989) 513.
E691 Collab., J. C. Anjos et al., Phys. Rev. Lett., **65** (1990) 2503.

[61] S. Frixione et al. "Heavy-Quark Production", hep-ph/9702287.

[62] R. K. Ellis, P. Nason, Nucl. Phys., **B312** (1989) 551.

[63] S. Dawson, P. Nason, R. K. Ellis, Nucl. Phys., **B303** (1988) 607.

[64] G. Altarelli, Phys. Rep., **81** (1982) 1.

[65] Ya. I. Kogan, M. A. Shifman, Yad. Fiz. **38** (1983) 1045.

[66] M. Cacciari, "Hadronic Production of Heavy Quarks", DESY 97-156, To appear in the Proceedings of the Ringberg Workshop "New Trends in HERA Physics", 25-30 May 1997.

[67] W. Beenakker, H. Kuijf, W. L. van Neerven, J. Smith, Phys. Rev. **D40** (1989) 54.

[68] M. L. Mangano, P. Nason, G. Ridolfi, Nucl. Phys., **B373** (1992) 295.

[69] S. Frixione et al., Phys. Lett., **B348** (1995) 633.
S. Frixione et al., Nucl. Phys., **B454** (1995) 3.

[70] B. A. Kniehl et al., Z. Phys. **C76** (1997) 677.
J. Binnewies et al., DESY 97-241, hep-ph/9712482, Phys. Rev. D (1998) in print.

[71] J. Binnewies et al., Z. Phys. **C76** (1997) 677.

[72] M. Cacciari, M. Greco, Phys. Rev. **D55** (1997) 7134.
M. Cacciari, M. Greco, S. Rolli, A. Tanzini, Phys. Rev. **D55** (1997) 2736.

[73] M. Drees, R. M. Godbole, Phys. Rev., **D39** (1989) 169.

[74] R. K. Ellis, Z. Kunszt, Nucl. Phys., **B303** (1988) 653.

[75] S. Frixione, M. Mangano, P. Nason, G. Ridolfi, Nucl. Phys., **B412** (1994) 225.

[76] M. L. Mangano, P. Nason, G. Ridolfi, Nucl. Phys., **B405** (1993) 507.

[77] B. Mele, P. Nason, G. Ridolfi, Nucl. Phys., **B357** (1991) 409.

[78] M. Cacciari, M. Greco, Z. Phys. **C69** (1996) 459.

[79] ZEUS Collaboration; J.Breitweg et al., "Measurement of inclusive $D^{*\pm}$ and associated dijet cross sections in photoproduction at HERA", DESY 98-085 (July 1998), accepted by The European Physical Journal - MS 1017.

[80] ZEUS Collaboration; J.Breitweg et al., Phys. Lett. **B401** (1997) 192-206.

[81] A. D. Martin, W. J. Stirling, R. G. Roberts, Phys. Lett. **B354** (1995) 155.

[82] M. Glück, E. Reya, A. Vogt, Phys. Rev. **D46** (1992) 1973. M. Glück, E. Reya, A. Vogt, Phys. Rev. **D45** (1992) 3986.

[83] C. Peterson et al., Phys. Rev. **D27** (1983) 105.

[84] J. Chrin, Z. Phys. **C36** (1987) 163.

[85] CTEQ collaboration, MSUHEP-60416, CTEQ-604.
H. Lai et al., Phys. Rev. **D55** (1997) 1280.

[86] ARGUS Collab., H. Albrecht et al., Z. Phys., **C52** (1991) 353.
OPAL Collab., R. Akers et al., Z. Phys., **C67** (1995) 27.

[87] M. Wing, "The study of Heavy Quark Production in High E_T Photoproduction at HERA using the ZEUS Detector", Ph.D. Thesis, January 1999.

[88] ZEUS Collaboration; J.Breitweg et al., Phys. Lett. **B437** (1998) 432.

[89] Talk given at 29TH International Conference On High-Energy Physics, 22-30 Jul 1998 , Vancouver, Canada: and proceedings, B.Naroska for the H1 Collaboration, "Photoproduction of Υ Mesons at HERA".

[90] L. L. Frankfurt, M. F. McDermott, M. Strikman, "Diffractive Photoproduction of Υ at HERA", DESY 98-196.

[91] Y. Tsipolitis, "First Observation of Open b Production at HERA", Talk given at DIS98 and proceedings, Brussels, 1998.
H1 Collaboration, C. Adloff et al., "Measurement of Open Beauty Production at HERA", DESY 99-126, hep-ex/9909029 / Phys. Lett. **B467** (1999) 156-164.

[92] ZEUS Collaboration,J. Breitweg *et al.*, "Measurement of the Beauty Photoproduction Cross Section at HERA for Events with a Lepton and Two Jets", to appear on the Proceedings of the conference EPS-HEP 1999, Tampere, Finland.

[93] P. Nason, S. Dawson, R. K. Ellis, Nucl. Phys., **B327** (1989) 49.
erratum:
P. Nason, S. Dawson, R. K. Ellis, Nucl. Phys., **B335** (1990) 260.

[94] W. Beenakker, W. L. van Neerven, R. Meng, G. A. Schuler, J. Smith, Nucl. Phys. **B351** (1991) 507.

[95] UA1 Collab., C. Albajar et al., Phys. Lett. **B256** (1991) 121.
erratum:
UA1 Collab., C. Albajar et al., Phys. Lett. **B262** (1991) 497.

[96] CDF Collab., F. Abe et al., Phys. Rev. Lett. **71** (1993) 500.
CDF Collab., F. Abe et al., Phys. Rev. Lett. **71** (1993) 2396.
CDF Collab., F. Abe et al., Phys. Rev. Lett. **68** (1992) 3403.
CDF Collab., F. Abe et al., Phys. Rev. **D50** (1994) 4252.
CDF Collab., F. Abe et al., Phys. Rev. Lett. **69** (1992) 3704.
CDF Collab., F. Abe et al., Phys. Rev. Lett. **71** (1993) 2537.

[97] D0 Collab., S. Abachi et al., Phys. Rev. Lett. **74** (1995) 3548.
D0 Collab., S. Abachi et al., Phys. Lett. **B370** (1996) 239.

[98] H1 Collaboration, C. Adloff et al., Z. Phys., **C72** (1996) 593 .

[99] J. Smith, W.L. van Neerven, Stony Book Report, ITP-SB-91-40 (1991).

[100] B. Andersson, G. Gustafson, G. Ingelman, T. Sjöstrand, Phys. Rep. **97** (1983) 33.

[101] PYTHIA 5.7; H.-U. Bengtsson, T. Sjöstrand, Computer Phys. Commun. **46** (1987) 43.

[102] S. Bentvelsen, J. Engelen, P. Kooijman, in "Physics at HERA", Vol.1, edited by W. Buchmüller, G. Ingelman (Proceedings of the Workshop, Hamburg 1991), p.23.

[103] F. Jacquet, A. Blondel, "Proceedings of the study of an *ep* facility for Europe", DESY 79-48 p.391.

[104] P. J. Bussey, EUCELL, ZEUS PHANTOM Users Library.

[105] P. de Jong, 'Status of the Uranium Calorimeter Reconstruction Software', ZEUS Note 92-019

[106] S. Catani, Yu. L. Dokshitzer and B. R. Webber, Phys. Lett. **B285** (1992) 291.

[107] S. Catani, Yu. L. Dokshitzer, M. H. Seymour, B. R. Webber, Nucl. Phys. **B406** (1993) 187.

[108] J. M. Butterworth, L. Feld, R. L. Saunders, 'Measurement of Dijet Cross Sections in Photoproduction at HERA', ZEUS Note 97-057.

[109] J. Huth et al., Proc. of the 1990 DPF Summer Study on High Energy Physics, Snowmass, Colorado, edited by E. L. Berger (World Scientific Singapore, 1992) p.134

[110] M. Seymour; pre-print hep-ph/9707349. "Jet Phenomenology". Contribution to "Proceedings of Les Rencontres de Physique de la Vallée d'Acoste: Results and Perspectives in Particle Physics" La Thuile, Italy March 2-8, 1997.

[111] S. D. Ellis, D. E. Soper, Phys. Rev. **D48** (1993) 3160.

[112] G. Abbiendi " Global Tracking of muons in the Barrel and Rear region", ZEUS-Note 99-063.

[113] S. Limentani, M. Posocco e L. Stanco, "Muon Barrel Reconstruction", ZEUS-Note 92-027 (1992).

[114] V. Innocente, M. Maire and E. Nagy, "GEANE: average tracking and error propagation package", procs. of MC91: Detector and event simulation in high energy physics (Amsterdam, 1991).

[115] L. Bellagamba "MVMATCH: A package to match FMUON tracks with Central Detectors", ZEUS-Note 96-051.

[116] "Application of Kalman filtering to tracks and vertex fitting", R. Fruhwirth, NIM **A262** (1987) 444-450.

[117] HERWIG 5.9; G. Marchesini, B. R. Webber, G. Abbiendi, I. G. Knowles, M. H. Seymour, L. Stanco, Computer Phys. Commun. **67** (1992) 465.

[118] GEANT 3.13, R. Brun, CERN DD/EE/84-1 (1987).

[119] ZGANA, ZEUS trigger simulation library, Els de Wolf (editor) et al.

[120] P. P. Chen, *The Entity-Relationship Model–Toward a Unified View of Data*,
ACM Trans. on Database Systems 1 (1976), 9.

[121] M. Sutton, "Charm in Dijet Photoproduction at HERA", Ph.D. Thesis, September 1998.

[122] ZEUS Collaboration; M.Derrick et al., "Measurement of the Cross Section for the Reaction Gamma p $\rightarrow$ J/Psi p with the ZEUS Detector at HERA DESY 95-052 (March 1995) Phys. Lett. **B 350** (1995) 120-134
ZEUS Collaboration; J.Breitweg et al., "Measurement of Elastic J/Psi Photoproduction at HERA" DESY 97-060 (March 1997) Z. Phys. **C75** (1997) 2, 215-228
ZEUS Collaboration; J.Breitweg et al. , "Measurement of Inelastic J/Psi Photoproduction at HERA" DESY 97-147 (July 1997) Z. Phys. **C76** (1997) 4, 599-612

[123] R. Brugnera in private communication, April 1999.

[124] M. Turcato and R. Brugnera in private communication, April 1999, results at heavy flavour working group.

[125] N. Coppola, Internal Note

[126] R. Nania, June 1999, Internal Note.

[127] `noise96s.cpp`, Noise suppression routine, PHANTOM Users Library.

[128] `calcorr.fpp`, Calorimeter correction routine, PHANTOM Users Library.

[129] J. Repond, "Jet Energy Corrections", ZEUS Note 96-104.

[130] H. Abramowicz, A. Caldwell, R. Sinkus, "Neural Network Based Electron Identification in the ZEUS Calorimeter", DESY 95-054.
R. Sinkus, Nucl. Instrum. Methods **A361** (1995) 290.

[131] C. Coldewey et al., "D* and associated dijet Photoproduction at HERA", ZEUS Note 98-047, 07/98.

[132] G. L. Kotkin et al., Z. Phys. **C39** (1988) 61.

[133] ZEUS Collaboration, M. Derrick et al., Z. Phys., **C72** (1996) 399.

[134] ZEUS Preliminary, shown to the DESY PRC of January 1999.

[135] G. Ingelman, J. Rathsman e G.A. Schuler, Comp. Phys. Com. **101**, 135 (1997)

[136] N. Dyce and K. Long, "ZEUS track extrapolation algorithm, issue 1", ZEUS-Note 90-128.

[137] G. Bruni, G. Iacobucci, T. P. Shah and L. Stanco, "The Global Tracking reconstruction program TGRECON", ZEUS-Note 94-009.

[138] W. Wittek, "Transformation of error matrices for different sets of variables which describe a particle trajectory in a magnetic field", EMC internal note EMCSW 80/39.

[139] S. Nussinov, Phys. Rev. Lett., **35** (1975) 1672.
G. J. Feldman et al., Phys. Rev. Lett., **38** (1977) 1313.

[140] OPAL Collaboration, K. Ackerstaff et al., Euro. Phys. J., **C1** (1998) 439.

[141] R. van Woudenberg, "Study of Charm Production at HERA using the ZEUS Detector", Ph.D. Thesis, September 1995.

[142] W. Verkerke, "Measurement of Charm Production in Deep Inelastic Scattering", Ph.D. Thesis, June 1998.

[143] R.M. Barnett et al., Phys. Rev. **D54** , 1 (1996) and 1997 off-year partial update for the 1998 edition available on the PDG WWW pages (URL: `http://pdg.lbl.gov/`).

[144] M. Glück, E. Reya, A. Vogt, Z. Phys. **C53** (1992) 127.

[145] S. Mengel, J. Lane, F. Corriveau, "The Magnetic Field in the ZEUS Central Tracking Region", ZEUS Note 92-098 (06/11/92)

[146] V. Noyes et al., "ZEUS Interaction Region Upgrade", ZEUS Note 97-035 (05/97)

[147] J.A.M. Vermaseren, *Axodraw,* Comp. Phys. Comm. 83 (1994), 45-58.

This thesis was typeset with LaTeX 2_ε. Plots were made using the CERN package PAW and incorporated into the LaTeX 2_ε-document using the `PSFIG` package. Most other figures were made with Axodraw [147], using PostScript and `dvips` from Radical Eye Software.

List of Figures

1.1 Scheme of the *ep* collider HERA, main design values are shown. The South zone accommodates the ZEUS detector. 5
1.2 Integrated luminosity delivered by HERA (a) and usable for ZEUS physics analysis (b), as of November 1999. 7
1.3 Cross sections of the ZEUS detector along (a) and perpendicular to the beam line (b). 9
1.4 Exploded axonometric view of the ZEUS detector with its components. For a description of the parts it is made of see the text. F, R, B have this meaning: F(*forward*) is in the direction of the outgoing proton, R(*rear*) is in the direction of the outgoing electron, B(*barrel*) is central. 11
1.5 Global HERA and ZEUS coordinate system. 12
1.6 Vertical longitudinal cross section of the inner tracking detectors. 13
1.7 (Negatively charged) Track in the CTD; the 'displaced' hits in the even numbered layers show the effect of the stereo angle of the wires. Ghost hits are also displayed. 14
1.8 The dE/dx versus momentum of tracks reconstructed in the CTD with curves illustrating the particle classes. 16
1.9 a) Schematic view of the ZEUS uranium calorimeter showing the division into three parts: FCAL, BCAL and RCAL. b) Tower structure in FCAL and RCAL; stacked towers together form a module; the BCAL is organized similar to the FCAL, but there EMC cells are projective in the RZ plane and the towers are wedge-shaped. 18
1.10 Single PMT time resolution as function of energy of a random Calorimeter cell, upper four plots. Single PMT time resolution for events with deposited energy larger than 1 GeV for a random Calorimeter cell, lower four plots. It is to be noted that the timing information is used if both the PMT's of the same cell have given a signal, in this case the time resolution is enhanced, respect the one shown in the plots. 19
1.11 A drawing of the Forward Muon Spectrometer. 23
1.12 Three-dimensional view of the chambers. 24

1.13 (a) Section of a BMUON chamber (we can see the Honeycomb structure). (b) Scheme of a BMUO chamber. 25
1.14 The monitor for the measure of the Luminosity (LUMI). 26
1.15 Three-dimensional view of the LPS. 27
1.16 Overview of the ZEUS trigger and data-acquisition system. The component trigger systems, pipelines and buffers are shown, together with the global trigger systems. 29
1.17 Timing 32

2.1 Lepton-proton scattering. Figure (a) represents neutral-current DIS, while figure (b) displays charged-current DIS. The four-momenta are indicated in brackets. 35
2.2 The first order splitting functions $P_{jk}\left(\frac{x}{y}\right)$ used in the DGLAP equations. 41
2.3 Parton evolution diagram showing the k_t ordered gluon emissions. 42
2.4 The differential cross section versus Q^2 for neutral and charged current scattering as measured by ZEUS in the 1993-1997 data sets. The results are compared to Standard Model expectations separately for e^+p and e^-p scattering. The cross sections all become comparable near $Q^2 = 10000$ GeV^2,as expected from electroweak unification [43]. 43
2.5 Leading order direct processes; (a) QCD Compton and (b) Boson gluon fusion. 46
2.6 Examples of leading order resolved processes. 47
2.7 General Leading Order picture for direct and resolved processes. . 48
2.8 Diagram for $e\gamma$ diagram with a virtual photon, γ^*, probing an on-shell photon, γ. 50
2.9 The $x_\gamma^{\rm obs}$distribution in dijet events for data (black dots) compared with HERWIG with and without MPI (solid line and dotted line), and PYTHIA with MPI (dashed line) Monte Carlo generators. The shaded area represents direct only events as generated by HERWIG and the vertical line is the experimental cut to separate direct and resolved processes. 51
2.10 Dijet angular cross-sections for resolved (black dots) and direct (open dots) compared to LO and NLO QCD predictions and HERWIG and PYTHIA Monte Carlo. 52
2.11 Total pair cross-section for c production in γN collisions from the NA14 [58], E687 [59] and E691 [60] collaborations compared to QCD predictions. The bands represent (for a given charm mass) the variation due to the choice of the renormalisation scale, where the limits shown here are, $\mu_R = m_c/2$ and $\mu_R = 2m_c$ (from [61]). . 54

2.12 Distribution in p_T^2 for charmed hadrons from the E687 [59] (left) and E691 [60] (right) collaborations compared to NLO pQCD (m_c = 1.5 GeV) and NLO pQCD with non-perturbative effects (from [61]). 55

2.13 Comparison between the massive (FMNR) and massless (PFF) calculations for charm photoproduction p_T distribution (from [66]). 57

2.14 Differential cross-section, $d\sigma/dp_\perp^{D^*}$, for D^* photoproduction for two decay channels. The data is compared to massive calculations and the two massless calculations. 60

2.15 Differential cross-section, $d\sigma/d\eta^{D^*}$, for D^* photoproduction for two decay channels in ranges of $p_\perp^{D^*}$. The data is compared to massive calculations and the two massless calculations. 61

2.16 CDF data on the integrated b-quark p_T distribution compared to NLO QCD (from [61]). 63

2.17 Comparison between experimental data and theory for the integrated b-quark p_T distribution (from [61]). 64

3.1 Geometric meaning of the $p_T^{\rm rel}$ variable. 75

4.1 ZEUS Programs 78

4.2 Hadron level Monte Carlo predictions for p_T^{rel} in the cross-section region to be measured. 84

4.3 Jet resolutions. The dependence of jet parameters on each other is shown separately for direct (open squares) and resolved (open triangles). The dependence of $E_T^{HADjet}/E_T^{CALjet}$, $\phi^{HADjet}-\phi^{CALjet}$ and $\eta^{HADjet}-\eta^{CALjet}$ on η^{CALjet} and ϕ^{CALjet} is shown. 87

4.4 The ratio of E_T^{HADjet} and E_T^{CALjet} versus E_T^{CALjet} in bins of η. The points and fit lines are shown for direct (open squares, dashed line), resolved (open triangles, dotted line) and resolved and direct combined (solid dots, solid line). The fit parameters shown are for the fit to the combined sample using the correction function, $C(E_T^{CALjet},\eta^{CALjet})$ 88

4.5 Result on the jet energy resolutions when applying the jet energy corrections. The resolutions are shown again for direct (open squares) and resolved (open triangles) separately. 89

4.6 Correction of the measurement of y. The correlation of y_{JB} and y_{true} (Left) is shown. Also displayed is the dependence of y_{JB}/y_{true} on $x_\gamma^{\rm obs}$ for direct (open circles) and resolved (open squares) and the combined sample (solid points) with the polynomial fit. 90

4.7 Effect of the y_{JB} correction for direct (right) and resolved (left) separately on the correlation (top) and projection (bottom). . . . 91

5.1 Disposition of the towers of the first level of trigger of the CAL along the beam axis. 98

5.2 Trigger efficiency of the outer muon chamber in the barrel region ($34° < \theta < 140°$) in the data as a function of the momentum p of the muon; the FLT branch taken in consideration is the 14 (see Section 5.4.1). 99

5.3 Trigger efficiency of the outer muon chamber in the rear region ($140° < \theta < 177°$) in the data as a function of the momentum p of the muon; the FLT branch taken in consideration is the 15 (see Section 5.4.1). 99

5.4 FMUON efficiency values $\epsilon(\eta)$ as a function of the pseudorapidity η^{μ} of the muon, the black squares are the measured data points, the solid line is the polynomial fit with the parameters as shown in the top right corner. 102

5.5 Effect of the cut to remove DIS electrons on Q^2 (Q in GeV) for the event simulated using the PYTHIA Monte Carlo. 105

5.6 The efficiency of the Dijet TLT as a function of TLT jet E_T threshold for offline thresholds 4, 6, 8 and 10 GeV. The dashed line shows the actual TLT threshold of 4 GeV [131]. Top plot, jets reconstructed off line using EUCELL, bottom, jets reconstructed using KTCLUS. 106

5.7 Distribution for the momentum p of a muon from a decays from a B meson (solid line), D meson (dashed line) and a light hadron (dotted line). 107

5.8 In the plots it is visible the resolution on the value of the J/ψ mass that can be reached with the use of the central tracking detector and the forward muon spectrometer: at the bottom there is the mass spectrum as it is obtained using the FMUON plus CTD detectors, in the middle the one using the informations coming from the FMUON and CTD component and using the Mpmatch algorithm, at the top the resolution of the CTD only reconstruction. It is to be noted that the use of the Mpmatch package improves the mass resolution as can be seen from the middle plot, the fit is a Gaussian one. 110

5.9 In the plots it is visible the comparison between Monte Carlo (dashed line) and data (solid line) using control variables for dijet events where a Mpmatch exists. A much improved agreement can be seen. We have applied a cut requiring at least a FMUON-track with 4 or more associated planes and a transverse momentum larger than 1.5 GeV/c. (a) Momentum p of the matched track, (b) pseudorapidity η of the matched track, (c) azimuthal angle ϕ of the matched track, (d) transverse momentum to the beam axis p_T of the matched track; the histograms are normalized, so that we can compare the differences in the shapes of the distributions. . . 111
5.10 Muon (a) and jet (b) multiplicities in the data for events that satisfy all the introduced cuts. 112
5.11 Distribution of the angular distance between a muon and its nearest jet in a beauty production event (a). Distribution of the angular distance between a decayed beauty hadron and its muon (b). . . . 113
5.12 $p_T^{\rm rel}$ distributions in the data, beauty, charm and light flavour Monte Carlo, for the sectors covered by the BRMUON detector. We can notice how, while the distributions for charm and light flavours are rather similar, the one of the beauty is characterized by the presence of much more events having large values of $p_T^{\rm rel}$. . 116
5.13 $p_T^{\rm rel}$ distributions in the data, beauty, charm and light flavour Monte Carlo, for the sectors covered by the FMUON spectrometer. We can notice how, while the distributions for charm and light flavours are rather similar, the one of the beauty is characterized by the presence of much more events having large values of $p_T^{\rm rel}$. . . . 117
5.14 Pseudorapidity (Left) and transverse momentum (Right) resolutions of the tracks from semi-leptonic decays to muons in the barrel and rear sector of the detector tagged by the BREMAT package. . 118
5.15 Pseudorapidity (Left) and transverse momentum (Right) resolutions of the tracks from semi-leptonic decays to muons in the forward sector of the detector tagged by the Mpmatch package. . . . 119
5.16 Pseudorapidity (Left) and transverse energy (Right) resolutions of the two highest E_T jets in events containing a semi-leptonic decay to a muons. 119
5.17 Resolutions of $x_\gamma^{\rm obs}$ and $p_T^{\rm rel}$ of events containing a muon in the final state. 120
5.18 Data (dots) and MC (solid line) for the samples of events selected in the BRMUON regions. The MC is a mixture of beauty, charm and light quark contributions according to the percentage given by the fits. The pseudorapidities of the associated jets are shown in (a), the pseudorapidities of the associated μ in (b), the transverse energies of the associated jets in (c) and the transverse momenta of the associated μ (d). 122

5.19 Data (dots) and MC (solid line) for the samples of events selected in the BRMUON regions. The MC is a mixture of beauty, charm and light quark contributions according to the percentage given by the fits. The quantity y ($y_{JB}^{\rm corr}$) of the event (left) and the angular distance between the associated muon and jet (right) are drawn, for the latter the dots and line show the distributions of Data and Monte Carlo before the $\delta r < 1.5$ cut is applied. 122

5.20 Data (dots) and MC (solid line) for the samples of events selected in the FMUON regions. The MC is a mixture of beauty, charm and light quark contributions according to the percentage given by the fits. The pseudorapidities of the associated jets are shown in (a), the pseudorapidities of the associated μ in (b), the transverse energies of the associated jets in (c) and the transverse momenta of the associated μ (d). 123

5.21 Data (dots) and MC (solid line) for the samples of events selected in the FMUON region. The MC is a mixture of beauty, charm and light quark contributions according to the percentage given by the fits. The quantity y ($y_{JB}^{\rm corr}$) of the event (left) and the angular distance between the associated muon and jet (right) are drawn, for the latter the dots and line show the distributions of Data and Monte Carlo before the $\delta r < 1.5$ cut is applied. 123

6.1 (a) Distribution of the number of events in $p_T^{\rm rel}$ in the BRMUON region. The experimental data (dots) are compared to a PYTHIA MC (solid line) prediction which has been normalized to the data. The beauty component (dotted line) and the charm plus light quark component (dashed line) are shown according to the percentages given by a fit. (b) Distribution of the number of events in $x_\gamma^{\rm obs}$in the BRMUON region. The experimental data are compared to PYTHIA MC (open histogram) with a mixture of beauty and charm plus light quark components according to the percentage given by the fit. The components from direct processes (vertically hatched area) and from resolved processes (diagonally hatched area) are shown separately. 128

6.2 (a) Distribution of the number of events in p_T^{rel} in the FMUON region. The experimental data (dots) are compared to a PYTHIA MC (solid line) prediction which has been normalized to the data. The beauty component (dotted line) and the charm plus light quark component (dashed line) are shown according to the percentage given by a fit. (b) Distribution of the number of events in x_γ^{obs}in the FMUON region. The experimental data are compared to PYTHIA MC (open histogram) with a mixture of beauty and charm plus light quark components according to the percentage given by the fit. The components from direct processes (vertically hatched area) and from resolved processes (diagonally hatched area) are shown separately. 129

6.3 BRMUON sample, summary of the systematic errors on the cross section, the values are fractional variations on the central value see Equation (6.13). The order of the plotted points is the same as the one of the listed errors in Table 6.3. 137

6.4 FMUON sample, summary of the systematic errors on the cross section, the values are fractional variations on the central value see Equation (6.13). The order of the plotted points is the same as the one of the listed errors in Table 6.4. 138

6.5 Cross section in p_T^{rel}, where the data points are shown with statistical (inner bars) and statistical and systematical errors added in quadrature (outer bars). The energy scale uncertainty is shown as the shaded band. The experimental data is compared to HERWIG MC (open histogram) predictions, which have been scaled up by a factor of 3.7. The components from beauty processes (vertically hatched histogram) and from charm plus light quark processes (diagonally hatched histogram) are shown separately [92]. 141

A.1 Simulation of the global trajectory of a muon. 148

List of Tables

1.1 Main design parameters of HERA [1] 4

1.2 Summary table of the integrated luminosity collected with the ZEUS detector since the year 1992. 8

1.3 Coverage of UCAL calorimeter parts and dimensions of cells. . . . 17

1.4 List of the minimum requirements that have to be met for the availability of the various calorimeter timing. 30

2.1 Predictions for the total $ep \to b\bar{b}X$ production cross section by several next to leading order calculations (the calculation of Eichler and Kunszt does not contain virtual correction), m_b is the mass of the beauty quark. The column denoted "Scheme" indicates the renormalization scheme used. 65

2.2 Dependence of the open quark b production cross section, expressed in nb, on different parameters. The default parameter setting corresponds to $\mu_R = \mu_F = m_b = 4.75$ GeV [75]. 66

2.3 Partial and total cross sections (measured in nb) for the process $\sigma(ep \to b\bar{b}X)$ at HERA ($\sqrt{s} = 314\ GeV$) within the renormalization schemes of DIS and $\overline{MS}$, the value of the mass of the b-quark is $m_b = 4.75\ GeV$ (as in ref. [99]). 67

4.1 List of the cuts applied on each event in the samples generated with the PYTHIA 6.1 program for heavy flavour photoproduction of charm and beauty quarks. 81

4.2 List of the cuts applied on each event in the samples generated with the HERWIG 5.9 program for heavy flavour photoproduction of charm and beauty quarks. 81

4.3 List of the cuts applied on each event in the samples generated with the PYTHIA 5.9 program for *light* flavour photoproduction of dijet events. 83

4.4 List of the cuts applied on each final state particle to define an *energetic particle* in events generated with the PYTHIA 5.9 program for *light* flavour photoproduction of dijet events, polar angles are measured in radians, p_T and p_L are the transverse and longitudinal momentum with respect to the beam axis. It is to be noted that the forward, barrel and rear sectors overlap geometrically. If no track satisfy any of these cuts the event is discarded. 86

5.1 Ratio of the number of events that have both the inner and outer chamber tag over the number of events that have just the inner chamber tag, for the samples described in the text. It is shown for comparison the same ratio in the case of data. 109
5.2 Number of events that compose the final sample, for the forward (FMUON) and barrel-real (BRMUON) regions. 113

6.1 Systematic errors on the determination of the percentage of beauty events p_b in the final samples as obtained by changing the composition of the Monte Carlo data. The values that are shown are the deviation from the central value. 127
6.2 Systematic uncertainties on the determination of the percentage of beauty events p_b in the final samples as obtained by changing the binning or the range involved in the measure. The values that are shown are the deviation from the central value. 130
6.3 BRMUON sample, summary of the systematic errors on the cross section, the values are fractional variations on the central value (see Equation (6.13)). 135
6.4 FMUON sample, summary of the systematic errors on the cross section, the values are fractional variations on the central value (see Equation (6.13)). 136

Acknowledgements

Quite a number of people helped me during the years of my D.Phil. studies.

First of all I am very grateful to my supervisor Prof. Maurizio Basile, for his continuous support, encouragement and particularly his inexhaustible patience in reading and commenting on this thesis.

I am very grateful to Dr. L. Gladilin, Dr. G. Iacobucci, Dr. R. Nania, Dr. L.E. Sinclair and Prof. J. Terron for enlightening discussions on theoretical aspects of heavy flavour physics and for always being prepared to comment on my reports, notes and this thesis.

I have to acknowledge Dr. R. Brugnera Prof. R. Carlin and Prof. L. Stanco both for the enlightening discussions on all the aspects of physics, their friendship and all the personal advices they have always been willing to give me.

I have to thank Dr. G. Abbiendi and Dr. L. Bellagamba for having provided me with their matching packages without which my research would have been much more difficult and much less profitable.

The work within the ZEUS collaboration and especially in the HFL group has always been enjoyable. I thank the coordinators Dr. D. Bailey, Dr. L. Gladilin and Dr. W. Zeuner for their encouragement, hints and the fruitful atmosphere they have been able to set up in the group. Special thanks go to Dr. M. Hayes and Dr. M. Wing for their ready answers they have always been able to give me and for their invaluable help just before the Tampere Conference, without them the results of my study would not have been published at that time.

I have to thank all the system administrators I met during these years: they have been listening quietly to all my complains on computers and on many other items.

The financial support of the University of Bologna and of the Istituto Nazionale di Fisica Nucleare gave me the opportunity to concentrate on my study and the capability to enjoy a long time in Germany.

Even if I have not been able to go hiking on the mountains, the last years have been full of happy things for my life. I have met quite a lot of people and appreciated their friendship. They have always been able to make me feel happy even when I was in bad or deep moods and I really want to thank all of them. Their list is long and I can just cite a few of them: Raphael, Andreas and Sonja, Alberto and Silvia, Dominik, Alessandro Bertolin, Shiva and Mohsen,

Enrico, Alessandro Polini, Davide, Alessia, Ali, Kristina, Peter, Bill, Lars, Mauricio, Vincenzo, Stefano, Patrick, Maria Carmela and Mario Carmelo, Antonio, Sean, Chris, Richard, Petra, Marc, Doug, Monica, Marcella, Roberto and Laura, Torsten Wildschek. The life with them has always been a joy. Some of them have even made me a double-uncle (or triple) with Davide and Aaron Yanick (Aidan William).

I have to apologize with the Italian friends: I have betrayed them not joining in any mountain trip they have made these last two years: Francesco (Checchino), Lorenzo (Lilloga) Marco, Michele (Calzino-tirato), Stefano (my Godfather) and all the people of the Royal Velic Club.

Finally, I would like to express my gratitude to my parents and relatives who have always been patient and understanding. They have always encouraged me to make the most out of opportunities.